MULTIMESSENGER ASTRONOMY WITH GRAVITATIONAL WAVES FROM CORE-COLLAPSE SUPERNOVAE

BY
MAREK JAN SZCZEPAŃCZYK

A Dissertation
Submitted to the Department of Physical Sciences
In partial fulfillment of the requirements
for the degree of
Doctor of Philosophy in Engineering Physics

08/2018
Embry-Riddle Aeronautical University

MULTIMESSENGER ASTRONOMY WITH GRAVITATIONAL WAVES FROM CORE-COLLAPSE SUPERNOVAE

by

Marek Jan Szczepańczyk

This dissertation was prepared under the direction of the candidate's Dissertation Committee Chair, Dr. Michele Zanolin, Professor, Prescott Campus, and Dissertation Committee Members Dr. Jo van den Brand, Professor, Nikhef Amsterdam, Dr. Sergey Klimenko, University of Florida, Gainesville, Dr. Anthony Mezzacappa, Professor, ORNL, Dr. Sergey Drakunov, Professor, Daytona Beach Campus. and has been approved by the Dissertation Committee. It was submitted to the Department of Physical Sciences in partial fulfillment of the requirements of the degree of
Doctor of Philosophy in Engineering Physics

THESIS COMMITTEE:

Dr. Michele Zanolin,
Committee Chair

Dr. Jo van den Brand, Amsterdam
Committee Member

Dr. Sergey Klimenko, Gainesville
Committee Member

Dr. Anthony Mezzacappa, ORNL
Committee Member

Dr. Sergey Drakunov,
Committee Member

Dr. Matthew Zettergren,
Graduate Program Chair,
Engineering Physics

Dr. Terry Oswalt,
Department Chair,
Physical Sciences

Dr. Karen Gains,
Dean, College of Arts and Sciences

Dr. Karen Gains,
Dean of Research and Graduate Studies

What indeed is more beautiful than heaven, which of course contains all things of beauty.
Mikołaj Kopernik (Nicolaus Copernicus, 1473 - 1543)

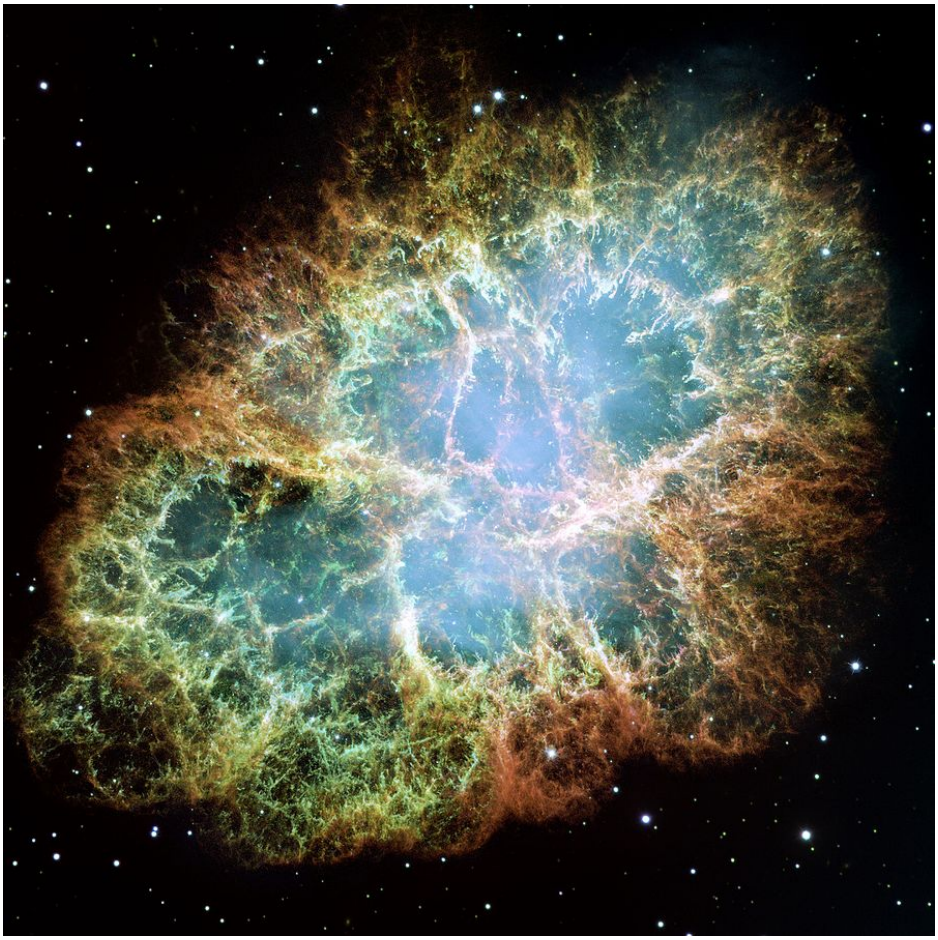

Figure 1: Crab Nebula, a remnant of Core-Collapse Supernova from 1054 A.D. (source [1])

Abstract

The Detection of Binary Neutron Stars on August 17th, 2017 gave birth to Gravitational Wave Multimessenger Astronomy. Core-Collapse Supernovae (CCSNe) are one of the most interesting astrophysical events emitting electromagnetic, neutrino and Gravitational Wave (GW) messengers. In this thesis, I summarize my research regarding Multimessenger Astronomy that can be performed with CCSN. The central problem of my research is the search for GW from CCSNe and the extraction of their physical properties from their signals. I will outline this in context of the current searches and discuss the perspectives with Advanced and Future interferometers.

Acknowledgments

First of all, I am very grateful to my PhD advisor, Dr. Michele Zanolin, for teaching me how to be a scientist. His patient guidance allowed me to systematically explore the worlds of Gravitational Wave Astronomy and the field of Core-Collapse Supernova research. The detection of gravitational waves was a very vital moment for me, my doctorate became an amazing journey. I feel blessed I went through this journey together with Michele.

Another special thanks I want to give to Jasmine Gill, a talented student. We had many great discussions and I have learned a lot through them.

As the LIGO/Virgo Supernova Working Group chair I was involved in many activities of the gravitational wave supernova science. Endless discussions shaped my understanding of the field and allowed me to develop new skills. I want to thank Travis Hansen, Kellie Ault, Anne-Marie Bals, Dr. Sergio Gaudio and Sophie Schwalbe for many hours we spent in working with different projects. My understanding of how the gravitational wave data should be analyzed is heavily based on Dr. Sergey Klimenko and Dr. Gabriele Vedovato help. I am very grateful for that, and thank you Gabriele for an extroardinary patience in helping me fixig countless issues. Similarly thanks to the rest of cWB team Marco Drago, Francesco Salemi, Claudia Lazzaro for your help. I want to thank Dr. Soma Mukherjee, Dr. Malik Rakhmanov for your support and many discussions, as well as Anton Gribovsky and Satzhan Sitmubakhetov for working toghether. I also want to express gratitude to Dr. Jade Powell and Vincent Roma for deepening my understanding of bayesian analysis, a well as Dr. Marco Cavaglia and Kai Staats who helped me to understand some machine learnig techniques. I thank Dr. Anthony Mezzacappa and Dr. Konstantin Yakunin for their help in understanding the supernova simulations.

During my PhD I gave more than 30 seminars and talks at various conferences in several countries. I met countless number of people I talked with, who allowed me deepen my understanding of what I present in this dissertation.

I am very grateful to my Mom and Dad. Thank you for shaping me who I am today. Thank you my brother and sister to support me in this journey. Also, I would like to thank Shichan Marek Krejpcio from whom I always try to learn a never-give-up attitude.

Contents

List of Tables

List of Figures

Preface

The first detection of a Binary Black Holes system on September 14th, 2015 [19], opened the new field of research of Gravitational Wave Astronomy. Since then, several sources of Gravitational Waves have been detected. The first detection of Binary Neutron Stars together with coincident Electromagnetic counterpart on August 17th, 2017 [21] began the new field of Multimessenger Gravitational Wave Astronomy. This newly born field of research opens unprecedented opportunities to study the dynamics of massive objects and the space distortions they produce. The next decades could bring new discoveries of GWs alone or with coincidence with other messengers.

Core-Collapse Supernovae are great laboratories that we cannot reproduce on Earth. They are huge nuclear fusion reactors creating elements without which planets, everything that we use in our daily life and ourselves would not exist. We know that stars explode and we observe the evolution of their remnants. However, after many decades of studying these powerful explosions, we do not fully understand why they explode. This is also reffered as a *supernova problem*. There are a lot of uncertainties associated with simulating these events that we are unable to constrain with astronomical or neutrino observations. We need to measure the dynamics of the explosions and it can be achieved wih Gravitational Waves.

Core-Collapse Supernovae (CCSNe) are multimessenger astrophysical events, emitting GWs, neutrinos, electromagnetic signals as well as cosmic rays. Each messenger carries different information about the exploding star. GWs are mainly emitted during the initial phase of the collapse and thus carry precious information about the dynamics and inner properties of the exploding stars. Such information include the shock revival mechanism, time evolution and rotational properties of the collapsed core and opportunities to test Kerr geometry with Black Hole formation or find neutrino mass hierarchy.

Central problem

The main purpose of the thesis can be summarized as:

Searching for GW from CCSN and extracting physical information.

The detection and extraction of physical features from GWs produced by CCSNe will require interplay in areas of GW data analysis, electromagnetic and neutrino observation, modeling of CCSNe sources and a deep understanding of GW detectors. CCSN searches can be divided into blind or triggered (by optical and/or neutrino triggers). The scientific potential of the searches and the specific tuning of the algorithms depend greatly on the detectors' noise properties. In this thesis I will present search results with the Initial LIGO/Virgo data as well as O1-O2 LIGO/Virgo data. I will also describe detection perspectives in the Advanced Detector Era and with proposed future interferometers.

During my Ph.D. I also devoted a fraction of my time in establishing the Science priorities of the LIGO/Virgo Supernova Working Group.

Detection perspectives

Detections of GW from CCSNe is a great challenge for several reasons. The energies of GW from CCSNe are orders of magnitude smaller comparable to the energies emitted by binary systems. Also, the rate of supernovae in the nearby universe is very small. Additionally, the GW signals are mostly non-deterministic. This is not the case, for instance, in binary systems.

Addressing the first limitation requires understanding of the distances at which the CCSNe signals become more pronaunced. Previous CCSNe rate estimates are based on optical observations since all supernovae so far were observed only in the electromagnetic spectrum (except SN 1987A when neutrino and light were both observed). This, however, also implies that SNe could have been missed not just because of distance, but also because of other reasons like the partial sky coverage and absorption.

The next Galactic CCSN event will be a great opportunity to study the physics of an exploding star. Since there is a variety of progenitors and possible GWs emitted from CCSNe, even if a specific GW could be detected up to the furthest edge of our Galaxy, we should strive to have the best possible conditions for the detection of all possible CCSNe emission models, including those with unfavorable conditions (like a low mass progenitor with relatively little turbulence). Unfortunately, given that the rate of CCSNe in the Milky Way is small, $\sim$1-2 per century, there is also a need to understand under which conditions, meaningful scientific information can be extracted from extragalactic CCSNe where rates are larger. A particularly interesting range is the Virgo cluster (10-15Mpc) since, in the enclosed volume, it is possible to optically observe a few CCSNe per year (Gill et al, in prep).

I am coauthor of this study to quantify the intrinsic rate of CCSNe in the local universe (up to 20Mpc) and to indentify their most probable locations for future CCSNe searches. In the study we choose 20Mpc in order to identify the distance at which the cummulative rate becomes a few per year and where there are (extreme) emission models which become detectable at distances within current detector sensitivies. I will provide implications to the GW SN searches.

In GW data analysis for short transients, all the approaches range between two methodologies: matched filtering and excess power. Matched filtering is suitable to search for waveforms with fully deterministic signatures and waveforms from binary black holes are great examples and can be calculated from General Relativity (for binary systems it is not possible in the merge phase). On the other side, when waveforms are not known or theory cannot provide a template, an excess power method must be used. A matched filter search allows a much smaller number of degrees of freedom to be explored in the reconstructed signal (and they are all chosen from theory) while pure excess power searches allow the maximum number of degrees of freedom to be set from the interferometer recordings with the extra constraint that temporary consistent traces need to be present in different interferometers. In the LIGO-Virgo Collaboration we started with searching un-modeled GW transients with pure excess power searches and we are progressively reducing the size of the parameter spaces with the aim to move the range sensitivities close to the one of matched filtering approach. The main tool I will be working with, is coherent Wave-Burst. This is the first algorithm to detect GWs, and is very efficient in searching for GW candidates.

New Results

Initial LIGO/Virgo Optically Triggered Search:

- Detection statements of GW from CCSN.
- First visible distance statements on GW SN waveforms.

O1-O2 Optically Triggered Search:

- Detection statements of GW from CCSN.
- First astrophysically interesting E_{GW} constraints
- First model exlcusion statements on CCSN engine based on GW data

Initial LIGO/Virgo Low Energy Neutrino Triggered Search:

- First search for coincident events.

While modeling of CCSNe and GW data analysis have decades long histories, the specialized methods dedicated to detect GW from CCSN have not been developed to the same degree of sophistication. In my thesis, I will discuss new tools and their predictions for GW SN Science. A particularly important case of this research program is the case of a Galactic Supernova.

I will present various studies using different features of CCSNe and their waveform morphologies to make the searches more sensitive. Additionally I will demonstrate how various pieces of information can be used to extract physics from CCSN.

I explore the detectability of GW from a variety of simulations: waveforms from realistic neutrino driven explosion models for slowly- and non-rotating progenitor stars in 2D and 3D as well as rapidly rotating models [22, 23]. I also discuss the scientific potential of semi-analytical and extreme models [24] or BH formation [25, 26].

Thesis Overview

This dissertation is divide into four parts. Part I presents a general overview to the Gravitational Wave Multimessenger Astronomy and Core-Collapse Supernova Science. Part II includes the results from Triggered GW CCSN Searches in the Initial Detector Era. Part III presents the results of the first Optically Triggered GW CCSN Search and detection perspectives in the Advanced Detector Era. Finally, Part IV focuses on detection perspectives with the Future Generation Detectors.

Part I - Introduction to CCSN Multimessenger Astronomy In chapter 1, I give a general overview of General Relativity and Gravitational Wave theory. I also describe the GW Detectors. Chapter 2 introduces briefly the theory of modeling CCSN. I describe here different models and their imprint in GW signatures. Chapter 3 gives an overview of GW Multimessenger Astronomy and describes GW CCSN Searches. In Chapter 4, I describe the main algorithm used for searching for GW from CCSN, coherent WaveBurst.

Part II - Initial Generation Detectors In Chapter 5, I describe and provide the results of the first Optically Triggered GW CCSN Search. Chapter 6 presents the elements of Low Energy Neutrino Triggered Search that I conducted with Casentini et al [27].

Part III - Advanced Generation Detectors Chapter 7 describes the perspectives of detecting SN in the Local Universe: CCSN rate and usage of counting techniques (Gill et al in prep). Chapter 8 presents the O1-O2 GW CCSN Optically Triggered Search (Abbott et al, leading author). In Chapter 9, I will describe some of the detection perspectives with design sensitivities of Advanced Detectors (Yakunin et al 2017 [28], Yakunin et al 2018 in prep) as well as upgrades of Advanced Detectors. Chapter 10 describes the current LIGO strategy in case of a Galactic Supernova. I will present here preliminary studies for searching for GWs from CCSNe with data from only one detector. The final Chapter 12 in part III, contains several studies regarding extracting physical information from a GW detection (Powell et al 2017 [29], Gill et al 2018 [30], Mukherjee et al. 2018 in prep).

Part IV - Future Generation Detectors In Chapter 13, I describe some of the challenges, strategies and detection perspectives. Chapter 14 focuses on studying signal-to-noise ratios of different SN models and future designed sensitivities. In Chapter 15, I explore the possibility of using non-parameter Distributional Methods for detecting populations of GW from CCSN (Szczepańczyk et al 2018 in prep).

Papers related to this thesis

Co-author of 65 (Jan 2018) LIGO-Virgo Scientific Collaboration papers (full list: Spires).
Papers where I directly contributed:

[1] B. P. Abbott et al. *First targeted search for gravitational-wave bursts from core-collapse supernovae in data of first-generation laser interferometer detectors*, Phys. Rev. D, 94:102001, Nov 2016. (leading author with M. Zanolin, C. Ott and P. Sutton)

[2] K. N. Yakunin, E. Endeve, A. Mezzacappa, **M. Szczepańczyk**, M. Zanolin, P. Marronetti, E. J. Lentz, S. W. Bruenn, W. R. Hix, O. E. B. Messer, J. M. Blondin, and J. A. Harris. *Gravitational wave signals from multi-dimensional core-collapse supernova explosion simulations*, arXiv:1710.08372

[3] Jade Powell, **M. Szczepańczyk**, and Ik Siong Heng. Inferring the core-collapse supernova explosion mechanism with three-dimensional gravitational wave simulations. Phys. Rev. D, 96:123013, Dec 2017.

[4] K. Gill, W. Wang, O. Valdez, **M. Szczepańczyk**, Michele Zanolin, and Soma Mukherjee. *Enhancing the sensitivity of searches for gravitational waves from core-collapse supernovae with a bayesian classification of candidate events*, 2018. arXiv:1709.00955 (submitted to PRD)

Papers in preparation:

[1] B. P. Abbott et al., *Optically Triggered Search for Gravitational-Wave Bursts from Core-Collapse Supernovae in First and Second Observational Data of Advanced Generation Laser Interferometer Detectors* (lead LIGO/Virgo author, internal review in progress) LIGO-P1700177

[2] K. N. Yakunin, A. Mezzacappa, **M. Szczepańczyk**, M. Zanolin, P. Marronetti, E. Endeve, E. J. Lentz, S. W. Bruenn, W. R. Hix, O. E. B. Messer, J. M. Blondin, and J. A. Harris. *Multi-dimensional core-collapse supernova explosion simulations.*

[3] K. Gill, M. Branchesi, M. Zanolin, **M. Szczepańczyk**, *Gravitational Wave Astronomy Prospectives for Core-Collapse Supernovae Populations* (draft completed) LIGO-P1500232

[4] S. Mukherjee, O. Valdez, **M. Szczepańczyk**, M. Zanolin, *Enhanced Efficiency in Detection of Gravitational Waves from Supernovae: Comparative results from coherent Wave Burst and Two-Step Denoising pipelines*, LIGO-P1700216

[5] M. Cavaglia, **M. Szczepańczyk**, T. Hansen, S. Gaudio, M. Zanolin, *Method to assess significance of a Gravitational Wave candidate for Galactic Supernova when only one detector is on-line.*

[6] J. M. Fedrow, C. D. Ott, **M. Szczepańczyk**, R. Haas, E. Schnetter **M. Szczepańczyk**, et al *Gravitational Waves from 3D Rotating Core-Collapse Supernovae*

[7] B. Bécsy, P. Raffai, T. Littenberg, M. Millhouse, K. Gill, **M. Szczepańczyk** *Interpreting gravitational-wave bursts: constraints on source properties without using astrophysical models* LIGO-P1800133

[8] **M. Szczepańczyk**, S. Schwalbe, M. Zanolin, B. Hughey *Distributional Tests for Supernova Gravitational Wave Detection*

Part I

Introduction to CCSN Multimessenger Astronomy

Chapter 1

General Relativity and Gravitational Waves

General Relativity (GR) was created by Albert Einstein in 1915; it sets a basis for our understanding of gravitation. In this chapter, I will provide a general description of GR, followed by the theory of GWs that will include their properties and polarization.

1.1 General Relativity

The considerations of General Relativity we will start from constructing a toy model of an empty space (e.g. between galaxies). It can be modeled as a cartesian grid made of unit length rods. In each corner of the grid we will put clocks that are synchronised. This way, each point is described in terms of time and space coordinates (x, y, z, t).

When a massive object is placed in the empty space (a planet or a star) then the lengths of the rods are no longer equal and the clocks, no longer synchronised; the space-time is now curved. For a dynamical sitation (e.g. coalescing objects), the space-time changes its curvature over time. The relation between curvature and mass distribution:

$$\begin{pmatrix}\text{Curveture of}\\ \text{space-time}\end{pmatrix} \sim \begin{pmatrix}\text{Dynamical movement of mass}\\ \text{in this space-time}\end{pmatrix}$$

This is a simplistic description of the Einstein Equations.

General Relativity is a succesful theory that passes all tests conducted experimentally up to now. Such a notable test is Mercury's precession. According to Newtonian gravity, when a planet is orbiting the Sun, the orbit is elliptical. However, observations contradict this, showing that the orbit deviates from the elliptical path. It is GR that provides predictions that are in agreement with these measurements.

Another confirmation of GR comes with the phenomenon of gravitational lensing. Light in vacuum propagates in a straight line. However, the line is bent when light is moving nearby a massive object. This phenomenon has been confiremed by an experiment in 1919, when the lensing was directly measured during a solar eclipse. In this experiment solar mass directly affected the curvature of spacetime. A visualization of the effect of spacetime curvature is show in figure 1.1 for a static and dynamical distribution of matter.

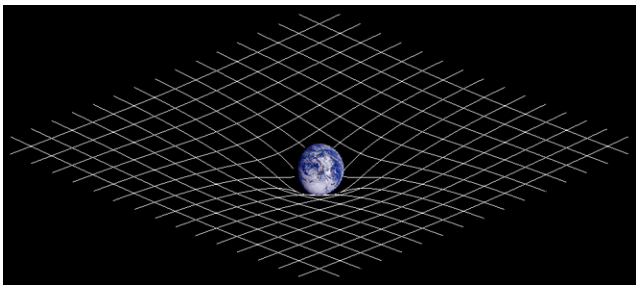
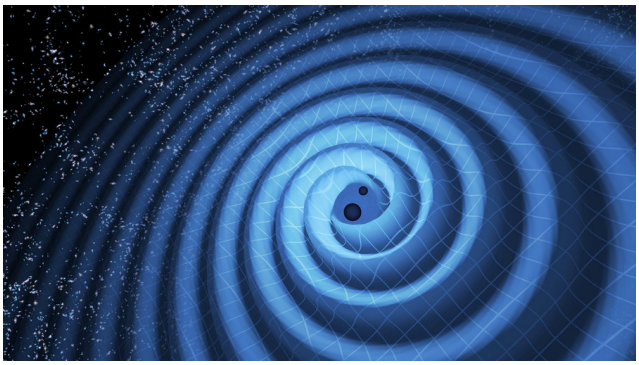

Figure 1.1: Curved spacetime. Left: static situation (image source [4]). Right: dynamical situation, coalescing Black Holes (image source [5]).

1.1.1 Einstein Equations

In General Relativity, the Einstein Equations relate the curvature of spacetime, the Einstein tensor $G_{\mu\nu}$, with the distribution of mass, the mass-energy tensor $T_{\mu\nu}$, (where $\mu, \nu \in \{0, 1, 2, 3\} = \{ct, x, y, z\}$, and c is speed of light). The equations describe the former as proportional to the latter:

$$G_{\mu\nu} = \frac{8\pi G}{c^4} T_{\mu\nu}, \tag{1.1}$$

where G is a gravitational constant. Einstein tensor is defined as:

$$G_{\mu\nu} = R_{\mu\nu} - \frac{1}{2} g_{\mu\nu} R, \tag{1.2}$$

where $R_{\mu\nu}$ is the Riemann tensor, and R the Ricci scalar. There are also the following definitions describing the curvature of spacetime:

$$\text{Christoffel symbol} \quad \Gamma^{\mu}_{\alpha\beta} = \frac{1}{2} g^{\mu\lambda} \left(\partial_\alpha g_{\lambda\beta} + \partial_\beta g_{\lambda\alpha} - \partial_\lambda g_{\alpha\beta} \right) \tag{1.3}$$

$$\text{Riemann tensor} \quad R_{\mu\nu\alpha\beta} = g_{\alpha\lambda} \left(\partial_\mu \Gamma^{\lambda}_{\beta\nu} - \partial_\nu \Gamma^{\lambda}_{\mu\beta} + \Gamma^{\lambda}_{\mu\eta} \Gamma^{\eta}_{\nu\beta} - \Gamma^{\lambda}_{\nu\eta} \Gamma^{\eta}_{\mu\beta} \right) \tag{1.4}$$

$$\text{Ricci tensor} \quad R_{\mu\nu} = g^{\varrho\sigma} R_{\varrho\mu\sigma\nu} \tag{1.5}$$

$$\text{Ricci scalar} \quad R = g^{\mu\nu} R_{\mu\nu} \tag{1.6}$$

$$\tag{1.7}$$

1.2 Gravitational Waves

In this section, I will linearize the Einstein Equations to arrive to a wave solution that describe Gravitational Waves. The linearization holds when the observer is far away from the source and the metric, $g_{\mu\nu}$, is written as:

$$g_{\mu\nu} = \eta_{\mu\nu} + h_{\mu\nu}, \tag{1.8}$$

where $\eta_{\mu\nu}$ is Minkowski flat metric:

$$\eta_{\mu\nu} = \begin{pmatrix} -1 & 0 & 0 & 0 \\ 0 & 1 & 0 & 0 \\ 0 & 0 & 1 & 0 \\ 0 & 0 & 0 & 1 \end{pmatrix}, \tag{1.9}$$

and $h_{\mu\nu}$ is a small perturbation, $|h_{\mu\nu}| \ll 1$. In this approximation the Einstein tensor (1.2) has only linear components in $h_{\mu\nu}$:

$$G_{\mu\nu} = \frac{1}{2}\left(\partial_\alpha\partial_\nu h^\alpha_\mu + \partial_\alpha\partial_\mu h^\alpha_\nu - \partial_\mu\partial_\nu h - \Box h_{\mu\nu} + \eta_{\mu\nu}(\Box h - \partial_\alpha\partial_\beta h^{\alpha\beta})\right), \tag{1.10}$$

where d'Alembertian $\Box = \partial^\alpha\partial_\alpha$, $h = h^\alpha_\alpha$. This expression can be shortened by defining:

$$\bar{h}_{\mu\nu} = h_{\mu\nu} + \frac{1}{2}\eta_{\mu\nu}h. \tag{1.11}$$

The Einstain tensor $G_{\mu\nu}$ then becomes:

$$G_{\mu\nu} = \frac{1}{2}\left(\partial_\alpha\partial_\nu \bar{h}^\alpha_\mu + \partial_\alpha\partial_\mu \bar{h}^\alpha_\nu - \Box\bar{h}_{\mu\nu} - \eta_{\mu\nu}\partial_\alpha\partial_\beta\bar{h}^{\alpha\beta}\right). \tag{1.12}$$

This can be further simplified by doing a proper coordinate tranformation. Defining new coordinates:

$$x'^\alpha = x^\alpha + \xi^\alpha(x^\beta) \tag{1.13}$$

assuming that $|\partial_\beta\xi^\alpha| \ll 1$. It is possible to choose ξ such that:

$$\partial^\nu\bar{h}_{\mu\nu} = 0. \tag{1.14}$$

This is also known as *Lorentz gauge*. In this weak field approximation, the Einstain tensor becomes:

$$G_{\mu\nu} = -\frac{1}{2}\Box\bar{h}_{\mu\nu}. \tag{1.15}$$

By substituting this form of the Einstein equation (1.1), we arrive at a linearized form of Einstain equations:

$$\Box\bar{h}_{\mu\nu} = -\frac{16\pi G}{c^4}T_{\mu\nu}. \tag{1.16}$$

1.2.1 Vacuum solution

One can solve the linearized Einstein Equations (1.16) in vacuum, i.e. $T_{\mu\nu} = 0$. Equation (1.16) then becomes:

$$\Box\bar{h}_{\mu\nu} = 0. \tag{1.17}$$

or

$$\left(-\frac{1}{c^2}\frac{\partial^2}{\partial t^2} + \triangle\right)\bar{h}_{\mu\nu} = 0, \tag{1.18}$$

where $\triangle = (\partial_x^2, \partial_y^2, \partial_z^2)$. This is a wave equation with the solution:

$$\bar{h}_{\mu\nu} = A_{\mu\nu} \cos(k_\alpha x^\alpha), \tag{1.19}$$

where $k_\alpha = (\omega, \mathbf{k})$ and ω is the frequency while $\mathbf{k}$ is the wave number. By substituting (1.19) to (1.17) we obtain the relation between ω and $\mathbf{k}$:

$$\omega = c|\mathbf{k}|. \tag{1.20}$$

The Lorentz gauge (1.14) gives an additional constraint in the amplitude:

$$A_{\mu\nu} k^\nu = 0. \tag{1.21}$$

This means that the wave is perpendicular to the direction of propagation; this solution, $A_{\mu\nu} \cos(k_\alpha x^\alpha)$, describes a wave front.

1.2.2 Transverse-Traceless gauge

Up to now, the amplitude $A_{\mu\nu}$ is constrained by equation (1.21). However, we have freedom in choosing ξ_α using the Lorentz gauge (1.14). Our choice will be:

$$\xi_\alpha = B_\alpha \cos(k_\mu x^\mu). \tag{1.22}$$

B_α can also be chosen in such a way that we further limit the amplitude $A_{\mu\nu}$:

$$A^\mu_\mu = 0 \tag{1.23}$$

and

$$A_{\mu\nu} U^\nu = 0, \tag{1.24}$$

where U^ν is a non-constrained four-vector ($q_{\mu\nu} = -1$). Equations(1.23) and (1.24) are called the *Transverse - Traceless gauge* (TT gauge). By using the TT gauge, the amplitude $A_{\mu\nu}$ will reduce the number of independent equations from 6 to 2.

One can choose four-velocity U^ν as $U^\nu = (1, 0, 0, 0)$ (we are free in the choice of four-velocity, so we will choose the simplest form). By using the gauge condition (1.24) we arrive at:

$$A_{\mu 0} = 0. \tag{1.25}$$

Consequently we assume that the wave is propagating in the z direction: $k_\mu = (k, 0, 0, k)$. From equations (1.21) and (1.24) we can find that:

$$A_{\mu z} = A_{\mu 0} = 0. \tag{1.26}$$

The gauge condition (1.23) makes it so that the diagonal of $A_{\mu\nu}$ disappears:

$$A_{yy} = -A_{xx}. \tag{1.27}$$

This way, we get that in the TT gauge, a wave propagating in the z direction will have the following form:

$$h_{\mu\nu}^{TT} = \begin{pmatrix} 0 & 0 & 0 & 0 \\ 0 & h_{xx} & h_{xy} & 0 \\ 0 & h_{xy} & -h_{xx} & 0 \\ 0 & 0 & 0 & 0 \end{pmatrix}. \tag{1.28}$$

It can be noticed that there are only two independent elements in this array, h_{xx} and h_{xy}, and we reduced the number of the independent equations to two. Furthermore, we will discuss the physical interpretation of this wave solution.

1.2.3 Interaction of a GW with Matter

Let us consider a free falling particle in vacuum in position $x = (x^\mu)$. The GW passing through the particle will interact with it. We know that the particle must follow a geodesics:

$$\frac{\mathrm{d}^2 x^\mu}{\mathrm{d}\tau^2} + \Gamma^\mu_{\nu\rho}(x)\frac{\mathrm{d}x^\nu}{\mathrm{d}\tau}\frac{\mathrm{d}x^\rho}{\mathrm{d}\tau} = 0 \tag{1.29}$$

The particle initially does not move. This means that the four-velocity is $\frac{\mathrm{d}x^\beta}{\mathrm{d}\tau} = \delta^\beta_0$. Initial acceleration is:

$$\left.\frac{\mathrm{d}^2 x^\mu}{\mathrm{d}\tau^2}\right|_{\tau=0} = -\Gamma^\mu_{00} = -\frac{1}{2}\eta^{\mu\beta}(\partial_0 h_{\beta 0} + \partial_0 h_{0\beta} - \partial_\beta h_{00}). \tag{1.30}$$

In the TT gauge the acceleration vanishes (equation (1.28)), which means that in every moment of time the particle is not moving

Figure 1.2: Two separate free falling particles that interact with GW.

Let us consider a second particle that is separated from the first one, and is at point $x^\mu + \zeta^\mu$ (Figure 1.2). The geodesic equation will look as follows:

$$\frac{\mathrm{d}^2(x^\mu + \zeta^\mu)}{\mathrm{d}\tau^2} + \Gamma^\mu_{\nu\rho}(x+\zeta)\frac{\mathrm{d}(x^\nu + \zeta^\nu)}{\mathrm{d}\tau}\frac{\mathrm{d}(x^\rho + \zeta^\rho)}{\mathrm{d}\tau} = 0. \tag{1.31}$$

We will approximate this equation by keeping only linear components in ζ.

Next we will subtract this equation from (1.29), and obtain the following:

$$\frac{\mathrm{d}^2\zeta^\mu}{\mathrm{d}\tau^2} + 2\Gamma^\mu_{\nu\rho}(x)\frac{\mathrm{d}x^\nu}{\mathrm{d}\tau}\frac{\mathrm{d}\zeta^\rho}{\mathrm{d}\tau}\zeta^\sigma\partial_\sigma\Gamma^\mu_{\nu\rho}(x)\frac{\mathrm{d}x^\nu}{\mathrm{d}\tau}\frac{\mathrm{d}x^\rho}{\mathrm{d}\tau} = 0. \tag{1.32}$$

Locally, in close proximity to x, the Christoffel symbols vanish:

$$\Gamma^{\mu}_{\nu\rho}(x) = 0, \tag{1.33}$$

which means:

$$\frac{\mathrm{d}^2\zeta^{\mu}}{\mathrm{d}\tau^2} + \zeta^{\sigma}\partial_{\sigma}\Gamma^{\mu}_{\nu\rho}(x)\frac{\mathrm{d}x^{\nu}}{\mathrm{d}\tau}\frac{\mathrm{d}x^{\rho}}{\mathrm{d}\tau} = 0. \tag{1.34}$$

If our two particles are moving slowly, i.e. $\mathrm{d}x^i/\mathrm{d}\tau \ll \mathrm{d}x^0/\mathrm{d}\tau$, then we can disregard components $\mathrm{d}x^i/\mathrm{d}\tau$:

$$\frac{\mathrm{d}^2\zeta^{i}}{\mathrm{d}\tau^2} + \zeta^{\sigma}\partial_{\sigma}\Gamma^{i}_{00}(x)\left(\frac{\mathrm{d}x^0}{\mathrm{d}\tau}\right)^2 = 0. \tag{1.35}$$

This implies that locally, around the point x, we find that $\zeta^{\sigma}\partial_{\sigma}\Gamma^{i}_{00} = \zeta^{i}\partial_{i}\Gamma^{i}_{00}$. We notice also that $\Gamma^{\mu}_{\nu\rho}(x) = 0$ and $\partial_0\Gamma^{i}_{0j} = 0$, so that:

$$R^{i}_{0j0} = \partial_j\Gamma^{i}_{00} - \partial\Gamma^{i}_{0j} = \partial_j\Gamma^{i}_{00} \tag{1.36}$$

and

$$\frac{\mathrm{d}^2\zeta^{i}}{\mathrm{d}\tau^2} = -R^{i}_{0j0}\zeta^{j}\left(\frac{\mathrm{d}x^0}{\mathrm{d}\tau}\right)^2. \tag{1.37}$$

If the particles are moving with non-relativistic velocities, then $\tau \approx t$ and $\mathrm{d}x^0/\mathrm{d}\tau \approx c$, which leads us to:

$$\ddot{\zeta}^{i} = -c^2 R^{i}_{0j0}\zeta^{j}. \tag{1.38}$$

The Riemann tensor (1.4) in a weak field approximation (1.8) becomes:

$$R_{\mu\nu\rho\sigma} = \frac{1}{2}\left(\partial_{\nu}\partial_{\rho}h_{\mu\sigma} + \partial_{\mu}\partial_{\sigma}h_{\nu\rho} - \partial_{\mu}\partial_{\rho}h_{\nu\sigma} - \partial_{\nu}\partial_{\sigma}h_{\mu\rho}\right), \tag{1.39}$$

and in the TT gauge, it becomes:

$$R^{i}_{0j0} = R_{i0j0} = -\frac{1}{2c^2}\ddot{h}^{TT}_{ij}. \tag{1.40}$$

The final equation describing the relative movement between two particles is:

$$\boxed{\ddot{\zeta}^{i} = \frac{1}{2}\ddot{h}^{TT}_{ij}\zeta^{j}.} \tag{1.41}$$

1.2.4 GW Polarization

Let us simplify the notation of (1.28) by substituting $h_{xx} = h_+ \sin\omega t$ and $h_{xy} = h_\times \sin\omega t$. We can further divide the tensor (1.28) into two components. These two components represent two *polarization* states: "+" and "×". The "+" component we will write as:

$$h^{TT}_{\mu\nu} = h_+ \sin\omega t \begin{pmatrix} 0 & 0 & 0 & 0 \\ 0 & 1 & 0 & 0 \\ 0 & 0 & -1 & 0 \\ 0 & 0 & 0 & 0 \end{pmatrix}. \tag{1.42}$$

We will consider now two particles laying on a plane (x, y) in cartesian coordinates. One of them we will put at point $(0, 0)$ and the other at point:

$$\vec{\zeta} = (x_0 + \delta x(t), y_0 + \delta y(t)), \tag{1.43}$$

where (x_0, y_0) is a fixed, non-perturbated position of the particle and $(\delta x(t), \delta y(t))$ is the perturbation caused by the GW. Both particles are moving on geodesics. By substituting $\vec{\zeta}$ to equation (1.41) we will get:

$$\begin{cases} \delta\ddot{x}(t) = -\frac{1}{2}h_+(x_0 + \delta x(t))\omega^2 \sin\omega t, \\ \delta\ddot{y}(t) = \frac{1}{2}h_+(y_0 + \delta y(t))\omega^2 \sin\omega t. \end{cases} \tag{1.44}$$

We will assume a small perturbation, that is, $\delta x(t) \ll x_0$ and $\delta y(t) \ll y_0$. The equations (1.44) are simplified then to:

$$\begin{cases} \delta\ddot{x}(t) = -\frac{1}{2}h_+ x_0\omega^2 \sin\omega t, \\ \delta\ddot{y}(t) = \frac{1}{2}h_+ y_0\omega^2 \sin\omega t. \end{cases} \tag{1.45}$$

After integrating them we get:

$$\begin{cases} \delta x(t) = \frac{1}{2}h_+ x_0 \sin\omega t, \\ \delta y(t) = -\frac{1}{2}h_+ y_0 \sin\omega t. \end{cases} \tag{1.46}$$

Similarly, when we consider the "$\times$" component of (1.28):

$$h^{TT}_{\mu\nu} = h_\times \sin\omega t \begin{pmatrix} 0 & 0 & 0 & 0 \\ 0 & 0 & 1 & 0 \\ 0 & 1 & 0 & 0 \\ 0 & 0 & 0 & 0 \end{pmatrix}, \tag{1.47}$$

we find that:

$$\begin{cases} \delta x(t) = \frac{1}{2}h_\times y_0 \sin\omega t, \\ \delta y(t) = \frac{1}{2}h_\times x_0 \sin\omega t. \end{cases} \tag{1.48}$$

Consequently, if we consider a ring of particles with the solutions (1.46) and (1.48), we can find out how the ring will behave when a GW is passing through it from the z direction. Figure 1.3 shows the movement of these particles for the two polarizations. From this figure it is visible why the two polarizations are called *plus* and *cross* polarizations.

1.2.5 GW Production

In this section we will derive how the GW signature, $h_{\mu\nu}$, looks for a source, $T_{\mu\nu}$. We will look for the solution of the equation (1.16):

$$\left(-\frac{\partial^2}{\partial t^2} + \bigtriangledown^2\right)\bar{h}_{\mu\nu} = -\frac{16\pi G}{c^4}T_{\mu\nu}. \tag{1.49}$$

In the volume V the solution is:

$$\bar{h}_{\mu\nu}(t, x^i) = \frac{4G}{c^2}\int_V \frac{T_{\mu\nu}(t - |x^i - y^i|/c, y^i)}{|x^i - y^i|}\mathrm{d}^3 y. \tag{1.50}$$

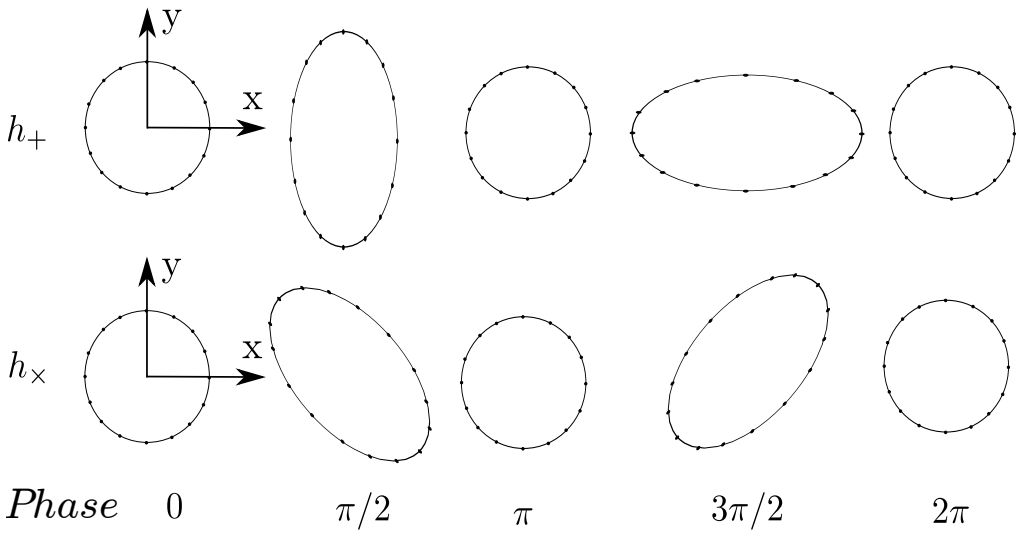

Figure 1.3: Rings of particles that interact with GW propagating perpendicular to the $x-y$ plane.

For convenience we will put the center of the coordinate system inside the source. When we go far away from the source, at a distance $r = |x^i| \gg |y^i|$, we will get:

$$\bar{h}_{\mu\nu}(t, x^i) \approx \frac{4G}{c^2 r} \int_V T_{\mu\nu}(t - r/c, y^i) \mathrm{d}^3 y. \tag{1.51}$$

Mass-energy conservation:

$$\partial_\nu T^{\mu\nu} = 0, \tag{1.52}$$

which we can also write as:

$$\int_V T_{\mu 0} \mathrm{d}^3 y = \text{const}, \tag{1.53}$$

implies $h_{\mu 0} = \text{const}$. Let us introduce the definition of quadrupole moment:

$$I^{kl} = \int_V T^{00} y^k y^l \mathrm{d}y. \tag{1.54}$$

By using the following identity (derived from energy-momentum conservation (1.52)):

$$\frac{\partial^2}{\partial t^2} \int T^{00} y^k y^l \mathrm{d}^3 y = 2 \int T^{kl} \mathrm{d}^3 y, \tag{1.55}$$

we get a final form:

$$\bar{h}_{ij} = \frac{2G}{c^2 r} \ddot{I}_{ij}(t - r/c), \tag{1.56}$$

where $\ddot{I}$ is a second time derivative of quadruopole moment.

1.2.6 GW Energy Radiated by the Supernova

For the detection of a GW, it is important to know its energy, using the quadrupole moment from SN simulations. In this section, I will derive the GW energy from a Supernova when the quadrupole moment or strain is directly available. There are several ways of equivalent formulations [31]. The choice of the formualation depends on the application. Here, I will present one formulation assuming a known quadrupole moment.

The total energy of gravitational waves (E_{GW}) emitted by a spherically asymmetric source can be expressed as:

$$E_{GW} = \int_{\mathbb{R}} \frac{\mathrm{d}E}{\mathrm{d}t} \mathrm{d}t \tag{1.57}$$

where $\mathrm{d}E/\mathrm{d}t$ is gravitational wave luminosity [32]:

$$\frac{\mathrm{d}E}{\mathrm{d}t} = \frac{G}{5c^5} \langle \dddot{\mathit{I}}_{ij} \dddot{\mathit{I}}^{ij} \rangle, \tag{1.58}$$

where $\dddot{\mathit{I}}_{ij}$ is the second time derivative of quadrupole moment 1.54. In order to write down E_{GW} in the frequency domain, one has to use a Fourier transform:

$$\ddot{\mathit{I}}_{ij}(t) = \int_{\mathbb{R}} \ddot{\tilde{\mathit{I}}}_{ij}(f) e^{-2\pi i f t} \mathrm{d}f, \tag{1.59}$$

along with Parseval's theorem, stating that:

$$\int_{\mathbb{R}} \mathrm{d}t \left| \ddot{\mathit{I}}_{ij}(t) \right|^2 = \int_{\mathbb{R}} \mathrm{d}f \left| \ddot{\tilde{\mathit{I}}}_{ij}(f) \right|^2. \tag{1.60}$$

The gravitational wave energy can then be written as:

$$E_{GW} = \frac{G}{5c^5} \int_{\mathbb{R}} \mathrm{d}t \langle \dddot{\mathit{I}}_{ij} \dddot{\mathit{I}}^{ij} \rangle \tag{1.61}$$

$$= \frac{G}{5c^5} \sum_{ij} \int_{\mathbb{R}} \mathrm{d}t \left(\frac{\mathrm{d}}{\mathrm{d}t} \ddot{\mathit{I}}_{ij}(t) \right)^2 \tag{1.62}$$

$$= \frac{G}{5c^5} \sum_{ij} \int_{\mathbb{R}} \mathrm{d}f (2\pi f)^2 \left| \ddot{\tilde{\mathit{I}}}_{ij}(f) \right|^2, \tag{1.63}$$

where $\ddot{\tilde{\mathit{I}}}_{ij} = \ddot{\tilde{I}}_{ij} - 1/3 \delta_{ij} \operatorname{Tr} \ddot{\tilde{I}}$ and $\operatorname{Tr} \ddot{\tilde{I}} = \ddot{\tilde{I}}_{xx} + \ddot{\tilde{I}}_{yy} + \ddot{\tilde{I}}_{zz}$.

Derivation from Quadrupole Moments A possible way to express E_{GW} in terms of elements of quadrupole moment is:

$$E_{GW} = \frac{G}{5c^5} \int_{\mathbb{R}} \mathrm{d}f (2\pi f)^2 \left(\left| \ddot{\tilde{\mathit{I}}}_{xx} \right|^2 + \left| \ddot{\tilde{\mathit{I}}}_{yy} \right|^2 + \left| \ddot{\tilde{\mathit{I}}}_{zz} \right|^2 + 2 \left| \ddot{\tilde{\mathit{I}}}_{xy} \right|^2 + 2 \left| \ddot{\tilde{\mathit{I}}}_{yz} \right|^2 + 2 \left| \ddot{\tilde{\mathit{I}}}_{zx} \right|^2 \right) \tag{1.64}$$

$$= \frac{2G}{5c^5} \int_0^{\infty} \mathrm{d}f (2\pi f)^2 \left(\left| \ddot{\tilde{I}}_{xx} - 1/3 \operatorname{Tr} \ddot{\tilde{I}} \right|^2 + \left| \ddot{\tilde{I}}_{yy} - 1/3 \operatorname{Tr} \ddot{\tilde{I}} \right|^2 + \left| \ddot{\tilde{I}}_{zz} - 1/3 \operatorname{Tr} \ddot{\tilde{I}} \right|^2 + \right. \tag{1.65}$$

$$\left. 2 \left| \ddot{\tilde{I}}_{xy} \right|^2 + 2 \left| \ddot{\tilde{I}}_{yz} \right|^2 + 2 \left| \ddot{\tilde{I}}_{zx} \right|^2 \right)$$

Alternative expression I The radiated energy can also be rewritten in the following fashion:

$$E_{GW} = \frac{G}{5c^5}\sum_{ij}\int_{\mathbb{R}} \mathrm{d}t \left(\frac{\mathrm{d}}{\mathrm{d}t}\ddot{\mathcal{I}}_{ij}(t)\right)^2 \tag{1.66}$$

$$= \frac{G}{5c^5}\int_{\mathbb{R}} \mathrm{d}t \left(\dddot{\mathcal{I}}^2_{xx} + \dddot{\mathcal{I}}^2_{yy} + \dddot{\mathcal{I}}^2_{zz} + 2\dddot{\mathcal{I}}^2_{xy} + 2\dddot{\mathcal{I}}^2_{yz} + 2\dddot{\mathcal{I}}^2_{zx}\right) \tag{1.67}$$

$$= \frac{G}{15c^5}\int_{\mathbb{R}} \mathrm{d}t \left(3(\dddot{\mathcal{I}}^2_{xx} + \dddot{\mathcal{I}}^2_{yy} + \dddot{\mathcal{I}}^2_{zz}) + 6(\dddot{\mathcal{I}}^2_{xy} + \dddot{\mathcal{I}}^2_{yz} + \dddot{\mathcal{I}}^2_{zx})\right) \tag{1.68}$$

$$= \frac{G}{15c^5}\int_{\mathbb{R}} \mathrm{d}t \left(3(\ddot{I}_{xx} - 1/3\,\mathrm{Tr}\,\ddot{I})^2 + 3(\ddot{I}_{yy} - 1/3\,\mathrm{Tr}\,\ddot{I})^2 + \right. \tag{1.69}$$
$$\left. 3(\ddot{I}_{zz} - 1/3\,\mathrm{Tr}\,\ddot{I})^2 + 6(\dddot{I}^2_{xy} + \dddot{I}^2_{yz} + \dddot{I}^2_{zx})^2\right)$$

$$= \frac{G}{15c^5}\int_{\mathbb{R}} \mathrm{d}t \left(3\dddot{I}^2_{xx} - 2\dddot{I}_{xx}\,\mathrm{Tr}\,\ddot{I} + 1/3(\mathrm{Tr}\,\ddot{I})^2 + \right. \tag{1.70}$$
$$3\dddot{I}^2_{yy} - 2\dddot{I}_{yy}\,\mathrm{Tr}\,\ddot{I} + 1/3(\mathrm{Tr}\,\ddot{I})^2 +$$
$$3\dddot{I}^2_{zz} - 2\dddot{I}_{zz}\,\mathrm{Tr}\,\ddot{I} + 1/3(\mathrm{Tr}\,\ddot{I})^2 +$$
$$\left. 6(\dddot{I}^2_{xy} + \dddot{I}^2_{yz} + \dddot{I}^2_{zx})\right)$$

$$= \frac{G}{15c^5}\int_{\mathbb{R}} \mathrm{d}t \left(2\dddot{I}^2_{xx} + 2\dddot{I}^2_{yy} + 2\dddot{I}^2_{zz} - 2\dddot{I}_{xx}\dddot{I}_{yy} - 2\dddot{I}_{xx}\dddot{I}_{yy} - 2\dddot{I}_{xx}\dddot{I}_{yy}\right. \tag{1.71}$$
$$\left. 6(\dddot{I}^2_{xy} + \dddot{I}^2_{yz} + \dddot{I}^2_{zx})\right)$$

$$= \frac{G}{15c^5}\int_{\mathbb{R}} \mathrm{d}t \left((\ddot{I}_{xx} - \ddot{I}_{yy})^2 + (\ddot{I}_{yy} - \ddot{I}_{zz})^2 + (\ddot{I}_{zz} - \ddot{I}_{xx})^2 + \right. \tag{1.72}$$
$$\left. 6(\dddot{I}^2_{xy} + \dddot{I}^2_{yz} + \dddot{I}^2_{zx})\right)$$

Applying Parseval's theorem:

$$E_{GW} = \frac{G}{15c^5}\int_{\mathbb{R}} \mathrm{d}f \left(|\dddot{\tilde{I}}_{xx} - \dddot{\tilde{I}}_{yy}|^2 + |\dddot{\tilde{I}}_{yy} - \dddot{\tilde{I}}_{zz}|^2 + |\dddot{\tilde{I}}_{zz} - \dddot{\tilde{I}}_{xx}|^2 + \right. \tag{1.73}$$
$$\left. 6(|\dddot{\tilde{I}}_{xy}|^2 + |\dddot{\tilde{I}}_{yz}|^2 + |\dddot{\tilde{I}}_{zx}|^2)\right)$$

$$= \frac{2G}{15c^5}\int_0^{\infty} \mathrm{d}f (2\pi f)^2 \left(|\ddot{\tilde{I}}_{xx} - \ddot{\tilde{I}}_{yy}|^2 + |\ddot{\tilde{I}}_{yy} - \ddot{\tilde{I}}_{zz}|^2 + |\ddot{\tilde{I}}_{zz} - \ddot{\tilde{I}}_{xx}|^2 + \right. \tag{1.74}$$
$$\left. 6(|\ddot{\tilde{I}}_{xy}|^2 + |\ddot{\tilde{I}}_{yz}|^2 + |\ddot{\tilde{I}}_{zx}|^2)\right)$$

Equation (1.74) is consistent with Müller+12, eqn. (34) (see [33]).

Alternative expression II Another way to calculate the gravitational wave energy of the source is:

$$E_{GW} = \frac{G}{5c^5}\sum_{ij}\int_{\mathbb{R}} \mathrm{d}t \left(\frac{\mathrm{d}}{\mathrm{d}t}\ddot{\boldsymbol{I}}_{ij}(t)\right)^2 \tag{1.75}$$

$$= \frac{4G}{15c^5}\int_0^\infty \mathrm{d}t \left(\dddot{I}_{xx}^2 + \dddot{I}_{yy}^2 + \dddot{I}_{zz}^2 - \dddot{I}_{xx}\dddot{I}_{yy} - \dddot{I}_{yy}\dddot{I}_{zz} - \dddot{I}_{zz}\dddot{I}_{xx} + 3(\dddot{I}_{xy}^2 + \dddot{I}_{yz}^2 + \dddot{I}_{zx}^2)\right) \tag{1.76}$$

Because of mixed terms, like $\dddot{I}_{xx}\dddot{I}_{yy}$, the Parseval's theorem cannot be used. After applying Fourier transform:

$$\tilde{E}_{GW} = \frac{4G}{15c^5}\int_0^\infty \mathrm{d}f \left(\dddot{\tilde{I}}_{xx}^2 + \dddot{\tilde{I}}_{yy}^2 + \dddot{\tilde{I}}_{zz}^2 - \dddot{\tilde{I}}_{xx}\dddot{\tilde{I}}_{yy} - \dddot{\tilde{I}}_{yy}\dddot{\tilde{I}}_{zz} - \dddot{\tilde{I}}_{zz}\dddot{\tilde{I}}_{xx} + 3(\dddot{\tilde{I}}_{xy}^2 + \dddot{\tilde{I}}_{yz}^2 + \dddot{\tilde{I}}_{zx}^2)\right) \tag{1.77}$$

$$= \frac{4G}{15c^5}\int_0^\infty \mathrm{d}f (2\pi f)^2 \left(\ddot{\tilde{I}}_{xx}^2 + \ddot{\tilde{I}}_{yy}^2 + \ddot{\tilde{I}}_{zz}^2 - \ddot{\tilde{I}}_{xx}\ddot{\tilde{I}}_{yy} - \ddot{\tilde{I}}_{yy}\ddot{\tilde{I}}_{zz} - \ddot{\tilde{I}}_{zz}\ddot{\tilde{I}}_{xx} + 3(\ddot{\tilde{I}}_{xy}^2 + \ddot{\tilde{I}}_{yz}^2 + \ddot{\tilde{I}}_{zx}^2)\right) \tag{1.78}$$

the total energy is the absolute value of equation (1.78):

$$E_{GW} = \left|\tilde{E}_{GW}\right|. \tag{1.79}$$

Equation (1.78) is consistent with Scheidegger et al 2010, eqn. (27), see [34].

Signal's root-sum-square, h_{rss} A strength of a GW signal with $h_+(t)$ and $h_\times(t)$ polarization components can be written in terms of root-sum-square, h_{rss}, value:

$$h_{\mathrm{rss}} = \sqrt{\int \left\langle h_+^2(t) + h_\times^2(t)\right\rangle_\Omega \mathrm{d}t}\ , \tag{1.80}$$

where $\langle\rangle_\Omega$ is an average over solid angle Ω of the source. h_{rss} is expressed in units of strain/$\sqrt{\mathrm{Hz}}$. As an illustration, assume that an average strain of a supernova waveform at 10kpc is $h \approx 10^{-22}$ and the signal lasts around $\tau \approx 0.5$s then the h_{rss} value can be approximated by:

$$h_{\mathrm{rss}} \approx \sqrt{\tau}h = 0.7 \times 10^{-22}\mathrm{strain}/\sqrt{\mathrm{Hz}}. \tag{1.81}$$

GW Energy for narrowband signals The expression for GW Energy emission can be approximated for isotropic emission of narrowband signals, e.g. a sine-Gaussian or long bar instability waveform. Following [35] the GW energy is:

$$E_{\mathrm{GW}} = \frac{\pi^2 c^3}{G} D^2 f_0^2 h_{\mathrm{rss}}^2\,. \tag{1.82}$$

where c is speed of light, G gravitational constant, D distance from the source and f_0 signal's peak frequency.

1.2.7 Linear and Elliptical Polarizations

A common method of extracting GW from quadrupole moment is a multipole expansion [36]:

$$h_+ - ih_\times = \frac{1}{D}\sum_{\ell=2}^{\infty}\sum_{m=-\ell}^{\ell} H_{\ell m}(t)\,{}^{-2}Y_{\ell m}(\theta,\phi) \tag{1.83}$$

The expansion parameters $H_{\ell m}(\ell = 2$ denotes the quadrupole) are complex functions of the retarded source time t. In order to express H_{2m} in terms of $\ddot{I}_{ij}$, one first expresses $h_+(\theta,\phi)$ and $h_\times(\theta,\phi)$ in terms of $\ddot{I}_{kl}$, then convolves these with ${}^{-2}Y^*_{lm}$. The result is:

$$H_{20}^{quad} = \sqrt{\frac{32\pi}{15}}\frac{G}{c^4}(\ddot{I}_{zz} - \frac{1}{2}(\ddot{I}_{xx} + \ddot{I}_{yy})), \tag{1.84}$$

$$H_{2\pm1}^{quad} = \sqrt{\frac{16\pi}{5}}\frac{G}{c^4}(\mp\ddot{I}_{xz} + i\ddot{I}_{yz}) \tag{1.85}$$

$$H_{2\pm2}^{quad} = \sqrt{\frac{4\pi}{5}}\frac{G}{c^4}(\ddot{I}_{xx} - \ddot{I}_{yy} \mp 2i\ddot{I}_{xy}) \tag{1.86}$$

For completeness, we give the definitions of the relevant ${}^{-2}Y^*_{lm}$:

$${}^{-2}Y_{22} = \sqrt{\frac{5}{64\pi}}(1+\cos\theta)^2 e^{2i\phi}, \tag{1.87}$$

$${}^{-2}Y_{21} = \sqrt{\frac{5}{16\pi}}\sin\theta(1+\cos\theta)e^{i\phi}, \tag{1.88}$$

$${}^{-2}Y_{20} = \sqrt{\frac{15}{32\pi}}\sin^2\theta, \tag{1.89}$$

$${}^{-2}Y_{2-1} = \sqrt{\frac{5}{16\pi}}\sin\theta(1-\cos\theta)e^{-i\phi}, \tag{1.90}$$

$${}^{-2}Y_{2-2} = \sqrt{\frac{5}{64\pi}}(1-\cos\theta)^2 e^{-2i\phi}, \tag{1.91}$$

$$I_{yz} = \int yz\rho\,\mathrm{d}x\,\mathrm{d}y\,\mathrm{d}z, \tag{1.92}$$

where ρ is mass density.

Axial symmetry around the z-axis shows that the integral above is zero, because we have equal contributions with $y > 0$ and $y < 0$. Similarly,

$$I_{xz} = 0 \tag{1.93}$$

and also

$$I_{xy} = 0 \tag{1.94}$$

also

$$I_{xx} = I_{yy} \tag{1.95}$$

as a consequence equations (1.85) and (1.86) are zero for an asymmetric motion and only (1.84) is non-zero. Given that (1.89) is real it means that (1.83) is real and therefore:

$$h_{\times} = 0 \tag{1.96}$$

because it multiplies by "i" on the left side of (1.83). Thus proving the linear polarization of a dynamical system with axial symmetry.

Polarization State for a GW Emission from a Standing Accretion Shock Instability (SASI The GW emission from a SASI is expected to be generated by a rotating perturbation on the protoneutron star. If we model this rotating perturbation as a rotating ellipsoid of inertia:

$$I = \begin{bmatrix} I_1 & 0 & 0 \\ 0 & I_2 & 0 \\ 0 & 0 & I_3 \end{bmatrix} \tag{1.97}$$

If we model this rotating perturbation as a rotating ellipsoid of inertia where I_1, I_2 and I_3 are the principal axis of inertia.

We will now define $I = I_1 + I_2$ and $\varepsilon = \frac{I_1 - I_2}{I_3}$. It can be shown that the GW strain for two polarizations become:

$$h_{+} = -\frac{4G\varepsilon I_3 \omega^2}{c^4 r} \frac{1 + \cos^2 \iota}{2} \cos 2\omega t \tag{1.98}$$

$$h_{\times} = \frac{4G\varepsilon I_3 \omega^2}{c^4 r} \cos \iota \sin 2\omega t \tag{1.99}$$

These equations represent extreme emission of long-bar mode instability while the deformation is present.

1.2.8 SN Memory

The late stages of the explosion that develop in a non spherically symmetric fashion is a low frequency component that can be named the memory or tail of a SN waveform. As illustrative examples we present here the calculation of the memory for two toy model explosions where axisymmetric distributions of masses expand in a prolate and oblate fashion. It is also worth mentioning that prolate explosions are more likely to develop in 2D simulations because of the development of large funnels of material around the theta axis of the coordinates.

Prolate Explosion Example

The mass M divides into two masses that proceed along the z axis at a velocity $f(t)$ and locations $z = f(t)$ and $z = -f(t)$ with a proper function $f(t)$. If t approaches ∞, $\dot{f}(t) = \alpha$ with α being a constant because the two masses will eventually stop interacting and the velocities become constant (zero gravitational force when t approaches ∞).

The density equation becomes:

$$\rho = \frac{M}{2}\delta(z - f(t))\delta x\delta y + \frac{M}{2}\delta(z + f(t))\delta x\delta y \tag{1.100}$$

$$I_{ij} = \delta_{i3}\delta_{j3}\int \rho z^2 dxdydz = \delta_{i3}\delta_{j3}[\int \frac{M}{2}\delta(z - f(t))z^2 dz] + \delta_{i3}\delta_{j3}[\int \frac{M}{2}\delta(z + f(t))z^2 dz] = \tag{1.101}$$

$$\delta_{i3}\delta_{j3}[\frac{M}{2}f(t)^2 + \frac{M}{2}f(t)^2] = \delta_{i3}\delta_{j3}M[f(t)^2]$$

As t approaches ∞:

$$\ddot{I}_{33} = M[2f\dot{f} + 2\dot{f}^2] = 2M\alpha^2 \tag{1.102}$$

For all other combinations of i and j:

$$\ddot{I}_{33} = 0 \tag{1.103}$$

From [32]:

$$h_+^{TT} = \frac{G}{c^4 D}(-\ddot{I}_{33}sin^2(\theta)) = -\frac{G2M\alpha^2}{c^4}sin^2(\theta) \tag{1.104}$$

Oblate Explosion Example

In spherical coordinates ρ becomes:

$$\rho = \frac{1}{2\pi}\frac{M}{r^2}\delta(\theta - \frac{\pi}{2})\delta(r - f(t)) \tag{1.105}$$

$$I_{33} = \int \rho x^2 d^3x = \int \frac{1}{2\pi}\frac{M}{r^2}\delta(\theta - \frac{\pi}{2})\delta(r - f(t))r\cos\theta\sin\theta d\theta d\phi dr = 0 \tag{1.106}$$

Which means the memory amplitude is dependent on θ but not the sign and that the relevant parameter is the asymptotic velocity of the two ejected masses. Therefore:

$$I_{3i} = I_{i3} = 0 \text{ for } i = 1, 2, 3 \tag{1.107}$$

$$I_{11} = \int px^2 d^3x = \int \frac{1}{2\pi}\frac{M}{r^2}\delta(\theta - \frac{\pi}{2})\delta(r - f(t))(r\sin\theta\cos\phi)^2 r^2\sin\theta d\theta d\phi dr = \tag{1.108}$$

$$\int \frac{M}{2\pi}f(t)^2\cos^2\theta d\phi = \frac{M}{4\pi}f(t)^2 = I_{22}$$

$$I_{12} = \int \frac{1}{2\pi}\frac{M}{r^2}\delta(\theta - \frac{\pi}{2})\delta(r - f(t))(r\sin\theta\cos\phi(r\sin\theta\sin\phi r^2\sin\theta d\theta d\phi dr = \tag{1.109}$$

$$\int \frac{M}{2\pi}\delta(r - f(t))r^2\cos\phi\sin\phi d\phi = 0 = I_{21}$$

In summary, the only non-zero terms are:

$$I_{11} = I_{22} = \frac{M}{4\pi}f(t)^2 \tag{1.110}$$

Using the relationship $\dot{f}(t) = \alpha$, we find:

$$\ddot{I}_{11} = \frac{M}{2\pi}\alpha^2 \tag{1.111}$$

According to [32] the GW signature becomes:

$$h_+^{TT} = \frac{G}{c^4 D}\sin^2\theta\frac{M}{2\pi}\alpha^2, \tag{1.112}$$

$$h_\times^{TT} = 0. \tag{1.113}$$

1.3 GW Detectors

The first attempt to detect GW was done by Joseph Weber in 60's. Weber was the first who believed in possibility of detecting GW. He was a pionier in building bar detectors. These detectors are cylinders with certain resonant frequency. GW passing throgh the detector excites it and a piezoelectric device measure the level of the vibration. This teachnique was further developed for the several decades. The bar detectors were operating in many countries like USA, Italy or Australia. These narrowband bar detectors however appeared to be not as sensitive as the later proposed interferometers.

The interferometric technique was invented more than a century ago by Albert Michelson. In 1887 in well known Michelson-Morley experiment this very sensitive techique gave negative result on detecting luminiferous aether This result gave revolution in our understanding of spacetime. Nowadays interferometry allowed detecting GW for the first time opening Gravitational Wave Astronomy and opening window for future discoveries.

Interferometers for GW detections were proposed in 60s and 70s of the last century. These designes later evolved into the proposals of broadband detectors with significantly better sensitivity in comparison to bar detectors. Over the years several interferometers were build such as TAMA 300 in Japan, GEO 600 in Germany, Virgo in Italy, KAGRA in Japan and LIGO in USA. Over the years these detectors were setting up various astrophysical constrains setting up the stage for GW detection.

Laser Interferometers are spacially separated to minimize the influence of the local enviromental disturbances on detecting GW and give a better sky localization. Their orientation in the future might allow to measure the two polarizations.

In the following section I will describe their operation principles. Section 1.3.1 describes the case of a simple Michelson interferometer.

1.3.1 Simple Michelson Interferometer

Interferometry is a widely used technique that uses light superposition (interference) to extract information. A simple Michelson interferometer consists of a light source, beamsplitter and two mirrors and a photodiode. Left panel in Figure 1.4 shows a schematic representation of an example of simple Michelson interferometer with a laser light as the source an with perpendicular arms. A similar configuration can be found in GEO 600 detctor with folded arms giving effective length of the arms of 1200m. For this simple configuration, the light from a laser is sent to the beamsplitter, splitted and going to be refleced by the mirrors at the ends of the arms. The light comes

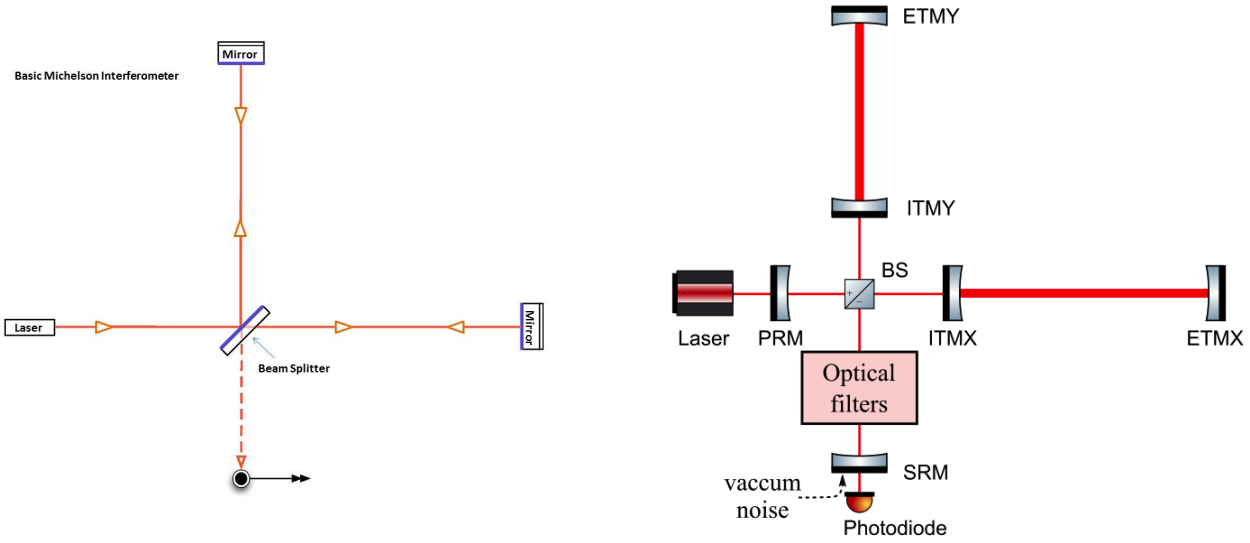

Figure 1.4: Outline of the interferometers. Left: simple Michelson (picture from [6]), Right: GW Interferometers with Optial Cavities, Signal Recycling Mirror (SRM) and Power Recycling Mirror (PRM), (picture from [7]).

back to the beamsplitter, split again and interfere in the photodetector. The detector is tuned to have destructive interference in the photodiode that is also called *dark fringe*. The interferometer is measuring the relative change in length $\delta L(t)$ of the arms and though the strain $h(t)$:

$$\delta L(t) = \delta L_x - \delta L_y = h(t)L \tag{1.114}$$

where δL_x and δL_x are indyvidual arm length changes and $L \approx L_x \approx L_y$. Given an example of GEO 600 sensitivity, the arm length is $L = 1200$m and currently measurable differential arm $\delta L(t) \approx 10^{-18}$m at around 100Hz we are able to measure strains of an order of $h(t) \approx 10^{-21}$. It is a remarkable number. However there are several methods that can be undertaken to improve it.

1.3.2 GW Interferometers

The most sensitive nowadays operating GW interferometers such as LIGO and Virgo are modified versions of a simple interferometer. The detectors operate in a homodyne configuration that allows extracting the GW phase [19]. A schematic representation is shown in right panel of Figure 1.4. There are three main advancements:

1. Resonant optical cavities - these Febry-Perot cavities allow to extend an effective length of the arms. In case of LIGO detectors the photons circulating inside the cavities are reflected by the mirrors around 300 tmes.

2. Power recycling cavities - given that the detector is kept in the dark fringe, the light after coming back from the arms is reflected by beamsplitter back to the laser. To prevent it, partially transmissive mirrors are placed in front of the laser to reflect the light back into the interferometer.

3. Signal recycling cavities - this is realized by placing another partially transmissive mirror at the output of the detector. The mirror sends the signal sidebands back to the detector where it is enhanced coherently. This

cavity broadens the frequency response of the interferometer. It also may be used to detune the detector to a version with improved narrowband sensitivity.

Even if the noise level at high frequencies depend on the readout, the main limiting factor is the photon *shot noise*. This noise origins from a non temporally uniform collapse of the photons wave functions with the photodiode This noise can be reduced by increasing the power circulating inside the arm cavities - increasing the laser power in the arms is expected to be a great technological challenge. The low frequency noise at power spectral density of the Interferometer is limited by the *seismic noise*. This is a displacement noise caused by motion of the ground and it is isolated by quadruopole-pendulum systems or seismic isolation. In intermediate frequencies the *thermal noise* is a dominant factor and it is minimized by optimizing the properties and designs of the low loss mirrors coatings and and their suspensions with low mechanical loss fused silica.

Other noise sources, like a scattered light, are minimized by the putting the system in ultra hight vacuum below 1μPa. Enviromental disturbences affect the data. Each detector is armed with large number of varoius sensors that monitor the enviroment: seismometers, weather sensors, microphones, magnetometers, cosmic ray detectors and others. The number of sensors for LIGO site is of an order of 200,000.

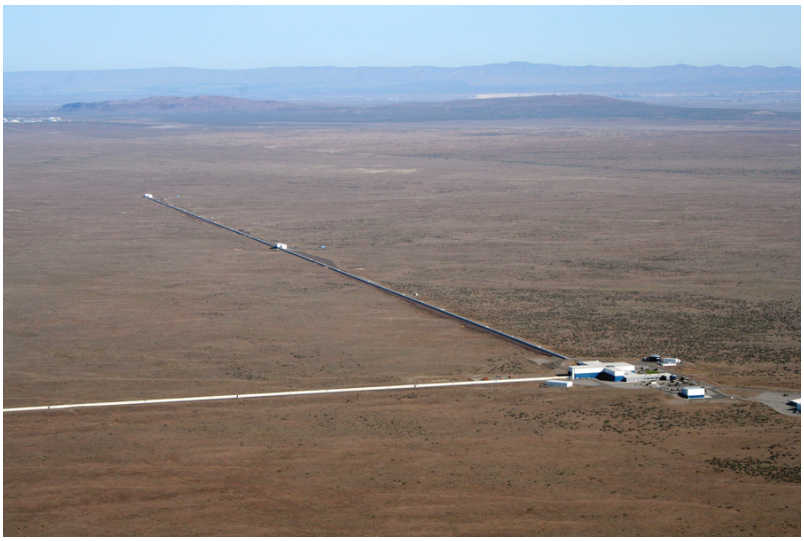

Figure 1.5: Aerial view of the Hanford detector (source [8])

1.3.3 Antenna Patterns

The GW detectors measure the arm length changes due to GW. The sensitivity will vary with the relative direction where the GW is coming from and the arm orientation with respect to this direction. This spatial sensitivity is reffered as *antenna pattern*. The antenna pattern depends on the detector shape. Most of the interferometers are L-shape with perpendicular arms. Some proposed future designs have different layouts, the most notable is Einstein Telescope with triangular configuration made of V-shape interferometers with 60^o between the arms.

Depending on the source orientation or on the uncertainty on the exact time the GW passage through the Earth, we might need either time independent antenna patterns or time dependant ones. For example, when the on-source

window is of the order of a few hours to one day. The spacial sensitivity will be changing over time too due to the rotation of Earth. The future space based detectors, like LISA, will have antenna patterns evolving over time in both geographical and sky coordinate systems.

For simplicity, in section 1.3.3 I will discuss the antenna pattern of a L-shape detector in the coordinate system associated with the detector.

L-shape detectors

Let's consider a detector with equal and perpendicular arms. Associate one of the arms with the x-axis and the second arm with y-axis, see Figure 1.6. The center of coordinate system is at the position of beamsplitter. Let's assume also that the GW is coming from direction z that is perpendicular to the $x-y$ plane.

When a GW is passing through the detector, the movement of the end mirrors is described by the equation (1.41):

$$\ddot{\zeta}^i_A = -\frac{1}{2}\ddot{h}^{TT}_{ij}\zeta^j_A, \tag{1.115}$$

where $A = 1, 2$ is a number of the mirrors placed in position $(L, 0)$ and $(0, L)$. The mirrors move then under the presence of GW:

$$\begin{aligned} \vec{\zeta_1} &= (\zeta_1^x, \zeta_1^y) = (L + \delta\zeta_1^x, 0 + \delta\zeta_1^y), \\ \vec{\zeta_2} &= (\zeta_2^x, \zeta_2^y) = (0 + \delta\zeta_2^x, L + \delta\zeta_2^y). \end{aligned} \tag{1.116}$$

We also assume that the mirrors move only along the arms, not perpendicular to them. This will simplify the

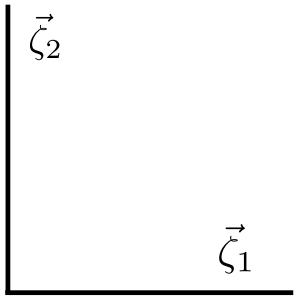

Figure 1.6: L-shape interferometer.

equations to:

$$\begin{aligned} \vec{\zeta_1} &= (\zeta_1^x, \zeta_1^y) = (L + \delta\zeta_1^x, 0), \\ \vec{\zeta_2} &= (\zeta_2^x, \zeta_2^y) = (0, L + \delta\zeta_2^y). \end{aligned} \tag{1.117}$$

Putting these equations to (1.115) we get:

$$\begin{cases} \delta\ddot{\zeta}_1^x = \frac{1}{2}\ddot{h}_{xx}(L + \delta\zeta_1^x), \\ \delta\ddot{\zeta}_2^y = \frac{1}{2}\ddot{h}_{yy}(L + \delta\zeta_2^y). \end{cases} \tag{1.118}$$

For a monochromatic wave with frequency Ω and amplitude A_{ij}, $h_{ij} = A_{ij}\cos(\omega t)$, we get:

$$\begin{cases} \delta\ddot{\zeta}_1^x = -\frac{1}{2}A_{xx}(L + \delta\zeta_1^x)\omega^2\cos(\omega t), \\ \delta\ddot{\zeta}_2^y = -\frac{1}{2}A_{yy}(L + \delta\zeta_2^y)\omega^2\cos(\omega t). \end{cases} \tag{1.119}$$

In order to solve these equations, we can assume that the changes in arm length are much smaller than the lengths of the arms, $\delta\zeta_A^i \ll L$. After integrating the equations we arrive to:

$$\begin{cases} L_x = \zeta_1^x = \frac{1}{2}A_{xx}L\cos(\omega t) = \frac{1}{2}h_{xx}L, \\ L_y = \zeta_2^y = \frac{1}{2}A_{yy}L\cos(\omega t) = \frac{1}{2}h_{yy}L. \end{cases} \tag{1.120}$$

Given that $h(t) = \frac{L_x - L_y}{L}$, the strain becomes:

$$h(t) = \frac{(L + \delta\zeta_1^x) - (L + \delta\zeta_2^y)}{L} = \frac{1}{2}(h_{xx} - h_{yy}). \tag{1.121}$$

General case

Equation (1.121) can be generalized as:

$$h(t) = \frac{1}{2}n_1^i\tilde{h}_{ij}n_1^j - \frac{1}{2}n_2^i\tilde{h}_{ij}n_2^j \tag{1.122}$$

$$= \frac{1}{2}\mathbf{n}_1 \cdot (\tilde{\mathbf{h}} \cdot \mathbf{n}_1) - \frac{1}{2}\mathbf{n}_2 \cdot (\tilde{\mathbf{h}} \cdot \mathbf{n}_2), \tag{1.123}$$

where $\mathbf{n}_1$ and $\mathbf{n}_2$ are unit vectors along the arms of an interferometer and $\tilde{\mathbf{h}}$ is a polarization matrix:

$$\tilde{\mathbf{h}}(t) = M(t)\mathbf{h}(t)M(t)^T, \tag{1.124}$$

where $\mathbf{h}(\mathbf{t})$ is described in TT gauge as (equation (1.28)):

$$\mathbf{h}(t) = \begin{pmatrix} h_+(t) & h_\times(t) & 0 \\ h_\times(t) & -h_+(t) & 0 \\ 0 & 0 & 0 \end{pmatrix}, \tag{1.125}$$

and $M(t)$ is a rotation matrix between the detector frame and the wave frame.

The GW strain is a function of the polarization states and the antenna pattern F_+ and $F_\times$:

$$h = F_+h_+(t) + F_\times h_\times(t), \tag{1.126}$$

The antenna paggerns F_+ and $F_\times$ depend on the sky position.

Antenna Pattern for a Single L-shape Detector For simplicity we assume that the detector is placed in a cartesian coordinate system (x, y, z), and the two arms are placed along x and y axes. When a wave is arriving from a direction (θ, ϕ) (in standard notation of the spherical coordinates), one can write a rotational matrix as:

$$M = \begin{pmatrix} \cos\psi & \sin\psi & 0 \\ -\sin\psi & \cos\psi & 0 \\ 0 & 0 & 1 \end{pmatrix} \begin{pmatrix} 1 & 0 & 0 \\ 0 & \cos\theta & \sin\theta \\ 0 & -\sin\theta & \cos\theta \end{pmatrix} \begin{pmatrix} \cos\phi & \sin\phi & 0 \\ -\sin\phi & \cos\phi & 0 \\ 0 & 0 & 1 \end{pmatrix}, \tag{1.127}$$

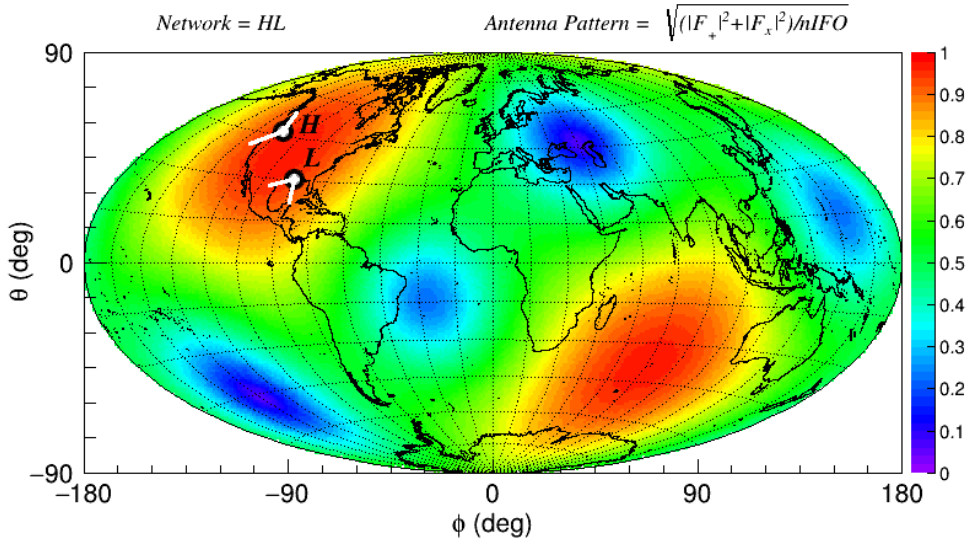

Figure 1.7: Antenna pattern for L1H1 detector network.

where ψ is polarization of the GW.

After applying (1.127) into (1.124) we get the following expressions for the detector's antenna patterns:

$$F_+ = \frac{1}{2}\left(1+\cos^2\theta\right)\cos 2\phi\cos 2\psi - \cos\theta\sin 2\phi\sin 2\psi \tag{1.128}$$

and

$$F_\times = \frac{1}{2}\left(1+\cos^2\theta\right)\cos 2\phi\sin 2\psi + \cos\theta\sin 2\phi\cos 2\psi. \tag{1.129}$$

The antenna pattern in the detector's frame does not change over time. The same applies to the network of detectors. However, due to the Earth rotation, the angular sensitivity is changing over time in celestial coordinates.

L1H1 Antenna Pattern Detector Network Example Figure 1.7 shows an example of the angular sensitivity of L1H1 detector network in Earth coordinate system. This sensitivity rotates in the sky together with Earth rotation. For a source that is fixed on the sky, like a supernova, the sensitivity in that sky location is changing periodically. From this illustration it is visible that in a particular moment of time some parts of the sky are more sensitivity than the other. It is visible that there are four blue spots where the sensitivity is much worse than the rest of the sky. It can be explained by the position of the L1 and H1 detectors with respect to each other. The arms of the detectors are roughly parallel (the Earth curvature, for example, is negligible in this case), so the arms point to the direction of the blind spots. In case when when a supernova explodes in the sky corresponding to one of these blind spots, the GW signal need to be around ten times more energetic to be detectable comparable to the positions in the sky with full sensitivity (red color).

Chapter 2

Core-Collapse Supernova

2.1 Introduction

Core-Collapse Supernova is the end of life for a massive star, $8 < M < 130 M_{\odot}$. During the life, the star burns its fuel through nuclear fusion of elements. The stars are initially formed by hydrogen. When the temperature and pressure is sufficient, the helium and heavier elements are produced. The heavier elements are moving closer to the center creating an onion-like shape. The heaviest element that can be produced through nuclear fusion is iron and an iron core is created. The electron degeneracy pressure and pressure generated by nuclear fussion counter the force of gravity prventing from the core from collapsing.

When the iron core exceedes $1.4 - 1.5 M_{\odot}$ the core becomes unstable the gravity becomes a dominant force and the core collapses. This collapse stops when the new formed proton-neutron star achieve nuclear densities. Albeit, in some cases, the iron core might also collapse to black hole shortly after the initial collapse. The initial iron core has around $1000 - 2000$km in diameter, while right after the collapse, the proto-neutron star is $50 - 100$km in diameter. This contraction makes electrons to break the Coulomb barrier and meet protons of the iron atoms. The neutrons and neutrinos are produced then through reverse beta decay.

The initial energy available to drive a supernova explosion is around $0.15 M_{\odot}$ (primarly potential energy of an iron core). 99% of the explosion energy is believed to be carried away with neutrinos. Around 1% of that energy is transformed into light and then only a small fraction of the explosion energy is converted into Gravitational Waves.

Since the neutrinos are interacting very weakly with matter, they are leaving the collapsed core and then further leave the star. Only a small amount of neutrinos (1-2%) interact with the star's matter. This massive production of neutrinos is also believed to be a dominant factor in explaining the explosion mechanism of a core collapse supernova for slowly rotating progenitors. The neutrinos that are leaving the star also produce Gravitational Waves, also known as Gravitational Wave Memory - asymmetric component of the neutrino emission. Unfortunately their dominant frequency is below 10Hz making them undetectable by the current GW Interferometers.

2.2 Explosion mechanism

After the core collapses, an initial shock propagating outward is created powered by the bounce of the core reaching nuclear densities. This shock dies out shortly after bounce with the infalling matter funneling onto the proto-neutron star. Observationally we know that the stars explode, there must be a mechanism creating a shock that reaches the surface and blow the star. It is unclear what is the exact mechanism, but it is believed that some amount of neutrinos that are leaving proto-neutron star interract with the matter heating it up. A produced pressure counters the infalling matter leading to the creation of a shock. When the heating is sufficient, the shock will expand leading to an explosion. This scenario is known as *neutrino driven explosion mechanism*. This mechanism has been studies for the scenario where the progenitor star rotates slowly. It is believed that 99% of all CCSN are exploding according to this mechanism if the fraction of neutron stars versus magnetars in the Universe correspond to the fraction of slowly rotating versus rapidly rotating progenitors.

Oservationally, there is about 1% of pulsars that rotate very quickly. They are believed to be formed from the progenitor stars that initially rotate rapidly and go supernova. In this scenario, the initial seed magnetic field in the iron core is magnified by the collapse of the core and its rapid rotation. The magnetic field could have a central role in pushing the matter outward creating a shock that drives a supernova. This is also known as *magnetorotationally driven explosion mechanism*.

2.3 Science with GW from CCSN

Core-Collapse Supernovae are astrophysical events where the micro-physics effects have impact on the macro-physics effects and vice-versa. Modeling of these sources is an extremely difficult and many approximations must be done due to lack of sufficient understanding of physical effects especially for rapidly rotating progenitors, extensive computational cost or numerical implementation.

CCSNe are observed regularly in the electromagnetic spectrum and a lot of our knowledge is coming from these observations. The light from a supernova is visible after the shock breaks the surface, which is hours of days after the iron core collapses. Unfortunately the information about the dynamics from the moment of the collapse is lost. The information of what is happening during the collapse can be observed only with neutrino luminosity and GW time series. So far the neutrinos from a CCSN were seen only from SN 1987A, while none of GW were seen from a CCSN. Different observables bring different information about the source (see section 3) and GW carry information about the dynamics of a CCSN. A detection of GW from CCSN gives an unique opportunity to understand the nature of exploding stars and possibly learn something new that is not yet embodied in Science.

2.3.1 Science Questions

Here I am listing few examples of Science Questions that can be addressed and lessons that we might learn in case of detection of GW from CCSN.

1. *What is the dominant explosion mechanism of a CCSN?*
2. *What is the main source of asymmetry in CCSN?*

3. *What is the neutrino mass hierarchy?*
4. *What is the speed of neutrinos?*
5. *What geometry is during BH formation?*
6. *What is the Nuclear Equation of State of dense matter?*
7. *What is the maximum mass of PNS?*
8. *We could learn about the evolution of the size of proto-neutron star.*
9. *We could learn about the accretion rate.*
10. *We could learn about rotational properties of PNS, rotational rate and rotational profile*
11. *We could learn what are the dominant GW emission processes (sources of asymmetry?)*

2.4 Emission processes

As we saw in section 1.2.5 Gravitational Waves are radiated by a large aspherical mass-energy movement, more precisely by the second time derivative of a quadruopole moment. CCSN has a large variety of different processes that break spherical symmetry emitting GW. The emission is associated with various modes of PNS pulasion, convection or SASI, asymmetric neutrino outflaw, core collapse and bounce, flatenning of the core and others. Table 2.1 presents a summary of different emission processes along with basic properties.

The energy of GW varies by several orders of magnitude depending on the emission process. A typical kinetic energy of the supernova ejecta is around $10^{-3}M_{\odot}c^2$ (for example, for SN 2015as the kinetic energy is $0.4\times10^{-3}M_{\odot}c^2$ [37]) and assuming that all kinetic energy is transformed into GW, it can be treated as an estimated upper limit for GW energy emission. However, typical energy emitted in GW for a realistic simulations is around to be of an order of $10^{-8}-10^{-7}M_{\odot}c^2$.

Table 2.1: SN Emission Processes

Emission Process	Duration [ms]	Spectrum [Hz]	Typical h @ 1 Mpc	Typical E_{GW} $[M_{\odot}c^2]$
Rotating Collapse & Bounce	$\sim$10	$\sim400-900$	$\sim5\times10^{-24}-2\times10^{-22}$	$\sim2\times10^{-11}-1\times10^{-7}$
Rotational Instabilities:				
Dynamical Shear	$10-\gtrsim100$	$\sim700-1000$	few $\times10^{-23}$	$10^{-7}\left(\frac{\Delta t}{100\text{ms}}\right)$
Bar Mode	$10-\gtrsim100$	$\sim1000-2000$	few $\times10^{-23}-10^{-21}$	$10^{-7}-10^{-2}\left(\frac{\Delta t}{100\text{ms}}\right)$
Convection:				
Prompt Convection	$10-30$	$\sim50-1000$	$\sim10^{-25}-10^{-23}$	$\sim10^{-12}-10^{-9}$
ν-Driven Convection/SASI	$100-500$	$\sim100-1000$	$\sim10^{-25}-10^{-23}$	$\sim10^{-12}-10^{-9}\left(\frac{\Delta t}{100\text{ms}}\right)$
Convection in the PNS	$\gtrsim1000$	$\sim600-1000$	$\sim10^{-23}-10^{-23}$	$\sim10^{-8}\left(\frac{\Delta t}{1\text{s}}\right)$
Black Hole Formation	$\lesssim1-2$	$\sim600-4000$	$\sim10^{-23}-10^{-22}$	$\sim10^{-8}-10^{-7}$
Aspherical Outflows	$\gtrsim100-1000$	~20	$\sim10^{-23}-10^{-22}$	$\lesssim10^{-11}$
Accretion Disk Instabilities	$\gtrsim1000$	$\sim100-1000$	$\sim10^{-22}-10^{-19}$	$\sim10^{-5}-10^{-1}$
Neutrino Outflow	$\gtrsim1000$	$\lesssim10$	$\sim10^{-21}-10^{-19}$	$\sim10^{-5}-10^{-1}$

2.5 Waveform morphologies

For the GW searches the most important quantity for detecting far sources is the GW energy. Another important property is the morphology of the signal. The detection capabilities vary depending on the time-frequency evolution of a waveform. This section describes few different types of SN models.

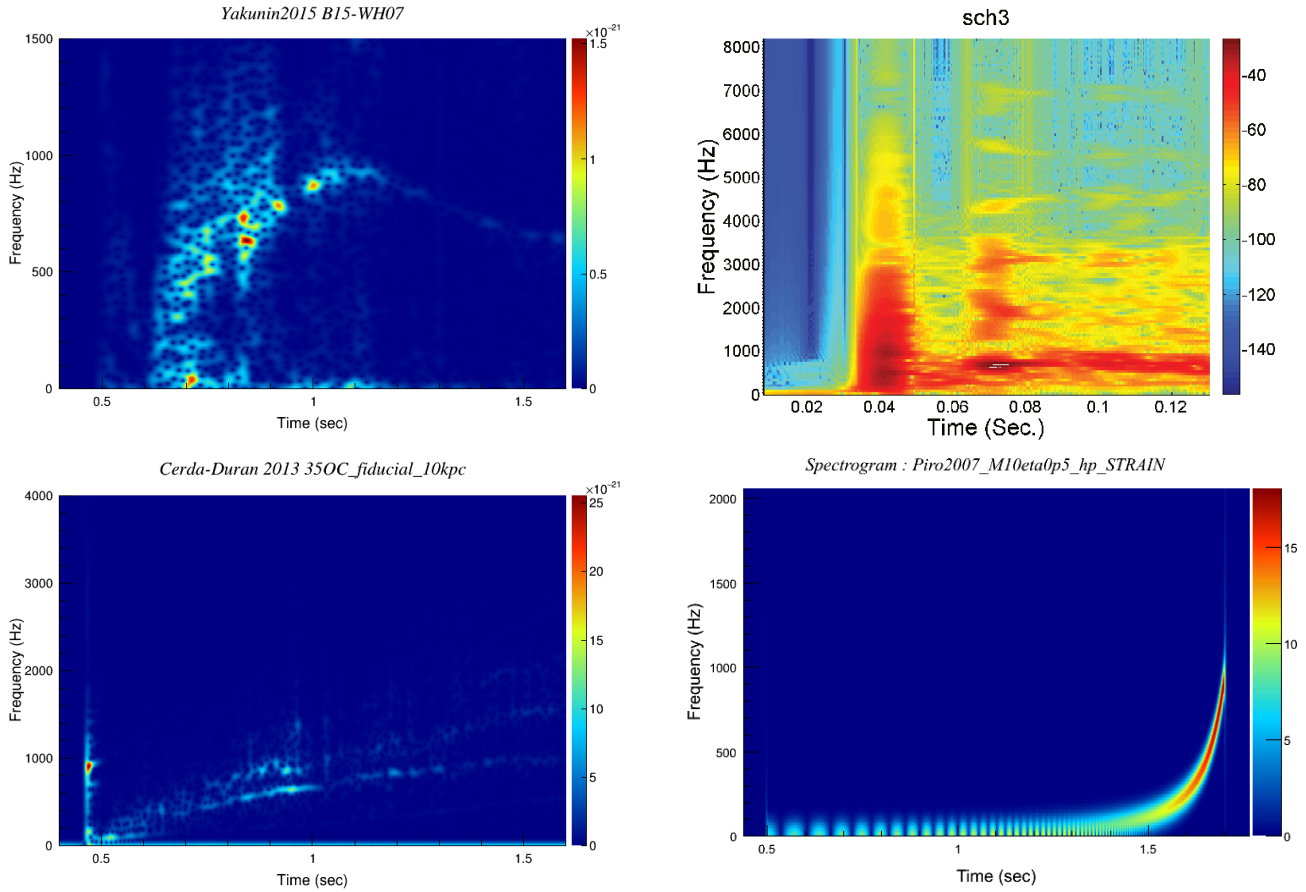

Figure 2.1: Example spectrograms of SN waveforms. Upper left: Neutrino Driven waveform - Yakunin 2015, Upper right: Magnetorotationally Driven waveforms - Scheidegger 2010, Lower left: Collapsar - Cerda-Duran 2013, Lower right: Exreme Emission Model - Piro 2010.

2.5.1 Neutrino Driven Explosions

The most realistic supernova waveforms are relatively long and broadband.

Yakunin et al 2015 [38]

We consider waveforms generated with four different progenitor masses: 12, 15, 20, 25$M_{\odot}$. These are obtained from two-dimensional numerical simulations of non-rotating stars. The effect of general relativity is taken into account by replacing the newtonian monopole gravitational potential with the correction due to relativity. Also,

for these waveform a Lattimer-Swesty EoS was used with a bulk compressibility modulus of 220 MeV.

Mueller et al 2012 [33]

This model is a three-dimensional simulation employing non-rotating 15 and 20 $M_{\odot}$ progenitor stars. In these simulations funnel of matter after collapse does not reach the dense part of the core and as a consequence the only low frequency GW signals are produced.

2.5.2 Magneto-hydrodynamically Driven Explosions

This explosion mechanism is proposed for progenitors that rotte fast. It is believed that only 1% of all supernovae explode with this scenatio. In this scenario the most distinguished signature is the initial core collapse and bounce.

Dimmelmeier et al 2008 [39]

This two-dimensional General Relativistic model of a rotating core collapse produces a robust explosion. The GW signature consists mainly from a semi-analitical signal from the core collapse and bounce. The remaining part of the signal is non-deterministic and weak. In this simulation rapid rotation does not allow SASI and convection to develop.

Scheidegger et al 2010 [40]

This model comes from three-dimensional supernova simulation with $15M_{\odot}$ rapidly rotating progenitor star. Due to the rapid rotation, the initial core collapse and bounce signature is present in the initial phase. Later, a co-rotational instability is developed that produces majority of GW energy.

2.5.3 Black Hole formation and Extreme Model Emission

Cerda-Duran et al 2013 [26]

It is an axisymmetric rotating model of Black Hole formation in a massive star. These types of collapse are believed to engines that drive GRB signals. The simulation shows that the BH formation is delayed and the GW signals last few seconds. Botttom left picture 2.1 sow an example of a waveform. After energetic collapse, the peak frequency of GW signal increases in time due to the oscillation of proto-neutron star due to the stiffening of the core, until the BH is formed and the GW signal dies out.

Piro et al 2010 [41]

A phenomenological model of a collapsar that is extreme, but plausible. It has not been ruled out observationally. In this scenario a Black Hole is created after the collapse and a dense $M_{\odot}$-scale fragment of matter is formed. This fragment falls into Black Hole creating a very strong chirp-like GW signal.

Chapter 3

GW Multimessenger Astronomy

CCSNe are a natural target for multimessenger astronomy since the simultaneous observation of neutrinos and photons during SN1987a. If someone wants to study the inner dinamics of a CCSN, is necessary to collect more than photons because the EM emissions originate thousands of kilometers away from the center of the explosion as well as hours to days after the onset of the collapse. Only GWs or neutrinos carry direct imprints of the initial stages of the collapse and possibly only GW observations can elucidate some of the details of the shock revival mechanism.

The numerical modelling of CCSNe which has been going on for several decades starting with Bethe, relies on all fundamental forces at the same time.Properly reproducing the physics with numerical simulations has evolved over time toward computer intensive (tens to hundreds of millions CPU hours are necessary for each waveform in the most demanding simulations) numerical schemes evolving neutrino radiation, (magneto) hydrodinamics and the metric in 3 dimensional space time grids. These girds also need sufficient resolution to capture all relevant fluid instabilities. What makes the study particularly delicate is that, for the majority of CCSNe progenitors, it is expected that the newly formed shock wave around the prothoneutron star quickly stalls because of ionization and momentum transfer with the infalling material and the revival mechanism depends on the interplay of a number of effects. Worth mentioning in these simulation efforts (more discussion is presented in section IV.B) is the recent achievement of a 3D simulation that produces an explosion of a slowly rotating progenitor.

3.1 Multimessenger Astronomy with GW from CCSN

The Universe is providing us a vast amount of information about happening there explosions, collisions, or exotic processes. These information we can divide into four distinctive messengers. Each of them teaches us of different properties of the source, its enviroment or history:

- Electromagnetic Radiation - emission processes, environment
- Neutrinos - mainly thermodynamics, hadronic/nuclear processes
- Gravitational Waves - mainly dynamics, mass distribution
- Cosmic Rays - acceleration processes, nucleosynthesis

Core-Collapse Supernovae are unique events that emit all four messengers. They appear at the different times of an explosion and have different detectability requirements.

Messenger	Binary Black Holes	Binary Neutron Stars	Core-Collapse Supernovae
Gravitational Waves	yes	yes	possible
Electromagnetic Radiation	possible	yes	yes
Neutrinos	possible	possible	yes
Cosmic Rays	possible	possible	yes

Table 3.1: Examples of three distinguished sources of GW together with prospects of multimessenger detection.

Figure 3.1 shows an example comparing the timings and energies of the messengers (taken from [9]). Initially, the star is going through silicon burning phase producing neutrinos that might be detectable for extremely close CCSN. When a star reaches the Chandrasekhar mass, the collapse happens with a very strong neutrino outflow that lasts around 100s. During the first second after the moment of the core collapse, the GW signal is produced. The inband signal is expected to be less than a second long and the energy is few orders of magnitude smaller than energy released with neutrinos. After that, the shock is propagating outword. The shock reaches the surface of the star after few hours or few days, depending on the progenitor star. The Shock breakout (SBO) is also a moment when the supernova starts to be visible optically. After the explosion, the remnant replaces the progenitor star. Then cosmic rays, after several years, can be observed from the remnant.

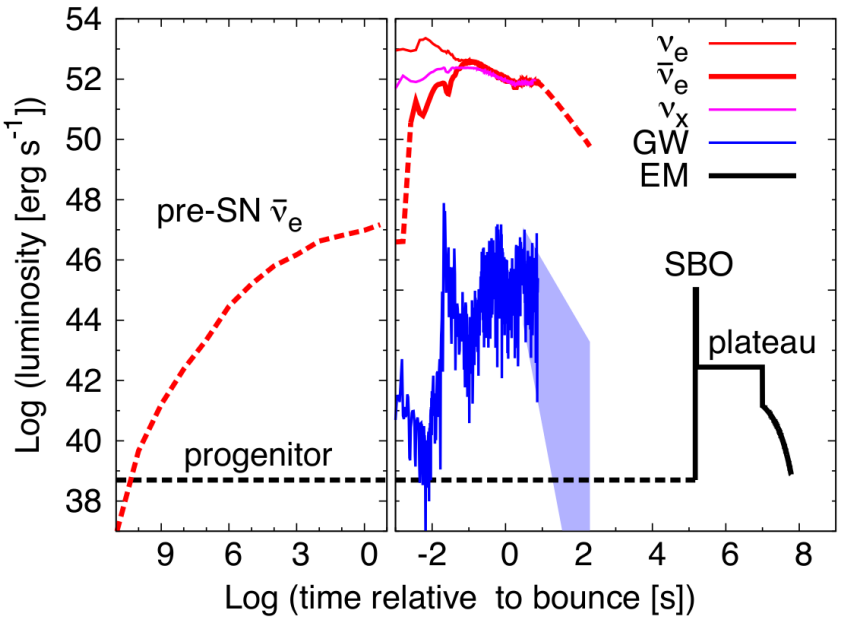

Figure 3.1: Timing and typical energies of GW, optical and neutrino messengers. Figure taken from [9].

The detection of GW is the main topic of this dissertation and the following considerations I will try to recognize how the neutrino and electromagnetic observables might help for the GW detection and parameter estimation purposes. I will not consider Cosmic Rays since they are observable years after the explosion and long after GW emission.

3.1.1 Electromagnetic radiation

Core-Collapse Supernovae are primarily observed in the electromagnetic spectrum allowing understanding of their properties, evolution and populations.

Lightcurves For each explosion the lightcurve bring several information that can help the search for GW:

- On-source window - this is an important component of the triggered searches. The optical observations can constrain the timing of GW up to few hours. See section 8.3.1 for more information.
- Sky localization - each CCSN is well localized in the sky. It gives an advantage of removing the noise triggers reconstructed far from the supernova location.
- Distance - it is usually available by recognizing the host galaxy. However, the lightcurves might provide a more precise estimation of a distance or provide the distance when host galaxy cannot be identified.
- Progenitor star mass - lightcurves might constrain the mass of the progenitor star. An estimated mass of the progenitor star could narrow the tuning of the pipelines to fewer waveforms morphologies and in turn provide a combination of better detection range and detection significance.
- Explosion type - from the energy measured the lightcurves we might estimate if the explosion can be associated with a typical supernova (slowly rotating) or hypernova (rapidly rotating).

Spectroscopy The observations of polarizations of the light [42, 43, 44] from CCSN could bring interesting information for the GW searches:

- SN orientation - the polarization of the light might be able to reveal the orientation of an axis of rotation. This particularly might help in searching for GW from rapidly rotating progenitors - the core collapse and bounce signature is produced for a view from equator.
- rotational properties - the polarization of the light could give an estimate of how fast the progenitor star was rotating.
- explosion asymmetry - the spectroscopy can reveal degree of asymmety of an explosion. This might help in estimating the GW energy.

Distributions The study of the populations of CCSN could help the GW searches in the following way:

- Rate - by analysing the populations of CCSNe we can estimate a detailed rate of CCSNe in the nearby Universe (see section 7)
- Most likely sky locations and distances for CCSN in Milky Way (e.g. Beteleugeuse) and in Local Universe (e.g. starburst galaxies)
- The observed locations and distances of distributions of optical CCSNe might help detecting a population of GW sources when the GW signals are weak.

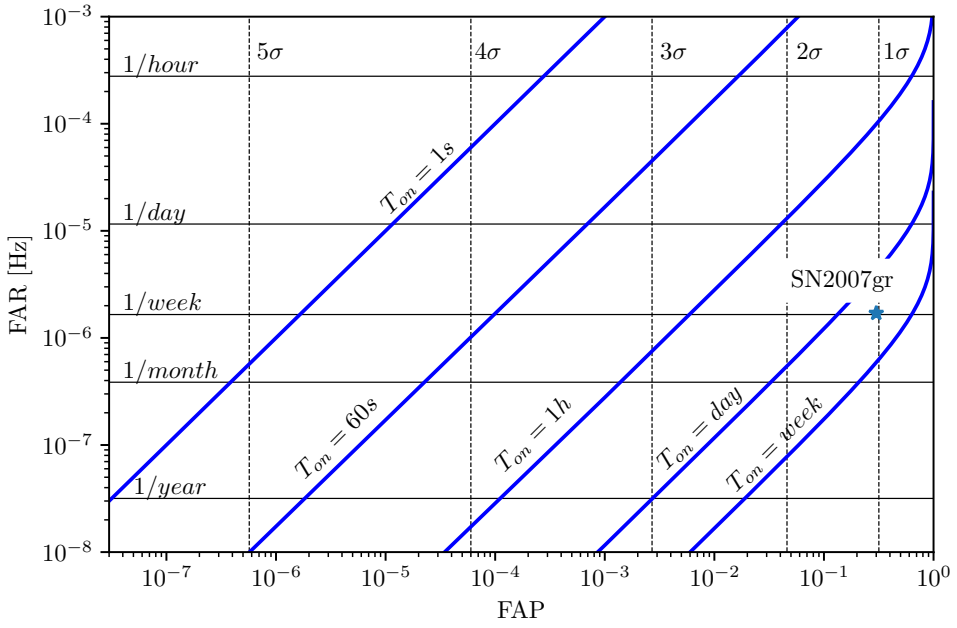

Figure 3.2: The dependance of the False Alarm Probability (FAP) and False Alarm Rate (FAR) depending on the on-source window duration. This plot illustrates how much the significance of GW candidates increases with constraining duration of the on-source window.

Others There are several other information that can be extracted from the SN optical observations:

- Disappearing stars, like red giants for the search for BH formation.
- Pulsar kick for estimating the GW Memory.
- Kinetic energy of the ejecta.

3.1.2 Neutrinos

A small flux of neutrinos was observed for SN 1987A. Although the number of observed neutrinos was small (around 25), they brought a large impact on understanding the properties of the exploding stars. With the next nearby supernova we will have much larger flux of neutrinos and it will bring even more understanding of the explosion properties. In particular, the detection of neutrinos might help GW searches in the following ways:

- On-source window - we will be able to constrain very well the timing of the collapse (useful for optically obscured CCSNe).
- Sky localization - large flux of neutrinos will give an approximate sky localization.
- Flux oscillations - the potential oscillations of the neutrino fluxes will bring indications of a strong SASI activity.

- Duration of nu emission - it will allow to estimate duration of the GW memory waveforms.
- Evolution of proto-neutron star - the radius and mass evolution can be estimated during the cooling phase (>1s). It could be matched with the initial evolution of proto-neutron star from GW detection.
- Early warnings from pre-supernova neutrinos [45] - this can achieved only for a nearby Galactic CCSN (less than 1kpc, e.g. Betelgeuse). The silicon burning is producing fluxes of pre-SN neutrinos, if integrated over a long time, can give an early warning of a nearby SN.

3.2 Relation between GW SN Searches and Parameter Estimation

The priority of LIGO Data Analysis activities are the searches for GW from various sources. One can divide the waveforms according to their duration and availability of a template. Table 3.2 gives a general overview of this division along with few examples. This division is not strict though.

Table 3.2: GW sources

	Modeled	Un-modeled
Short	CBC (BBH, BNS)	Burst (BNS, SN, cosmic string)
Long	Continuous Waves (pulsars)	Stochastic (sum of NS)

Figure 3.3 shows a relation between the Search and Parameter Estimation. When the search is conducted, GW candidates are extracted and their significance is assigned then the next natural step is to extract physical information from the GW candidate (Parameter Estimation).

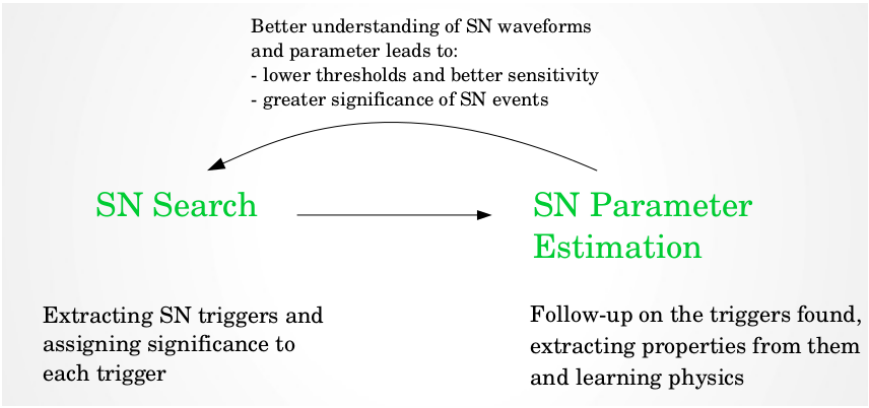

Figure 3.3: A comparison between the GW SN Search and Parameter Estimation

The search and PE are separate steps of the analysis, but in order to improve each of them there is need to have interplay between them. Better understanding of SN waveforms or their robust features leads to lower thresholds leading to better search sensitivity and greater significance of SN events Better understanding of the parameter space of the progenitors allows us to tune the pipelines to the parameters we want to explore.

3.3 GW SN Searches

The strategies for GW searches can vary according to detection of different messangers. It may happen that GW are produced while no electromagnetic or nautrino counterpart is detected. In the case we observe only light from a nearby supernova a triggered search is performed. In the case we observe low significance neutrinos then subprime neutrino search may be performed. The searches can dedicated according to robust emission processes, like g-mode, for more details see section 12.3. Special attention is placed when a SNEWS alert detects a Galactic or nearby extragalactic supernova, like in case of supernova SN1987A, which exploded in the Large Magellanic Cloud, a neighbor galaxy of the Milky Way. At the time, no detector with sufficient sensitivity to detect GWs from a supernova was operational.

The SN triggered search is characterized by:

1. On-source window – period that we think contains GW, derived from optical or neutrino observations. Timescales:

   1.1. Neutrino triggered search - seconds to minutes

   1.2. Optically triggered search - hours to few day

2. Sky location – usage of skymask

3. Distance

The main purpose of data analysis is the detection of GW. An algorithm first searches for GW candidates and assigns significance of these candidates. It is done by a search pipeline and we primarly use cWB for this. Section 4.1 describes the process of obtaining the GW candidates with cWB.

3.4 SN Parameter Estimation

After a succesful search, when GW is detected, the next step is to estimate physical parameters of the source.The task is well defined for the binary sources. General Relativity provides a very well defined parameter space that allows to span the possible waveforms using indicators, like the initial masses, spins, inclination angle or the source distance.

The task of defining a parameter space for Core-Collapse Supernovae is much more difficult because many parameters are not as naturally defined. CCSNe models are characterized by a large number of parameters spanning the micro-scale Physics up to macro-scale Physics. The process during the explosion depends on many ingredients, like the progenitor star properties and the evolution of the collapsing star, that can lead to a supernova or Black Hole formation. Beside the physical parameters also signal processing parameters can be computed on the reconstructed GW that quantify duration and bandwidth for example. This difficulty in parametrizing the CCSN simulations brings also a challenge in defining parameter space of SN waveforms.

CCSN models vary in terms of sophistication and realism. The GW energy from these models can vary orders of magnitude. For example, the energies of neutrino driven waveforms are much different from the extreme emission models or collapsars. Parameter estimation could also be performed in two stages:

1. a model is chosen or identified with some procedure,

2. parameters of that model are estimated.

Model selection of this approach is reflected in the O1-O2 SN Search paper (see section 8), when the waveforms families are divided into three categories: neutrino and magnetorotationally driven explosions and extreme emission models. The division cannot be done strictly, of course, but it allows to recognize the most important ingredients. More extensive description and studies can be found in section 12.

The detection on binary neutron stars on August 17th, 2017 has initiated a new way for observing the Universe. For the first time both GW and electromagnetic radiation were observed from the same source inaugurating GW Multimessenger Astronomy. Different messengers carry different information about the source.

The most remarkable example of a multimessenger event from a point of view of Supernova research is SN 1987A that exploded in Large Magellanic Cloud, $\sim$ 50kpc away. This supernova was observed by neutrino and astronomical observatories. Around 25 neutrinos associated with this supernova were observed by three neutrino detectors. These neutrinos appeared in the detectors three hours before the shock breakout that lead to observation of light. This small amount of neutrinos confirmed that a massive amount of neutrinos is created during the collapse of a core. It is believed that this large flux of neutrinos play a crucial role in an explosion. The remnant of this supernova is still of a great interest, after 3 decades, the research on this supernova is still ongoing.

Core Collapse Supernovae mutimessenger astronomy for GWs is roughly divided in two scenarions where (a) multiple messengers are used to perfom parameter estimation and (b) to enhance the chances to detect a GW from CCSNe.

3.4.1 Multimessenger Parameter Estimation for CCSNe

In the first case we need first to establish that the messengers of the CCSNe were detected and collected by the different instruments, usually in the presence of stochastic noise and fluctuations. In this case, the goal is to define what is the best parameter estimation metodology, and establish what parameters are reasonable to estimate and with which accuracy.

It is worth stressing that there are tools to address minumum conditions to estimate parameters with a desired accuracy even before a specific alghorithm is designed [46]. These methodologies also provide insight on how extra messengers can reduce the errors in the parameter estimation process.

The starting point of understanding how promising is a parameter estimation scenario, is the statistical modelling of the data. For example the data at a laser interferometer and a neutrino detector could be modelled as:

$$x_{GW}(t) = h(t) + n_{GW}(t) \tag{3.1}$$

and

$$x_{nu}(t) = s(t) + n_{nu}(t), \tag{3.2}$$

where $s(t)$ is the deterministic component of the neutrino luminosity observed at the detector. As a toy model of the SASI neutrino signal is

$$s(t) = (a/D(1 + b\cos(2\pi f_s t))) \times W(t), \tag{3.3}$$

where a is a model specific constant, D the distance from the SN, b the relative amplitude of the luminosity oscillations induced by the SASI, f_s is the frequency of the SASI oscillations and $W(\tau)$ is a window function with a duration τ. In this case a,b,f_s and τ are the parameter of the signal.

$n_{nu}(t)$ it is the noise at the neutrino detector. It can include instrumental events which are not induced by neutrinos produced in a CCSN but it also depends on the signal s(t). The reason is that only a small fraction of the neutrinos results into an event at a Neutrino detector and the fraction itself is expected to fluctuate like a Poissonian process around the mean $s(t)$. Accordingly the amplitude of these fluctuations is expected to be the $\sqrt{s(t)}$.

It is important to immediately notice that both (I) the Possionian oscillations of the observed neutrino luminosity and (II) the SASI oscillations of amplitude b perturb the mean neutrino signal of amplitude a/D. The difference between these two oscillations is that while the relative amplitude of (I) increases with the distance the relative amplitude of (II) is constant with the distance. This intuitively means that for any signal with SASI oscillations we expect to have a maximum sitance distance where the parameters of the SASI oscillations can be measured accurately (or measured at all).

$h(t)$ is the gauge invariant response of the interferoeter which can be modelled as a linear combination of the two polarizations in a specific frame. In general h(t) could be modelled as a stochastic process given that the stochasitc nature of the evolution could produce waveforms with slightly features. Here as an illustrative example we focus on the deterministic periodic oscillation in the GW which are produced by the SASI modes. We treat this scenario with a deterministic h(t). The polarization state of this GW is expected to be elliptical given the rotating time evolution of the excitations on the prothoneutron star.

n_{GW} is the LIGO interferometer noise that for PE purposes it can usually be modelled as a colored Gaussian noise. This assumption is reasonable because the non Gaussian component of the noise are rare enough to be unlikely to concide with a GW but frequent enough to be dealt instead for assessing the false alarm probability of a candidate GW event.

Under the assumption that $h(t)$ and $s(t)$ are deterministic the full probability distribution of the data is given by the product of the probability distibution of $x_{GW}(t)$, indicated as $p(x_{GW}(t), \vec{\theta})$ and the one of for $x_{nu}(t)$, indicated as $p(x_{nu}(t), \vec{\theta})$ where $\vec{\theta}$ represents the whole set of parameter that can be extracted.

How easily parameters can be extracted is indicated by how quickly the value of the probability distribution changes if we used the observed velue of $x_{GW}(t)$ $x_{nu}(t)$ into

$$p_{\text{multimessenger}} = p(x_{GW}(t), \vec{\theta}) * p(x_{nu}(t), \vec{\theta}) \tag{3.4}$$

and vary the value of the parameters around the correct one. The ideal scenario is when $p_{\text{multimessenger}}$ is a very peaked function of the parameters around the true value. The width of the peak can be used to estimate the achievable accuracy and if an estimator exists that can achieve that accuracy is the so called Maximum Likelihood estimator. It is possible to prove that for sufficiently strong signals the minimum achievable error is described by the elements of the inverse of the so called inverse Fisher Matrix.

The elements of the Fisher matrix are given by:

$$I_{i,j} = \langle -\frac{\partial^2 \ln p_{\text{multimessenger}}}{\partial\theta_i \partial\theta_j} \rangle \tag{3.5}$$

and the symbols $\langle ... \rangle$ indicate the expectation value of what is inside. The first important observation is that the fact that the total probability distribution is the productcts of the probability distributions of the different mutimessenger observations, means that the logarithm becomes the sum and that the total Fisher information matrix becomes the sum of the Fisher information matrices of the different multi messenger observers:

$$I_{i,j} = \langle -\frac{\partial^2 \ln p_{multimessenger}}{\partial\theta_i \partial\theta_j} \rangle \tag{3.6}$$

$$= \langle -\frac{\partial^2 \ln p_{GW}}{\partial\theta_i \partial\theta_j} \rangle + \langle -\frac{\partial^2 \ln p_{nu}}{\partial\theta_i \partial\theta_j} \rangle. \tag{3.7}$$

This expression illustrates how each mutimessenger observation adds more "information" on the parameters, because the more terms you add the smaller the elements of the inverse matrix become. This also means that the scientific potential of parameter estimation improves with more multimessenger observations.

Chapter 4

coherent Wave-Burst

The coherent Waveburst (cWB) is an excess power pipeline based on the Maximum Likelihood mathematical framework. This is the primarly algorithm used in the Supernova GW searches and it will be described extensively in this section. The description of cWBis done in the context of searching for GW from CCSN.

The cWBanalysis can be divided into two stages:

1. Production - in this stage the data is prepared, configuration set and the list of triggers is generated, this is described in section 4.3.

2. Post-production - in this stage the vetoes, selection cuts applied and reports with various statistics are produced, see section 4.5 for more details.

A default output of cWBalgorithm is a list of triggers that are GW candidates. The significance of each event is calculated from their false alarm rate and false alarm probability once a specific duration of data is identified. The mathematical foundation of constraining the likelihood of the triggers is described in section 4.2. For each trigger, cWBestimates properties like duration, bandwith, central frequency and others (with specific definitions defined in section 4.4). By default, cWBdoes not do a detailed reconstruction of the triggers, like time or Fourier series. The reason is the computational cost, the reconstruction of each trigger is not needed to obtain robust results. The speed that is gained allows to test variety of tunings and process large amount of data very quickly. The reconstruction of interesting triggers or the whole population of trigger can be done separately. The reconstruction of the triggers is ralized with the *Coherent Event Display* that will be further described in section 12.2. The analysis of the populations of the triggers is described in section 4.5.

4.1 cWBoverview

The cWB[47, 13] is based on computing a constrained likelihood function. In brief, each detector data stream is decomposed into 7 different wavelet decompositions (each one with different time and frequency resolutions). The data are whitened, and the largest 0.1 percent of wavelet magnitudes in each frequency bin and decomposition for each interferometer are retained (we call these "black pixels"). We also retain "halo" pixels, which are those that surrounding each black pixel. In order to choose pixels that are more likely related to a GW transient (*candidate*

event) we identify clusters of them. Once all of the wavelet decompositions are projected into the same time frequency plane, clusters are defined as sets of contiguous retained pixels (black or halo). Only the pixels involved in a cluster are used in the subsequent calculation of the likelihood. These clusters also need to be consistent between interferometers for the tested direction of arrival. For each cluster of wavelets, a Gaussian likelihood function is computed, where the unknown GW is reconstructed with a maximum-likelihood estimator.

The likelihood analysis is repeated over a grid of sky positions covering the range of possible directions to the GW source. Since the sky location of each of the analyzed CCSNe is well known, we could choose to apply this procedure only for the known CCSN sky location. However, the detector noise occasionally forces the cWB likelihood to peak in a sky location away from the true sky location. As a consequence, some real GW events could be assigned a smaller likelihood value, lowering the capability to detect them. Because of this, we consider triggers that fall within an error region of 0.4 degrees of the known CCSN sky location and that pass the significance threshold, even if they are not at the peak of the cWB reconstructed sky position likelihood. The 0.4 degree region is determined empirically by trade-off studies between detection efficiency and FAR.

The events reported for a given network configuration are internally ranked for detection purposes by cWB using the coherent network amplitude statistic ρ defined in [48]. Other constraints related to the degree of similarity of the reconstructed signal across different interferometers (the "network correlation coefficient" *cc*) and the ability of the network to reconstruct both polarizations of the GW signal (called *regulators*) are applied to reject background events; these are also described in [48] and briefly in 4.2.2.

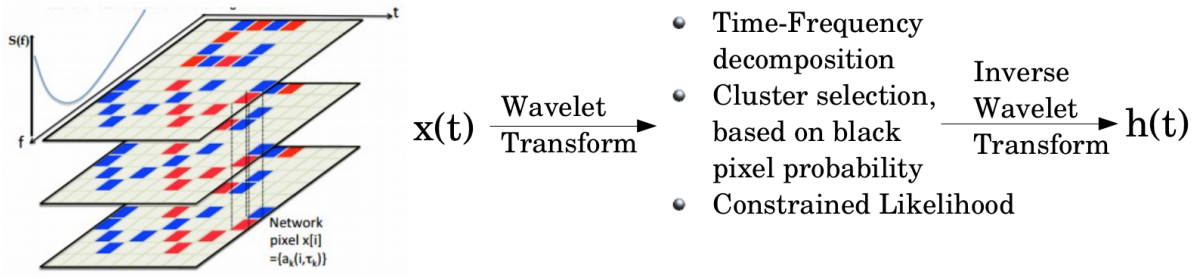

Figure 4.1: Decomposition of time series into time-frequency maps.

4.2 Constrained Likelihood Analysis

Coherent Wave-Burst performes a constrained likelihood analysis and the pipeline assigns significance to an GW candiadate and provide reconstructed waveform. The mathematical formulation has been developing over the years and it is beyond the scope of this dissertation to present an extensive the state-of-the-art of mathematical foundation. Instead, this section provides only selected elements of this foundation which will help to understand the usage of cWBfor searching for GW from CCSNe and reconstructing the waveforms.

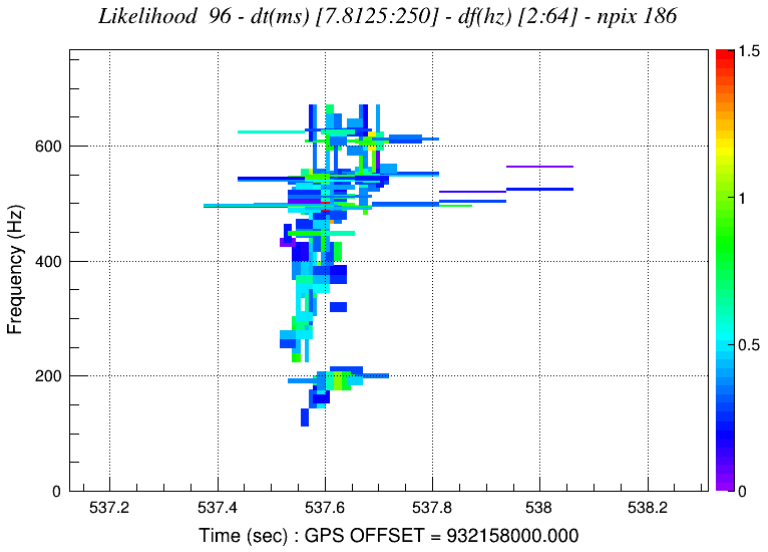

Figure 4.2: An example of a time-frequency cluster.

4.2.1 Single Detector Assuming Gaussian Noise

The GW signal h is additive to the detector noise n:

$$x(t) = h(t) + n(t), \tag{4.1}$$

and the signal can be expressed in terms of the antenna patterns, equation (1.126):

$$h(t) = F_+ h_+(t) + F_\times h_\times(t). \tag{4.2}$$

Calculating the likelihood for a single detector, we introduce the hypothesis test, which requires the definition of a decision rule in order to select one of the two mutually exclusive hypotheses: the absence (H_0, null) and the presence (H_1, alternative) of the identified signal in the data stream.

The Neyman-Pearson criterion states that when H_1 is a simple hypothesis and the data is a single Gaussian measurement, the decision rule that uses the likelihood ratio has the highest detection for a fixed false alarm probability. The likelihood ratio, $\Lambda(x)$, is defined as the following:

$$\Lambda(x) = \frac{p(x \mid H_1)}{p(x \mid H_0)}, \tag{4.3}$$

where $\Lambda(x)$ is greater than the threshold value that is fixed by a specific false alarm probability.

With the assumption of Gaussian white noise with a zero mean, the probability densities associated to the two hypotheses, H_0 and H_1, are the following with σ being the standard deviation of the noise:

$$p(x \mid H_0) = \prod_i \frac{1}{\sqrt{2\pi\sigma}} \exp\left(-\frac{x^2[i]}{2\sigma^2} \right) \tag{4.4}$$

$$p(x \mid H_1) = \prod_i \frac{1}{\sqrt{2\pi\sigma}} \exp\left(- \frac{(x[i] - \xi[i])^2}{2\sigma^2} \right) \tag{4.5}$$

Using the logarithmic value of the likelihood ratio, we obtain the likelihood as the following:

$$L = ln(\Lambda(x)) = \sum_i \frac{1}{\sigma^2}(x[i]\xi[i] - \frac{1}{2}\xi^2[i]). \tag{4.6}$$

In order to calculate the likelihood, we introduce complex representations of the data. Complex waveforms ζ and antenna patterns A are defined as the following, with $\imath$ being an imaginary unit:

$$\zeta = h_+ + \imath h_x, \tag{4.7}$$

$$A = \frac{1}{2}\left(F_+ + \imath F_\times\right). \tag{4.8}$$

As a result, the detector response becomes:

$$\xi = \zeta \cdot \tilde{A} + \tilde{\zeta} \cdot A. \tag{4.9}$$

We notice that ξ does change when we apply rotation of the polarization angle ψ:

$$\zeta' = e^{i\psi}\zeta, \tag{4.10}$$

$$A' = e^{i\psi}A. \tag{4.11}$$

4.2.2 Network of detectors

In case of having several detectors in the network, we use a similar notation as previously. We can write the GW data from N detectors as:

$$X_\sigma = \xi_\sigma + N_{ull}, \tag{4.12}$$

where we use vectors normalized to k^{th} detector noise σ_k:

$$X_\sigma = \left(\frac{x_1}{\sigma_1}, \ldots, \frac{x_N}{\sigma_N}\right), \tag{4.13}$$

$$\xi_\sigma = \left(\frac{\xi_1}{\sigma_1}, \ldots, \frac{\xi_n}{\sigma_N}\right), \tag{4.14}$$

and N_{ull} represents null stream data.

Similarly, we introduce normalized vectors of antenna patterns:

$$f_+ = \left(\frac{F_{1+}}{\sigma_1}, \ldots, \frac{F_{N+}}{\sigma_N}\right), \tag{4.15}$$

$$f_\times = \left(\frac{F_{1\times}}{\sigma_1}, \ldots, \frac{F_{N\times}}{\sigma_N}\right), \tag{4.16}$$

$$A_\sigma = \left(\frac{A_1}{\sigma_1}, \ldots, \frac{A_N}{\sigma_N}\right). \tag{4.17}$$

and the gravitational signal in each detector becomes:

$$\xi_k = \zeta_k \cdot \tilde{A}_k + \tilde{\zeta}_k \cdot A_k. \tag{4.18}$$

Consequently, the total likelihood we define as:

$$L = ln(\Lambda(x)) = \sum_k \sum_i \frac{1}{\sigma_k^2}(x_k[i]\xi_k[i] - \frac{1}{2}\xi_k^2[i]). \tag{4.19}$$

For simplicity, we use time domain for explaining the likelihood method. However, the cWBanalysis is performed at time-frequency maps, see [47]. In this regard, the $i \in C$ are elements of the time-frequency cluster C and figure 4.2 shows example of a cluster. Also note, that we also assume that the noises from the different detectors themselves are uncorrelated.

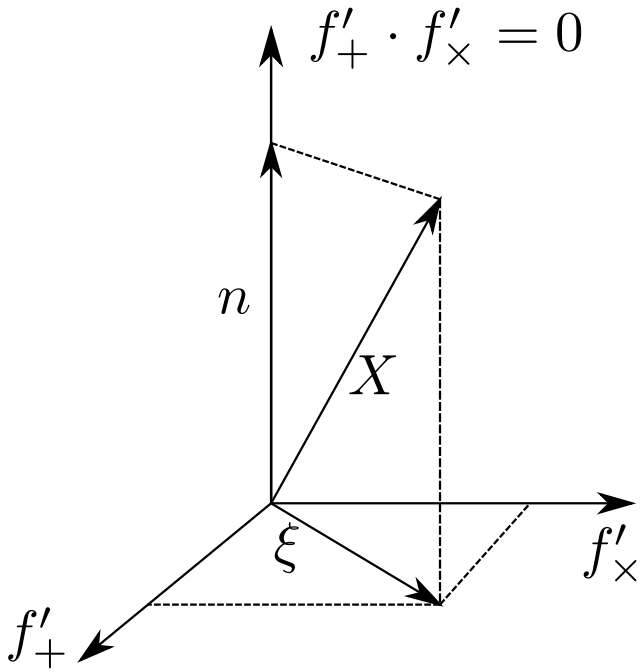

Figure 4.3: GW signal ξ depicted in the Dominant Polarization Frame. It lays in the $(f'+, f'_\times)$ plane.

Dominant Polarization Frame

It is convenient to rotate the normalized antenna pattern vectors of an angle γ:

$$f'_{k+} = f_{k+}\cos(\gamma) + f_{k\times}\sin(\gamma), \tag{4.20}$$

$$f'_{k\times} = -f_{k+}\sin(\gamma) + f_{k\times}\cos(\gamma), \tag{4.21}$$

and $A'_k = A_k e^{-\imath\gamma}$. Using this rotation we write:

$$\begin{aligned} A'^2_\sigma &= A'_\sigma \cdot A'_\sigma && (4.22)\\ &= \frac{1}{2}(f'_+ + \imath f'_\times)\cdot\frac{1}{2}(f'_+ + \imath f'_\times) && (4.23)\\ &= \frac{1}{4}(f'^2_+ - f'^2_\times) + \frac{1}{2}\imath(f'_+ \cdot f'_\times). && (4.24)\end{aligned}$$

The Dominant Polarization Frame (DPF) is defined when the f'_+ and $f'_\times$ vectors are ortogonal to each other, simply:

$$f'_+ \cdot f'_\times = 0. \tag{4.25}$$

To calculate γ angle, we take $A_k = A'_k e^{\imath\gamma}$ and write:

$$\begin{aligned} A^2_\sigma &= A_\sigma \cdot A_\sigma && (4.26)\\ &= \frac{1}{2}(f_+ + \imath f_\times)\cdot\frac{1}{2}(f_+ + \imath f_\times) && (4.27)\\ &= \frac{1}{4}(f^2_+ - f^2_\times) + \frac{1}{2}\imath(f_+ \cdot f_\times) && (4.28)\\ & && (4.29)\end{aligned}$$

and

$$\begin{aligned} A^2_\sigma &= (A'^2 e^{\imath\gamma})^2 && (4.30)\\ &= \mid A'^2 \mid e^{2\imath\gamma} && (4.31)\\ &= \mid A'^2 \mid (\cos 2\gamma + \imath \sin 2\gamma). && (4.32)\end{aligned}$$

Given that $\mid A'_\sigma \mid = \mid A_\sigma \mid$, we arrive with:

$$\mid A^2_\sigma \mid \cos(2\gamma) = (f^2_+ - f^2_\times)/4, \tag{4.33}$$

$$\mid A^2_\sigma \mid \sin(2\gamma) = (f_+ \cdot f_\times)/2. \tag{4.34}$$

Therefore, the angle γ becomes:

$$\gamma = \frac{1}{2}\arctan\frac{f_+^2 - f_\times^2}{2f_+^2 \cdot f_\times^2}. \tag{4.35}$$

More detailed information can be found in Ref. [49].

Figure 4.3 shows an example of a signal ξ that lays in the $(f'+, f'_\times)$ plane. The noise N is projected along axis ortogonal to $(f'+, f'_\times)$ plane. It is also important to mention that the angle γ is related to the waveform polarization angle ψ as:

$$\gamma = \Psi - \psi, \tag{4.36}$$

where Ψ is the DPF angle.

Maximum Likelihood

Using the simplified notation introduced in the previous section, the likelihood (4.19) can written as:

$$L = (X_\sigma \cdot \xi_\sigma - \frac{1}{2}\xi_\sigma \cdot \xi_\sigma) \tag{4.37}$$

$$= \left[X_\sigma \cdot (f'_+ h_+ + f'_x h_\times) - \frac{1}{2}(f'_+ h_+ + f'_\times h_\times) \cdot (f'_+ h_+ + f'_\times h_\times)\right] \tag{4.38}$$

$$= \left[X_\sigma \cdot f'_+ h_+ + X_\sigma \cdot f'_\times h_\times - \frac{1}{2}(f'^2_+ h_+^2 + f'^2_\times h_\times^2)\right]. \tag{4.39}$$

The maximum the likelihood we calculate the first derivates over h_+ and $h_\times$ and equal them to zero:

$$\frac{\delta L}{\delta h_+} = X_\sigma \cdot f'_+ - \mid f'_+ \mid^2 h_+ = 0, \tag{4.40}$$

$$\frac{\delta L}{\delta h_\times} = X_\sigma \cdot f'_\times - \mid f'_\times \mid^2 h_\times = 0. \tag{4.41}$$

Based on maximizing the likelihood, we can reconstrut the h_+ and $h_\times$ components of the GW signal:

$$h_+ = \frac{X_\sigma \cdot f'_+}{\mid f'_+ \mid^2}, \tag{4.42}$$

$$h_\times = \frac{X_\sigma \cdot f'_\times}{\mid f'_x \mid^2}. \tag{4.43}$$

We can now plug in equations (4.42) and (4.43) to (4.39):

$$L_{max} = [X_\sigma \cdot f'_+ h_+ + X_\sigma \cdot f'_x h_x - \frac{1}{2}(f'^2_+ h_+^2 + f'^2_\times h_\times^2)] \tag{4.44}$$

$$= \left[X_\sigma \cdot f'_+ \frac{X_\sigma \cdot f'_+}{\mid f'_+ \mid^2} + X_\sigma \cdot f'_\times \frac{X_\sigma \cdot f'_\times}{\mid f'_\times \mid^2} - \frac{1}{2}(f'^2_+ \frac{(X_\sigma \cdot f'_+)^2}{\mid f'_+ \mid^4} + f'^2_\times \frac{(X_\sigma \cdot f'_\times)^2}{\mid f'_\times \mid^4}\right] \tag{4.45}$$

$$= \left(\frac{(X_\sigma \cdot f'_+)^2}{\mid f'_+ \mid^2} + \frac{(X_\sigma \cdot f'_x)^2}{\mid f'_\times \mid^2}\right). \tag{4.46}$$

Now we can write the form of the reconstruced GW signal as:

$$\xi_\sigma = h_+ f'_+ + h_\times f'_\times \tag{4.47}$$

$$= \frac{X_\sigma \cdot f'_+}{\mid f'_+ \mid^2} f'_+ + \frac{X_\sigma \cdot f'_\times}{\mid f'_x \mid^2} f'_\times \tag{4.48}$$

$$= \frac{X_\sigma \cdot f'_+}{\mid f'_+ \mid^2} e'_+ + \frac{X_\sigma \cdot f'_\times}{\mid f'_x \mid^2} e'_\times, \tag{4.49}$$

where $e'_+ = \frac{f'_+}{|f'_+|}$ and $e'_\times = \frac{f'_\times}{|f'_\times|}$ are the unitary vectors. The maximum likelihood solution is then a projection of the vector X_σ onto a $(f'+, f'_\times)$ plane and therefore the likelihood can be expressed as:

$$L_{max} = \frac{(X_\sigma \cdot \xi_\sigma)^2}{\mid \xi_\sigma \mid^2}. \tag{4.50}$$

Signal-to-Noise Ratio

Signal-to-Noise Ratio (SNR) for k^{th} detector is defined as:

$$\mathrm{SNR}_k = \frac{\xi_k}{\sigma_k}. \tag{4.51}$$

In the Dominant Polarization Frame, the total SNR has a form ($\xi_\sigma \cdot n = 0$):

$$\mathrm{SNR} = \sum_k \frac{\xi_k}{\sigma_k} \tag{4.52}$$

$$= \xi_\sigma \cdot \xi_\sigma = L. \tag{4.53}$$

Regulators

The regulators are network constraints that allow eliminating triggers that give unlikely solutions to the maximum likelihood. For example, when GW comes from the sky location where the network of detecotors is not very sensitive, then the cross component of antenna pattern can be negligible: $|F_\times| << |F_+|$. More information about the definitions and meanings of these regulators can be found in Ref. [47].

Gamma Regulator The Gamma regulator Γ is defined as:

$$\Gamma = \sqrt{e^2 + \sin^2 \gamma}, \tag{4.54}$$

where e is waveform elipticity.

Delta Regulator The Delta Regulator Δ is defined as:

$$\Delta = 1/I_e - \alpha|\nu(e_+) - \nu(e_\times)|. \tag{4.55}$$

I_e is an event index, which calculates an effective number of coincident detectors contributing to the measurement:

$$I_e = \frac{|\xi_+|^2 + |\tilde{\xi}|^2}{|\xi|^2\nu(v_+) + |\tilde{\xi}|^2\nu(\tilde{v})}, \tag{4.56}$$

where ξ is a reconstructed waveform, $v = \xi/|\xi|$, $\tilde{v} = \tilde{\xi}/|\tilde{\xi}|$, $\nu(v) = \sum_k v_k^4$ and $\alpha = |f_\times|/|f_+|$ is an alignment factor.

4.3 Production stage

The main purpose of this analysis stage is identifying GW candidates, or "production" of triggers. This identification depends on initial configuration or tuning of the algorithm that will be briefly discussed in this section (for more etailed tuning for the purpose of the O1-O2 SN Search see section 8.2). In this stage the data is prepared through various tools like whitenig or denoising. After the data is processed, the algorithm gives lists of triggers with their properties.

4.3.1 cWBconfiguration

The first step of the production analysis is to set up the configuration of cWBto a particular purpose. The rest of the analysis will depend on these settings. cWBoffers large flexibility to perform different types of searches, adjust the searches to be sensitive to particular waveform morphologies or to test new methods and algorithms.

Generally, the searches vary on the GW morphologies and the astrophysical information. Specifically, I will focus here how the search with cWBcan be tuned to the supernova searches. Different implementations and considerations regarding the tuning can be found throughout the dissertation. Especially, section 8.2 describes different tests done with some of the configurations described below for various SN waveform morphologies.

Frequency range Realistic GW from supernovae are usually broadband signals with energies below 1kHz. For rapidly rotating waveforms, collapsars or extreme models, a significang GW energy is produced above 1kHz, however the noise increases in higher frequencies. A tradoff for the GW SN searches an be set to [16, 2048]Hz.

cWBplugins Plugins are algorithms modules that can be inserted between some of the analysis steps or they can replace existing codes with the existing ones. This feature allows testing the performance of new methods. Examples of plugins:

- Ring Skymask - Accepting only events with a reconstructed supernova locations with assigned error tolerance. More information in section 8.2.4.
- Two Step Denoising - an algorithm applying different type of whitening. More details are in section 12.7

4.3.2 Data preparation

This step prepares the data for the the further analysis. It includes:

1. Whitening - a linear transformation that removes the frequency dependent predictable noise and normalizes the energy of the data. As a consequence, the data becomes Gaussian with unit standard deviation.

2. Regression - a transformation that allows removal of the calibration lines and some spurious features when a predictor filter appears to be effective, e.g. enviromental noise.

4.3.3 Time-Frequency Decomposition

The GW signal can be characterized by time series or in frequency domain. These two approaches carry the same information, but they are not always suitable for burst searches. The Time-Frequency domain signal was found to be the most search effective represention of the GW signal. This decomposition carries information about evolution of the signal's frequency over time. Time-Frequency decomposition is usually realized by the *Wavelet Transform*. The efficiency of detecting GW signals depends greatly on the choice of the basis. cWBuses *fast Wilson-Daubechies* basis [10].

Each wavelet basis can be represented as pixel in Time-Frequency map. Figure 4.2 shows an example of a cluster. In this example, number of wavelet bases (or pixels) used to represent a detected signal is 186. These pixels are later used for the reconstruction of the time series and Fourier spectra. Left panel of Figure 4.4 shows a Fourier representation of one of the WDM base wavelet. Right panel of the same figure presents an example of reconstructed Yakunin 2015 waveform and imprinted WDM wavelet basis.

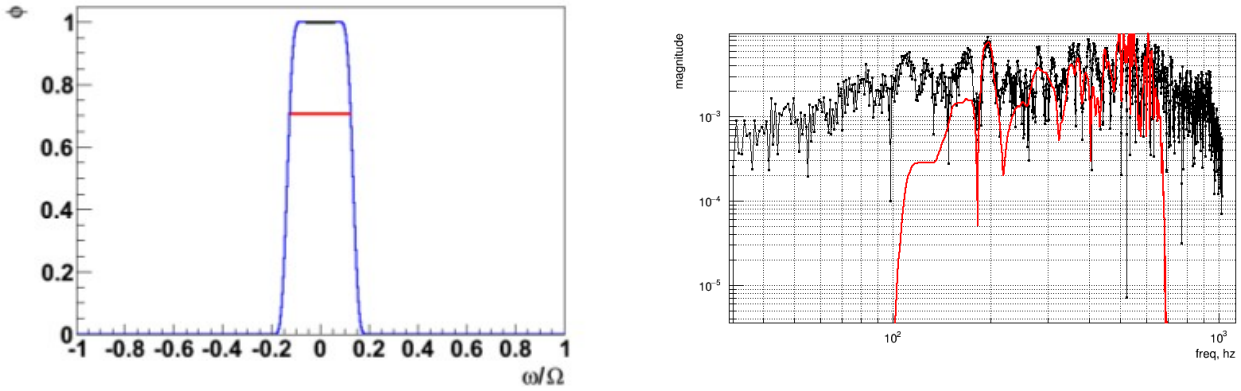

Figure 4.4: Left: example of the WDM wavelet basis [10]. Right: Example of a reconstructed Yakunin 2015 waveform (red) with visible (in low frequency) imprinted wavelet bases.

4.3.4 Pixel selection

After the time series of data is decomposed into Time-Frequency maps, the algorithm chooses the most energetic pixels. Two parameters govern this choice: black pixel probability (bpp) and Acore.

bpp This parameter defines the cWBexcess-power threshold used for selection of loud (black) pixelsIt is approximately to the fraction of loud pixels selected by the algorithm for each Time-Frequency resolution. Assuming that the data is 600s long and the search bandwidth is 2048Hz then for a value of bpp=0.001, for example the algorithm selects 2000pixels.

Acore This parameter sets a threshold for selection of core pixels. The value is in units of rms and Acore=1.5 mean that we select only pixels with energies above 1.5σ of an average rms value. This allows to remove efficiently noise pixels.

4.3.5 Cluster selection and trigger generation

After core pixels are selected, the next step is to cluster them and identify burst events. Firstly, the clustering is done at single resolution levels. Figure 4.5 shows an example of how a cluster ove pixels is selected. When the pixels between detectors coincide and their combined energy passes certain thresholds. Otherwise they are rejected.

After single resolution clusters are identified, then the clustering happens between different resolutions. Figure 4.2 shows an example of a cluster with pixels collected across different Time Frequency resolutions. Such a collection of pixels becomes a trigger which can be further rejected after the Constrained Likelihood Analysis.

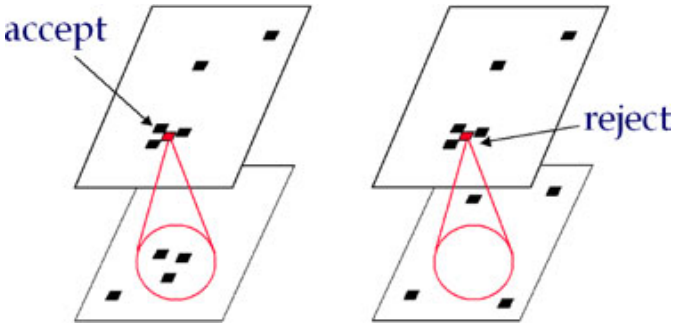

Figure 4.5: Clustering pixels on a single resolution level [11].

4.3.6 Wavelet Packets

A particularly interesting type of clustering the pixels is offered with the *wavelet packets*. These packets allow to increase sensitivity of the search for some morpologies. The packets are specific ways of collecting the energy from the pixels in the time-frequency maps. Figure 4.6 shows graphically various available ways of clustering the pixels and Table 4.1 provides a detailed description.

In the standard approach, cWB chooses the pixels in time-frequency maps that pass some threshold. In this case, each pixel has associated energy only from it's own. In the wavelet packets mode cWB collects energy from the neighboring pixels, according to a pre-defined pattern, and place the collectd energy in the middle pixel.

For example, for pattern=5 the energy is collected from 5 pixels along a diagonal and then it is placed in the pixel in the middle. On average, the algorithm becomes more sensitive to the GW that have peak frequency growing in time. The most significant examples are CBC waveforms or the chirps - the frequency is growing over time. However, this pattern is also useful in the for the Supernova searches. The growing peak frequency due to the stiffening of the proto-neutron star can be more detectable with this pattern.

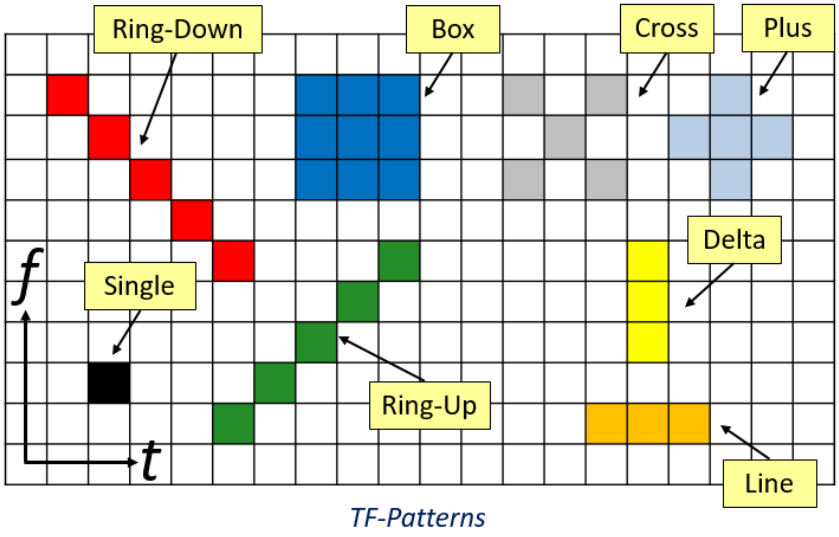

Figure 4.6: wavelet packets

Table 4.1: Wavelet Packets with definitions and example applications.

Packet (pattern)	Explanation	Example Application
pattern = 0	"*" - single pixel	standard search
pattern = 1	"3|" - packet	delta-like morphologies
pattern = 2	"3-" - packet	Long waveforms, or SASI
pattern = 3	"3/" - packet	Chirp signals, g-mode rump up
pattern = 4	"3\" - packet	Ring-down signals
pattern = 5	"5/" - packet	Chirp signals, g-mode ramp up
pattern = 6	"5\" - packet	Ring-down signals
pattern = 7	"3+" - packet	
pattern = 8	"3x" - packet	
pattern = 9	"9p" - packet (9-pixel square)	Long and broadband morphologies

4.4 Triggers properties

The goal of the production stage is creation of a list of GW candiadates. For each triggers, the pipeline estimates their properties or in other words event *parameters*. The production stage provides a list of reconstructed parameters for particular trigger, such as SNR, correlation between detectors, duration, bandwidth, number of pixels etc. By default, it does not provide more detailed information like the reconstructed waveform in time, frequency and time-frequency domains, sky statistics or other. This approach gives a large advantage in lowering the computational cost and a limited list of properties is sufficient to distinguish the falsely identified triggers fromm correctly identified triggers. This distinction is done, however, in the post-production stage (see section 4.5).

In this section I will not go over all reconstructed parameters, but I will focus on these parameters that were used so far for the puprose of SN searches and this dissertation. They are summarized in table 4.2.

4.5 Post-production

I will describe three important parts of the analysis of the search:

1. **Background** - this stage of the analysis provides information on the noise events produced by data.
2. **Simulation** - this stage of analysis provides information how sensitive is the pipeline to detector GW signals.
3. **Receiving Operating Characteristic (ROC) curves** - the curves give information on how the sensitivity of the search is changing when we increase the significance of the GW candidates. These curves are usual tool for comparing different tunings or pipelines.

4.5.1 Background

Before describing in details the process of obtaining background in GW data analysis, I will make an initial comment on potential ambiguity of a word "background". Usually a background noise is referred to be a time series of the strain or its spectra. However, in the GW data analysis the background is a discribution of noise transients that are identified as GWs candiadates. This meaning will be held throughout this dissertation, unless stated otherwise for exceptions.

Every physical measurement needs to take into account level of a background noise. For example when we a photodiode measures the incoming light, we have to know how much voltage is produced by a photodiode when no source of light is present. For example, caused by the electronics or the light of the neighborhood. We can simply shield the photodiode by putting a black screen.

Unfortunately we cannot shield the GW interferometers from GW radiation and we cannot measure the background caused by the detector or the enviroment. Every signal in the detector might be a GW. In the background studies we measure how often GW detector data produces false events that look like GW. Moreover the backround analysis is used to assign significance of the GW candidates. In summary, during the bakground analysis:

1. every produced trigger is certainly not a GW,
2. the lifetime of an experiment is enlarged.

The background population is produced by artificially shifting the data from one detector with respect to another by more than the maximum deley we would have with any signal traveling at the speed of light.

This makes sure that no real GW is present. The typical time shift is in multiplies of one second that is much larger than GW travel time between different detectors (e.g. 10ms between LIGO Hanford and LIGO Livingstion). This allows to estimate the False Alarm Rate (FAR) of events that are not GWs:

$$FAR = N/T_{\mathrm{bkg}}, \tag{4.57}$$

where N is the number of false events and T_{bkg} is the total livetime of the accumulated artificially shifted data. Thoughout the dissertation the number N is the number of all events accumulated above certain threshold of the statistics ρ. Precisely, it is a *cummulative FAR* which is reffered in literature and thoughout the dissertation simply as FAR.

A significance of an event is usually described in terms of a False Alarm Probability (FAP). For example, the first detected GW has a significance above 5σ, which means that the GW detector are able to produce a waveform that is coincidend between two detectors with probability less than 10^{-7}. Given a FAR value R, the probability $FAP(FAR)$ of noise producing one or more events of FAR less than or equal to FAR during one or more CCSN on-source windows of total duration $T_{\rm on}$ is

$$FAP = 1 - \exp\left(-T_{\rm on} \times FAR\right). \tag{4.58}$$

The smallest false alarm probability (FAP) that can be measured given a background (time-shifted) data duration $T_{\rm bkg}$ is approximately $T_{\rm on}/T_{\rm bkg}$. Several thousand time shifts are therefore sufficient to measure FAP values of $O(10^{-3})$. We require a FAP below 0.001, which exceeds 3-σ confidence, in order to consider an event to be a possible GW detection candidate. Figure 4.7 shows an example of a FAR and corresponding FAP with an example of SN 2016B.

Lags and super-lags. The method of artificially shifting data is a powerful tool. The techical term for a shift of the data is a *lag*. Usually during a single lag the data from one detector is shifted one second with respect to the other. In the standard cWB analysis, the data is divided into segments, usually 10min long. For example, if we take an on-source window to be $T_{\rm on} = 1200$s (20min), then the data is divided into two 10min long segments. With the standard lags we can make 600 shifts in each segment. The lags allow to create background data to be $T_{\rm bkg} = 600 \times 600s + 600 \times 600s \approx 8.3$ days. Moreover, cWB has also implemented *super-lags*. In this procedure, the whole segments are shifted. For example, let's consider the above on-source window that is divided into two equal size segments. The algorithm can prerform the lag analysis inside each segment and then it can shift the segments itself and repeat the lag analysis again. In this case we can achieve background data of $T_{\rm bkg} = 2 \times (600 \times 600s + 600 \times 600s) \approx 16.6$ days. Te significance of the GW candidates are estimated using the lag and super-lag procedures. In general, let's assume that we have available N segments, each segment is $T_{\rm seg}$ long and we can do $N_{\rm seg}$ lags (e.g. if $T_{\rm seg} = 600$s and we do one-second shifts then $N_{\rm seg} = 600$). In this case the total amount backgroudn that can be produced for two detector case is:

$$T_{\rm bkg} = T_{\rm seg} \times N_{\rm seg} \times N!. \tag{4.59}$$

Seach with data from only one interferometer. In case of a very important astrophysical event, such a galactic CCSN, it might happen that no data from only one detector will be available. In this special case, it is impossible to do the lags, and different methods need to be applied. More discussion is in section 10.4.

4.5.2 Simulation

An important aspect of the GW search presented in this study is to understand how sensitive the GW detector networks are to GWs emitted by the considered CCSNe.

A note on ambiguity of a word "simulation". Commonly this word refers to the modeling an astrophysical source, in this case, modeling or simulating a CCSN. In GW data analysis this word means simulating the performance of an algorithm to detect particular emission model.

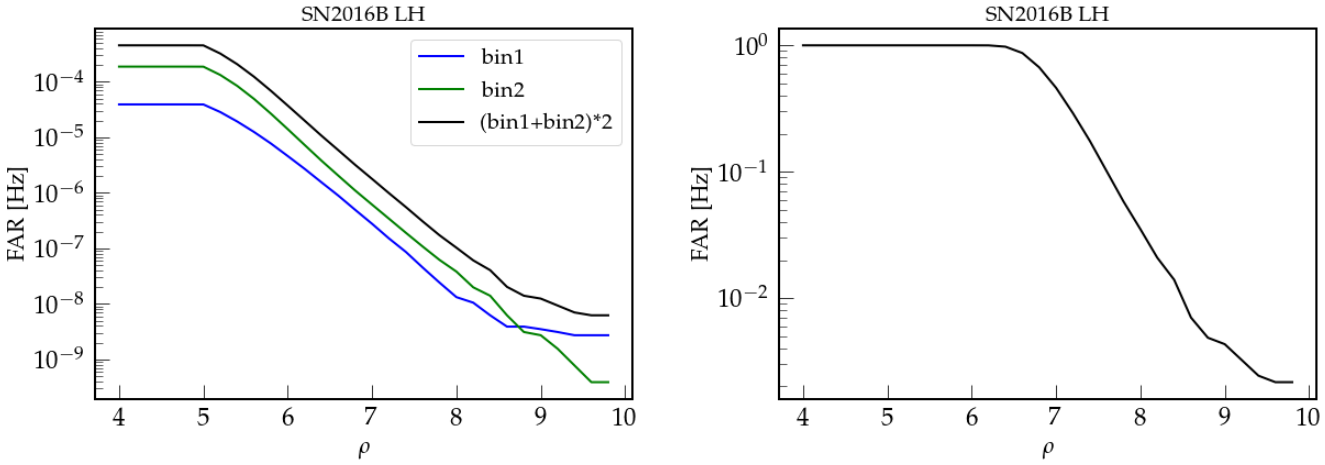

Figure 4.7: An example background analysis for SN 2016B. Left: False Alarm Rate (FAR), Right: False Alarm Probability (FAP).

We establish sensitivity via Monte Carlo simulation in the following way:

1. We determine the loudest event in the on-source window that is consistent with the CCSN location (and the angular uncertainty of the search algorithms) if used.

2. We "inject" (add) theoretical waveforms scaled to a specific distance (or emitted GW energy) every 100 s plus a randomly selected time in $[-10, 10]$ s into the time-shifted background data. We compare the loudness of the recovered injections with the loudest on-source event and record the fraction of the injections that passed the coherent tests and data quality cuts and were louder than the loudest on-source event. This fraction is the *detection efficiency*.

3. We repeat step (2) for a range of distances (or emitted GW energies) to determine the detection efficiency as a function of distance, emitted GW energy, hrss or SNR.

Figure 4.8 presents two ways of displaying sensitivity curves. In the first one the algorithm is tested for detectability of sine-Gaussian morphologies with different central frequencies. As it will be described in the later sections it allows to constrain constrain GW energy for certain types of potential GW morphologies. In the second picture, the sensitivity curves are derived in terms of the source distance. This representation is particularly important for the searches for GW from CCSNe. When we observe CCSN opticallly, the distance can be estimated from EM observations. The simulation analysis allows to measure how far particular SN models are detectable.

The detection efficiencies can be calculated according to different quantities, for example: distance to the source, SNR of the trigger or $h_{\rm rss}$ of the waveform. The choice depends on the conducted study. The following presents a useful conversion between the square-root of a waveform strain at 50% detection efficiency, $h_{rss,50\%}$, and the visible distance at 50% detection efficiency, $d_{50\%}$:

$$d_{50\%} = \frac{h_{rss}}{h_{rss,50\%}} d, \tag{4.60}$$

where h_{rss} is the square-root value at the distance d.

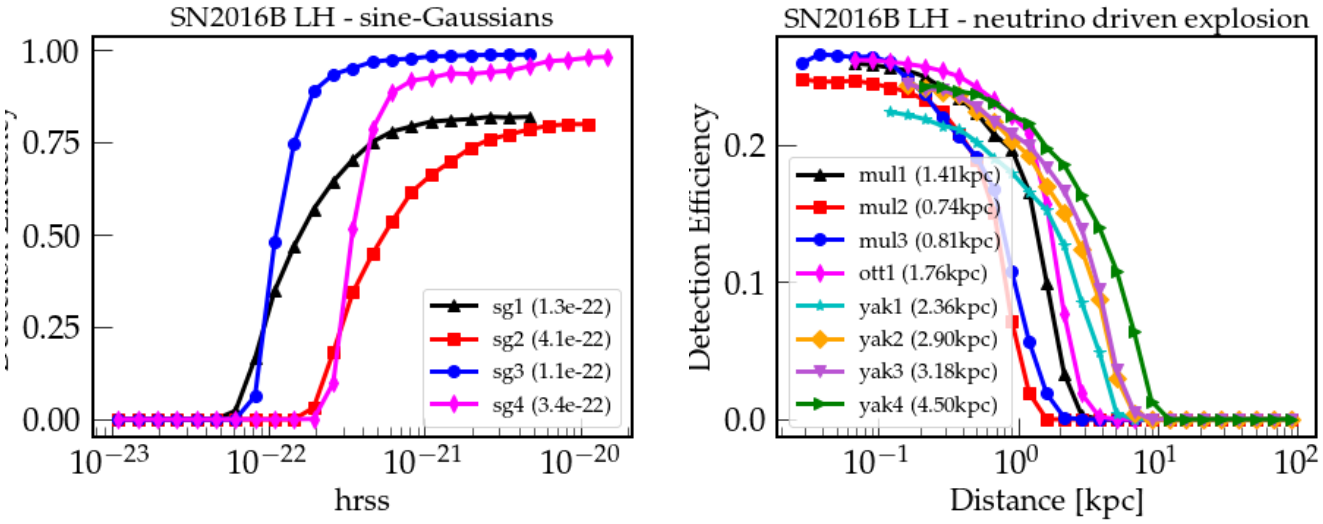

Figure 4.8: An example detection efficiency for SN 2016B (O1 public data). Left: detection sensitivity versus $h_{\rm rss}$ for sine-Gaussian. Right: detection effciency versus distance for real waveforms.

4.5.3 Receiving Operating Characeristic curves

It is possible to make the search algorithm more sensitive to detect GW by lowering the thresholds on the control indicators computed for the events.. Unfortunately, lowering the thresholds also increases FAR. This impacts the search in lowering the significance of the candidates. A tool to quantify the performance of the search is the Receiver Operating Characeristic (ROC) curve. ROCs also allow to compare the performances of different tunings, methods or algorithms.

There are many different ways of creating ROC curves. Here I will describe creating efficiency vs FAR curves. Figure 4.9 shows an example of backgrouund, simulation and an associated ROC. An ROC is produced for a fixed population (for example, fixed distance). The slope of the curve depends on the spatial distribution of the noise events versus the injection events in the sometimes multidimensional space. If the distribution of GW induced events are clearly separated by the one of noise events, ROCs tend to become more flat. If the two distributions are more overlapped, the ROCs have larger gradient. If someone produces several ROC curves for different scale factors in the injections ROC surfaces can be produced too.

Table 4.2: Part of the cWB parameter space. The second column introduces short names of the parameters that are used for Machine Learning (ML) application.

cWB parameter	ML label	Description
time[0]	tL	L1: central time of the event.
time[1]	tH	H1: central time of the event.
volume[0]	pv	L1: number of wavelet time-frequency pixels composing the events (core+halo).
size[0]	ps	L1: number of wavelet time-frequency pixels composing the events (core).
duration[0]	dL	Energy weighted duration estimated in time/freq domain for all resolutions.
duration[1]	dH	Difference between event stop and start.
frequency[0]	fL	Central frequencies of the event computed from the reconstructed waveform.
frequency[1]	fH	Energy weighted central frequency estimated from in time/freq domain for all resolutions.
low[0]	low	L1 : Minimum frequency associated to the time-frequency map pixels.
high[0]	hgh	L1 : Maximum frequency associated to the time-frequency map pixels.
bandwidth[0]	bw0	Energy weighted bandwidth estimated in time/freq domain for all resolutions.
bandwidth[1]	bw1	Difference between event high and low.
netcc[0]	cc0	Network correlation coefficient: netcc[0] = Ec/(Ec+(Np+Ed+Gn)).
netcc[1]	cc1	Network correlation coefficient: netcc[1] = Esub/(Esub+Nmax).
netcc[2]	cc2	Sub-network correlation coefficient: netcc[2] = Esub/(Esub+Nmax).
netcc[3]	cc3	likelihood ratio: netcc[3] = Lp/Ep.
rho[0]	rho0	Effective correlated SNR; rho[0] = rho*sqrt(Cp/ch2).
rho[0]	rho1	Effective correlated SNR; rho[1] = sqrt(Ec*netcc[0]/(K-1)).
norm	nrm	Norm Factor or ellipticity.
penalty	pty	Penalty factor.

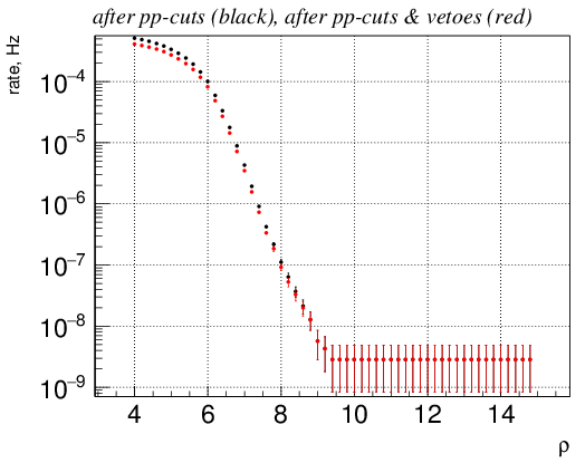

(a)

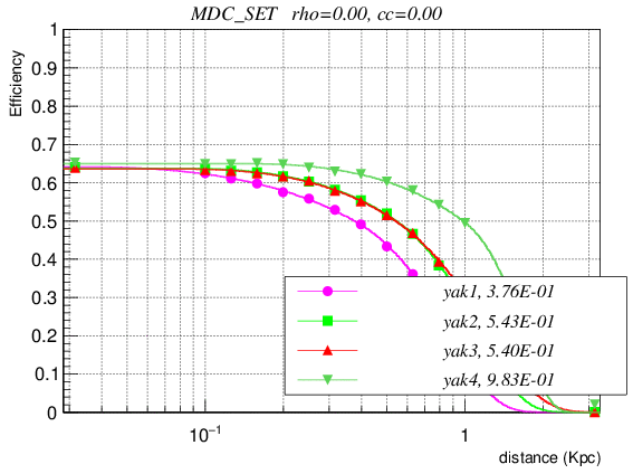

(b)

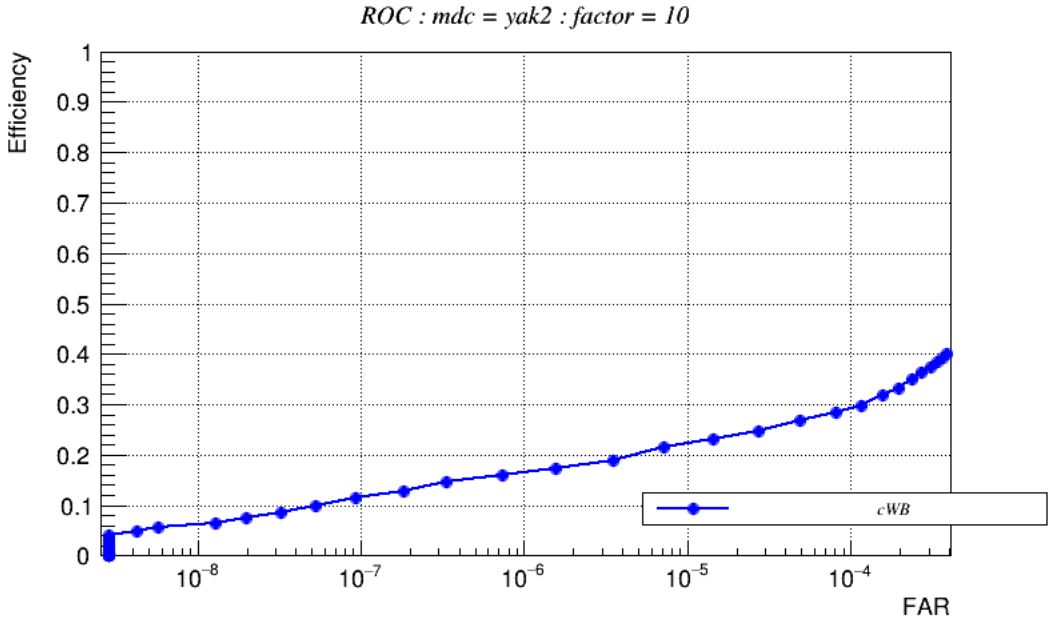

(c)

Figure 4.9: Example ROC curve with corresponding background and simulation.

Part II

Initial GW Detector Era

Chapter 5

Optically Triggered Search

5.1 Introduction

In this chapter, we present a targeted search for GWs from CCSNe using the first-generation Initial LIGO (iLIGO) [50], GEO 600 [51], and Virgo [52] laser interferometer detectors. The data searched were collected over 2005–2011 in the S5, A5, and S6 runs of the iLIGO and GEO 600 detectors, and in the VSR1–VSR4 runs of the Virgo detector. From the set of CCSNe observed in this period [53], we make a preliminary selection of four targets for our search: SNe 2007gr, 2008ax, 2008bk, and 2011dh. These CCSNe exploded in nearby galaxies ($D \lesssim 10\,\mathrm{Mpc}$), have well constrained explosion dates, and at least partial coverage by coincident observation of more than one interferometer. SNe 2008ax and 2008bk occurred in the *astrowatch* (A5) period between the S5 and S6 iLIGO science runs. In A5, the principal goal was detector commissioning, not data collection. Data quality and sensitivity were not of primary concern. Preliminary analyses of the gravitational-wave data associated with SNe 2008ax and 2008bk showed that the sensitivity was much poorer than the data for SNe 2007gr and 2011dh. Because of this, we exclude SNe 2008ax and 2008bk and focus our search and analysis on SNe 2007gr and 2011dh. It is also worth mentioning that a matched filter search for a Type Ib/c supernovae GW database was performed on publicly released LIGO data [54] with no detection claimed. The search was not targeted in the sense used here.

We find no evidence for GW signals from SNe 2007gr or 2011dh in the data. Using gravitational waveforms from CCSN simulations, waveforms generated with phenomenological astrophysical models, and *ad-hoc* waveforms, we measure the sensitivity of our search. We show that none of the considered astrophysical waveforms would likely be detectable at the distances of SNe 2007gr and 2011dh for the first-generation detector networks. Furthermore, even a very strong gravitational wave could potentially be missed due to incomplete coverage of the CCSN on-source window by the detector network. Motivated by this, we provide a statistical approach for model exclusion by combining observational results for multiple CCSNe. Using this approach, we quantitatively estimate how increased detector sensitivity and a larger sample of targeted CCSNe will improve our ability to rule out the most extreme emission models. This suggests that observations with second-generation "Advanced" interferometers [55, 56, 57] will be able to put interesting constraints on GW emission of extragalactic CCSN at $D \lesssim 10\,\mathrm{Mpc}$.

The remainder of this chapter is structured as follows. In section 5.2 we will show how the paths of supernovae are shown in different reference frames.In Section 5.3, we discuss the targeted CCSNe and the determination of

their on-source windows. In Section 5.4, we describe the detector networks, the coverage of the on-source windows with coincident observation, and the data searched. In Section 5.5, we present our search methodology and the waveform models studied. We present the search results in Section 5.6 and conclusions in Section 5.7.

5.2 Tracking supernovae paths in different coordinate systems

In this section I will describe the the paths of four supernovae in different coordinate systems (celestial, geographical, detector frames). The supernovae in this study were used in the targeted CCSNe search. Traditionally in remote sensing applications we have trust that the best angular resolution in estimating the direction of arrival of the source is for directions perpendicular to the plane made by detectors. We want to find out the angle of incidance at the LHV plane.

Firstly I will describe the supernovae positions in the celestial coordinates section 5.2.1. Then I will show how these paths look in geographical coordinates, section 5.2.2. Finally in section 5.2.3 I describe the paths of supernovae in the three detector network coordinates.

5.2.1 Celestial coordinates

There are several celestial coordinate systems such as equatorial or galactic coordinate system which allow to describe position of a supernova on celestial sphere.I will use equatorial coordinate system that I describe below.

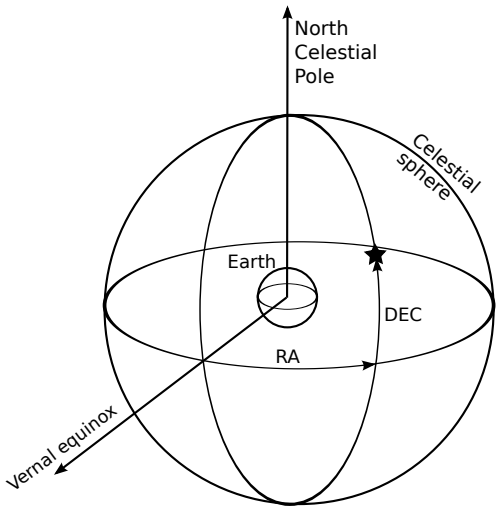

Figure 5.1: This figure introduces equatorial coordinates. These coordinates are defined by Earth as the center of coordinate system, the Earth's rotational axis defines the north and south celestial poles and the Vernal equinox points into $(RA, DEC) = (0°, 0°)$.

Equatorial coordinates (RA, DEC) are spherical coordinates defined by an origin at the center of the Earth as it is shown on Figure 5.1. The celestial equator $DEC = 0°$ is a projection of the Earth's equator and the primary direction is defined toward vernal equinox which is located in Pics constellation. The line indicating vernal equinox is the intersection beetwen the Earth's equatorial plane and the ecliptic. A coordinate RA is called the

right ascension and it is counted eastward from vernal equinox with values from 0^h to 24^h or equivalently from $0°$ to $360°$. The second coordinate DEC is called declination and it ranges from $-90°$ to $90°$. Table 5.1 contains positions of four supernovae which are drawn on Figure 5.2.

Equatorial coordinates can be used not only to locate astronomical objects on the sky but also to determine the position of Earth with respect to the stars. This is possible if we associate right ascension with sidereal time. One rotation of Earth around its axis with respect to a distant star is equal to 24 sidereal hours or $360°$ and it is called sidereal day.

It is worth to mention that sidereal day is not equal to the solar day. The reason of that difference is the rotation of Earth around the Sun. Let's assume for a moment that the direction of vernal equinox is parallel to the line connecting Earth and Sun and the meridian of Greenwich is at this line. After one solar day the Greenwich meridian is again on line Earth-Sun but this line is now not parallel to the direction of vernal equinox because Earth's position is shifted. The relation between sideral and solar day is as follow:

$$1 \text{ sidereal day} = 23.9345 \text{ (solar) hours.} \tag{5.1}$$

We can write sidereal time using sidereal hours, sideral minutes and sidereal seconds, but in this document we use decimal convention, e.g. $2^{\text{sid h}}30^{\text{sid min}}40^{\text{sid s}} = 2 + 30/60 + 40/3600^{\text{sid h}} = 2.5111^{\text{sid h}}$. It can be also written in degrees: $2.5111^{\text{sid h}}/24^{\text{sid h}} \times 360° = 37.67°$.

Sidereal time is different for each Earth's meridian and we will work with Greenwich Sidereal Time GST. When meridian $0°$ of Greenwich is crossing vernal equinox and then the sidereal day begins. The way to find sidereal time based on Universal Time UT is complicated and to calculated it the MICA software was used. Table 5.1 shows both UT and GST times.

	Time of explosion, $\Delta = T_E - T_S$				
Name	Start, T_S	End, T_E	Δ [sid h]	RA [deg]	DEC [deg]
2007gr	UT 2007.08.10 08:09:36 GST 2007.08.10 5.38875	UT 2007.08.15 12:14:24 GST 2007.08.15 9.80597	5.12 days 124.419	40.8666	+37.34567
2008ax	UT 2008.03.03 02:09:36 GST 2008.03.03 12.9085	UT 2008.03.03 10:48:00 GST 2008.03.03 21.5722	1.26 days 8.66366	187.67	+41.6374
2008bk	UT 2008.03.14 12:00:00 GST 2008.03.14 23.4983	UT 2008.03.24 12:00:00 GST 2008.03.24 0.155397	12.64 days 240.263	359.4479	-32.5567
2011dh	UT 2011.05.31 07:46:00 GST 2011.05.31 0.330999	UT 2011.05.31 20:10:00 GST 2011.05.31 12.7649	1.52 days 12.434	202.5214	+47.1698

Table 5.1: Times and positions of supernovae.

5.2.2 Geographical coordinates

When a supernova appears on the sky at position (RA, DEC) the line between that supernova and Earth always meet some meridian L and a circle of latitude l. We want to find those (l, L) for a given sidereal time of Greenwich GST (e.g. moment of explosion of supernova). Figure 5.3 shows the way to convert right ascension and meridian.

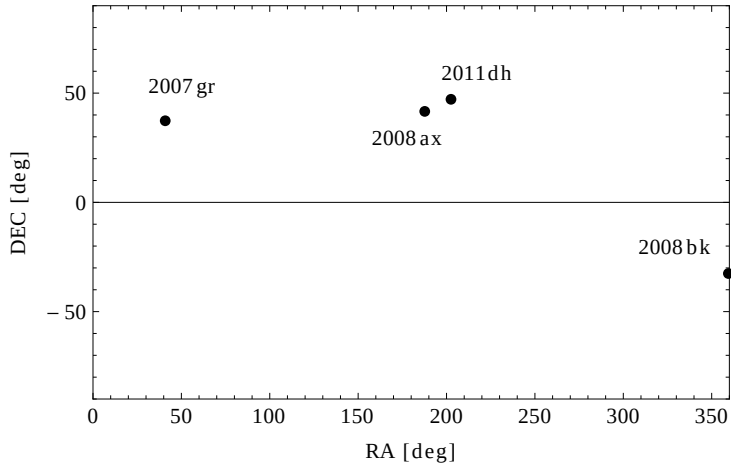

Figure 5.2: Position of the supernovae in equatorial reference frame

The convertion between equatorial and geographical coordinates is given by:

$$\begin{cases} l &= DEC, \\ L &= RA + 360^\circ - GST, \end{cases} \tag{5.2}$$

where all quantities are expressed in deegres. Circle of lattitude is from -90° to 90° and the longitude from 0° to 360° eastward. The paths of four supernovae given in table 5.1 are shown in Figure 5.4.

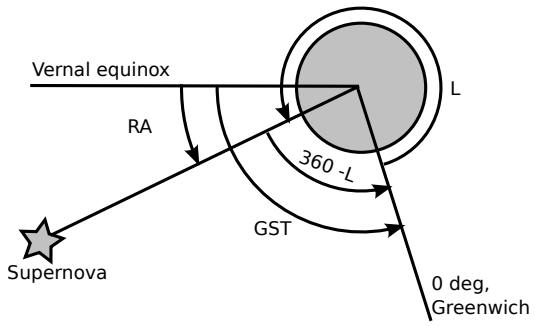

Figure 5.3: Relationship of longitude with the right ascension

5.2.3 Detectors (HLV) coordinates

In this document we take into account three interferometers, two of them are situated in the United States namely Hanford H, Livingston L and the third Virgo V in Italy. Sensitivity of each detector is the best for the direction perpendicular to the plane made of its arms. Traditionally in remote sensing applications we have trust that the best angular resolution in estimating the direction of arrival of the source is for directions perpendicular to the plane made by detectors. We want to find out the angle of incidance at the LHV plane.

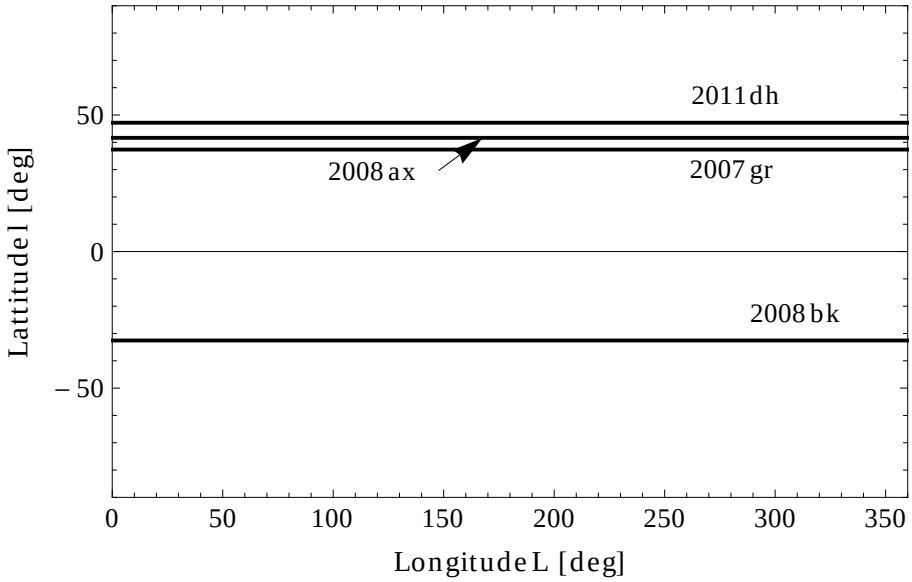

Figure 5.4: The path of supernovae on source time window in geographical coordinates

Let's introduce cartesian coordinates depicted in Figure 5.5 which origin is in Livingston $\vec{L}$ and the z axis is along $\vec{H} - \vec{L}$. Three interferometers make angle α. The y axis lays on the LHV plane at the angle $\pi/2 - \alpha$. x axis is along a vector product of $\vec{V} - \vec{L}$ and $\vec{H} - \vec{L}$. Vector $\vec{D}$ is an unit vector pointing the supernova and is described by two angles: θ measured from $0°$ to $180°$ and ϕ from $-180°$ to $180°$. From geometry of the system we find that

$$\theta = \arccos\left(\frac{c\tau_1}{d_1}\right), \tag{5.3}$$

where c is a speed of light, $\tau_1 = (\vec{H} - \vec{L})\vec{D}/c$ and $d_1 = |\vec{H} - \vec{L}|$. The ϕ angle can be calculated using the equation:

$$\phi = \arcsin\left(\frac{c\tau_2/d_2 - \cos\theta\sin\alpha}{\sin\theta\sin\alpha}\right) \tag{5.4}$$

where $\tau_2 = (\vec{V} - \vec{L})\vec{D}/c$ and $d_2 = |\vec{V} - \vec{L}|$. The plane of the network is situated on angles $\phi = 90°$ and $\phi = 270°$.

The result is shown in Figure 5.6. The dashed lines indicate the plane of the network and the solid lines show the paths of supernovae in the HLV cartesian frame. As we can see from the picture, there becomes a problem with the position of supernovae. Suppose that the source of gravitational waves is at the angle θ and ϕ. The response of the network will be actually the same as in the situation when the source is at the angle θ and $\pi - 180°$, because time arrivals τ_1 and τ_2 will be in both cases the same. Therefore the HLV network will not be able to recognize the exact location of the supernova.

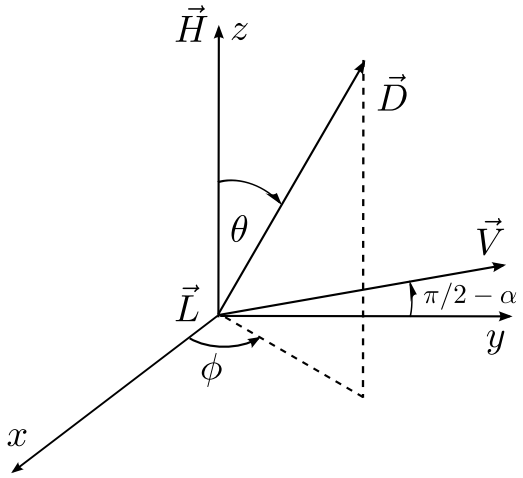

Figure 5.5: HLV coordinates.

5.3 Targeted Core-Collapse Supernovae

For the present search it is important to have an estimate of the time of core collapse for each supernova. This time coincides (within one to a few seconds; e.g., [58]) with the time of strongest GW emission. The better the estimate of the core collapse time, the smaller the *on-source window* of detector data that must be searched and the smaller the confusion background due to non-Gaussian non-stationary detector noise.

For a Galactic or Magellanic Cloud CCSN, the time of core collapse would be extremely well determined by the time of arrival of the neutrino burst that is emitted coincident with the GW signal [59]. A very small on-source window of seconds to minutes could be used for such a special event.

For CCSNe at distances $D \gtrsim 1\,\mathrm{Mpc}$, an observed coincident neutrino signal is highly unlikely [60, 61, 62]. In this case, the time of core collapse must be inferred based on estimates of the explosion time, explosion energy, and the radius of the progenitor. The explosion time is defined as the time at which the supernova shock breaks out of the stellar surface and the electromagnetic emission of the supernova begins. Basic information about the progenitor can be obtained from the lightcurve and spectrum of the supernova (e.g., [63]). Much more information can be obtained if pre-explosion imaging of the progenitor is available (e.g., [64]). A red supergiant progenitor with a typical radius of $\sim 500 - 1500\,R_\odot$ produces a Type IIP supernova and has an explosion time of $\sim 1 - 2\,\mathrm{days}$ after core collapse and a typical explosion energy of $10^{51}\,\mathrm{erg}$; sub-energetic explosions lead to longer explosion times (e.g., [65, 66, 67]). A yellow supergiant that has been partially stripped of its hydrogen-rich envelope, giving rise to a IIb supernova (e.g., [68]), is expected to have a radius of $\sim 200 - 500\,R_\odot$ and an explosion time of $\lesssim 0.5\,\mathrm{days}$ after core collapse [68, 67]. A blue supergiant, giving rise to a peculiar type IIP supernova (such as SN 1987A), has a radius of $\lesssim 100\,R_\odot$ and an explosion time of $\lesssim 2 - 3\,\mathrm{hours}$ after core collapse. A Wolf-Rayet star progenitor, giving rise to a Type Ib/c supernova, has been stripped of its hydrogen (and helium) envelope by stellar winds or binary interactions and has a radius of only a few to $\sim 10\,R_\odot$ and shock breakout occurs within $\sim 10 - 100\,\mathrm{s}$ of core collapse [65, 66].

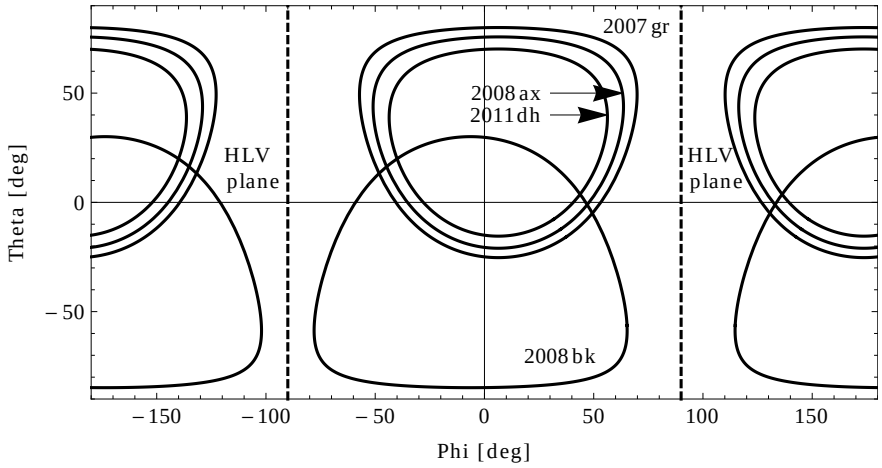

Figure 5.6: Path of supernovae in a Earth fixed reference frame

The breakout of the supernova shock through the surface of the progenitor star leads to a short-duration high-luminosity burst of electromagnetic radiation with a spectral peak dependent on the radius of the progenitor. The burst from shock-breakout preceeds the rise of the optical lightcurve which occurs on a timescale of days after shock breakout (depending, in detail, on the nature of the progenitor star; [63, 69, 68, 67]).

With the exception of very few serendipitous discoveries of shock breakout bursts (e.g., [70, 71]), core-collapse supernovae in the 2007–2011 time frame of the present GW search were usually discovered days after explosion and their explosion time is constrained by one or multiple of (*i*) the most recent non-detection, i.e., by the last date of observation of the host galaxy without the supernova present; (*ii*) by comparison of observed lightcurve and spectra with those of other supernovae for which the explosion time is well known; (*iii*) by lightcurve extrapolation [72]; or, (*iv*), for type IIP supernovae, via lightcurve modeling using the expanding photosphere method (EPM; e.g., [73, 74]).

More than 100 core-collapse supernovae were discovered in the optical by amateur astronomers and professional astronomers (e.g., [53]) during the S5/S6 iLIGO and the VSR2, VSR3, VSR4 Virgo data taking periods. In order to select optically discovered core-collapse supernovae as triggers for this search, we impose the following criteria: (*i*) distance from Earth not greater than $\sim 10 - 15$ Mpc. Since GWs from core-collapse supernovae are most likely very weak and because the observable GW amplitude scales with one-over-distance, nearer events are greatly favored. (*ii*) A well constrained time of explosion leading to an uncertainty in the time of core collapse of less than $\sim$2 weeks. (*iii*) At least partial availability of science-quality data of coincident observations of more than one interferometer in the on-source window.

The core-collapse supernovae making these cuts are SN 2007gr, SN 2008ax, SN 2008bk, and SN 2011dh. Table 5.2 summarizes key properties of these supernovae and we discuss each in more detail in the following.

SN 2007gr, a Type Ic supernova, was discovered on 2007 August 15.51 UTC [75]. A pre-discovery empty image taken by KAIT [76] on August 10.44 UTC provides a baseline constraint on the explosion time. The progenitor of this supernova was a compact stripped-envelope star [77, 78, 79, 80] through which the supernova shock propagated within tens to hundreds of seconds. In order to be conservative, we add an additional hour to the interval between

Table 5.2: Core-collapse supernovae selected as triggers for the gravitational-wave search described in this paper. Distance gives the best current estimate for the distance to the host galaxy. t_1 and t_2 are the UTC dates delimiting the on-source window. Δt is the temporal extent of the on-source window. iLIGO/Virgo run indicates the data taking campaign during which the supernova explosion was observed. Detectors lists the interferometers taking data during at least part of the on-source window. The values in the brackets in the last column provide the relative coverage of the on-source window with science-quality or Astrowatch-quality data of at least two detctors. For SN 2007gr, the relative coverage of the on-source window with the most sensitive network of four active interferometers is 67%. See the text in Section 5.3 for details and references on the supernovae and Section 5.4 for details on the detector networks, coverage, and data quality.

Identifier	Type	Host Galaxy	Distance [Mpc]	$t_1 - t_2$ [UTC]	Δt [days]	iLIGO/Virgo Run	Active Detectors
SN 2007gr	Ic	NGC 1058	10.55 ± 1.95	Aug $10.39 - 15.51$	5.12	S5/VSR1	H1,H2,L1,V1 (93%)
SN 2008ax	IIb	NGC 4490	$9.64^{+1.38}_{-1.21}$	Mar $2.19 - 3.45$	1.26	A5	G1,H2 (8%)
SN 2008bk	IIP	NGC 7793	$3.53^{+0.21}_{-0.29}$	Mar $13.50 - 25.14$	11.64	A5	G1,H2 (38%)
SN 2011dh	IIb	M51	8.40 ± 0.70	May $30.37 - 31.89$	1.52	S6E/VSR4	G1,V1 (37%)

discovery and last non-detection and arrive at a GW on-source window of 2007 August 10.39 UTC to 2007 August 15.51 UTC. The sky location of SN 2007gr is R.A. $= 02^{\rm h}43^{\rm m}27^{\rm s}.98$, Decl. $= +37^\circ 20' 44''.7$ [75]. The host galaxy is NGC 1058. Schmidt *et al.* [81] used EPM to determine the distance to SN 1969L, which exploded in the same galaxy. They found $D = (10.6 + 1.9 - 1.1)\,\mathrm{Mpc}$. This is broadly consistent with the more recent Cepheid-based distance estimate of $D = (9.29 \pm 0.69)\,\mathrm{Mpc}$ to NGC 925 by [82]. This galaxy is in the same galaxy group as NGC 1058 and thus presumed to be in close proximity. For the purpose of the present study, we use the conservative combined distance estimate of $D = (10.55 \pm 1.95\,\mathrm{Mpc})$.

SN 2008ax, a Type IIb supernova [83], was discovered by KAIT on 2008 March 3.45 UTC [84]. The fortuitous non-detection observation made by Arbour on 2008 March 3.19 UTC [85], a mere 6.24 h before the SN discovery, provides an excellent baseline estimate of the explosion time. Spectral observations indicate that the progentior of SN 2008ax was almost completely stripped of its hydrogen envelope, suggesting that is exploded either as a yellow supergiant or as a Wolf-Rayet star [86, 87]. Most recent observations and phenomenological modeling by [88] suggest that the progenitor was in a binary system and may have had a blue-supergiant appearance and an extended $(30 - 40\,R_\odot)$ low-density (thus, low-mass) hydrogen-rich envelope at the time of explosion. To be conservative, we add an additional day to account for the uncertainty in shock propagation time and define the GW on-source window as 2008 March 2.19 UTC to 2008 March 3.45 UTC. The coordinates of SN 2008ax are R.A. $= 12^{\rm h}30^{\rm m}40^{\rm s}.80$, Decl. $= +41^\circ 38' 14''.5$ [84]. Its host galaxy is NGC 4490, which together with NGC 4485 forms a pair of interacting galaxies with a high star formation rate. We adopt the distance $D = (9.64 + 1.38 - 1.21)\,\mathrm{Mpc}$ given by Pastorello *et al.* [89]

SN 2008bk, a Type IIP supernova, was discovered on 2008 March 25.14 UTC [90]. Its explosion time is poorly constrained by a pre-explosion image taken on 2008 January 2.74 UTC [90]. Morrell & Stritzinger [91] compared a spectrum taken of SN 2008bk on 2008 April 12.4 UTC to a library of SN spectra [92] and found a best fit to the spectrum of SN 1999em taken at 36 days after explosion [91]. However, the next other spectra available for SN 1999em are from 20 and 75 days after explosion, so the uncertainty of this result is rather large. EPM modeling by Dessart [93] suggests an explosion time of March 19.5 ± 5 UTC, which is broadly consistent with the

Table 5.3: Overview of GW interferometer science runs from which we draw data for our search. H1 and H2 stand for the LIGO Hanford 4-km and 2-km detectors, respectively. L1 stands for the LIGO Livingston detector. V1 stands for the Virgo detector and G1 stands for the GEO 600 detector. The duty factor column indicates the approximate fraction of science-quality data during the observation runs. The coincident duty factor column indicates the fraction of time during which at least two detectors were taking science-quality data simultaneously. The A5 run was classified as *astrowatch* and was not a formal science run. The H2 and V1 detectors operated for only part of A5. The Virgo VSR1 run was joint with the iLIGO S5 run, the Virgo VSR2 and VSR3 runs were joint with the iLIGO S6 run, and the GEO 600 detector (G1) operated in iLIGO run S6E during Virgo run VSR4. When iLIGO and Virgo science runs overlap, the coincident duty factor takes into account iLIGO, GEO 600, and Virgo detectors.

Run	Detectors	Run Period	Duty Factors	Coin. Duty Factor
S5	H1,H2,L1,G1	2005/11/04–2007/10/01	∼75% (H1), ∼76% (H2), ∼65% (L1), ∼77% (G1)	∼87%
A5	G1,H2,V1	2007/10/01–2009/05/31	∼81%(G1), ∼18% (H2), ∼5% (V1)	∼18%
S6	L1,H1,G1	2009/07/07–2010/10/21	∼51% (H1), ∼47% (L1), ∼56% (G1)	∼67%
S6E	G1	2011/06/03–2011/09/05	∼77%	∼66%
VSR1/S5	V1	2007/05/18–2007/10/01	∼80%	∼97%
VSR2/S6	V1	2009/07/07–2010/01/08	∼81%	∼74%
VSR3/S6	V1	2010/08/11–2010/10/19	∼73%	∼94%
VSR4/S6E	V1	2011/05/20–2011/09/05	∼78%	∼62%

lightcurve data and hydrodynamical modeling presented in [94]. The progenitor of SN 2008bk was most likely a red supergiant with a radius of $\sim 500\,R_\odot$ [95, 96, 97], which suggests an explosion time of ~ 1 day after core collapse [65, 66, 67]. Hence, we assume a conservative on-source window of 2008 March 13.5 UTC to 2008 March 25.14 UTC. The coordinates of SN 2008bk are R.A. $= 23^{\rm h}57^{\rm m}50^{\rm s}.42$, Decl. $= -32^\circ 33' 21''.5$ [98]. Its host galaxy is NGC 7793, which is located at a Cepheid-distance $D = (3.44 + 0.21 - 0.2)$ Mpc [99]. This distance estimate is consistent with $D = (3.61 + 0.13 - 0.14)$ Mpc obtained by [100] based on the tip of the red giant branch method (e.g., [101]). For the purpose of this study, we use a conservative averaged estimate of $D = (3.53 + 0.21 - 0.29)$ Mpc.

SN 2011dh, a type IIb supernova, has an earliest discovery date in the literature of 2011 May 31.893, which was by amateur astronomers [102, 103, 104, 105]. An earlier discovery date of 2011 May 31.840 is given by Alekseev [106] and a most recent non-detection by Dwyer on 2011 May 31.365 [106]. The progenitor of SN 2011dh was with high probability a yellow supergiant star [107] with a radius of a few $100\,R_\odot$ [68, 108, 109]. We conservatively estimate an earliest time of core collapse of a day before the most recent non-detection by Dwyer and use an on-source window of 2011 May 30.365 to 2011 May 31.893. SN 2011dh's location is R.A. $= 13^{\rm h}30^{\rm m}05^{\rm s}.12$, Decl. $= +47^\circ 10' 11''.30$ [110] in the nearby spiral galaxy M51. The best estimates for the distance to M51 come from Vinkó *et al.* [108], who give $D = 8.4 \pm 0.7$ Mpc on the basis of EPM modeling of SN 2005cs and SN 2011dh. This is in agreement with Feldmeier *et al.* [111], who give $D = 8.4 \pm 0.6$ Mpc on the basis of planetary nebula luminosity functions. Estimates using surface brightness variations [112] or the Tully-Fisher relation [113] are less reliable, but give a somewhat lower distance estimates of $D = 7.7 \pm 0.9$ and $D = 7.7 \pm 1.3$, respectively. We adopt the conservative distance $D = 8.4 \pm 0.7$ Mpc for the purpose of this study.

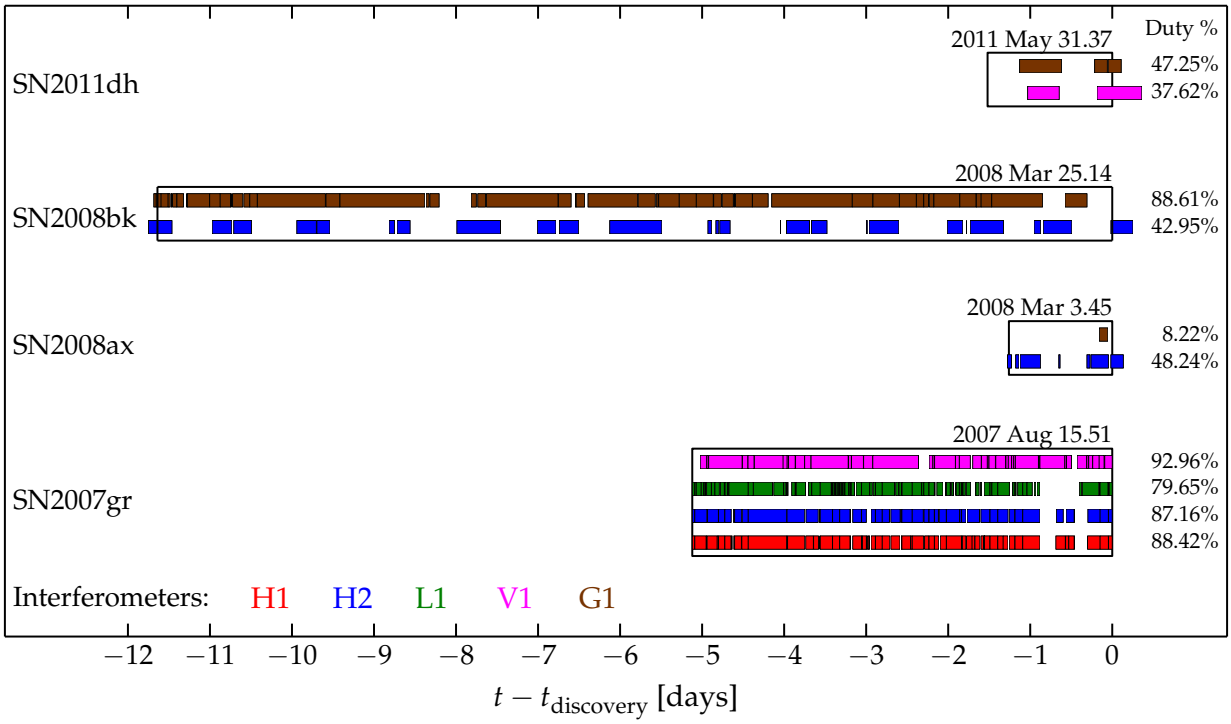

Figure 5.7: On-source windows as defined for the four core-collapse supernovae considered in Section 5.3. The date given for each core-collapse supernova is the published date of discovery. Overplotted in color are the stretches of time covered with science-quality and Astrowatch-quality data of the various GW interferometers. The percentages given for each core-collapse supernova and interferometer is the fractional coverage of the on-source window with science or astrowatch data by that interferometer. See Table 5.2 and Sections 5.3 and 5.4 for details.

5.4 Detector Networks and Coverage

This search employs data from the 4 km LIGO Hanford, WA and LIGO Livingston, LA interferometers (denoted **H1** and **L1**, respectively), from the 2 km LIGO Hanford, WA interferometer (denoted as **H2**), from the 0.6 km GEO 600 detector near Hannover, Germany (denoted as **G1**), and from the 3 km Virgo interferometer near Cascina, Italy (denoted as **V1**).

Table 5.3 lists the various GW interferometer data taking periods ("runs") in the 2005–2011 time frame from which we draw data for our search. The table also provides the duty factor and *coincident* duty factor of the GW interferometers. The duty factor is the fraction of the run time a given detector was taking science-quality data. The coincident duty factor is the fraction of the run time at least two detectors were taking science quality data. The coincident duty factor is most relevant for GW searches like ours that require data from at least two detectors to reject candidate events that are due to non-Gaussian instrumental or environmental noise artifacts ("glitches") but can mimic real signals in shape and time-frequency content (see, e.g., [50, 114]).

One notes from Table 5.3 that the duty factor for the first-generation interferometers was typically $\lesssim 50 - 80\%$. The relatively low duty factors are due to a combination of environmental causes (such as distant earthquakes causing loss of interferometer lock) and interruptions for detector commissioning or maintenance.

The CCSNe targeted by this search and described in Section 5.3 are the only 2007–2011 CCSNe located within

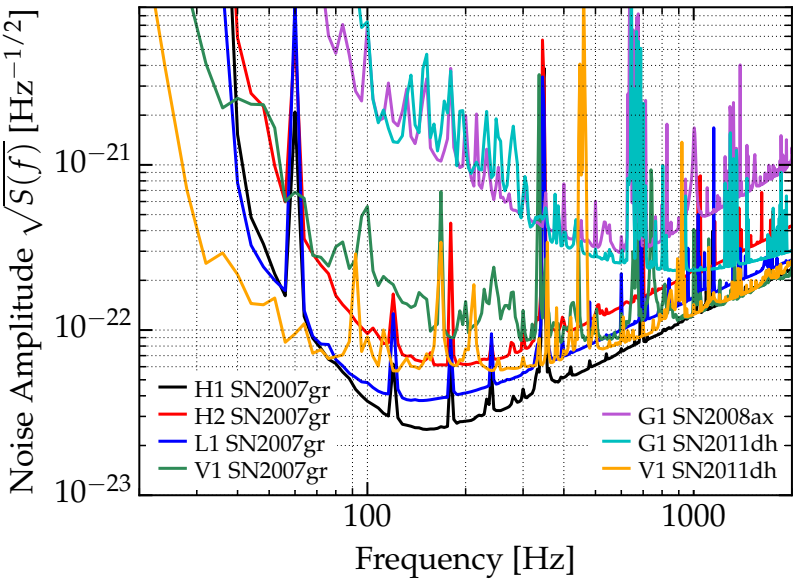

Figure 5.8: Noise amplitude spectral densities of the GW interferometers whose data are analyzed for SNe 2007gr and 2011dh (see Section 5.4). The curves are the results of averaging $1/S(f)$ over the on-source windows of the SNe (see Table 5.2). We plot the G1 noise spectrum also for SN 2008ax to demonstrate the improvement in high-frequency sensitivity due to GEO-HF [12] for SN 2011dh.

$D \lesssim 10 - 15\,\mathrm{Mpc}$ for which well-defined on-source windows exist and which are also covered by extended stretches of coincident observations of at least two interferometers. In Figure 5.7, we depict the on-source windows for SNe 2007gr, 2008ax, 2008bk, and 2011dh. We indicate with regions of different color times during which the various interferometers were collecting data.

SN 2007gr exploded during the S5/VSR1 joint run between the iLIGO, GEO 600, and Virgo detectors. It has the best coverage of all considered CCSNe: 93% of its on-source window are covered by science-quality data from at least two of H1, H2, L1, and V1. We search for GWs from SN 2007gr at times when data from the following detector networks are available: H1H2L1V1, H1H2L1, H1H2V1, H1H2, L1V1. The G1 detector was also taking data during SN 2007gr's on-source window, but since its sensitivity was much lower than that of the other detectors, we do not analyze G1 data for SN 2007gr.

SNe 2008ax and 2008bk exploded in the A5 *astrowatch* run between the S5 and S6 iLIGO science runs (cf. Table 5.3). Only the G1 and H2 detectors were operating at sensitivities much lower than those of the 4-km L1 and H1 and the 3-km V1 detectors. The coincident duty factor for SN 2008ax is only 8% while that for SN 2008bk is 38%. Preliminary analysis of the available coincident GW data showed that due to a combination of low duty factors and low detector sensitivity, the overall sensitivity to GWs from these CCSNe was much lower than for SNe 2007gr and 2011dh. Because of this, we exclude SNe 2008ax and 2008bk from the analysis presented in the rest of this paper.

SN 2011dh exploded a few days before the start of the S6E/VSR4 run during which the V1 and G1 interferometers were operating (cf. Table 5.3). G1 was operating in GEO-HF mode [12] that improved its high-frequency ($f \gtrsim 1\,\mathrm{kHz}$) sensitivity to within a factor of two of V1's sensitivity. While not officially in a science run during the SN 2011dh on-source window, both G1 and V1 were operating and collecting data that passed the data quality standards necessary for being classified as science-quality data (e.g., [115, 116, 117]). The coincident G1V1 duty factor is 37%

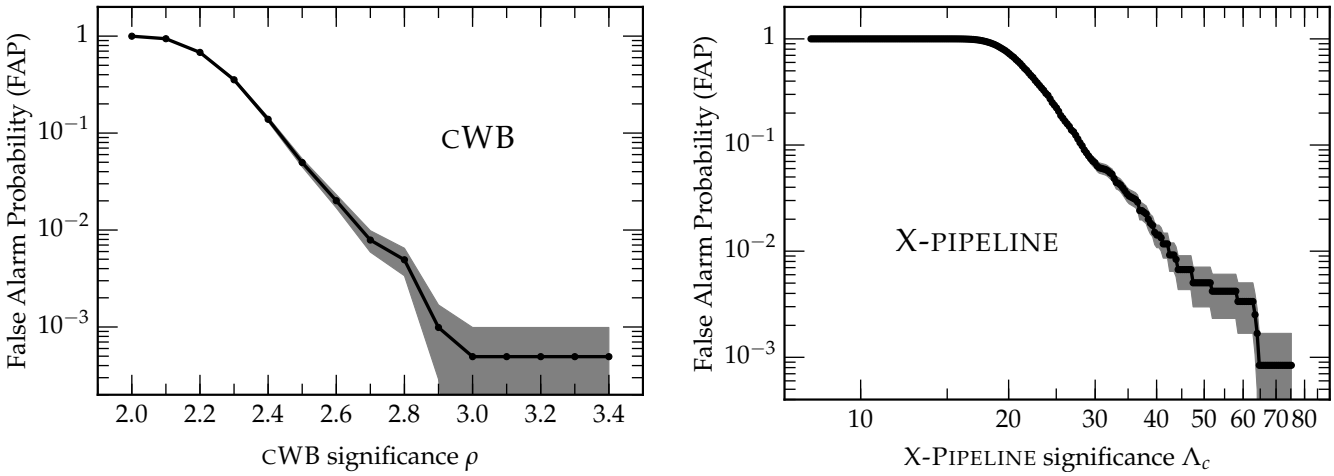

Figure 5.9: False Alarm Probability [FAP, Equation (4.58)] distributions of the background events for SN 2007gr and the H1H2L1V1 detector network. The FAP indicates the probability that an event of a given "loudness" (significance) is consistent with background noise. The left panel shows the FAP distribution determined by the cWB pipeline as a function of its loudness measure, ρ, (see [13] for details). The right panel depicts the same for X-Pipeline as a function of its loudness measure, Λ_c, (see [14, 15] for details). The shaded regions indicate $1-\sigma$ error estimates for the FAP.

for SN 2011dh.

In Figure 5.8, we plot the one-side noise amplitude spectral densities of each detector averaged over the on-source windows of SNe 2007gr and 2011dh. In order to demonstrate the high-frequency improvement in the 2011 G1 detector, we also plot the G1 noise spectral density for SN 2008ax for comparison.

5.5 Search methodology

Two search algorithms are employed in this study: X-Pipeline [14, 15] and Coherent WaveBurst (cWB) [13]. Neither algorithm requires detailed assumptions about the GW morphology and both look for subsecond GW transients in the frequency band 60 Hz to 2000 Hz. This is the most sensitive band of the detector network, where the amplitude of the noise spectrum of the most sensitive detector is within about an order of magnitude of its minimum. This band also encompasses most models for GW emission from CCSNe (cf. [58, 118, 119]). The benefit of having two independent algorithms is that they can act as a cross check for outstanding events. Furthermore, sensitivity studies using simulated GWs show some complementarity in the signals detected by each pipeline; this is discussed further in Section 5.6.

The two algorithms process the data independently to identify potential GW events for each supernova and network combination. Each algorithm assigns a "loudness" measure to each event; these are described in more detail below. The two algorithms also evaluate measures of signal consistency across different interferometers and apply thresholds on these measures (called coherence tests) to reject background noise events. The internal thresholds of each algorithm are chosen to obtain robust performance across a set of signal morphologies of interest. We also reject events that occur at times of environmental noise disturbances that are known to be correlated with transients in the GW data via well-established physical mechanisms; these so-called "category 2" data quality cuts

are described in [120].

The most important measure of an event's significance is its false alarm rate (FAR): the rate at which the background noise produces events of equal or higher loudness than events that pass all coherent tests and data quality cuts. Each pipeline estimates the FAR using background events generated by repeating the analysis on time-shifted data — the data from the different detectors are offset in time, in typical increments of $\sim 1\,\mathrm{s}$. The shifts remove the chance of drawing a sub-second GW transient into the background sample since the largest time of flight between the LIGO and Virgo sites is 27 milliseconds (between H1 and V1). To accumulate a sufficient sampling of rare background events, this shifting procedure is performed thousands of times without repeating the same relative time shifts among detectors. Given a total duration T_{off} of off-source (time-shifted) data, the smallest false alarm rate that can be measured is $1/T_{\mathrm{off}}$.

On-source events from each combination of CCSN, detector network, and pipeline are assigned a FAR using the time-slide background from that combination only. The event lists from the different CCSNe, detector networks, and pipelines are then combined and the events ranked by their FAR. The event with lowest FAR is termed the *loudest event*.

In order for the loudest event to be considered as a GW detection it must have a False Alarm Probability (FAP) low enough that it is implausible to have been caused by background noise. Given a FAR value R, the probability $p(R)$ of noise producing one or more events of FAR less than or equal to R during one or more CCSN on-source windows of total duration T_{on} is

$$p = 1 - \exp\left(-RT_{\mathrm{on}}\right). \tag{5.5}$$

The smallest such false alarm probability (FAP) that can be measured given an off-source (time-shifted) data duration T_{off} is approximately $T_{\mathrm{on}}/T_{\mathrm{off}}$. Several thousand time shifts are therefore sufficient to measure FAP values of $O(10^{-3})$. We require a FAP below 0.001, which exceeds 3-σ confidence, in order to consider an event to be a possible GW detection candidate. Figure 5.9 shows examples of the FAP as a function of event loudness for cWB and X-Pipeline for the H1H2L1V1 network during the SN 2007gr on-source window.

The loudest surviving events of the current search are reported in Table 5.4. In practice, none of these events has a FAP low enough to be considered a GW candidate (see Section 5.6 for further discussion). We therefore set upper limits on the strength of possible GW emission by the CCSNe. This is done by adding to the data simulated GW signals of various amplitudes (or equivalently sources at various distances) and repeating the analysis. For each amplitude or distance we measure the fraction of simulations that produce an event in at least one pipeline with FAP lower than the loudest on-source event, and which survive our coherence tests and data quality cuts; this fraction is the *detection efficiency* of the search.

5.5.1 Coherent WaveBurst

The cWB [13] analysis is performed as described in [114], and it is based on computing a constrained likelihood function. In brief: each detector data stream is decomposed into 6 different wavelet decompositions (each one with different time and frequency resolutions). The data are whitened, and the largest 0.1 percent of wavelet magnitudes in each frequency bin and decomposition for each interferometer are retained (we call these "black pixels"). We also retain "halo" pixels, which are those that surround each black pixel. In order to choose pixels that are more likely related to a GW transient (*candidate event*) we identify clusters of them. Once all of the wavelet decompositions

are projected into the same time frequency plane, clusters are defined as sets of contiguous retained pixels (black or halo). Only the pixels involved in a cluster are used in the subsequent calculation of the likelihood. These clusters also need to be consistent between interferometers for the tested direction of arrival. For each cluster of wavelets, a Gaussian likelihood function is computed, where the unknown GW is reconstructed with a maximum-likelihood estimator.

The likelihood analysis is repeated over a grid of sky positions covering the range of possible directions to the GW source. Since the sky location of each of the analyzed CCSNe is well known, we could choose to apply this procedure only for the known CCSN sky location. However, the detector noise occasionally forces the cWB likelihood to peak in a sky location away from the true sky location. As a consequence, some real GW events could be assigned a smaller likelihood value, lowering the capability to detect them. Because of this, we consider triggers that fall within an error region of 0.4 degrees of the known CCSN sky location and that pass the significance threshold, even if they are not at the peak of the cWB reconstructed sky position likelihood. The 0.4 degree region is determined empirically by trade-off studies between detection efficiency and FAR.

For SN 2011dh, the noise spectra were very different for the G1 and V1 detectors, with the consequence that the network effectively had only one detector at frequencies up to several hundred Hz, and therefore location reconstruction was very poor. As a consequence we decided to scan the entire sky for candidate events for this CCSN.

The events reported for a given network configuration are internally ranked for detection purposes by cWB using the coherent network amplitude statistic ρ defined in [48]. Other constraints related to the degree of similarity of the reconstructed signal across different interferometers (the "network correlation coefficient" *cc*) and the ability of the network to reconstruct both polarizations of the GW signal (called *regulators*) are applied to reject background events; these are also described in [48].

5.5.2 X-Pipeline

In the X-Pipeline [14, 15, 121] analysis, the detector data are first whitened, then Fourier transformed. A total energy map is made by summing the spectrogram for each detector, and "hot" pixels are identified as the 1% in each detector with the largest total energy. Hot pixels that share an edge or vertex (nearest neighbors and next-nearest neighbors) are clustered. For each cluster, the raw time-frequency maps are recombined in a number of linear combinations designed to give maximum-likelihood estimates of various GW polarizations given the known sky position of the CCSN. The energy in each combination is recorded for each cluster, along with various time-frequency properties of the cluster. The procedure is repeated using a series of Fourier transform lengths from 1/4 s, 1/8 s, ... 1/128 s. Clusters are ranked internally using a Bayesian-inspired estimate Λ_c of the likelihood ratio for a circularly polarized GW, marginalized over the unknown GW amplitude σ_h with a Jeffreys (logarithmic) prior σ_h^{-1}; see [122, 123, 15] for details.

When clusters from different Fourier transform lengths overlap in time-frequency, the cluster with the largest likelihood Λ_c is retained and the rest are discarded. Finally, a post-processing algorithm tunes and applies a series of pass/fail tests to reject events due to background noise; these tests are based on measures of correlation between the detectors for each cluster. The tuning of these tests is described in detail in [14]. For more details see also [2].

Table 5.4: False alarm rate (FAR) of the loudest event found by each pipeline for each detector network. No on-source events survived the coherent tests and data quality cuts for the cWB analysis of the H1H2L1 and H1H2 networks for SN 2007gr. The lowest FAR, 1.7×10^{-6} Hz, corresponds to a FAP of 0.77, where the total livetime analysed was $T_{\rm on} = 873461$ s.

Network	cWB	X-Pipeline
H1H2L1V1	1.7×10^{-6} Hz	2.5×10^{-6} Hz
H1H2L1	no events	1.1×10^{-5} Hz
H1H2V1	1.2×10^{-5} Hz	5.3×10^{-6} Hz
H1H2	no events	7.1×10^{-5} Hz
L1V1	4.8×10^{-5} Hz	4.1×10^{-3} Hz
G1V1	1.2×10^{-5} Hz	2.7×10^{-5} Hz

5.5.3 Simulated Signals and Search Sensitivity

In this paper, we employ three classes of GW signals for our Monte Carlo studies: (1) representative waveforms from detailed multi-dimensional (2D axisymmetric or 3D) CCSN simulations; (2) semi-analytic phenomenological waveforms of plausible but extreme emission scenarios; and (3) *ad-hoc* waveform models with tuneable frequency content and amplitude to establish upper limits on the energy emitted in GWs at a fixed CCSN distance. We briefly summarize the nature of these waveforms below. We list all employed waveforms in Tables 5.5 and 5.6 and summarize their key emission metrics. In particular, we provide the angle-averaged root-sum-squared GW strain,

$$h_{\rm rss} = \sqrt{\int \left\langle h_+^2(t) + h_\times^2(t) \right\rangle_\Omega \mathrm{d}t} \ , \tag{5.6}$$

and the energy $E_{\rm GW}$ emitted in GWs, using the expressions given in [2].

Waveforms from Multi-Dimensional CCSN Simulations Rotation leads to a natural axisymmetric quadrupole (oblate) deformation of the collapsing core. The tremendous acceleration at core bounce and proto-neutron star formation results in a strong linearly-polarized burst of GWs followed by a ring-down signal. Rotating core collapse is the most extensively studied GW emission process in the CCSN context (see, e.g., [124, 125, 126, 127, 128, 39, 129, 130] and [58, 118, 119] for reviews). For the purpose of this study, we select three representative rotating core collapse waveforms from the 2D general-relativistic study of Dimmelmeier *et al.* [39]. The simulations producing these waveforms used the core of a 15-$M_\odot$ progenitor star and the Lattimer-Swesty nuclear equation of state [131]. The waveforms are enumerated by Dim1–Dim3 prefixes and are listed in Table 5.5. They span the range from moderate rotation (Dim1-s15A2O05ls) to extremely rapid rotation (Dim3-s15A3O15ls). See [39] for details on the collapse dynamics and GW emission.

In non-rotating or slowly rotating CCSNe, neutrino-driven convection and the standing accretion shock instability (SASI) are expected to dominate the GW emission. GWs from convection/SASI have also been extensively studied in 2D (e.g., [133, 134, 135, 136, 137, 138, 139, 132, 38]) and more recently also in 3D [33, 140]. For the present study, we select a waveform from a 2D Newtonian (+ relativistic corrections) radiation-hydrodynamics simulation of a CCSN in a 15-$M_\odot$ progenitor by Yakunin *et al.* [132]. This waveform also captures the frequency content of more recent 3D waveforms [34, 141]. This waveform and its key emission metrics are listed as Yakunin-s15 in Table 5.5. Note that since the simulation producing this waveform was axisymmetric, only the + polarization is

Table 5.5: Injection waveforms from detailed multi-dimensional CCSN simulations described in the text. For each waveform, we give the emission type, journal reference, waveform identifier, angle-averaged root-sum-squared strain $h_{\rm rss}$, the frequency $f_{\rm peak}$ at which the GW energy spectrum peaks, the emitted GW energy $E_{\rm GW}$, and available polarizations. See [2, 3] for details.

Emission Type	Ref.	Waveform Identifier	$h_{\rm rss}$ $[10^{-22}@10\,{\rm kpc}]$	$f_{\rm peak}$ [Hz]	$E_{\rm GW}$ $[10^{-9} M_\odot c^2]$	Polarizations
Rotating Core Collapse	[39]	Dim1-s15A2O05ls	1.052	774	7.685	+
Rotating Core Collapse	[39]	Dim2-s15A2O09ls	1.803	753	27.873	+
Rotating Core Collapse	[39]	Dim3-s15A3O15ls	2.690	237	1.380	+
2D Convection/SASI	[132]	Yakunin-s15	1.889	888	9.079	+
3D Convection/SASI	[33]	Müller1-L15-3	1.655	150	3.741×10^{-2}	+, ×
3D Convection/SASI	[33]	Müller2-N20-2	3.852	176	4.370×10^{-2}	+, ×
3D Convection/SASI	[33]	Müller3-W15-4	1.093	204	3.247×10^{-2}	+, ×
PNS Pulsations	[58]	Ott-s15	5.465	971	429.946	+

available.

CCSNe in Nature are 3D and produce both GW polarizations (h_+ and $h_\times$). Only a few GW signals from 3D simulations are presently available. We draw three waveforms from the work of Müller *et al.* [33]. These and their key GW emission characteristics are listed with Müller1–Müller3 prefixes in Table 5.5. Waveforms Müller1-L15-3 and Müller2-W15-4 are from simulations using two different progenitor models for a 15-$M_\odot$ star. Waveform Müller2-N20-2 is from a simulation of a CCSN in a 20-$M_\odot$ star. Note that the simulations of Müller *et al.* [33] employed an *ad-hoc* inner boundary at multiple tens of kilometers. This prevented decelerating convective plumes from reaching small radii and high velocities. As a consequence, the overall GW emission in these simulations peaks at lower frequencies than in simulations that do not employ an inner boundary (cf. [132, 38, 139, 140]). For example, the expected signal-to-noise ratios of waveforms from the simulations of [140] are 2-3 times higher than those of Müller *et al*, so their detectable range should be larger by approximately the same factor.

We also do not include any waveforms from 3D rotating core collapse. However, the study in [142], which used X-Pipeline and realistic LIGO noise, did include waveforms from the 3D Newtonian magnetohydrodynamical simulations of Scheidegger *et al.* [40]. The two selected waveforms were for a 15 $M_\odot$ progenitor star with the Lattimer-Swesty equation of state. These simulations exhibited stronger GW emission, and the detectable range was typically 2-3 times further than for the 2D Dimmelmeier *et al.* waveforms.

In some 2D CCSN simulations [143, 144], strong excitations of an $\ell = 1$ g-mode (an oscillation mode with gravity as its restoring force) were observed. These oscillations were found to be highly non-linear and to couple to GW-emitting $\ell = 2$ modes. The result is a strong burst of GWs that lasts for the duration of the large-amplitude mode excitation, possibly for hundreds of milliseconds [58, 145]. More recent simulations do not find such strong g-mode excitations (e.g., [146, 139]). We nevertheless include here one waveform from the simulations of [144] that was reported by Ott [58]. This waveform is from a simulation with a 15-$M_\odot$ progenitor and is denoted as Ott-s15 in Table 5.5.

Phenomenological Waveform Models In the context of rapidly rotating core collapse, various non-axisymmetric instabilities can deform the proto-neutron star into a tri-axial ("bar") shape (e.g., [147, 148, 149, 150, 151, 129, 34]), potentially leading to extended ($\sim$10 ms $-$ few s) and energetic GW emission. This emission occurs at twice the

proto-neutron star spin frequency, with a 90 degree phase shift between the plus and cross modes (similar to the waveforms from some more realistic 3D simulations), and with amplitude dependent on the magnitude of the bar deformation [152, 34, 129]. We use the simple phenomenological bar model described in [153]. Its parameters are the length of the bar deformation, L, in km, its radius, R, in km, the mass, M, in $M_\odot$, involved in the deformation, the spin frequency, f, and the duration, t, of the deformation. We select six waveforms as representative examples. We sample the potential parameter space by chosing $M = \{0.2, 1.0\}\, M_\odot$, $f = \{400, 800\}$ Hz, and $t = \{25, 100, 1000\}$ ms. We list these waveforms as "Long-lasting Bar Mode" in Table 5.6 and enumerate them as LB1–LB6. The employed model parameters are encoded in the full waveform name. One notes from Table 5.6 that the strength of the bar-mode GW emission is orders of magnitude greater than that of any of the waveforms computed from detailed multi-dimensional simulations listed in Table 5.5. We emphasize that the phenomenological bar-mode waveforms should be considered as being at the extreme end of plausible GW emission scenarios. Theoretical considerations (e.g., [58]) suggest that such strong emission is unlikely to obtain in CCSNe. Observationally, however, having this emission in one or all of the CCSNe has not been ruled out.

We also consider the phenomenological waveform model proposed by Piro & Pfahl [41]. They considered the formation of a dense self-gravitating $M_\odot$-scale fragment in a thick accretion torus around a black hole in the context of collapsar-type gamma-ray bursts. The fragment is driven toward the black hole by a combination of viscous torques and energetic GW emission. This is an extreme but plausible scenario. We generate injection waveforms from this model using the implementation described in [154]. The model has the following parameters: mass $M_{\rm BH}$ of the black hole in $M_\odot$, a spatially constant geometrical parameter controlling the torus thickness, $\eta = H/r$, where H is the disk scale height and r is the local radius, a scale factor for the fragment mass (fixed at 0.2), the value of the phenomenological α-viscosity (fixed at $\alpha = 0.1$), and a starting radius that we fix to be $100 r_g = 100 G M_{\rm BH}/c^2$. We employ four waveforms, probing black hole masses $M_{\rm BH} = \{5, 10\}\, M_\odot$ and geometry factors $\eta = \{0.3, 0.6\}$. The resulting waveforms and their key emission metrics are listed as "Torus Fragmentation Instability" and enumerated by Piro1–Piro4 in Table 5.6. The full waveform names encode the particular parameter values used. As in the case of the bar-mode emission model, we emphasize that also the Torus Fragmentation Instability represents an extreme GW emission scenario for CCSNe. It may be unlikely based on theoretical considerations (e.g., [58, 154]), but has not been ruled out observationally.

Ad-Hoc Waveforms: sine-Gaussians Following previous GW searches, we also employ *ad-hoc* sine-Gaussian waveforms to establish frequency-dependent upper limits on the emitted energy in GWs. This also allows us to compare the sensitivity of our targeted search with results from previous all-sky searches for GW bursts (e.g., [114, 120, 155])

Sine-Gaussian waveforms are, as the name implies, sinusoids in a Gaussian envelope. They are analytic and given by

$$h_+(t) = A\frac{1+\alpha^2}{2}\exp\left(-t^2/\tau^2\right)\sin(2\pi f_0 t)\,, \tag{5.7}$$

$$h_\times(t) = A\alpha\exp\left(-t^2/\tau^2\right)\cos(2\pi f_0 t)\,. \tag{5.8}$$

Here, A is an amplitude scale factor, $\alpha = \cos\iota$ is the ellipticity of the waveform with ι being the inclination angle, f_0 is the central frequency, and $\tau = Q/(\sqrt{2}\pi f_0)$, where Q is the quality factor controlling the width of the Gaussian and

Table 5.6: Injection waveforms from phenomenological and *ad-hoc* emission models described in the text. For each waveform, we give the emission type, journal reference, waveform identifier, angle-averaged root-sum-squared strain $h_{\rm rss}$, the frequency $f_{\rm peak}$ at which the GW energy spectrum peaks, the emitted GW energy $E_{\rm GW}$, and available polarizations. See [2, 3] for details. As sine-Gaussian waveforms are *ad-hoc*, they can be rescaled arbitrarily and do not have a defined physical distance or $E_{\rm GW}$ value.LBM stands for Long-lasting Bar Mode, tFI - Torus Fragmentation Instability, SG - sine-Gaussian.

Emission Type	Ref.	Waveform Identifier	$h_{\rm rss}$ $[10^{-20}@10\,{\rm kpc}]$	$f_{\rm peak}$ [Hz]	$E_{\rm GW}$ $[M_\odot c^2]$	Polarizations
LBM	[153]	LB1-M0.2L60R10f400t100	1.480	800	2.984×10^{-4}	$+, \times$
LBM	[153]	LB2-M0.2L60R10f400t1000	4.682	800	2.979×10^{-3}	$+, \times$
LBM	[153]	LB3-M0.2L60R10f800t100	5.920	1600	1.902×10^{-2}	$+, \times$
LBM	[153]	LB4-M1.0L60R10f400t100	7.398	800	7.459×10^{-3}	$+, \times$
LBM	[153]	LB5-M1.0L60R10f400t1000	23.411	800	7.448×10^{-2}	$+, \times$
LBM	[153]	LB6-M1.0L60R10f800t25	14.777	1601	1.184×10^{-1}	$+, \times$
TFI	[41]	Piro1-M5.0η0.3	2.550	2035	6.773×10^{-4}	$+, \times$
TFI	[41]	Piro2-M5.0η0.6	9.936	1987	1.027×10^{-2}	$+, \times$
TFI	[41]	Piro3-M10.0η0.3	7.208	2033	4.988×10^{-3}	$+, \times$
TFI	[41]	Piro4-M10.0η0.6	28.084	2041	7.450×10^{-2}	$+, \times$
SG	[156]	SG1-235HzQ8d9linear	—	235	—	$+$
SG	[156]	SG2-1304HzQ8d9linear	—	1304	—	$+$
SG	[156]	SG3-235HzQ8d9elliptical	—	235	—	$+, \times$
SG	[156]	SG4-1304HzQ8d9elliptical	—	1304	—	$+, \times$

thus the duration of the signal. Since the focus of our study is more on realistic and phenomenological waveforms, we limit the set of sine-Gaussian waveforms to four, enumerated SG1–SG4 in Table 5.6. We fix $Q = 8.9$ and study linearly polarized ($\cos\iota = 0$) and elliptically polarized ($\cos\iota$ sampled uniformly on $[-1, 1]$) waveforms at $f = \{235, 1304\}$ Hz. We choose this quality factor and these particular frequencies for comparison with [114, 120, 155].

5.5.4 Systematic Uncertainties

Our efficiency estimates are subject to a number of uncertainties. The most important of these are calibration uncertainties in the strain data recorded at each detector, and Poisson uncertainties due to the use of a finite number of injections (Monte Carlo uncertainties). We account for each of these uncertainties in the sensitivities reported in this paper.

We account for Poisson uncertainties from the finite number of injections using the Bayesian technique described in [157]. Specifically, given the total number of injections performed at some amplitude and the number detected, we compute the 90% credible lower bound on the efficiency assuming a uniform prior on $[0, 1]$ for the efficiency. All efficiency curves reported in this paper are therefore actually 90% confidence level lower bounds on the efficiency.

Calibration uncertainties are handled by rescaling quoted $h_{\rm rss}$ and distance values following the method in [158]. The dominant effect is from the uncertainties in the amplitude calibration; these are estimated at approximately 10% for G1, H1, and H2, 14% for L1, and 6%-8% for V1 at the times of the two CCSNe studied [159, 160]. The individual detector amplitude uncertainties are combined into a single uncertainty by calculating a combined root-sum-square signal-to-noise ratio and propagating the individual uncertainties assuming each error is independent (the signal-to-noise ratio is used as a proxy for the loudness measures the two pipelines use for ranking events). This

combination depends upon the relative sensitivity of each detector, which is a function of frequency, so we compute the total uncertainty at a range of frequencies across our analysis band for each CCSN and select the largest result, 7.6%, as a conservative estimate of the total 1-σ uncertainty. This 1-σ uncertainty is then scaled by a factor of 1.28 (to 9.7%) to obtain the factor by which our amplitude and distance limits must be rescaled in order to obtain values consistent with a 90% confidence level upper limit.

5.6 Search Results

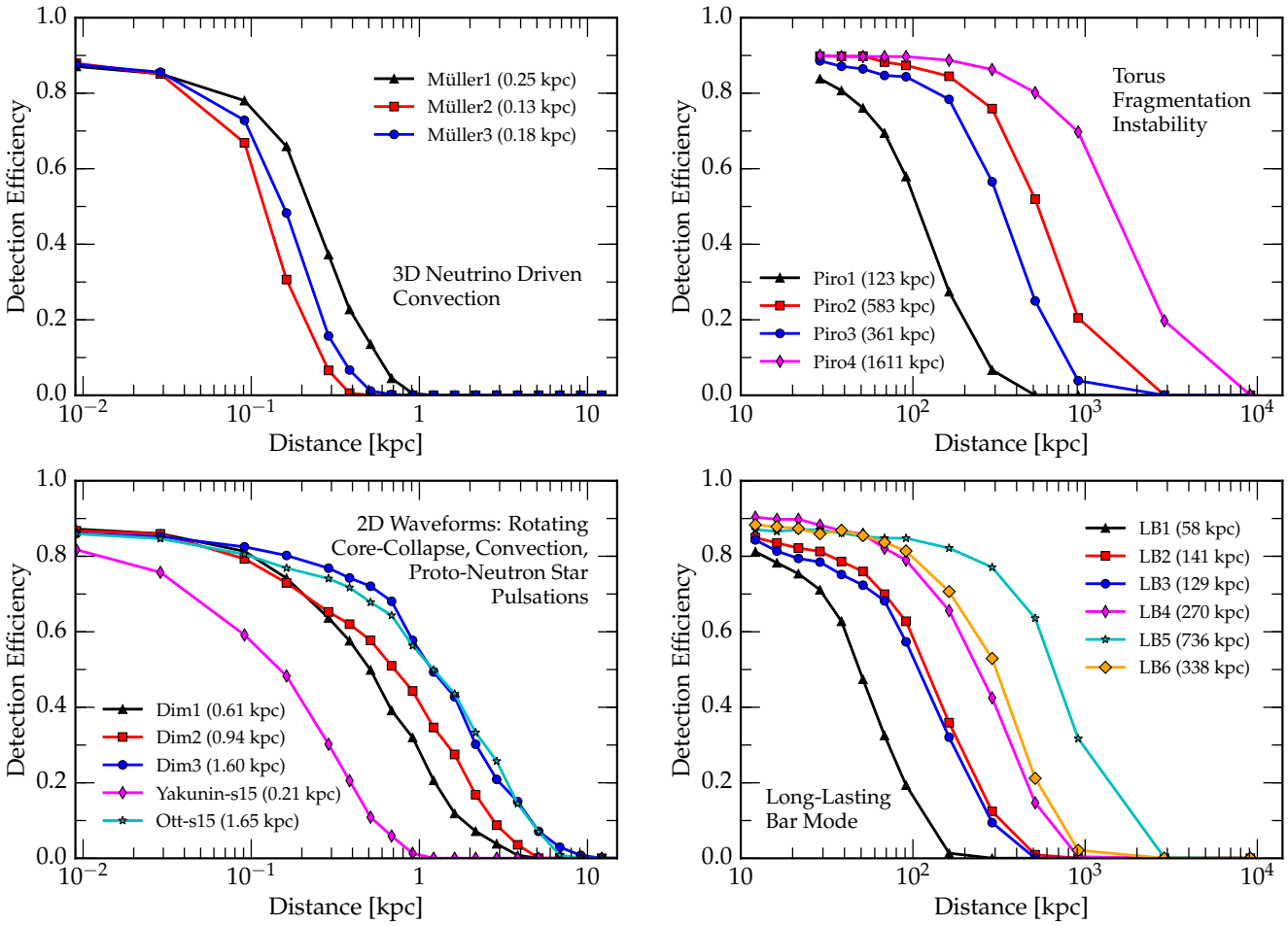

Figure 5.10: SN 2007gr detection efficiency versus distance for the waveforms from multi-dimensional CCSN simulations (left) and the phenomenological waveforms (right) described in Tables 5.5 and 5.6. Simulated GW signals are added into detector data with a range of amplitudes corresponding to different source distances. A simulated signal is considered detected if cWB or X-Pipeline reports an event that survives the coherent tests and data quality cuts with a FAR value lower than that of the loudest event from the SN 2007gr and SN 2011dh on-source windows. These efficiencies are averaged over all detector network combinations for SN 2007gr. The efficiencies are limited to $\leq 93\%$ at small distances due to the fact that this was the duty cycle for coincident observation over the SN 2007gr on-source window. The numbers in brackets for each model are the distances at which the efficiency equals 50% of the asymptotic value at small distances.

As discussed in Section 5.5, on-source events from each combination of CCSN, detector network, and pipeline are assigned a false alarm rate by comparing to time-slide background events. Table 5.4 lists the FAR values of the loudest event found by each pipeline for each network and CCSN. The lowest FAR, 1.7×10^{-6} Hz, was reported by cWB for the analysis of SN 2007gr with the H1H2L1V1 network. This rate can be converted to a false alarm probability (FAP) using equation (4.58). The total duration of data processed by cWB or X-Pipeline for the two CCSNe was $T_{\rm on} = 873461$ s. Equation (4.58) then yields a false-alarm probability of 0.77 for the loudest event; this is consistent with the event being due to background noise. We conclude that none of the events has a FAP low enough to be considered as a candidate GW detection.

We note that the loudest events reported by cWB and X-Pipeline are both from the analysis of SN 2007gr with the H1H2L1V1 network; this is consistent with chance as this network combination accounted for more than 60% of the data processed. In addition, the times of the loudest X-pipeline and cWB events differ by more than a day,

5.6.1 Detection efficiency vs. distance

Given the loudest event, we can compute detection efficiencies for the search following the procedure detailed in Section 5.5.3. In brief, we measure the fraction of simulated signals that produce events surviving the coherent tests and data quality cuts and which have a FAR (or equivalently FAP) lower than the loudest event.

Figures 5.10 and 5.11 show the efficiency as a function of distance for the CCSN waveforms from multi-dimensional simulations and the phenomenological waveforms discussed in Section 5.5.3 and summarized in Tables 5.5 and 5.6. For SN 2007gr, the maximum distance reach is of order 1 kpc for waveforms from detailed multi-dimensional CCSN simulations, and from ∼100 kpc to ∼1 Mpc for GWs from the phenomenological models (torus fragmentation instability and long-lived rotating bar mode). The variation in distance reach is due to the different peak emission frequencies of the models and the variation in detector sensitivities with frequency, and is easily understood in terms of the expected signal-to-noise of each waveform relative to the noise spectra of Figure 5.8. For example, the distance reach for the Yakunin waveform is similar to those of the Müller waveforms even though the Yakunin energy emission is more than two orders of magnitude higher; this is due to the emission being at much higher frequency where the detectors are less sensitive. Similarly, of the three Müller waveforms the distance reach is largest for Müller1 because the peak frequency is 150 Hz, where the LIGO detectors have best sensitivity.

The distance reaches for SN 2011dh are lower by a factor of several than those for SN 2007gr; this is due to the difference in sensitivity of the operating detectors, as also evident in Figure 5.8. Finally, we note that at small distances the efficiencies asymptote to the fraction of the on-source window that is covered by coincident data, approximately 93% for SN 2007gr and 37% for SN 2011dh (up to a few percent of simulated signals are lost due to random coincidence with data quality cuts).

We do not show the efficiencies for the multi-dimensional simulation CCSN waveforms for SN 2011dh, as the detection efficiency was negligible in this case. This is due to the fact that the relative orientation of the G1 and V1 detectors – rotated approximately 45° with respect to each other – means that the two detectors are sensitive to orthogonal GW polarizations. In order for the coherent cuts to reject background noise X-Pipeline needs to assume some relationship between these two polarizations. We require that the h_+ and $h_\times$ polarizations are out

of phase by 90°, as would be expected for emission from a rotating body with a non-axisymmetric quadrupole deformation. We choose this because the strongest GW emission models are for rotating non-axisymmetric systems (the fragmentation instability and long-lived bar mode). Unfortunately, the waveforms from multi-dimensional CCSN simulations are either linearly polarized (i.e. have only one polarization) or exhibit randomly changing phase. Hence, they cannot be detected by the search performed for SN 2011dh with X-PIPELINE. The tuning of CWB did not use these constraints, however the G1 noise floor was about a factor of 2 higher than V1 around 1000 Hz and the difference was even greater at lower frequencies. This issue weakened the internal CWB measures of correlation of the reconstructed signal between the two interferometers and severely reduced the detection efficiencies at distances beyond a few parsecs.

The distances shown in Figures 5.10 and 5.11 show the probability of a GW signal producing an event with FAP lower than that of the loudest event. The physical interpretation of the efficiency ϵ at a distance d for a given model is related to the prospect of excluding the model with observations. Explicitly, the non-observation of any events with FAP lower than the loudest event gives a frequentist exclusion of that GW emission model for a source at distance d with confidence ϵ. However, in this search the loudest event had a large FAP (0.77). In order for an event to be considered as a possible detection it would need to have a FAP of order 10^{-3} or less; we find that imposing this more stringent requirement lowers the maximum distance reach by approximately 5%-25% depending on the waveform model.

Unfortunately, none of the models have distance reaches out to the ∼10 Mpc distance of SN 2007gr or SN 2011dh; we conclude that our search is not able to constrain the GW emission model for either of these CCSNe.

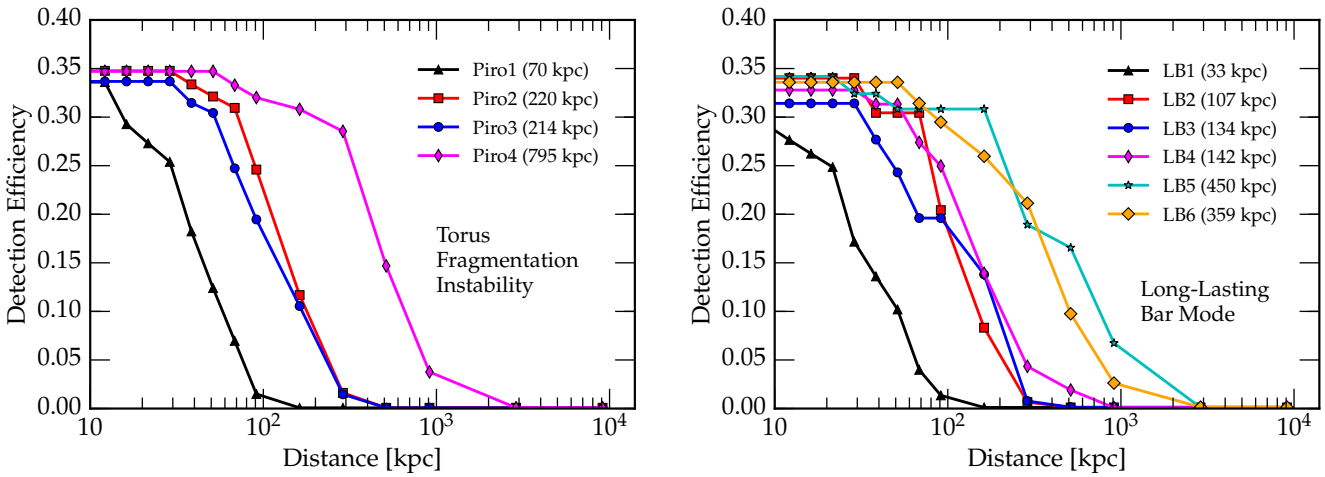

Figure 5.11: SN 2011dh detection efficiency versus distance for the phenomenological waveforms described in Table 5.6. Simulated GW signals are added into detector data with a range of amplitudes corresponding to different source distances. A simulated signal is considered detected if either CWB or X-PIPELINE reports an event that survives the coherent tests and data quality cuts with a FAR value lower than that of the loudest event from the SN 2007gr and SN 2011dh on-source windows. The efficiencies are limited to $\leq 37\%$ at small distances due to the fact that this was the duty cycle for coincident observation over the SN 2011dh on-source window; some simulations are also vetoed by data quality cuts. The numbers in the brackets are the distances at which the efficiency equals 50% of its maximum value for each model.

5.6.2 Constraints on Energy Emission

In addition to the astrophysically motivated phenomenological and multi-dimensional CCSN simulation waveforms, we employ the *ad-hoc* sine-Gaussian waveforms specified by equations (5.7) and (5.8) to establish frequency-dependent upper limits on the emitted energy in GWs. This also allows us to compare the sensitivity of our targeted search with results from previous all-sky searches for GW bursts (e.g., [114, 120, 155])

The detection efficiency is computed using the same procedure as for the other waveforms. However, since these *ad hoc* waveforms have no intrinsic distance scale, we measure the efficiency as a function of the root-sum-square amplitude $h_{\rm rss}$, defined by equation (5.6). If we use the sin-Gaussian of a SASI component of a SN a certain amplitude is equivalent to a specific distance. For this study, we use the two sine-Gaussian waveforms described in Section 5.5.3, which have central frequencies of 235 Hz and 1304 Hz. These are standard choices for all-sky burst searches [155]. Table 5.7 lists the $h_{\rm rss}$ values at which the efficiency reaches half of its maximum value. Note that we use the half-maximum efficiency rather than 50% efficiency here, since the maximum efficiency is limited by the fraction of the on-source window that is covered by coincident data. The half-maximum gives a measure of the distance reach of the instruments independent of their duty cycle.

These $h_{\rm rss}$ values can be converted to limits on energy emission by assuming a specific angular emission pattern of the source [35]. For simplicity, we assume isotropic emission, for which

$$E_{\rm GW} = \frac{\pi^2 c^3}{G} D^2 f_0^2 h_{\rm rss}^2 \,. \tag{5.9}$$

Here f_0 is the peak frequency of the GW and D is the distance of the source. We use distances of 10.55 Mpc for SN 2007gr and 8.40 Mpc for SN 2011dh. Table 5.7 also lists the energy emission values at which the efficiency reaches half of its maximum value. If the total amount of energy emitted in GWs was larger than the numbers quoted in the table, we would have had a greater than 50% chance of seeing a signal from the CCSN at the estimated distance, provided coincident observation with the most sensitive detector network. Note, however, that the on-source window did not have 100% coverage (see Section 5.4).

The most stringent constraints are a few percent of a mass-energy equivalent of a solar mass emitted in GWs at 235 Hz, where the noise floor is low. The 1304 Hz results indicate that with this data set, we should not expect to be able to detect extra-Galactic GWs at kHz frequencies, since the limits are less stringent, $O(10)\ M_\odot c^2$ or more.

The above results can be compared with the energy available in CCSNe, which are powered by the gravitational energy released in core collapse. The total available energy is set by the binding energy of a typical $1.4\,M_\odot$ neutron star and is roughly 3×10^{53} erg, corresponding to $\sim 0.15\,M_\odot c^2$ (e.g., [161]). The observation of neutrinos from SN 1987A confirmed that ~99% of that energy is emitted in the form of neutrinos in proto-neutron star cooling (e.g., [162]). The typical CCSN explosion kinetic energy is $\sim 10^{51}$ erg ($\sim 10^{-3}\,M_\odot c^2$). Considering these observational constraints, the energy emitted in GWs is unlikely to exceed $O(10^{-3})\,M_\odot c^2$. Hence, the energy constraints obtained by this search for SNe 2007gr and 2011dh are not astrophysically interesting.

5.6.3 Standard Candle Model Exclusion Confidence

As we have seen, it is unlikely that we will have coincident science-quality data covering an entire multi-day on-source window for any given CCSN. In the present analysis, the coverage of the on-source windows is approximately

Table 5.7: Gravitational-wave energy emission constraints at half-maximum detection efficiency for SN 2007gr and SN 2011dh. These assume distances of 10.55 Mpc for SN 2007gr and 8.40 Mpc for SN 2011dh.

Waveform	SN 2007gr			SN 2011dh		
	$h_{\rm rss}$ [Hz$^{-1/2}$]	$E_{\rm GW}$ [erg]	$E_{\rm GW}$ [$M_\odot c^2$]	$h_{\rm rss}$ [Hz$^{-1/2}$]	$E_{\rm GW}$ [erg]	$E_{\rm GW}$ [$M_\odot c^2$]
SGel2 SG235Q9	5.4×10^{-22}	$6.7{\times}10^{52}$	0.038	9.1×10^{-21}	$1.2{\times}10^{55}$	6.8
SGlin2 SG235Q9	6.6×10^{-22}	$1.0{\times}10^{53}$	0.058	4.8×10^{-20}	$3.4{\times}10^{56}$	$1.9{\times}10^{2}$
SGel2 SG1304Q9	2.1×10^{-21}	$3.1{\times}10^{55}$	17	2.2×10^{-21}	$2.3{\times}10^{55}$	13
SGlin2 SG1304Q9	2.5×10^{-21}	$4.6{\times}10^{55}$	26	n/a	n/a	n/a

93% for SN 2007gr and 37% for SN 2011dh. Considering that data-quality cuts typically remove another few percent of livetime, we cannot expect to exclude even fairly strong GW emission at the 90% confidence level for a single CCSN. In simple terms, if we have a detection efficiency equal to 90% then we can claim that the model is wrong with 90% confidence if we did not make a detection. It is important to point out though that when we use loudest event efficiencies which involve thresholds that no event was able to pass in the zero lag data. However, by combining observations of multiple CCSNe, it is straightforward to exclude the simple model in which all CCSNe produce identical GW signals; i.e., assuming *standard-candle* emission.

Consider a CCSN model $M_{\rm SN}$ which predicts a particular GW emission pattern during the CCSN event (e.g., one of the waveforms considered in Section 5.5.3). In the case that no GW candidates are observed, we can constrain that model using observations from multiple CCSN events at known distances d_i using the measured detection efficiencies $\epsilon_i(d_i)$ for each supernova (e.g., as in Figure 5.10). These $\epsilon_i(d_i)$ can be combined into an overall model exclusion probability [163], $P_{\rm excl}$:

$$P_{\rm excl} = 1 - \prod_{i=1}^{N} (1 - \epsilon_i(d_i)) \tag{5.10}$$

It is also straightforward to marginalize over uncertainties in the d_i (as in Table 5.2) by the replacement

$$\epsilon_i(d_i) \to \epsilon_i \equiv \int_0^\infty d\bar{d}\, \pi_i(\bar{d}) \epsilon_i(\bar{d}) \tag{5.11}$$

where π_i is our prior on the distance to CCSN i (e.g., a Gaussian).

In the light of the measured sensitivity ranges in Figures 5.10 and 5.11, it is clear that we cannot exclude any of the considered models of GW emission for SN 2007gr and SN 2011dh with the current data. However, LIGO and Virgo were upgraded to advanced configurations, with a final design sensitivity approximately a factor of ten better than for the period 2005-2011 considered in this paper. It is therefore instructive to consider what model exclusion statements the advanced detectors will be able to make using CCSNe similar to SN 2007gr and SN 2011dh. The extrapolation of our results to Advanced LIGO / Advanced Virgo design sensitivity indicates that waveforms predicted by multi-dimensional CCSN simulations will be individually detectable only to distances of $O(10)$ kpc. We therefore focus on the phenomenological waveform models of plausible but more extreme GW emission, where we expect to reach sooner large standard candle model exclusion probabilities. Specifically, we analyze the rotating bar and torus fragmentation scenarios (see also the discussion in [2]).

Figure 5.12 presents model exclusion confidence plots for four of the phenomenological waveform models. These

plots are based on the measured efficiencies for SN 2007gr and SN 2011dh, but assume the detector noise spectra have been lowered by a factor of A, so the search would be expected to have the same efficiency for a particular source at A-times the distance, and the number of CCSNe in the sample has been increased by a factor of p. For example, $A = 10$ represents having a sensitivity 10 times better than the 2005–2011 data, which is realistic for Advanced LIGO and Advanced Virgo, while $p = 2$ corresponds to having two CCSNe similar to SN 2007gr and two similar to SN 2011dh. The curves correspond to the experimentally derived values based on the 2005-2011 data set. It is worth stressing that the power of excluding models from this data set almost exclusively originates from SN 2007gr, given the more sensitive interferometers available at the time of that supernova. For example, in the bottom left panel of Fig. 5.12, the curves, when A is smaller than 9, depend almost exclusively on the contribution of SN 2007gr. In this regard, the presented model exclusion probabilities will be reached with less than $2p$ CCSNe if the sample contains more data sets comparable in coverage and sensitivity to the rescaled SN 2007gr data set than a rescaled SN 2011dh data set. In summary, Fig. 5.12 shows that it is a reasonable expectation that extended coincident observations with advanced-generation detectors will rule out extreme CCSN emission models.

5.6.4 Sensitivity Advantage of the Triggered Search

As noted in Section 5.1, targeted searches have the advantage over all-time all-sky searches that potential signal candidates in the data streams have to arrive in a well-defined temporal on-source window and have to be consistent with coming from the sky location of the source. Both constraints can significantly reduce the noise background. Here we assess the improved sensitivity of a triggered search by comparing our $h_{\rm rss}$ sensitivities to linearly polarized sine-Gaussian waveforms for SN 2007gr to those of an all-sky search of the same data.

The most straightforward way to compare two searches is to fix the FAR threshold and compare the $h_{\rm rss}$ values at 50% efficiency. The S5/VSR1 all-sky all-time search [120] using cWB was run on 68.2 days of coincident H1H2L1V1 data with thresholds to give a FAP of 0.1 or less in the frequency band up to 2000 Hz. The livetime for the cWB SN 2007gr analysis of the H1H2L1V1 network was 3.25 days, so a FAP of 0.1 corresponds to a FAR of 3.56×10^{-7} Hz. Including calibration and Monte Carlo uncertainties, the $h_{\rm rss}$ values at 50% efficiency for this FAR are $5.0 \times 10^{-22}\,{\rm Hz}^{-1/2}$ at 235 Hz and $2.2 \times 10^{-21}\,{\rm Hz}^{-1/2}$ at 1304 Hz. After adjusting for systematic differences in the antenna responses and noise spectra[1] between the S5/VSR1 all-sky search and the SN 2007gr search, the effective all-sky $h_{\rm rss}$ values are $7.0 \times 10^{-22}\,{\rm Hz}^{-1/2}$ at 235 Hz and $2.9 \times 10^{-21}\,{\rm Hz}^{-1/2}$ at 1304 Hz, approximately 30% to 40% higher than the targeted search. Equivalently, the distance reach of our targeted search is larger than that of the all-time all-sky search by 30% to 40% at this FAP.

Alternatively, we can compare the two searches without adjusting to a common FAR. After allowing for systematic differences in the antenna responses and noise spectra between the S5/VSR1 all-sky search and the SN 2007gr search, we find that the $h_{\rm rss}$ values at 50% efficiency are identical (to within a few percent). However, the FAR of the SN 2007gr search is lower by an order of magnitude: 1.8×10^{-9} Hz compared to 1.7×10^{-8} Hz for the all-sky search. This is consistent with expectations for restricting from an all-sky search to a single sky-position search. Furthermore, the FAP for a trigger produced by the SN 2007gr search will be smaller than that of a trigger from the all-sky search at the same FAR because the SN 2007gr on-source window (3.5 days for cWB and X-Pipeline combined) is a factor of 20 shorter than the all-sky window (68.2 days). So if we consider a surviving trigger that

[1] In particular, during the on-source window of SN 2007gr the noise spectral density for L1 was about 50 percent worse at low frequencies than the average value during the whole of S5.

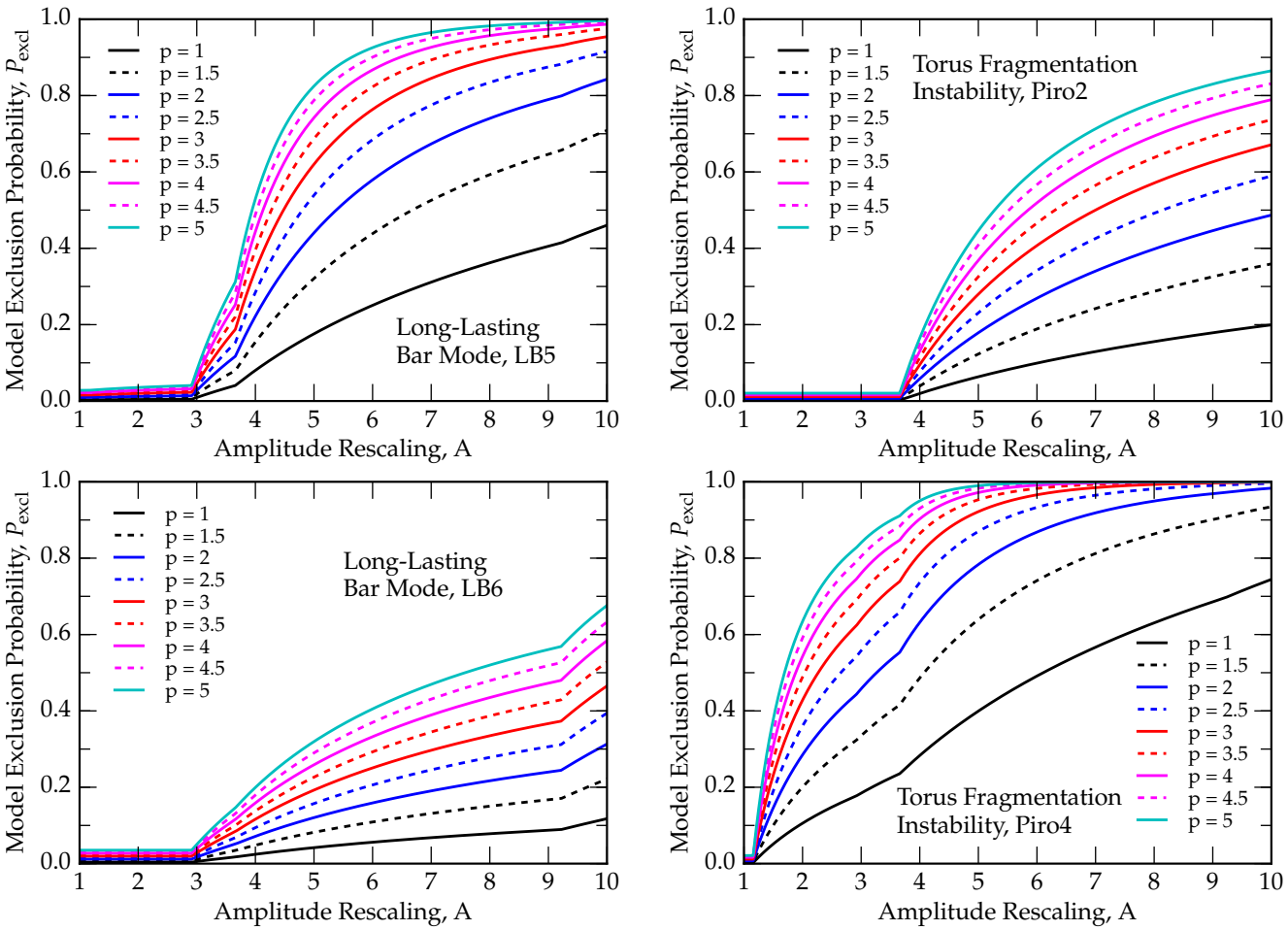

Figure 5.12: Expected model exclusion probabilities for example waveforms as a function of amplitude sensitivity rescaling, A, and supernova sample size rescaling, p, based on the SN 2007gr and SN 2011dh sample (e.g. $p = 5$ corresponds to 10 supernovae). The naming convention is described in Table 5.6. Currently none of the emission models can be exluded, but for the advanced detectors with better sensitivity and more nearby CCSNe it is realistic to expect to rule out some of the extreme emission models.

is just above threshold in the two searches, the SN 2007gr trigger will have an FAP a factor of approximately 200 lower than an all-sky trigger with the same $h_{\rm rss}$.

5.7 Summary and Discussion

We presented the results of the first LIGO-GEO-Virgo search for gravitational-wave (GW) transients in coincidence with optically detected core-collapse supernovae (CCSNe) observed between 2007 and 2011. Two CCSNe, SN 2007gr and SN 2011dh, satisfied our criteria of proximity, well-constrained time of core collapse, and occurrence during times of coincident high-sensitivity operation of at least two GW detectors. No statistically significant GW events were observed associated with either CCSN.

We quantified the sensitivity of the search as a function of distance to the CCSNe using both representative

waveforms from detailed multi-dimensional CCSN simulations and from semi-analytic phenomenological models of plausible but extreme emission scenarios. The distances out to which we find signals detectable for SNe 2007gr and 2011dh range from $O(\lesssim 1)$ kpc for waveforms from detailed simulations to $O(1)$ Mpc for the more extreme phenomenological models. From the known distances of our two target supernovae, we estimated the minimum energy in gravitational waves corresponding to our sensitivity limits using *ad-hoc* sine-Gaussian waveforms. These range from $O(0.1)\, M_{\odot}c^2$ at low frequencies to $\gtrsim O(10)\, M_{\odot}c^2$ above 1 kHz.

This first search for GWs from extragalactic CCSNe places the most stringent observational constraints to-date on GW emission in core-collapse supernovae. A comparison of our search's sensitivity with the standard all-sky, all-time search for generic GW bursts in the same GW detector data shows a 35%-40% improvement in distance reach at fixed false alarm probability. This improvement comes from knowledge of the sky positions of the CCSNe and approximate knowledge of the collapse times. It is, hence, clearly beneficial to carry out targeted searches for GWs from CCSNe.

The results of our search do not allow us to exclude astrophysically meaningful GW emission scenarios. We have extrapolated our results to the sensitivity level expected for Advanced LIGO and Virgo. Considering the improved detector sensitivity and assuming the analysis of multiple CCSNe, we find that at design sensitivity (c. 2019, [164]) this network will be able to constrain the extreme phenomenological emission models for extragalactic CCSNe observed out to distances of $\sim$10 Mpc. Detection of the most realistic GW signals predicted by multi-dimensional CCSN simulations will require a Galactic event even at the design sensitivity of the Advanced detectors. These are consistent with the results of the study in [2], which used data from iLIGO and Virgo recoloured to match the advanced detector design sensitivities. We conclude thatthird-generation detectors with a sensitivity improvement of a factor of $10 - 20$ over the Advanced detectors may be needed to observe GWs from extragalactic CCSNe occurring at a rate of $1 - 2$ per year within $\sim$10 Mpc.

Chapter 6

Low Energy Neutrino Triggered Search

In this section I will present some of the results of the joint search of GW and Low Energy Neutrinos.

6.1 Introduction

Gravitational Waves are the only messengers that can probe the inner of a Core-Collapse Supernova. GW carry primarily information about the multi-dimensional dynamics of the central engine while neutrinos carry information about the theromdynamics information. Coincident detection with the next nearby supernova will bring unique chance to increase our knowledge in astrophysics, nuclear and neutrino physics of a stellar collapse. Moreover, joint search might reveal core collapses that will not be visible in opticla spectrum g for CCSN obscured by Galactic dust, failed supernovae, BH formation, collapsars or exotic Quark Novae.

Common feature for these events is a large flux of leaving neutrinos. Energy of a core-collapse is about $1 - 5 \times 10^{53}$erg and 99% of this energy escapes with neutrinos. Majority of the neutrinos leave the collapsed core during first 10s after the collapse.

We expect that only small number of netrinos are detected by neutrino detectors. This is a consequence of the Poissonian statistics.

For a Galactic Supernova we expect a shower of neutrinos. In this analysis we focus on the subthreshold neutrino events detected by neutrino detectors. These low statistics neutrino fluxes might come from distant supernovae that we do not observe optically. These supernovae might be visible in the GW spectrum. Given that neutrino and GW are emitted around very small time window, we might detect a coincidence between subthreshold neutrino and GW events.

In this joing analysis we analyze archival data from LVD, Borexion and IceCube neutrino detectors, as well as LIGO/Virgo data from Science Runs between 2005 and 2010.

6.1.1 Joint statistics

The background analysis based on shifting the data from one detector with respect to another (see section 4.5.1) identifies False Alarm Rate (FAR) for earch GW and neutrino trigger, FAR_{GW} and FAR_{nu} respectively. A joint

FAR, $FAR_{\rm joint}$ can be written as [165]:

$$FAR_{\rm joint} = FAR_{\rm GW} \times FAR_{\rm nu} \times 2 \times T_{\rm coinc}, \tag{6.1}$$

where $T_{\rm coinc}$ is a window of coincidence between GW and neutrino events. The neutrino emission in supernova lasts around 10s so we choose $T_{\rm coinc} = 10$s.

We choose thresholds to be $FAR < 1$/day for LVD, Borexino and LIGO/Virgo detectors, $FAR < 10$/day for IceCube detector. This gives joint FAR to be $FAR_{\rm joint} < 1/(12{\rm years})$ for LVD/Borexino and LIGO/Virgo detectors and $FAR_{\rm joint} < 1/(1{\rm years})$ for IceCube and LIGO/Virgo detectors.

6.2 Neutrino detectors and neutrino triggers

Expected flux of neutrinos:

$$\mathcal{F}_\nu = \frac{E}{6\langle E_\nu \rangle} \frac{1}{4\pi D^2} \tag{6.2}$$

where E is an energy of explosion of a core collapse, $\langle E_\nu \rangle$ is an average energy of neutrinos, typically $10 - 15$MeV and D is the distance to the source. Neutrinos interact weakly with matter. This allows them to go through the Earth without scattering, but unfortunately it also means that they are not easily detectable. Larger detectors have better chance of detecting neutrinos due to their volume. The largest neutrino detector is Super Kamiokandze built in Kamioka mountain in Japan. For Super Kamiokandze we expect to detect O(10,000) for a Galactic event at 10kpc and O(100) of neutrinos for a extragalactic CCSN at 100kpc.

In this search we analyze data from smaller neutrino detectors such as LVD and Borexino. We also analyze data from IceCube that is primarily detector of high energy neutrinos, but it has also capabilities to detect low energy neutrino fluxes from supernovae. The neutrino events are clusters of few low energy neutrinos staning above background that happened within a 20s window.

LVD Large Volume Detector (LVD) is a neutrino detector based in San Grasso in Italy [166]. The detector consistst of ~ 1000 tons of liquid scintillator. It can detect both neutral current and charged current interactions. Average neutrino energy threshold is 5MeV. During the search we used data from November 2005 through October 2007 and from July 2009 through October 2010;

Borexino Borexino [167] is a liquid scintillator neutrino detector that is viewed by photomultipliers (PMTs). It is shielded by a water tank to protect from external radiation and tag cosmic muons. An event is obtained when a selected number of PMTs detect at least one hit within a time window of typically 90ns. The detector is able to reconstruct position of an event (based on triangulation) and its energy (based on the number of PMTs hits and/or the charge). During the search we used data from December 2009 through October 2016;

IceCube IceCube neutrino observatory that looks for violent events in the Unievrse, like supernovae [168]. It is a cubic-kilometer detector build in Antarctic ice, buried beneath the surface and reaching a depth of about 2.5 km. During the search we used data from December 2009 through December 2014;

6.3 GW triggers

In this search we analyzed LIGO/Virgo data from November 2005 through October 2007 and from July 2009 through October 2010. Total livetime is 462.59 days. Table 6.2 shows all analyzed periods and detector networks. LIGO Science Run number 5 (S5) lasted 2 years and during the first year (S5Y1) only LIGO detectors were taking Science data. During the second year (S5Y2) both LIGO and Virgo detectors were on-line. In order to maximize time of this search we considered various networks of detectors and taking exclusive times. During S6 we analyzed four periods, S6A, S6B and S6D periods using LIGO/Virgo data and S6C using only LIGO data.

6.3.1 Sky location reconstruction

In this search we consider potential supernovae that occured nearby and they are not visible optically. We will search within a Galactic plane. For this purpose the reconstructed sky location of the GW triggers needs to be located in the Galactic plane.

Figure 6.1 shows an example of galactic skymask in celestial coordinates. The area of the skymask is around 16%. We consider a network of L1, H1 and V1 detectors and the archival S5/S6 data. The right panel of figure 6.1 shows that the distribution noise triggers is uniform over the sky. This gives potentially an advantage of removing around 6× more triggers comparable to the all-sky search.

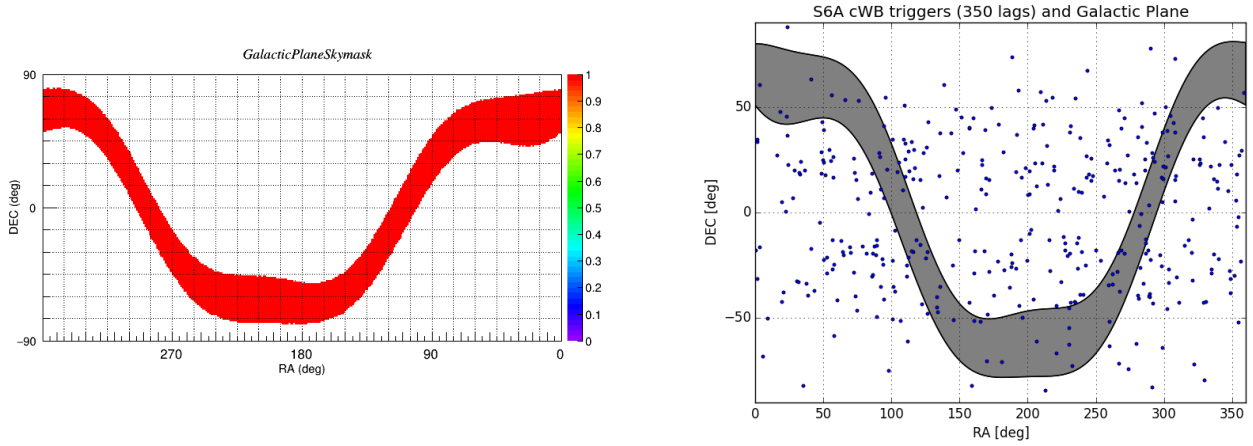

Figure 6.1: Left: Galactic Plane Skymask in celestial coordinates. This skymask area is around 16% of the total sky area. Right: The distribution of reconstructed noise triggers for L1H1V1 network.

On the other side, we need to consider how well the cWB reconstructs the sky location. We add the SN waveforms to the detector noise and estimate how well the sky location is reconstructed. We consider here the L1H1V1 network of GW detectors during S6A-VSR1 period. Several realistic waveform morphologies were tested, see table 6.1 for the list of waveforms. The left panel in figure 6.2 shows how the error in reconstruction of sky localization changes with the injected SNR. For the waveforms injectd with SNR=15 the error in the reconstructed angle is 48.3 degrees.

Moreover the error increases when the signal is weaker. We notice that the error of the reconstructed angle is larger than the width of the Galactic plane. This study was done with 3-detector network, we expect even worse

result with 2-detector network. In this case the usage of a skymask will harm the detectability of SN waveforms more than the benefit of removing noise events. In the final results the galactic Skymask is not used.

Another item under consideration is the overall reconstruction of SNR. In this joint search we are considering the subthreshold GW and neutrino triggers with low SNR. Right panel in figure 6.2 shows how well the alorithm is able to reconstruct the injected SNR. The reconstructed SNR agrees overall with the injected SNR. It is worth to mention that the minimum detecable SNR is ~ 10. In this study one of the issue is the reconstruction of very loud injections with very low SNR. Potential cause is that the algorithm detect two very nearby events. Another issue is the reconstruction of very weak injections. This might be caused by the fact that some waveforms are injected at the time when a glitch occured and the glitch is reconstructed.

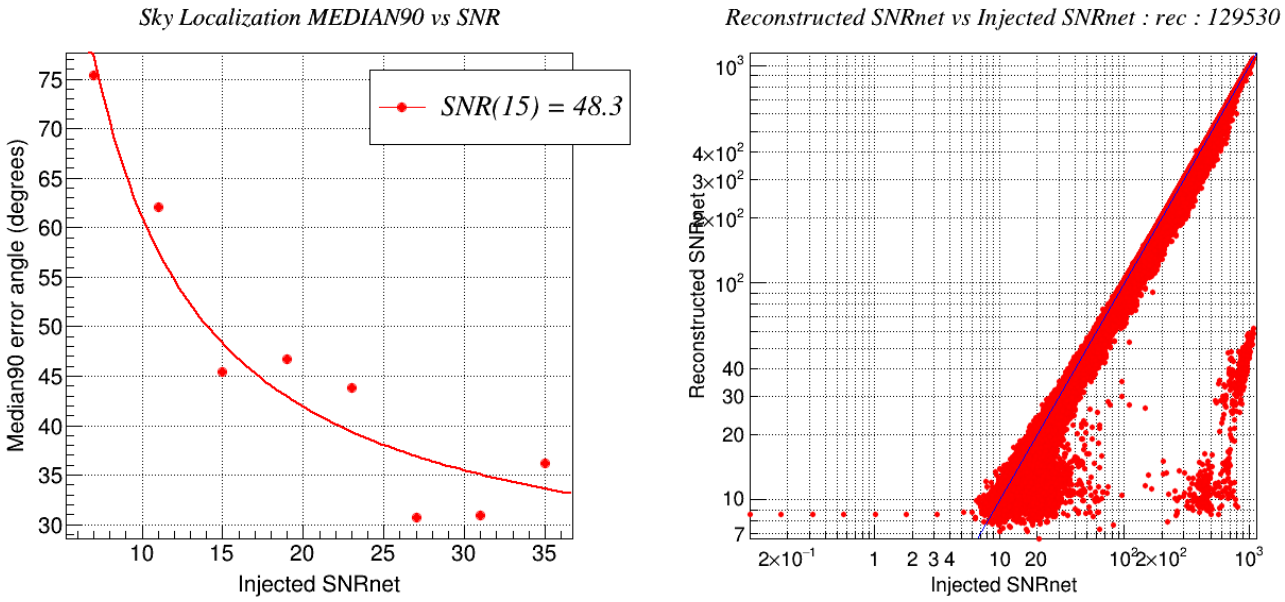

Figure 6.2: Reconstruction of SN waveforms studies with L1H1V1 network with S6A and VSR1 data. Left: Sky localization error. Right: Comparison btween reconstructed and injected network SNR.

6.3.2 Visible distances

We performed a study of visible distance for different SN models. The visible distance is defined as the distance at 50% detection efficiency level. Table 6.1 constains studied morphologies and shows the results. We consider the realistic neutrino and magnetorotationally driven explosions as well two models of BH formation. For the most realistic models, the visible distance does not exceed a distance of 1kpc, while for MHD driven explosions the visible distance is of an order of few kpc. A similar range of few kpc is for the BH formation model. These visible distances show that if we have Supernova in our Galaxy that we do not see optically, we might see a large flux of neutrinos while no GW would be detected. However, as metioned in the introduction to this search, various other scenarios might happen that we need to be prepared for.

Table 6.1: Visible distance study for various SN morphologies. Two data sets were used: S5Y1 (first year of S5 Science run, here 20 days of data were used) and S6A.

Explosion mechanism	Waveform identifier	S5Y1, dist [kpc]	S6A, dist [kpc]
Neutrino driven explosions	yak1/yak2/yak3/yak4	0.57/0.76/0.88/1.17	0.33/0.53/0.56/0.77
	ott1	0.58	0.37
	mul1/mul2/mul3	0.17/NaN/NaN	0.20/0.13/0.12
MHD driven explosions	sch1/sch2/sch3	0.06/3.31/3.45	0.08/6.58/7.13
	dim1/dim2/dim3	1.04/1.40/1.97	NaN/1.99/2.58
BH Formation	cer1/cer2	4.06/NaN	6.76/1.79

6.4 Search Results

Table 6.2 shows the number of GW triggers for the particular periods of S5 and S6 Science Runs. The total number of analyzed GW events is 436.

Three neutrino and GW networks were analyzed and only one coincident event was found:

- LVD and LIGO/Virgo - no coincident event
- Borexino and LIGO/Virgo - no coincident event
- IceCube and LIGO/Virgo - one coincident event

This event is analyzed further.

Table 6.2: Triggers produced for the coincident search, FAR = 1/day.

Row	Science Run	Network	Pediod	Coincident data	Nr of events
1	S5Y1	L1H1H2	Nov 4, 2006 - Nov, 14, 2007	140.82 days	131
2	S5Y2	L1H1H2V1	Nov 14, 2006 - Nov 08, 2007	62.21 days	71
3	S5Y2	L1H1H2	Nov 14, 2006 - Nov 08, 2007	111.40 days	111
4	S5Y2	V1H1H2	Nov 14, 2006 - Nov 08, 2007	12.10 days	11
5	S5Y2	L1H1V1	Nov 14, 2006 - Nov 08, 2007	2.54 days	4
6	S5Y2	H1H2	Nov 14, 2006 - Nov 08, 2007	30.81 days	5
7	S5Y2	L1H1	Nov 14, 2006 - Nov 08, 2007	3.67 days	3
8	S5Y2	L1H2	Nov 14, 2006 - Nov 08, 2007	1.75 days	1
9	S5Y2	L1V1	Nov 14, 2006 - Nov 08, 2007	3.98 days	3
10	S6A	L1H1V1	2009, Jul 8 - Aug 30	9.35 days	9
11	S6B	L1H1V1	2009, Sep 26 - 2010 Jan 8	14.04 days	10
12	S6C	L1H1	2010 Jan 8 - Jun 26	47.44 days	52
13	S6D	L1H1V1	2010 Aug 11 - Oct 19	22.48 days	25

6.4.1 Coincident event

During the search, none of the coincident events were found for LVD and LIGO/Virgo detectors, and Borexino and LIGO/Virgo detectors. However, one coincident event was found for IceCube and LIGO/Virgo detectors. This event was further analyzed and it is likely to be a coincident noise event.

The trigger was observed on October 6th, 2010 12:20:33 UTC by IceCube and 9s later in L1, H1 and V1 detectors, that is S6D Scienc run. It was found that:

- $FAR_{\mathrm{GW}} = 1/\mathrm{day}$
- $FAR_{\mathrm{nu}} = 8/\mathrm{day}$
- $FAR_{\mathrm{joint}} = 1/(2\mathrm{years})$

False Alarm Probability (FAP) is 0.083 which is $< 2\sigma$. Given this, the event is very likely to be induced by coincident noise events.

We considered also the properties of the GW trigger. Left panel of figure 6.3 shows the spectrogram of this event in Virgo detector and the right panel dopicts spectrogram in Livingston detector, while the bottom panel shows the pixels that are used in the reconstruction. The event is reconstructed to be narrowband, 100Hz wide, with peak frequency around 2kHz. In Virgo detector, the event is very well visible and it is wideband, 2000Hz wide. Most of the energy comes Virgo detector that is the least sensitive. For true GW most of the energy should appear in more sensitive detector. However it might be explained with antenna pattern - we do not know the true sky location of the source if this is a real GW. It seems that disproportionality of energy between the signals in the detectors can be explained by reasoning that there is a noise transient in Virgo detector that is coincident with noises of two LIGO detectors

6.5 Future perspectives

In this joint search on archival data it was possible to find interesting astrophysically results, however it was rather unlikely. Indeed, the final results confirm this statement. This search allowed to develop base methodology and test it against real data.

GW and neutrinos are the only probes of a stellar collapse and joint analysis might help in understanding the explosion mechanism. Future search development will depend on defining a common parameter space between GW and neutrino signals. For example, one of the physical parameters that might be probed is the evolution of proto-neutron star radius. The GW peak frequency for the first second after collapse grows over time due to decreasing size of the proto-neutron star. Pass one second after the collapse, the GW signal vanishes and for the next 10s the proto-neutron star goes through a cooling phase emitting neutrinos. The neutrino energies depend on the proto-neutron star that depends on the its size.

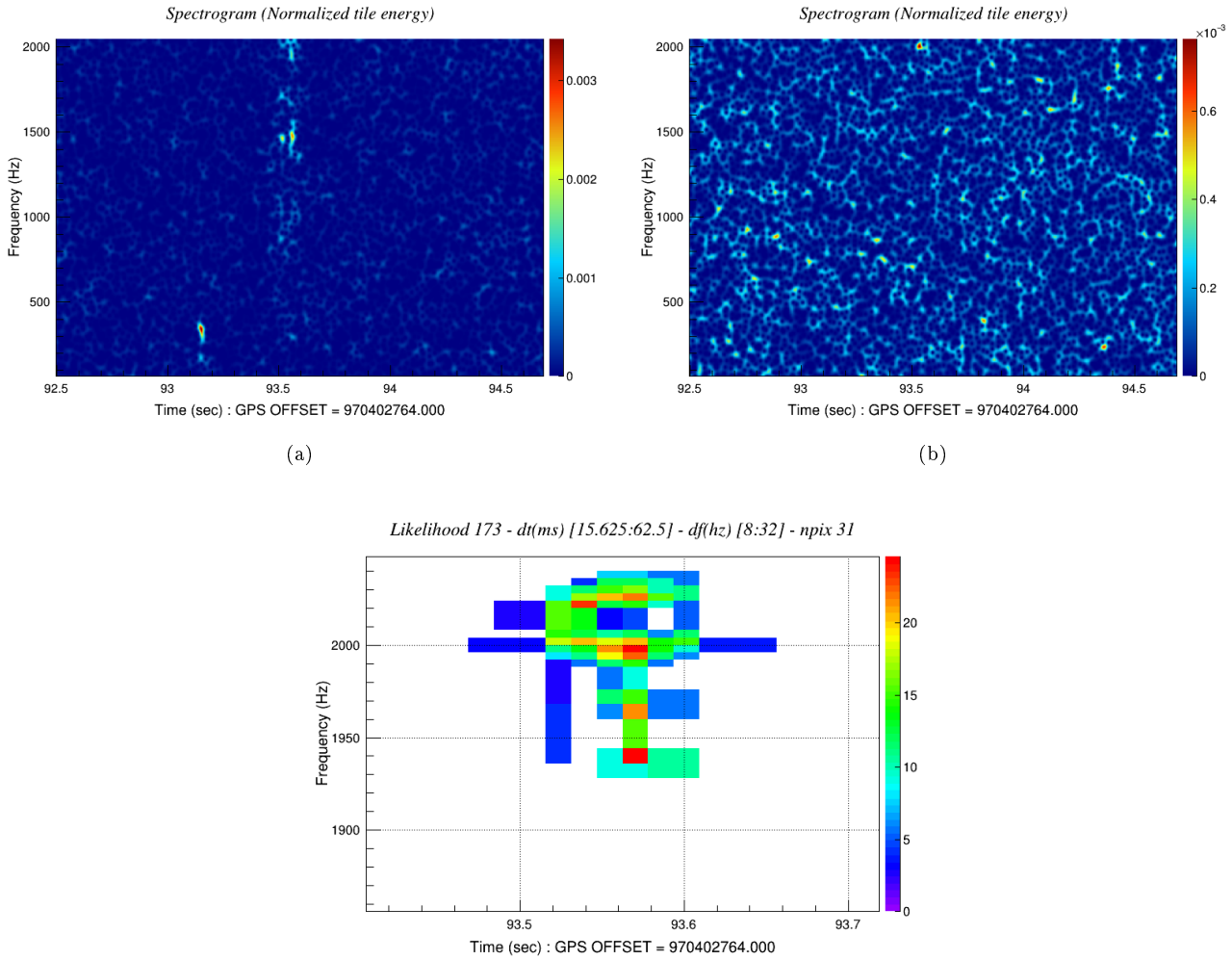

Figure 6.3: Properties of the GW trigger of the GW-neutrino coincident event. Left: Spectrogram of the event in Virgo detector. Right: Spectrogram of the event in Livingston detector. Bottom: Scalogram of coherent likelihood between L1, H1 and V1 detectors.

Part III

Advanced GW Detector Era

Chapter 7

Prospects for the Searches

In this chapter we will present a current status of estimating the rate of CCSNe in the Local Universe and the consequencies on the GW SN searches. This chapter is based on Gill K., Branchesi M., Zanolin M. and Szczepańczyk M. work in preparation *Gravitational Wave Astronomy Prospectives for Core-Collapse Supernovae Populations.*

A supernova in our Galaxy will be a very interesting event that hopefully will allow us to explore the dynamics of exploding stars. Unfortunately the rate of CCSNe in our Galaxy is only around one per century, so it is also imporant to understand how the cummulative CCNSe rate evolves with the distance from the Earth.

The study described here provides an updated intrinsic CCSN rate in the Local Universe within 20Mpc. This distance is of interest for GW SN Searches, previous rate estimates show that within enclosed volume, we expect few optical supernovae a year and that the GW detection range reaches these distances for some of the models. Previous estimates[169, 170, 171, 172] focus on far supernovae while we are interested in the most nearby ones. GWs can go through the matter practically without loosing energy while light can be scattered by a galactic dust. This fact gives a motivation to study the intrinsic supernovae rate versus the observed one. Previous rate estimates are have certain biases that we try to minimize. First part 7.1 contains brief overview of the methods estimating the rate of CCSNe in the local universe and the challenges. The secont part 7.2 describes the consequences of the estimated rate on the GW SN Searches.

7.1 SN Rate estimate

In the simplest approach to calculate the rate of CCSN, one needs to count the number of supernovae in a given volume and then divide by time of observations. In practice, however, this estmation approach has biases. There are several factors that can skew the estimates. The telescopes usually observe only part of the sky, the observations has to be done during the night, the sky can be covered by clouds. Also, the supernovae might not be visible, they can be obscured by the dust of the local galaxy or the supernova might be faint. All these factors need to be considered carefully when doing the estimate of the rate.

It was found that the rate of supernovae depends on the galaxy type and its luminosity. A common general approach to find the rate of CCSNe in a particular volume (volumetric rate) is to convert the rate of supernovae per galaxy type using the galaxy luminosity density. The rate of each galaxy is multiplied by local galaxy luminosity

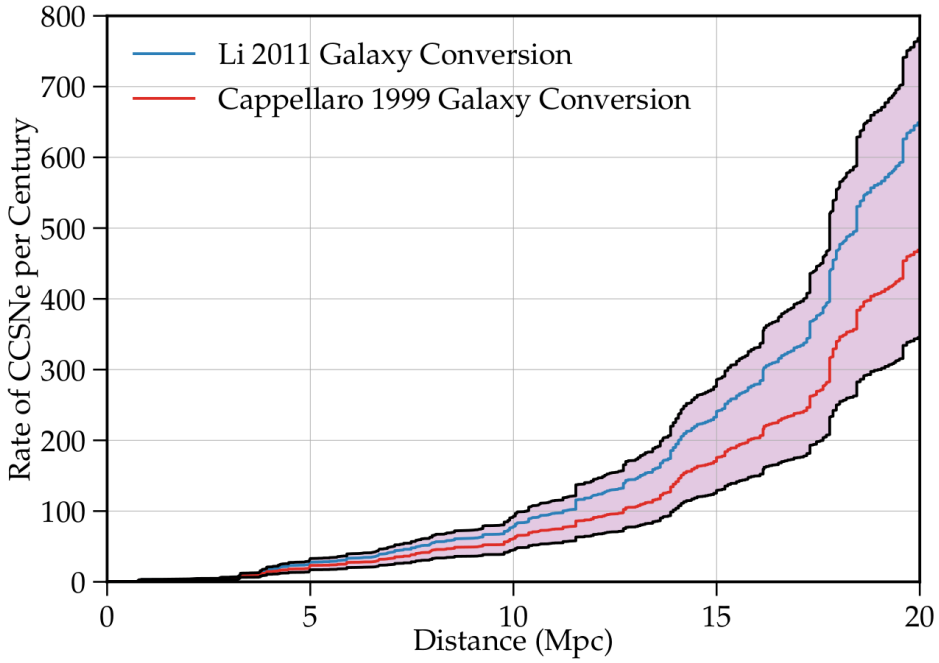

Figure 7.1: Cumulative CCSNe rate as a function of distance within 20 Mpc.

density according to the Hubble classification.

The approach typically followed to convert CCSN rate per galaxy type to a volumetric CCSN rate use the local galaxy luminosity density [173]. More precisely, the rates for galaxies of different morphology are multiplied for the local galaxy luminosity density of galaxies of different Hubble types [174]. The present work evaluates the single CCSN rate for a galaxy by galaxy case and obtains the volumetric rate as sum of each real local galaxy contribution up to 20 Mpc. This approach gives a more precise cumulative rate as a function of distance, which takes into account the spatial distribution of the local galaxies, also indicating the most likely location of the SN.

The nearby observed CCSNe rate comes from optical surveys carried out in the local universe over the past years. One of the key difficulties in obtaining accurate rate estimates is due to the fact that SNe are rare events. Therefore it is necessary to collect several years or decades of observations to reach a sufficient, robust statistic. Reference studies of local SN rate estimates were conducted by [169, 170, 171] and [172]. Cappellaro et al. 1999 (C99) [172] combined five surveys for a total number of 136 SN detections. More recently, the largest and most homogeneous set of 726 nearby SNe to evaluate the rate was assembled by the Lick Observatory Supernova Search (LOSS) which collected CCSNe detections over many years of surveys of galaxies within about 200 Mpc [175, 174, 176]. C99 and L11 correct the observed rate for the major selection biases, such as the nuclear bias (it is more difficult to discover a SN in the bright central region of a galaxy than in its outskirts) and the galaxy inclination bias (SNe occurring in the disk of inclined spirals appear on average fainter than those in face-on spirals because of the increased optical depth through the dust layer). The SN rates are typically normalized to the blue light (B-band) luminosity of the host galaxies and given for the different galaxy morphological type.

The methodology to estimate the intrinsic CCSN rate up to 20 Mpc, includes the data used and the adopted corrections for the methodology and observational biases (dust-obscuration in starburst galaxy, incompleteness of

galaxy morphology info, galactic plane galaxy obscuration, hidden/faint and dark SNe).

In Figure 7.1 we present the estimate of the intrinsic cummulative core-collapse supernovae rate up to 20Mpc from Earth, which is the largest distance of interest for the searches of their gravitational wave signals detectable by ground-based detectors in the near future. It gives an accurate cumulative rate as a function of distance and hint on the most probable host galaxies and regions of the sky where the GW signals of CCSNe can come from. The blue band is derived using the Li CCSNe rate, while the red band is derived using the Cappellaro CCSNe rate for different galaxy morphologies. The black band represents the upper and lower limits of the cumulative rate estimations. We evaluate a CCSN rate of $470.95^{+307.55}_{-123.16}$ and $657.91^{+120.59}_{-310.12}$ CCSNe per century within 20 Mpc using C99 and L11 conversion factors respectively.

7.2 Consequences to SN GW searches

7.2.1 SN Rate and False Alarm Rate

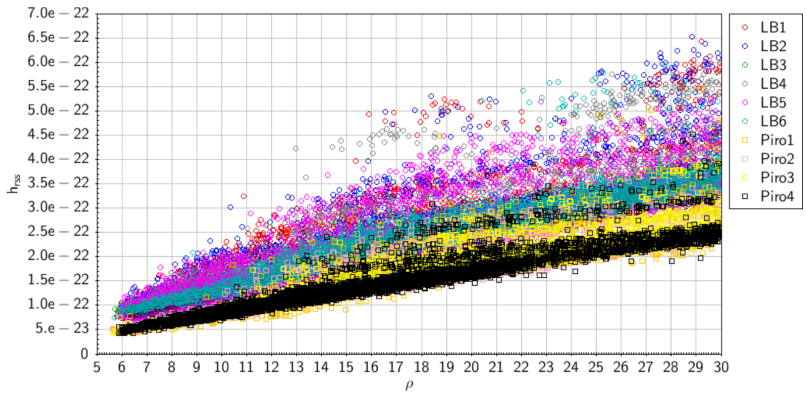

Figure 7.2: $h_{\rm rss}$ versus ρ conversion example for extreme emission models.

Figure 7.3 presents the comparison of an example of cummulative false alarm rate with respect to SNR for S5 data and rate of expected rate for a realistic SN model of emission. In order to estimate the expected rate versus ρ, we assume linear dependence between ρ and h_{rss} experimentally derived from cWB simulation, figure 7.2. To calculate the rate versus ρ we started from calculating h_{rss} of the waveform at a particular distance and then converting it into ρ.

Taking multiple sources within a volume of 20 Mpc with varying waveform morphologies, we rescale h_{rss} according to distance, convert distance to the appropriate ρ values based on realistic cWB simulations, and illustrate the relationship between the FAR with respect to the CCSNe rate. The slope of the noise events distribution and of the GW induced events appear to be different in this example. What this means is that if future runs have similar rate vs ρ distributions but lower average noise, the signal distribution would shift to the right that would eventually dominate the large ρ population. However, if the noise has a non-gaussian tail with a flatter slope then the signal would not change the overall shape of the loudest events population but could be still detectable with the population techniques searches.

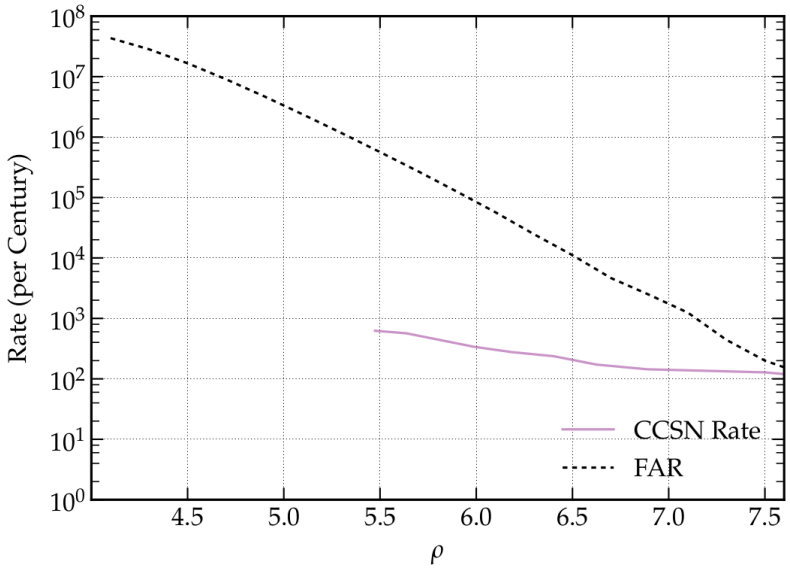

Figure 7.3: FAR versus cummulative rates comparison between a realistic GW background and realistic model of emission.

7.2.2 Model Exclusion Probability

In this section, we explore the implications for the the standard candle-model exclusion probability introduced in the iLIGO/Virgo CCSN search [17] in order to provide collective statements on a population of CCSNe triggers. We use the loudest event detection efficiencies for each of the individual CCSNe candidates in order compute the statistical confidence of successfully excluding an emission model [17].

Explicitly if the loudest event detection efficiency, P_i, for the CCSN trigger, i, that was at a distance $\mathrm{d_i}$, the MEP becomes [17]:

$$\mathrm{MEP} = 1 - \prod_{i=1}^{N}(1 - P_i(d_i)) \tag{7.1}$$

Table 7.1 shows how the predicted MEP for a model with average 50% loudest event detection efficiency changes during when the observational time increases and further illustrates how predicted MEP efficiency, realistically ranging from $10\% - 50\%$, changes for different number of SN triggers.

Table 7.1: Given multiple events (4 CCSN/year), this table illustrates how much MEP confidence is gained with observational time.

Observing Time	Number of CCSNe	$P_i(d_i)$ 10%	20%	30%	40%	50%
6 months	2 CCSNe	19%	36%	51%	64%	75%
1 year	5 CCSNe	41%	67%	83%	92%	97%
5 years	7 CCSNe	52%	79%	92%	97%	99%
10 years	15 CCSNe	79%	97%	99%	99%	99%

Chapter 8

Optically Triggered Search with O1-O2 LIGO/Virgo data

We report on a search for GWs from Core Collapse supernovae (CCSNe) in the local universe (within roughly 20 megaparsecs) with the specific constrain to be compatible with the optical observation of a CCSN.

The sensitivity studies in figure 5 of this paper represent the current detectability estimates for a number of emission models. These estimates are conservative since the information from the likely coincident neutrino detections (like the tight on-source window - tens of seconds or less) that would happen with a galactic CCSN are not folded in this analysis. Also, the estimates do not account for the planned sensitivity improvements, even if we comment on the expected perspectives for the detectability of a galactic SN with the design advenced interferometer sensitivties. In general GW astronomy for CCSNe is a challenging field both because the in band GW energy emission (see table V for a summary of the emission models used in this analysis) and for the rates that become of the order of a few per year only when reaching the Virgo cluster (or about 20 Megaparsecs).

The optimization of the detection and parameter estimation alghorithms is a necessity regardless of the distance of the CCSN, but the extraction of physical information has different idiosyncrasies for a Galactic SN source and multiple extragalactic SN scenarios. In this analysis we focus on optical CCSNe recorded during the first and second LIGO observational runs as well as the first Virgo observational run at distances rougly up to 20 megaparsecs. Similarly to [17], we derive standard candle model exclusion statements for a selection of waveforms which were computed from first principle numerical simulations and that are representative of different emission mechanisms and progenitors. We also use phenomenologican waveforms representing possible but somehow extreme emission models. Finally we also adopt had hoc sine Gaussians waveforms that can be used to quantify the emission in specific time frequency regions and that allow us to derive upper limits on the emitted GW from a specific SN.

Period	Name	Discovery Time [UT]	Host galaxy	D [Mpc]	Type	Included in Search?
ER8	SN 2015aq	2015/09/21.072	UGC 5015	22-26	IIP	No
ER8	iPTF15eqv	2015/09/27.811	NGC 3430	23.5	IIb	No
O1	ASASSN-15oz	2015/08/31	HIPASS J1919-33	30.8	II	No
O1	SN 2015as	2015-11-15.778	UGC5460	17-20	II	Yes
O1	PSN	2015-12-15.066	NGC5483	27	Ib	No
O1	SN 2016B	2016-01-3.62	PGC 037392	22.7	IIP	Yes
O1	SN 2016C	2016-01-03.836	NGC5247	22.2	IIP	Yes
O1	SN 2016X	2016-01-19.487	UGC 08041	15.8	IIP	Yes
O1	SN 2016adj	2016-02-08.563	NGC 5128	3.66	Ib	No
O2	SN 2016iae	2016/11/07	NGC 1532	15.4	Ic	No
ER10	SN 2016ija	2016/11/22.712	NGC 1532	15.4	II	Yes
O2	AT 2016irh	2016-12-02.15	anonymous	3.12	unknown	No
O2	SN 2017aym	2017-01-13.575	NGC 5690	24.5	IIP	No
O2	SN 2017bzb	2017/03/07	NGC 7424	14	II	No
O2	SN 2017eaw	2017/05/14.238	NGC 6946	5	II	Yes
O2	SN 2017ein	2017/05/25	NGC 3938	12	Ic	No
O2	SN 2017gkk	2017-08-31	NGC2748	21.9	IIb	No

Table 8.1: ER8, O1, ER10 and O2 Optical SN candidates. Note: full name of PSN is PSN J14102342-4318437.

8.1 Preparation for the Search

8.1.1 Supernovae of Interest

Initial list

Several sources were used to search for optical SN candidates. First source is Astronomical Telegram (ATel [177]) that provides a quick information about various astronomical transients. Other sources include different surveys and databases of astronomical transients or confirmed supernovae. Optical SN candidates were collected using the following on-line catalogs: ASAS-SN [178], ASRAS [179], TNS [180], OSC [181], CBAT [182].

ATel alerts are open access, they can be subscribed. This quick information allows scheduling additional follow-up observations for better estimation of the on-source window, type of SN transients, progenitor star, the distance and others. For example, transient AT 2015Y was initially classified as a possible supernova, but further observations found otherwise. Before final classification, two possibilities appeared, either it is a core-collapse at distance 13Mpc or it is different transient at much further distance. Since the transient was obscured by dust, it was not of an interest for astronomers. However, given possible very close distance, additional observations were requested and the transient was classified not to be CCSN.

During the search for optical supernovae, several issues need to be managed like the speed of reaction, telescopes time, observations depending on the type of telescope, distance measurements, lag in appearing candidate in catalog, ambiguity of initial observations (type and distance), huge databases of transients, OSW might happen during the run even if SN was discoverd during break,

Table 8.1 summarizes several events and optical SN candidates during ER8, O1, ER10 and O2. Their identification comes with monitoring the Astronomical Telegrams for rapid udates about nearby CCSNe events. Only few of them were included in the final list of SN Search GW candidates. Distances of some of the collected optical SNe

Table 8.2: Core-collapse supernovae selected as triggers for the gravitational-wave search.

Identifier	Type	Host Galaxy	Distance [Mpc]	$t_1 - t_2$ [UTC]	Δt [days]	Run	Active Detectors	Coincident Coverage
SN 2015as	IIb	UGC 5460	19.2	2015.11.14.77-16.23	1.47	O1	H1,L1	35.0%
SN 2016B	IIP	PGC 037392	19.1	2015.12.23.51-27.55	4.03	O1	H1,L1	36.1%
SN 2016C	IIP	NGC 5247	20.1	2015.12.21.55-21.97	0.42	O1	H1,L1	7.6%
SN 2016X	IIP	UGC 08041	15.2	2016.01.17.72-20.56	2.86	O1	H1,L1	15.5%
SN 2016ija	II	NGC 1532	20.0	2016.11.20.02-21.10	1.09	ER10	H1,L1	96.0%
SN 2017eaw	IIP	NGC 6946	6.7	2017.04.26.56-27.96	1.39	O2	H1,L1	48.3%
SN 2017gax	Ib/c	NGC 1672	19.7	2017.08.09.31-15.24	5.93	O2	H1,L1,V1	63.9%

exceeds the range of 20Mpc that was initially considered. This is mainly due to the fact that the initial optical observations do not allow recognize the host galaxy or find the estimate the distance reliably. Specific cxamples of problems are:

- SN 2015aq - this supernova was detected relativaly late and a follow-up observatins were requested. However, the on-source window could not have been reliable calculated.
- iPTF15eqv and ASASSN-15oz - only one photometry point was available.
- SN 2016adj - only 11h (L1, Jan28/29, 2016) and 20h (H1, Feb7/8, 2016) of GW data were available.
- SN 2017aym - the event was classified as a supernova Type IIP two months after its discovery.
- SN 2017bzb - DLT40 data observed roughly the peak of the light curve and only have it in the infrared band. The OSW right without any other bands is 24 days long.
- SN 2017ein - the supernova exploded during the O2 commisioning break.
- SN 2017gkk - this supernova exploded shortly after O2.

Final list

The initial list of CCSN candidates comes from optical observations and the on-source window calculations that follow the observational data. The next requirement is the availability of the GW data to perform a meaningful analysis.

In the final list of optical CCSNe we used those that are at the distances smaller than 25Mpc. Table 8.2 presents the list final list of of supernovae. Four of them happened during O1, two of them during O2 and one right before O2, during the Engineering Run ER10. Majority of them are Type II supernovae originating usually from red giant progenitor stars. For each of them the host galaxy was identified. The distance is estimated either according to the estimated distance to host galaxy or by using the observed lightcurve. Figure 8.1 shows the sky locations of each supernova with comparison to the Milky Way Galaxy disc.

SN 2015as This supernova type IIb was discovered on 2015-11-15 00:00:00 during O1. The host galaxy is UGC 5460 at distance 19.2 Mpc away [37]. However, SN spectrum transition to SN Type Ib around 75 days after explosion. The progenitor star is either a main sequence $\sim 15M_{\odot}$ star or $\sim 20M_{\odot}$ Wolf-Rayet star. Supernova ejecta is estimated to be $1.1 - 2.2M_{\odot}$.

SN 2016B This supernova was discovered on 2016-01-03 14:52:48 during O1 by ASAS-SN. The progenitor star is a typicl red supergiant with radius $1000R_{\odot}$.

SN 2016C The supernova was found in NGC 5247 ($\sim$ 20Mpc) on 2016-01-03 20:10:14. It was classified as a typical Type IIP explosion.

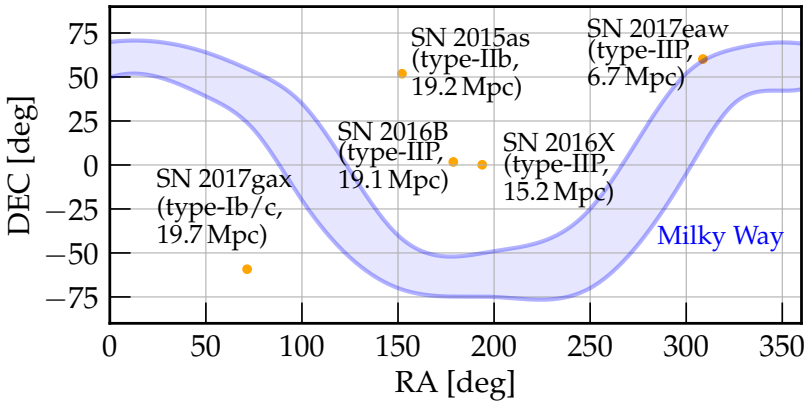

Figure 8.1: Supernovae and their sky locations

SN 2016X This supernova Type IIP exploded in a spiral galaxy UGC 08041 ($\sim$ 15Mpc). Optical observations [183] indicate that the progenitor star is a massive red supergiant with a initial mass larger than $19 - 20M_{\odot}$ and radius $930 \pm 70R_{\odot}$.

SN 2016ija This supernova Type II was discovered by DLT40 survay on 2016-11-22 17:05:16 during Engineering Run 10 (ER10) right before O2. The explosion happened in NGC 1532 ($\sim$ 20Mpc). The progenitor star was a typical RSG star with a mass of $8 - 17M_{\odot}$. The radius is estimated to be $30 - 660M_{\odot}$ [184].

SN 2017eaw This supernova Type II exploded in the nearby Universe in NGC 6946 galaxy which is estiamted to be 6.7Mpc away. This is the closest supernova considered in the search. The analyses [185, 186] indicate that the red supergiant is a progenitor star. The initial mass is $\sim 13M_{\odot}$ and the radius is estimated to be $4000R_{\odot}$.

SN 2017gax This CCSN was found in NGC 1672 ($\sim$ 20Mpc). This is the only non-standard supernova classified as Type Ib/c. It was discovered by DLT40 survay on 2017-08-14 17:05:16. Unfortunately little is known about the progenitor star.

8.1.2 Exploratory Results

Potential of the O1-O2 Dataset for Constraining the Extreme Emission Models

The following studies indicate that it is feasible to be able to constrain extereme emission models with O1-O2 data. As indicator of the scientific potential, a standard candle is used to choose the interest in producing standard candle model exclusion probabilities because if a SN is too far away to be useful for a lb5, it is usually too far for all the other emission models under consideration.

The studies were performed with the initial available information. The distances and on-source windows (OSWs) for each supernova were identified from the initial optical observation data. The durations of the on-source windows (OSW) in table 8.3 are different from the ones presented in table 8.2. The improvement in sensitivity between iLIGO/Virgo data during SN 2007gr and O1 data is around ∼10 times at peak frequency of lb5 model (800Hz). All results are derived at FAR=1.0e-6Hz.

Identifier	Galaxy Distance [Mpc]	OSW Duration	Visible Distance [Mpc]	MEP lb5 model
SN 2015aq	22.0	4 days	8.0	0.5%
SN 2015as	19.6	4 days	10.9	10-15%
MASTER	13	1 day	8.6	5%
SN 2016B	26	1 day	10.6	5%
SN 2016C	22.2	1 day	8.7	1%
AT 2016Y	13	2 days	11.3	43%
SN 2016X	22.2	2 days	8.7	1%

Table 8.3: Initial sensitivity studies for lb5 emission model. Note: full name of MASTER is MASTER OT J124235.77-000444.0

Extreme Emission Models

The next step of the initial analysis is the study of the MEP for all extreme emission models (lb1-6 and piro1-4). Table 8.4 presents predicted MEP statemenent. Two supernovae wre considered, SN 2016B and SN 2016X. The analysis is performed on O1 data, and on rescaled O1 sensitivity to predicted O2 sensitivity. The False Alarm Rate is assumed to be 1.0e-6Hz. Based on the results from table 8.4 we can conclude that the search might constrain at least two estreme emission models.

Conclusions

The improvements are consistent across the supernovae in comparison to the initial search. These improvements should allow to constrain the most extreme emission models. This gives motivation to investigate further the potential of performing combined O1-O2 SN Search.

Waveform	MEP, SN2016B		MEP, SN2016X	
	O1	O2 (rescaled)	O1	O2 (rescaled)
lb1	0%	0%	0%	0%
lb2	0%	0%	0%	0%
lb3	0%	0%	0%	0%
lb4	0%	0%	0%	0%
lb5	1.5%	28%	0.5%	5.5%
lb6	0%	0%	0%	0%
piro1	0%	0%	0%	0%
piro2	0%	0.5%	0%	0%
piro3	0%	0%	0%	0%
piro4	4%	21%	4.5%	9.5%

Table 8.4: MEP for the extreme emission models.

8.2 Tuning

The following section describes the investigation for identifying an optimal tuning for the SN search. I started from the default cWB tuning and I studied the impact of tuning of individual cWB parameters.

8.2.1 Choice of the search pipeline

Supernova	Pipeline	Network	hrss@50%	
			FAR=1.0e-6 Hz	FAP = 0.001
SN 2007gr	cWB1G+X	H1H2L1V1	-	3.16e-21
SN 2007gr	cWB2G	H1H2L1V1	1.89e-21	2.38e-21
SN 2016B	cWB1G	H1L1	2.47e-22	3.06e-22
SN 2016B	cWB2G	H1L1	1.85e-22	2.29e-22

Table 8.5: Comparison of performence between cWB1G, cWB2G and cWB+X on detectability of lb5 model. For both, SN 2007gr and SN 2016B the performance of 2nd generation version of cWB2G is better than combined results of cWB1G+X.

One of the initial decisions to be made before exploring the tuning is the choice of the search pipeline. We considered the search pipelines used in the initial LIGO/Virgo search: first generation of cWB pipeline (cWB1G) and X-pipeline (X). Then the results were compared with the performance of the second generation cWB pipeline (cWB2G). The considered waveform is lb5. The analysis was performed for a SN in initial LIGO/Virgo data, SN 2007gr, and for the O1-O2 data, SN 2016B. The table 8.5 presents the comparison results. Two thresholds were used: FAR=1.0e-6 Hz and FAP = 0.001.

The table indicates that for SN 2007gr the search sensitivity of cWB2G alone is better than cWB1G+X for both considered thresholds, around 30% improvement. A similar situation is isible for SN 2016B when the performance of cWB2G is 30% better than cWB1G. The values of $h_{\rm rss}$ were not calculated for cWB1G+X and FAR=1.0e-6Hz because of technical issues at the time of performing the studies, while for FAP=0.001 the results were already established. On-source window for SN 2007gr is 5.12 days and for SN 2016B a tentative 1 day of data was used (optical observations were on-going during these studies). Given that the improvements are consistently of an order of 30% it was decided to use only cWB2G as a search pipeline. The cWB2G is denoted later simply as cWB.

8.2.2 Quantifying impact of the tuning parameters

This section presents exploratory studies to find an impact of tunig cWB paramenters individually on the search.

Black Pixel Probability

Black Pixel Probability (bpp) describes how many Time-Frequency pixels are used in the search for GW transients. More details cn be found in section 4.3.4.

Table 8.6 shows the results of applying different values of bpp. The default value of bpp is 0.002. I tested larger values (better sensitivity, more noise transients detected) and smaller values (worse sensitivity, less noise transients detected). As it can be seen from the table, the improvement in sensitivity is not a monotonic funcion of the bpp value - larger improvements can be obtained for both larger and smaller values of bpp.

Table 8.6: Tuning bpp.

bpp	hrss@50%	Improvement
0.001	1.72e-22	+4.4%
0.002 (default)	1.80e-22	-
0.005	2.08e-22	-15.6%
0.0001	1.74e-22	+3.3%

Acore

This parameter sets a threshold for selection of core pixels. See section 4.3.4 for more details.

Table 8.7 shows the obtained results of implying different thresholds on Acore. The impact on the sensitivity seems to be marginal.

Table 8.7: Tuning Acore.

Acore	hrss@50%	Improvement
2.0	1.72e-22	0.0%
1.7 (default)	1.72e-22	-
1.5	1.71e-22	+0.6%
1.2	1.71e-22	+0.6%
1.0	1.73e-22	-0.6%

Two-step denoising

In this study the TSD filter was tested. The filter at the time of doing this study was in the development stage. More extensive studies are presented in section 12.7.

In this tunig study two extreme models were tested: lb4 (100ms long) and lb5 (1s long). Frequency band 16-1024Hz and FAR=1.0e6, Table 8.8 shows the obtained results. The advantage of using the filter seems to depend on the duration of the waveforms.

Table 8.8: Tuning using TSD

Waveform	hrss@50%		Improvement
	cWB	cWB+TSD	
lb4	2.15e-22	1.57e-22	+27.0%
lb5	1.96e-22	2.11e-22	-7.6%

Regulators

The network constraints, or regulators, allow to remove events that are unlikely solutions of the Constrained Likelihood analysis. Section 4.2.2 provides details of their usage.

Figure 8.2 shows the distribution of the background events and reconstructed injections in the parameter space of the ellipticity e and $\sin^2(\gamma)$. The Gamma regulator Γ is defined according to equation 4.54. From this plot one can conclude that a threshold in Γ to remove majority of noise events can be set to 0.75.

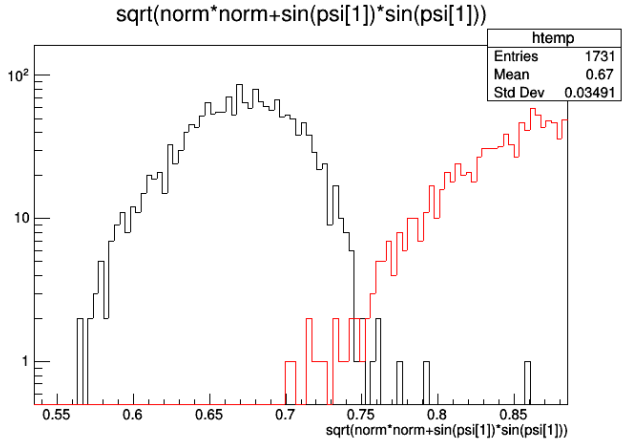

Figure 8.2: Example of gamma regulator values for background (black) and injections (red). An optimal threshold cut for the gamma is 0.75.

All-sky search constrains

One of the differences between all-sky searches and SN searches is the amount of data processed and consequently computation. Assuming typical on-source window of a supenova to be 4 days, the amonut of data to process is only 3% of the whole O1 Science run (130 days). At the moment of these studies a hard-coded all-sky constrain was applied in order to remove from the analysis very weak events.

Clustering One of the all-sky constraints discards events during the clustering stage when the clusters of energy are too separated in the time-frequency plane.

Table 8.9 shows the results comparing results of the default cWB settings with the constraint applied and then with the constrain removed. Removing the constraint initially has a negative impact on the sensitivity. It is because many more weak noise events are detected increasing FAR. However, by applying the value of regulators from the previous studies, the improvement becomes positive. Moreover, when we use information about the sky location of

the supernova (Ring Skymask), then many more noise triggers are removed giving a final improvement in sensitivity of around 10%.

Table 8.9: Tuning comparing applied (default) and removed all-sky search settings.

All-sky constraint	γ regulator	Skymask	hrss@50%	Improvement
Applied (cWB default)	0.0	No skymask	2.12e-22	-
Removed	0.0	No skymask	2.21e-22	-4.2%
Removed	0.75	No skymask	2.06e-22	+2.8%
Removed	0.75	Ring skymask	1.91e-22	+9.9%

Sky localization The estimation of the sky location is relatively heavy computationally. The *netRHO* (network coherent SNR) and *netCC* (correlation coefficient) parameters limit the computation of the sky locations.

Selection cuts with ρ vs cc

The first cWB statistics that were explored is the effective correlated SNR - rho0, rho1. and network correlation coefficient - cc0, cc1, cc2 cc3.

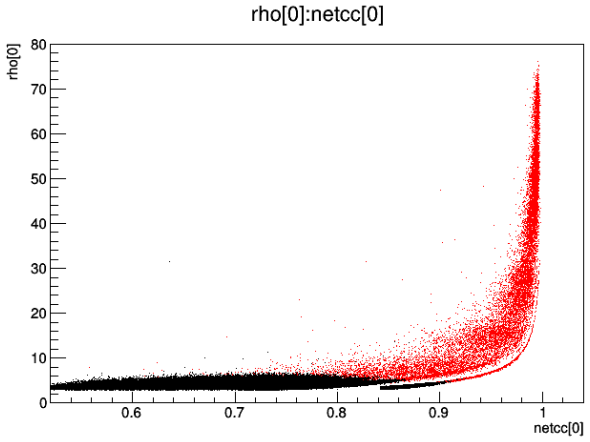

Figure 8.3: Example comparison between reconstructed background (black) versus injection (red) events parameters ρ and cc.

Figure 8.3 shows examples of rho and cc distributions. It is visible that background events are less coherent than injected SN events.

Table 8.10 shows results obtained when using different cuts. The example cuts from the table were obtained from comparing the bkg and sim distributions. The largest impact seems to be placed on using the correlation coefficients. The best improvement obtained 7.5%.

Blip glitches removal

One of the most problematic noise transients in aLIGO data are so called blip glitches. These glitches are very loud and their origin is so far unknown. Figure 8.4 shows an example of a blip glitch. It is a very short narrowband,

Table 8.10: Tuning of ρ and cc coefficients at fixed FAR=1.0e-6Hz.

Selection cut	hrss@50%	Improvement
No cuts - default	2.12e-22	-
(cc0>0.65)&(cc2>0.5)	2.11e-22	+0.5%
(cc2>0.65)&(cc3>0.55)	2.09e-22	+1.4%
(cc1>0.73)&(cc2>0.65)&(cc3>0.55)	2.09e-22	+1.4%
(cc1>0.84)&(cc2>0.65)&(cc3>0.55)	1.96e-22	+7.5%
rho1>(-50*cc3+30)	2.11e-22	+0.5%
(cc1>0.84)&(cc2>0.65)&(cc3>0.55)&(rho1>(-50*cc3+30))	1.96e-22	+7.5%
(cc1>0.84)&(cc2>0.80)&(cc3>0.70)	2.04e-22	+3.7%

usually low frequecy signal. These signals are relatively loud and create strong non-Gaussian tail in Fals Alarm Rate plots.

The signature of blip glitches is distinctive from the other noise glitches and they can be removed by dividing the search background into two exclusive bins:

- bin1 - bin polluted by blip glitches,
- bin2 - bin polluted by other types of glitches.

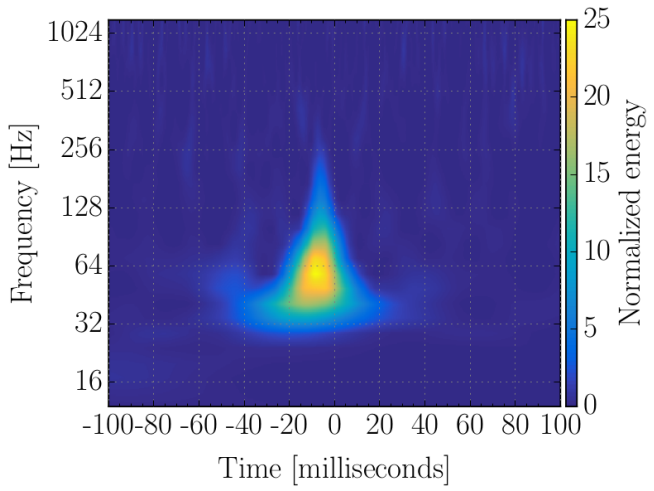

Figure 8.4: Example of blip glitch (image source [16].)

8.2.3 Application of Wavelet packets

Table 8.11 shows results of applying Wavelet Packets. More information about description of differnt Wavelet Packets are in section 4.3.6. Several waveforms were used in the studies, both extreme (piro4 and lb5) as well realistic (yak3). Both O1 real and O1 simulated Gaussian data were used for the studies. In all cases there is an improvement in detectability. The larger improvement is visible when the study is applied to the real data. It is caused by the fact that real data contain loud non-Gaussian noise transients that are not present in Gaussian

data and it seems that Packets are efficient not only with increasing sensitivity of the search, but also efficient with removing the noise transients.

Table 8.11: Tuning Wavelet Packets.

Waveform	Data used	Wavelet Packet	hrss@50%		Improvement
			cWB	cWB+WP	
piro4	O1 data	pattern=5	3.53e-22	2.38e-22	32%
lb5	O1 data	pattern=5	1.53e-22	1.29e-22	15%
piro4	Simulated O1 data	pattern=5	5.11e-22	5.04e-22	1%
piro4	Simulated O1 data	pattern=1	5.11e-22	4.74e-22	7%
yak3	Simulated O1 data	pattern=9	1.98e-21	1.71e-21	13%
yak3	Simulated O1 data	pattern=5	1.98e-21	1.71e-21	9%

8.2.4 Using Information about SN Sky Location

In Optically Triggered Searches the sky location of supernovae is known. It gives an advantage over all-sky searches when the location of the GW source is unknown. For the burst searches, the sky location for a GW candidate is calculated from the triagulation.

Circular Skymask

The spatial resolution of GW detectors is not as accurate as the ones of optical telescopes. A simple application of sky locaiton information is accepting triggers that are reconstruced in the are af the sky around the event. In this case, we accept reconstructed triggers' sky locations in a circle around the sky location of a supernova. The redius depends on the waveforms, the properties of the noise and others. A typical radius of the circle is 5deg or 10deg.

Ring Skymask

Overview In two detector case (H and L interferometers) GW causes a delay when passing between detectors. However the true location of the source cannot be reconstructed because the delay can be produced by sources from many locations situated symmetrically around the projection of a baseline between two detectors. Those locations make a ring or a circle (circle without inside) on the sky.

The aperture of the ring (its width) to be tuned to maximize the efficiency at fixed FAR. The location of the supernova will be specified by SNEWS alerts.

Choice of skymask coordinate system cWB pipeline uses two types of coordinate systems: Celestial and Earth Coordinate Systems (tests of the simple skymasks in Earth coordinates are here). The skymasks used in current searches uses fixed locations in either of those coordinates systems. The problem which arises with ring skymask is that the ring changes the radius depending on the position of two detectors and supernova. Specifically:

Lets assume Celestial Coorinates. The SN source is fixed on the sky (and it is fixed point on the ring at any time), but the HL baseline moves and its projection on the sky (the center of the circle) also moves. So the circle changes its radius. Lets assume Earth Coordinates. The projection of HL baseline is fixed in that map (meaning the center of the circle does not change). However the SN location in that coordinates moves causing changing the

radius of the circle. I decided to use Earth Coordinate System, because the position of the point where HL baseline is pointing is fixed for any SN source (I call that point pHL).

SN2007gr example ring skymask The example of SN2007gr ring sky mask is shown below. The script for this example is produced by this script.

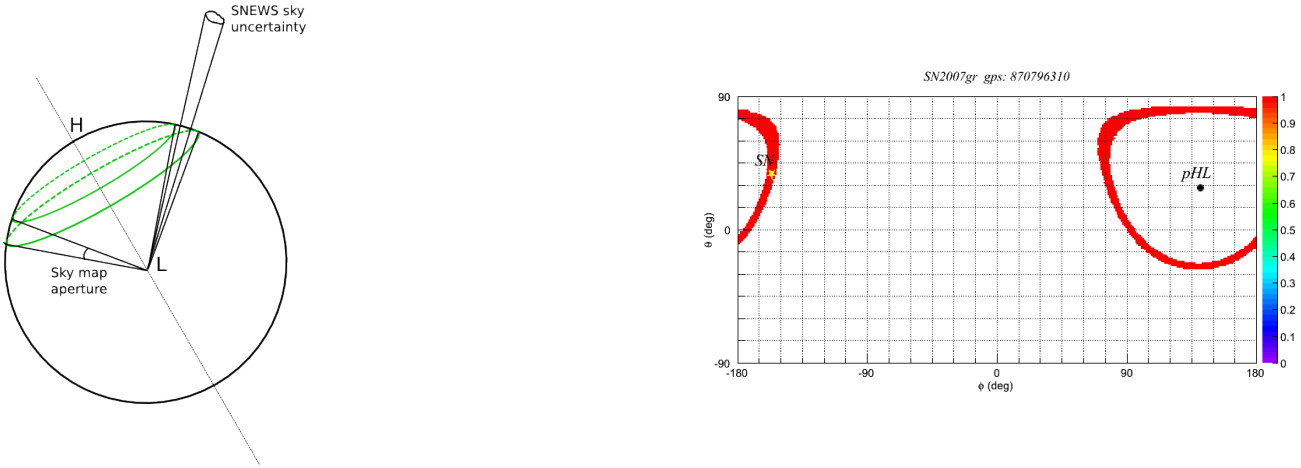

Figure 8.5: Ring Skymask

Double Ring Skymask

In case if the on-source windows overlap then two GW might be present in a given interval and we accept events from the ovelaping regions of the sky then the loudest event statistics is no longer true. Two loudest events might be the GWs. This situation was a case for the initial on-source window calculations of SN 2016B and SN 2016C.

- SN 2016B: discovered 2016-01-3.62, initial distanc estimare 22.7Mpc, (RA,DEC) = (11:55:4.245, +01:43:06.77)
- SN 2016C: discovered 2016-01-3.84, initial distanc estimare 22.2Mpc, (RA,DEC) = (13:38:05.30, +17:51:15.30)

Figure 8.6 illustrates two possibilities of ring skymasks behavior. There are periods when skymasks overlap. For time step 0.5h of the skymask moving across the sky, skymasks cross each other twice, so the ring skymasks overlap each other for 1h every day which is 4%.

Comparison of performance between different skymasks

Table 8.12 presents comparison of performance of the search sensitivity when different skymasks and no skymask are applied. For this test two linearly polarized sine-Gaussians with Q=8.9 and peak frequency $f_0 = 235$Hz (sg1) and $f_0 = 1304$Hz (sg2). The results are produced at the fixed FAR for each network.

For H1H2L1 detector network the usage of Circular and Ring Skymasks allows to detect signals that are two times weaker comparable to the detectability without any skymask. This advantage applies for both sg1 and sg2. For H1H2V1 detector network the advantage of using circular skymask gives is not significant. The Ring Skymask gives around 28% and 24% advantage for sg1 and sg2 respectively. For L1V1 network the advantage is not that robust (up to $\sim 12\%$ improvement). These results show consistent advantages of using the skymasks.

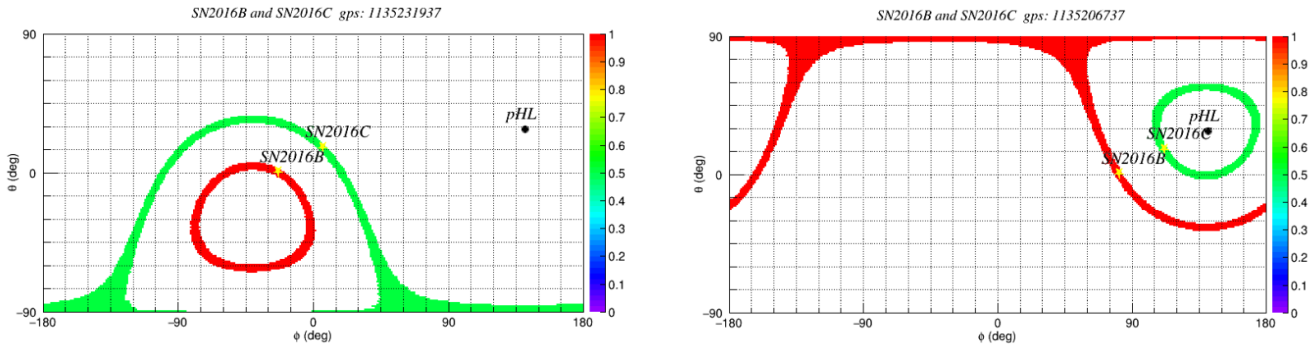

Figure 8.6: Double Ring Skymask

Network	cWB	FAR [Hz]	No Skymask		Circular skymask 4deg		Ring Skymask 1deg	
			sg1	sg2	sg1	sg2	sg1	sg2
H1H2L1	cWB1G	3.0e-8	9.20e-22	4.22e-21	4.51e-22	2.04e-21	4.64e-22	2.11e-21
H1H2V1	cWB1G	1.1e-8	7.99e-22	2.90e-21	7.50e-22	2.60e-21	5.77e-22	2.20e-21
L1V1	cWB1G	1.0e-6	1.38e-21	3.72e-21	-	-	1.14e-21	3.28e-21
L1V1	cWB2G	1.0e-6	1.44e-21	3.68e-21	-	-	1.27e-21	3.38e-21

Table 8.12: Comparison between performance between different skymasks

8.2.5 Exploring optimal search tuning

After exploring the impact of tuning cWB parameters individually and the impact of sky location information, the next step is to explore an optimal search tuning in the overall multidimensional parameter space. SN 2016B, L1H1 detector network and Yakunin 2015 et al waveforms are used to illustrate the tuning impact. The search tuning runs are divided into two exclusive bins (polluted by blip glitches and polluted by other noise sources). All results are presented at Inverse False Alarm Rate (IFAR) of 1 year (FAR$\approx 3.17 \times 10^{-8}$Hz).

Table 8.13 shows the tuning results. The first raw shows a default optimal configuration of cWB and the differences in configurations are highlighted in bold. Overall, the improvements in detectable $h_{\rm rss}$, if appeared, is rather marginal and is not consistent. Given that some extreme emission models have peak frequency above 1kHz, we are considering going to 2kHz. This change does not affect the waveforms detectability. As mentioned in section 8.2.3, the wavelet packets allow to detect weaker signals. In this study the usage wavelet packets make the detectability even worse (rows 3, 4, 5). The considered waveforms are broadband, so we tested $T_{gap} = 256$Hz, but the detectability does not improve. The circular skymask destroys the sensitivity (row 7), and this skymask is not considered later on. Interestingly, a minimal improvement comparable to the default configuration is achieved by using the ring skymask (row 1 and 8). Further usage of a wavelet packets do not make the search more sensitive (row 9). The advantage of using ring skymask seems to be consistent (rows 10 and 11, 12 and 13, 14 and 15, 16 and 17, 18 and 19).

The next steps in tuning exploration is lowering the thresholds. We quantitied an impact of netRHO, bpp, Acore and F_{gap}. Lowering bpp and Acore (rows 12-15) make the search sensitivity worse. The reason is a significant increase of detectd noise events. At the same time netRHO (rows 10,11) and F_{gap} (rows 17,18) do not damage the sensitivity, but also they do not help. Finally, when all considered thresholds are lowered, they worsen the search

Row	WP	f_{max} [Hz]	netRHO	bpp/ Acore	F_{gap} [Hz]	Skymask	hrss@50% ($\times 10^{-22}$) yak1/yak2/yak3/yak4
1	10	1024	6.0	0.001/1.7	0	No skymask	6.86/4.96/5.46/4.74
2	10	**2048**	6.0	0.001/1.7	0	No skymask	6.89/5.10/5.68/4.80
3	**5**	1024	6.0	0.001/1.7	0	No skymask	7.75/5.81/7.08/5.22
4	**9**	1024	6.0	0.001/1.7	0	No skymask	7.55/5.68/8.02/5.41
5	**1**	1024	6.0	0.001/1.7	0	No skymask	7.08/5.35/5.89/5.05
6	10	1024	6.0	0.001/1.7	**256**	No skymask	6.95/4.98/5.44/4.75
7	10	1024	6.0	0.001/1.7	0	Circular 10deg	- / - / - / -
8	10	1024	6.0	0.001/1.7	0	Ring 5deg	6.81/4.95/5.38/4.72
9	**5**	1024	6.0	0.001/1.7	0	Ring 5deg	7.75/5.80/7.10/5.22
10	10	**2048**	**5.0**	0.001/1.7	0	No skymask	6.89/5.10/5.68/4.80
11	10	**2048**	**5.0**	0.001/1.7	0	Ring 5deg	6.84/5.06/5.64/4.77
12	10	**2048**	6.0	**0.002**/1.7	0	No skymask	7.48/5.45/6.25/5.04
13	10	**2048**	6.0	**0.002**/1.7	0	Ring 5deg	7.48/5.41/6.31/5.01
14	10	**2048**	6.0	0.001/**1.2**	**256**	No skymask	7.31/5.61/6.21/5.28
15	10	**2048**	6.0	0.001/**1.2**	**256**	Ring 5deg	7.24/5.52/6.13/5.26
16	10	**2048**	6.0	0.001/1.7	**256**	No skymask	6.89/5.12/5.68/4.80
17	10	**2048**	6.0	0.001/1.7	**256**	Ring 5deg	6.84/5.08/5.64/4.77
18	10	**2048**	**5.0**	**0.002**/**1.2**	**256**	No skymask	8.22/6.13/7.02/5.63
19	10	**2048**	**5.0**	**0.002**/**1.2**	**256**	Ring 5deg	8.22/6.07/7.08/5.59

Table 8.13: Exploring optimal search tuning. The optimization for Set parameters: Δ/Γ = 0.5/-1.0, netCC=0.5, T_{gap}=0s.

sensitivity even more.

For the future investigations, one should considered also exploring other parameters. Based on the obtained results, the task of choosing an optimal SN search tuning is not trivial. The reason why the search sensitivity does not improve with modifying the parameter values is partially due to the fact that the waveforms are not easily detectable with low SNR. They are spread in time-frequency maps and collecting energy is difficult. The events need to be sufficiently strong (minimum SNR 20-30) to be well detectable.

8.2.6 Final Search Tuning

Parameters Choice

Between the SN search sensitivity studies and final choise of the search parameters, the cWB pipeline was under developement and under review for other GW searches. Moreover, an advantage of sky location depends on the sky location of the SN for a duration of the on-source window. The tuning should be then different for different supernovae. The final on-source windows depend greatly on the optical observations that may take several months. Taking all into account, the choice of the optimal parameter SN search tuning is based on the short duration (<1s) low-frequency ([16-1024]Hz) all-sky search tuning. Examples of the parameter choice:

- Frequency range: [16,2048] Hz,
- pattern = 10,
- bpp/Acore = 0.001/1.7,

- T_{gap}/F_{gap} = 0.2s / 128Hz,
- Δ/Γ = 0.5/-1.0,
- netRHO/netCC = 5.0, 0.5.

Selection Cuts

Similarily, the post-processing selection cuts are based on short duration low-frequency all-sky search tuning. Some of the choice of the selection cuts:

- norm>2.5
- bin1 frequency cut: [32,1990]Hz
- bin1 frequency cut: [48,1990]Hz
- netcc[0]>0.8 and netcc[2]>0.8

The choice of the minimum and maximum frequency cut is related to the violin modes (arrowband signals) in high and low frequencies. Figure 8.7 shows an example Amplitude Spectral Density for one day around SN 2016B. Large noise is visible around 2kHz. This noise is removed with a high frequency cut of 1990Hz. This does not affect the search sensitivity because the highest peak frequency of SN waveforms is 1600Hz.

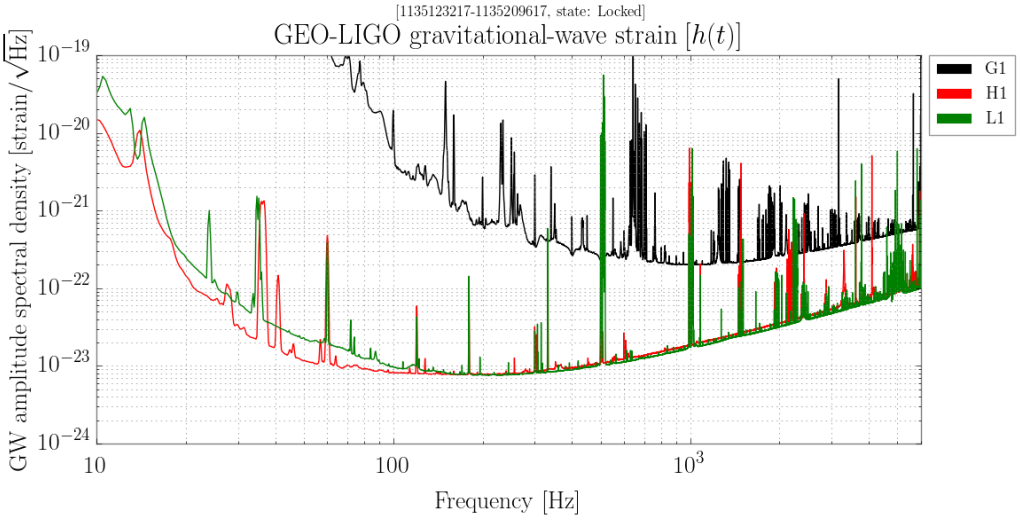

Figure 8.7: Amplitude Spectral Density on December 26th, 2017 during SN 2016B on-source window.

8.3 Methodology

8.3.1 OSW calculations

The moment of core-collapse triggers the explosion of a star. Depending on the size of the progenitor star, the ensuing shock propagates outwards for a period of seconds to days [187, 67]. When it reaches the surface, i.e

shock breakout, a CCSN is visible on the sky. Because of the weather conditions, limited sky coverage, and many other problems, astronomical surveys typically record CCSNe hours to months after shock breakout. The ability to extrapolate backwards in time to the moment of core-collapse (and GW transient emission), depends primarily on how quickly a CCSN is detected and the properties of its progenitor star.

In this search, similarly to Ref. [17], we use two methodologies for the calculation of the on-source window (OSW). We apply an *early observation method* when a supernova is observed within a few days and the progenitor star is known. When (a) the time of discovery is of an order of a week or more, (b) the distance to the host galaxy is unknown, or (c) the type of progenitor star is unknown, we use an *expanding photosphere method (EPM)*. We represent an on-source window as a period $[t_1, t_2]$, where t_1 and t_2 are the beginning and end times respectively.

In an early observation method, t_2 is the time when a supernova is observed. To determine t_1 , we need to take into account the moment of the last observation of a host galaxy without a supernova present, $t_{\rm Null}$, and the shock propagation travel time between moment of explosion and shock brakout, $\Delta t_{\rm SB}$. We get that $t_1 = t_{\rm Null} - \Delta t_{\rm SB}$. $\Delta t_{\rm SB}$ depends mainly on the type of a progenitor star. Wolf-Rayet stars are stripped of helium and hydrogen and they lead to type-Ib/c supernovae. Their radii are on the order of a few $R_\odot$ with a typical shock breakout times ranging from a few seconds up to a minute [187]. Red supergiant stars have radii of 500-1000 $R_\odot$ [64] and typical $\Delta t_{\rm SB}$ ranges from more then ten hours up to few days [67]. We calculated the OSW with an early observation method for four supernovae: SN 2015as, SN 2016B, SN 2016X and SN 2017gax. For each of them we identified $t_{\rm Null}$ and t_2 based on the astronomical surveys. We calculated $\Delta t_{\rm SB}$ from information about their progenitor stars. To account for uncertainties in the progenitor star information and to make sure that our OSW contains the GW transient, we added additional time to $\Delta t_{\rm SB}$ (increased from 15 h to 24 h).

The expanding photosphere method is used in astronomy primarily to calculate distances to CCSNe, but we employ it to estimate the time of a core-collapse [188]. We briefly describe the method, but a detailed explanation can be found in Refs. [189, 190, 191, 192, 193, 194]. When the shock breaks through a star's surface, it heats up the outer layers and pushes them outwards. The hot ejected material (photosphere) expands and radiate in the electromagnetic spectrum. Measuring the light allows us to estimate the angular size of the expanding photosphere. As a consequence, we can extrapolate backward in time to the moment of an explosion and estimate t_1 and t_2. SN 2017eaw was obseverd over a week after explosion and we used EPM to calculate the OSW. This supernova triggered an interest (see e.g. Refs [185, 186]), and good follow-up observations allowed to constrain the OSW sufficiently for the purposes of this search.

8.3.2 Detector Networks and coverage

In this paper we search for GW signals in a large frequency band, 16-2048 Hz, without specific assumptions about the signal morphology. This frequency band allows us to cover most of the main emission processes inside a CCSN. We employ coherent WaveBurst (cWB) [195] as the search algorithm and it will described in the following section. The pipeline produce candidates for GWs that we refer to as events or triggers.

As was mentioned earlier, each GW detector is constantly monitored with various sensors that allow us to exclude poor data from the analysis. However, it is not possible to remove all sources of noise. GW interferometers randomly produce coincident glitches that can be falsely identified as GW transients. To estimate how often the network of detectors produce such noise events we perform a background analysis, similarly to Ref [17] and references

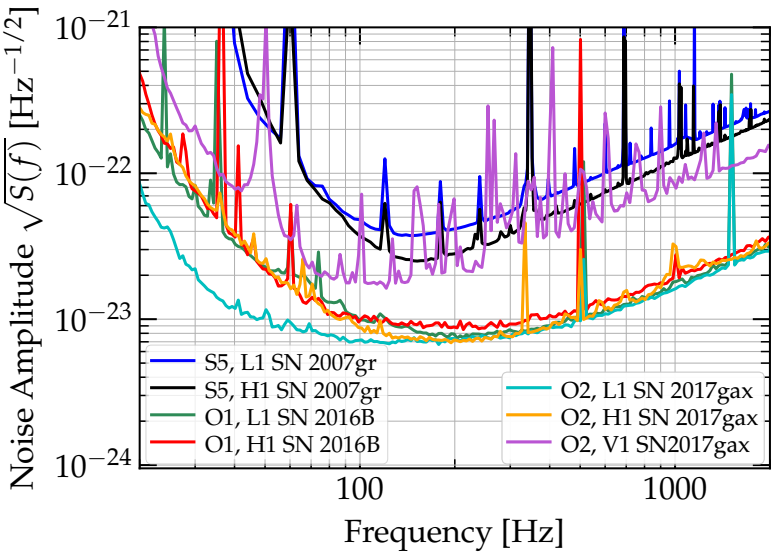

Figure 8.8: Noise amplitude spectral densities of the GW interferometers. For SN 2016B and SN 2017gax we chose ten random periods inside of corresponding on-source windows. Each period was 10 minutes long. We calculated the noise spectra for each and then took an average. Amplitude spectra for SN 2007gr is reproduced from Ref. [17].

therein, where the search pipeline artificially shifts the data in one detector with respect to the other. The typical time shift is a multiple of one second, which is much longer than the GW travel time between different detectors (e.g. 10 ms between H1 and L1). This allows us to estimate the False Alarm Rate (FAR) of the events that are falsely recognized as GWs. We accumulated around a few years of background data for each supernova. We rank triggers with an inverse FAR, IFAR=1/FAR. The significance of each event is assessed by calculating its False Alarm Probability (FAP) [17]:

$$FAP = 1 - \exp\left(-T_{\rm on} \times FAR\right) \tag{8.1}$$

where $T_{\rm on} = t_2 - t_1$ is the duration of an on-source window (see Sec.8.3.1).

For each supernova, potential GW candidates are triggers obtained from the data that is not shifted in time. We assume that the event with the largest IFAR is our GW candidate and refer to it as a *loudest event*. In order for the loudest event to be considered as a GW detection candidate, the FAP must be sufficiently low. The significance level that we require for a loudest event to be considered a GW detection candidate is 3σ, which corresponds to a FAP of approximately 2.7×10^{-3}. If a loudest event for some supernova were to exceed the 3σ confidence level, we would then check to see if the recontructed morphology was consistent with the waveforms from the emission models that could feasibly be detected at such a distance. If there is an agreement, then a team would be appointed that reviews further consistency checks. Otherwise, we would discuss if such a team should be appointed.

We also determine how sensitive the pipeline is to particular waveform families. In this analysis cWB adds (*injects*) supernova waveforms to the detector data inside the on-source window and performs an analysis searching for the injected waveforms. The fraction of the injected waveforms that can be detected is the *detection efficiency*. The injection procedure is repeated with waveform amplitudes corresponding to different source distances. In this targeted search we know the sky locations of each supernova and the waveforms are injected accordingly. We accept

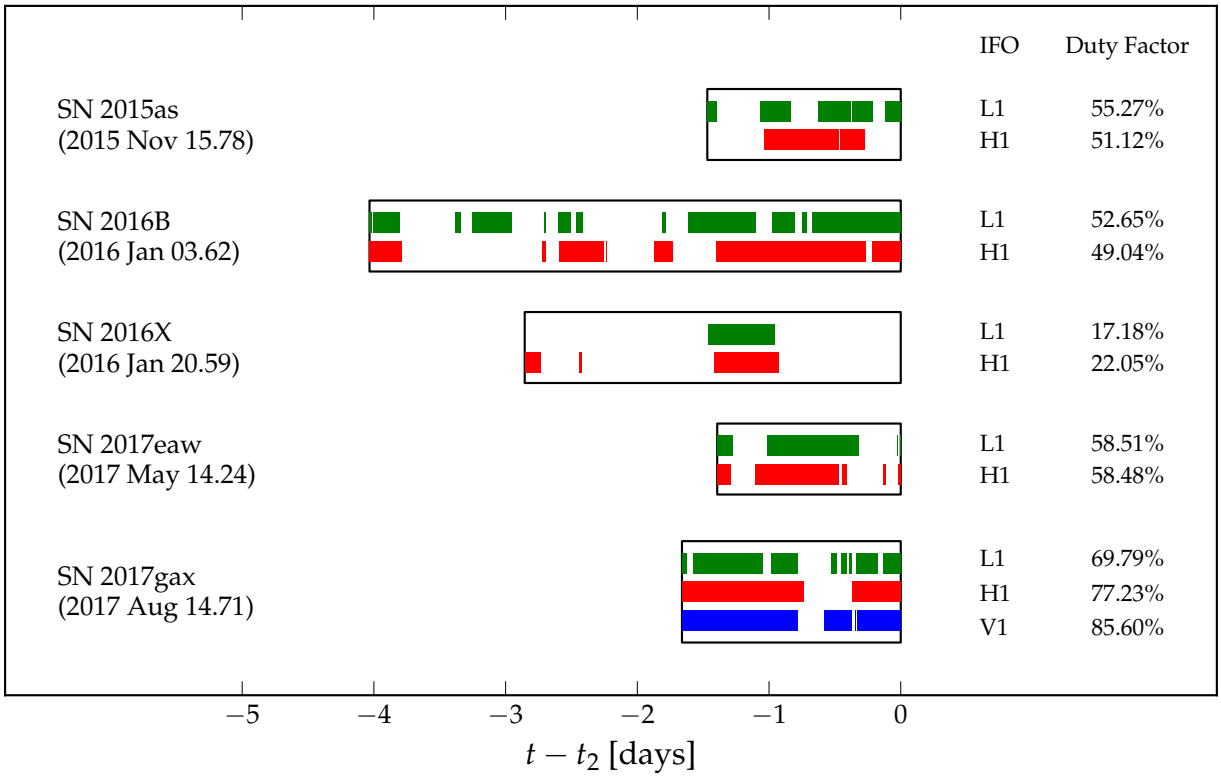

Figure 8.9: Visual representation of the on-source window and detectors duty cycles for each SN candidate

every trigger that passes the selection cuts and has a significance larger than the loudest event.

8.3.3 SN waveforms

In this paper, we consider two sets of multidimensional supernova explosion models, extreme emission models, and *ad hoc* waveforms. Tables 8.14 and 8.15 list the waveforms selected for the search sensitivity studies. For all of the waveforms included we provide the peak frequency, number of polarizations, and other quantities. For the waveforms from multidimensional CCSN simulations and extreme emission models, we provide the emitted GW energy, $E_{\rm GW}$, emitted during the explosion and the angle-averaged root-sum-squared GW strain, $h_{\rm rss}$, defined as:

$$h_{\rm rss} = \sqrt{\int \left\langle h_+^2(t) + h_\times^2(t) \right\rangle_\Omega \mathrm{d}t}\,. \tag{8.2}$$

Waveforms from multidimensional CCSN simulations

The main mechanism behind a CCSN explosion is not yet fully understood. We describe briefly the current understanding of a possible explosion scenario. More extensive review can be found in Refs. [196, 197, 135, 198] and in references therein. We divide the waveforms from multidimensional CCSN simulations into two sets according to their explosion mechanisms. In the first set of waveforms from CCSN simulations we assume a *neutrino-driven* explosion mechanism for non or slowly-rotating progenitor stars. We employ three waveforms families: Müller, Ott

Table 8.14: Waveforms from detailed multidimensional CCSN simulations described in the text. For each waveform, we give the emission type, journal reference, waveform identifier, angle-averaged root-sum-squared strain $h_{\rm rss}$, the frequency $f_{\rm peak}$ at which the GW energy spectrum peaks, the emitted GW energy $E_{\rm GW}$, and available polarizations. See [2, 3] for details.

Waveform Family	Waveform Identifier	$h_{\rm rss}$ $[10^{-22}@10\,{\rm kpc}]$	$f_{\rm peak}$ [Hz]	$E_{\rm GW}$ $[10^{-9}M_\odot c^2]$	Polarizations
Müller [33] 3D Convection and SASI	mul1-L15-3	1.655	150	3.741×10^{-2}	+, ×
	mul2-N20-2	3.852	176	4.370×10^{-2}	+, ×
	mul3-W15-4	1.093	204	3.247×10^{-2}	+, ×
Ott [140] 3D Convection and SASI	ott1-s27fheat1p05	0.345	250	7.34×10^{-1}	+, ×
Yakunin [38] 2D Convection and SASI	yak1-B12-WH07	4.23	523	17.4	+
	yak2-B15-WH07	19.4	503	41.0	+
	yak3-B20-WH07	4.43	443	21.6	+
	yak4-B25-WH07	24.7	512	77.4	+
Scheidegger [40] Rotating Core-Collapse	sch1-R1E1CA$_L$	0.093	399	1.04×10^{-1}	+, ×
	sch2-R3E1AC$_L$	6.27	527	2.14×10^{2}	+, ×
	sch3-R4E1FC$_L$	6.67	630	3.42×10^{2}	+, ×
Dimmelmeier [39] Rotating Core-Collapse	dim1-s15A2O05ls	1.052	774	7.685	+
	dim2-s15A2O09ls	1.803	753	27.873	+
	dim3-s15A3O15ls	2.690	237	1.380	+

and Yakunin. The second set of waveforms, with simulations from the Scheidegger and Dimmelmeier groups, utilizes the *magnetohydrodynamically-driven (MHD-driven)* explosion mechanism model for rapidly rotating progenitor stars. We will discuss each waveform family later in this section.

In the neutrino-driven mechanism scenario the neutrino heating plays a crucial role leading up to an explosion. The collapsing core launches an initial shock that propagates outward until it stalls. For a successful explosion, the stalled shock must aquire sufficient energy to be revived. One method of acquisition comes from fluid instabilities in the stellar core, which become relevant in boosting neutrino luminosities and are thus related to the deposition of energy behind the shock. Another method takes place in the gain radius, just underneath the shock, where an instability, referred to as neutrino-heating convection, develops in the material due to an entropy gradient [199, 200, 132, 38]. This might help lead to an explosion considering it aids in pushing the shock outward toward the shallower regions of the gravitational potential. Hydrodynamic studies in quasi-stationary shock have also led to shock reheating due to non-spherical perturbations. These give rise to a standing accretion shock instability (SASI) [201]. This mechanism may indirectly help neutrino heating, and therefore the explosion. It also may be responsible for the asymmetric nature of the explosion. Both of these convective and SASI processes result in gravitational-wave emissions. During the prompt convection, in the initial stages post bounce, GWs are emitted in the frequency range from 100-300 Hz, while at later times, GWs up to 1000 Hz are expected. Frequency ranges above 1000 Hz are noted to have a more turbulent component. A typical duration for an explosion is of an order of 0.5-1 s [202, 196, 203].

If the rotation of a progenitor star is very rapid, however, then this rotation has a dominant role in creating the MHD-driven explosion. The tremendous rotation magnifies a seed magnetic field that was present in an iron core. After its collapse, the magnetic field pushes the material along the rotational axis leading to an explosion. Note that it is estimated that nearly all [204, 205] CCSN explosions come from slowly rotating progenitor stars.

Table 8.15: Waveforms from phenomenological and *ad hoc* emission models described in the text. For each waveform, we give the emission type, journal reference, waveform identifier, angle-averaged root-sum-squared strain $h_{\rm rss}$, the frequency $f_{\rm peak}$ at which the GW energy spectrum peaks, the emitted GW energy $E_{\rm GW}$, and available polarizations. See [2, 3] for details. As sine-Gaussian waveforms are *ad hoc*, they can be rescaled arbitrarily and do not have a defined physical distance or $E_{\rm GW}$ value.

Emission Type	Waveform Identifier	$h_{\rm rss}$ [10^{-20}@10 kpc]	$f_{\rm peak}$ [Hz]	$E_{\rm GW}$ [$M_\odot c^2$]	Polarizations
Long-lasting Bar Mode [153]	lb1-M0.2L60R10f400t100	1.480	800	2.984×10^{-4}	$+, \times$
	lb2-M0.2L60R10f400t1000	4.682	800	2.979×10^{-3}	$+, \times$
	lb3-M0.2L60R10f800t100	5.920	1600	1.902×10^{-2}	$+, \times$
	lb4-M1.0L60R10f400t100	7.398	800	7.459×10^{-3}	$+, \times$
	lb5-M1.0L60R10f400t1000	23.411	800	7.448×10^{-2}	$+, \times$
	lb6-M1.0L60R10f800t25	14.777	1601	1.184×10^{-1}	$+, \times$
Torus Fragmentation Instability [41]	piro1-M5.0η0.3	2.550	2035	6.773×10^{-4}	$+, \times$
	piro2-M5.0η0.6	9.936	1987	1.027×10^{-2}	$+, \times$
	piro3-M10.0η0.3	7.208	2033	4.988×10^{-3}	$+, \times$
	piro4-M10.0η0.6	28.084	2041	7.450×10^{-2}	$+, \times$
sine-Gaussian [156]	sg1-235HzQ8d9linear	—	235	—	$+$
	sg2-1304HzQ8d9linear	—	1304	—	$+$
	sg3-235HzQ8d9elliptical	—	235	—	$+, \times$
	sg4-1304HzQ8d9elliptical	—	1304	—	$+, \times$

Müller et al [33] performed 3D simulations with a zero age main sequence (ZAMS) mass progenitor star of $15\,M_\odot$ (L15-3 and W15-4), and a $20\,M_\odot$ (N20-2) ZAMS, which we also refer to as mul1, mul2 and mul3 respectively. The simulations are three-dimensional and thus result in two polarizations. The main contribution to the GW signal is the convective movement of matter leading to low frequency GW emission. The infalling matter does not reach the newly formed protoneutron star, which results in the lack of a high frequency component in the GW signal.

Ott et al [140] produced 3D simulation with a $27\,M_\odot$ ZAMS progenitor star (ott1 waveform). The explosion becomes aspherical due to a strong convective motion of matter. SASI motion is small. This model employs rotation and an initial strong burst of GWs appears at the beginning of the explosion.

Yakunin et al [38] delivers waveforms from four 2D simulations (providing only one polarization state) corresponding to $12\,M_\odot$, $15\,M_\odot$, $20\,M_\odot$, $25\,M_\odot$ ZAMS progenitor stars. We denote them as yak1, yak2, yak3 and yak4 respectively. These waveforms capture several stages of the explosion. They show both low (SASI/convection) and high (g-mode) frequency components in their signals. Due to axisymmetry, the strain grows artificially over time, resulting in higher GW amplitudes than the 3D neutrino driven models.

Scheidegger et al [40] considers effects on the GW signature due to the equation of state, the initial rotation rate, and the magnetic fields. From an extensive set of waveforms, we extract three models, R1E1CA$_L$, R3E1AC$_L$, and R4E1FC$_L$, which we refer to as sch1, sch2, and sch3, respectively. All of these models are derived from the explosion of a $15\,M_\odot$ ZAMS progenitor star. The models are three dimensional and produce two GW polarization states. The degree of rotation varies between the models; model R1E1CA$_L$ has no rotation, which results in much lower GW energy in comparison to the rotating R3E1AC$_L$ and R4E1FC$_L$ models.

Dimmelmeier et al [39] performed 2D simulation (providing linearly polarized waveforms) with a $15\,M_\odot$ ZAMS progenitor star. The waveforms contain very strong GW emission originating from the core-collapse and bounce

that lasts less than 20 ms. The tremendous rotation suppresses the post-bounce convective motion, which in turn, diminishes the GW emission. We employ three waveforms with various degrees of rotation from moderate to rapid (dim1-dim3).

Extreme emission models

Along with the more realistic simulated CCSN explosions, we also consider two extreme scenarios: the *Long-Lasting Bar Mode* [153], and the *Torus Fragmentation Instability* [41]. The same extreme models were used in Ref. [17]. The GW emission predicted by the extreme emission models is very unlikely to occur, but plausible [206].

In the first scenario, a very rapidly rotating progenitor star induces a bar mode instability. This leads to high amplitude GWs that depend on the properties of the rotating bars. In this model, we use the following parameterization: the mass deviatiation from spherical symmetry $M = \{0.2, 1.0\}\, M_\odot$, the radius $r = 10\,\mathrm{km}$ and length $L = 60\,\mathrm{km}$ of the bar, the spin frequency $f = \{400, 800\}\,\mathrm{Hz}$ along the direction perpendicular to the bar, and the duration $t = \{25, 100, 1000\}\,\mathrm{ms}$ of the deformation. We consider six waveforms, denoted as lb1-lb6 (see Table 8.15 for more details).

In the second scenario, Piro and Phafl [41] predict the formation of a central black hole of mass M and a thick accretion torus with a self-gravitating fragment. This model also predicts strong GW emission that depends on the mass of the central black hole $M = \{5, 10\}\, M_\odot$ and properties of the disk. The torus thickness is defined as $\eta = H/r$, where H is the disk scale height (fixed at 0.2), and r is the local radius. We assume $\eta = \{0.3, 0.6\}$. We employ four waveforms, piro1-piro4 (see Table 8.15 for more details).

***Ad-hoc* waveforms**

Following Ref. [17], we employ *ad hoc* waveforms to establish time-frequency upper limits on the emitted GW energy. We use sine-Gaussian signals with a fixed central frequency $f_0 = \{235, 1304\}\,\mathrm{Hz}$ and duration $\tau = Q/(\sqrt{2}\pi f_0)$ where $Q = 8.9$ is the quality factor. In our analysis, we use four *ad hoc* waveforms denoted as sg1-sg4 that are linearly and elliptically polarized, see Table 8.15. These *ad hoc* waveforms represent low and high frequency GW emission.

8.3.4 Systematic uncertainties

Our efficiency estimates are subject to a number of uncertainties. The most important of these are calibration uncertainties in the strain data recorded at each detector, and Poisson uncertainties due to the use of a finite number of injections (Monte Carlo uncertainties). Similarly to Ref. [17], we account for each of these uncertainties in the sensitivities reported in this paper.

We account for Poisson uncertainties from the finite number of injections using the Bayesian technique described in [207]. Specifically, given the total number of injections performed at some amplitude and the number detected, we compute the 90% credible lower bound on the efficiency assuming a uniform prior on $[0, 1]$ for the efficiency. All efficiency curves reported in this paper are therefore actually 90% confidence level lower bounds on the efficiency.

Calibration uncertainties are handled by rescaling the quoted h_{rss} and distance values following the method in [208]. The dominant effect is from the uncertainties in the amplitude calibration; these vary between a few percent at lower frequencies to 10% at higher frequencies in both L1 and H1. For this analysis, uncertainties are

conservatively set to 10% for H1 and L1 at the times of the five CCSNe studied [209, 210, 211]. The individual detector amplitude uncertainties are combined into a single uncertainty by calculating a combined root-sum-square signal-to-noise ratio and propagating the individual uncertainties, where we assume the errors for H1 and L1 are independent according to [212](the signal-to-noise ratio is used as a proxy for the loudness measures that the two pipelines use for ranking events).

This combination depends upon the relative sensitivity of each detector, which is a function of frequency, so we compute the total uncertainty at a range of frequencies across our analysis band for each CCSN and select the largest result, 7.1%, as a conservative estimate of the total 1-σ uncertainty. This 1-σ uncertainty is then scaled by a factor of 1.28 (to 9.1%) to obtain the factor by which our amplitude must be rescaled in order to obtain values consistent with a 90% confidence level upper limit. For the rescaling of the distance limits the reciprocal of the amplitude error correction factor is applied.

8.4 Search Results

8.4.1 Loudest events

This section will be filled with results after they are aproved

8.4.2 Detection efficiency vs. distance

This section will be filled with results after they are aproved

8.4.3 Constraints on Energy Emission

This section will be filled with results after they are aproved

8.4.4 Model Exclusion Statements for Extreme Emission Models

This section will be filled with results after they are aproved

8.4.5 Minimum Detectable SNR

The efficiency of detecting GW signals depends mainly on their energies, but it also depends on their morophologies. It is easier to detect signals that are short and narrowband than long and wideband ones. When the energy is spread over a large area of time-frequency map then it is difficult to create clusters of pixels. I investigate how the detection changes with the injected SNR for different SN waveforms morphologies. The results are produced for SN 2016B. As a minimum detectable SNR for particular waveforms I refer as a SNR at 50% detection efficiency. All results are estimated at fixed FAR=1/year.

Figure 8.10 shows the detection efficiency versus injected SNR for few GW emission models and table 8.16 gives a more detailed information on detectable SNR at 10%, 50% and 90% detection efficiencies. The easiest detectable waveforms are the long-bar waveforms from extremely rotating progenitor stars. These waveforms are narrowband

and very compact in time-frequency map. The Scheiddegger et al 2010 waveforms from rapidly rotating progenitor star models require larger SNR to be detectable. The efficiency for these waveforms increases with SNR, but does not flatten until SNR of 40. The less detectable waveforms are the Dimmelmeier et al 2008 waveforms and waveforms for neutrino driven explosions. The signals are more complex, they are non-deterministic. Their energies spread in time-frequency maps and they may have "island" of energy in these maps that are separated in time and frequency (e.g. strong funnels of material onto proto-neutron star in different moments of time). The least detectable GWs are Yakunin et al 2010 waveforms for non-rotating progenitor stars, they are relatively long and broadband. A lot of energy for these waveforms represented in time-frequency maps is comparable to the level of the detector noise and the energy is not spread uniformly. The detectable SNR for these waveforms is around 30.s

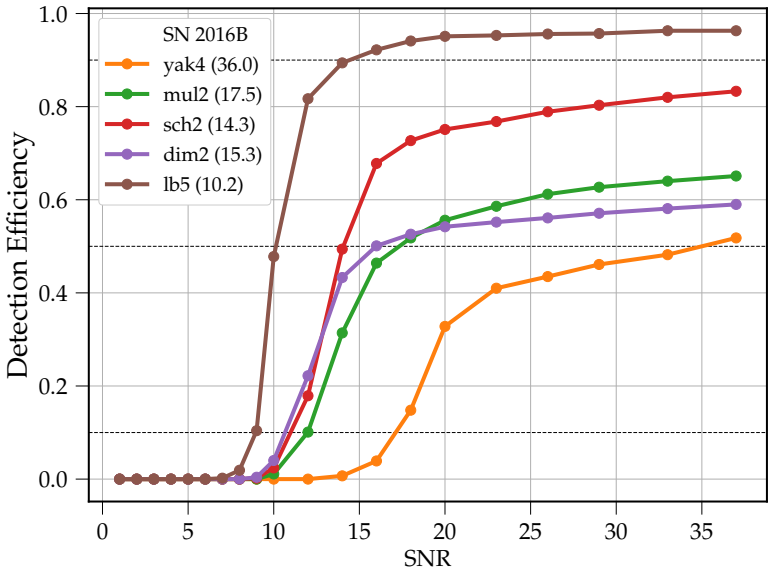

Figure 8.10: Comparison of detection efficiency versus SNR between few waveforms used in the search. The SNR at 50% detection efficiency is written in the brackets.

8.5 Interesting noise events during O1-O2

This section describes other studies that I have done during O1-O2 Observational Runs. The main GW sources that are currently detectable are the binary sources. GW from CCSNe are not likely to be detectable with the current interferometer sensitivities. However, during the observations we need to be prepared for variety of scenarios that theoretically we are unable to predict. For example, one scenario is the detection of GW without the detection of neutrino fluxes and when the supernova is invisible optically.

In sections 8.5.1 and 8.5.2 I will describe GraceDB interferometers noise events that triggered attention during course of the O1-O2 Science Runs.

Waveform	SNR at Detection Efficiency		
	10%	50%	90%
mul1	10.8	14.7	NaN
mul2	11.7	17.5	NaN
mul3	11.9	18.0	NaN
ott1	12.1	17.1	NaN
yak1	16.9	NaN	NaN
yak2	19.4	NaN	NaN
yak3	16.9	31.0	NaN
yak4	17.0	36.0	NaN
sch1	10.6	15.1	NaN
sch2	11.1	14.3	NaN
sch3	10.1	12.5	NaN
dim1	11.4	15.8	NaN
dim2	10.8	15.3	NaN
dim3	9.3	12.2	NaN
piro1	15.1	18.1	NaN
piro2	11.4	14.0	NaN
piro3	NaN	NaN	NaN
piro4	12.4	16.0	NaN
lb1	8.9	10.4	14.4
lb2	8.7	10.3	14.8
lb3	8.7	10.2	13.9
lb4	8.8	10.2	13.8
lb5	8.8	10.2	13.6
lb6	9.2	10.6	14.8
sg1	9.2	12.1	NaN
sg2	9.6	12.7	NaN
sg3	9.0	10.5	14.6
sg4	9.4	11.1	18.6

Table 8.16: SNR that is detectable at certain detection efficiency for SN 2016B with fixed FAR = 1/year. "NaN" means that the detection efficiency was not achieved.

8.5.1 G270580

During the course of O1 a GraceDB (system collecting GW candidates from on-line searches) event triggered attention for a potential detection of GW from CCSN. An event with a number G270580 was detected on Jan 20, 2017 12:30:59 UTC. The significance of this event is relatively high, FAR = 1.573e-07 Hz (4.96 per year), and it triggered attention of GW community. The left panel of figure 8.12 shows the CED reconstruction of the trigger from on-line analysis. The reconstructed waveforms of this event does not look like a signal from a binary system and the distance cannot be estimated. A question was raised if this might be a signature from a CCSN.

I did the analysis with estimating visile distances for various SN waveforms with O1 data. I have gathered some of my O1 simulations (FAR=1.0e-6Hz) and I plotted corresponding efficiency vs distance curves for:

- Extreme emission: rotbar
- Magnetorotational driven explosion: Scheiddegger 2013
- Neutrino driven explosion: Ott 2013, Yakunin 2015

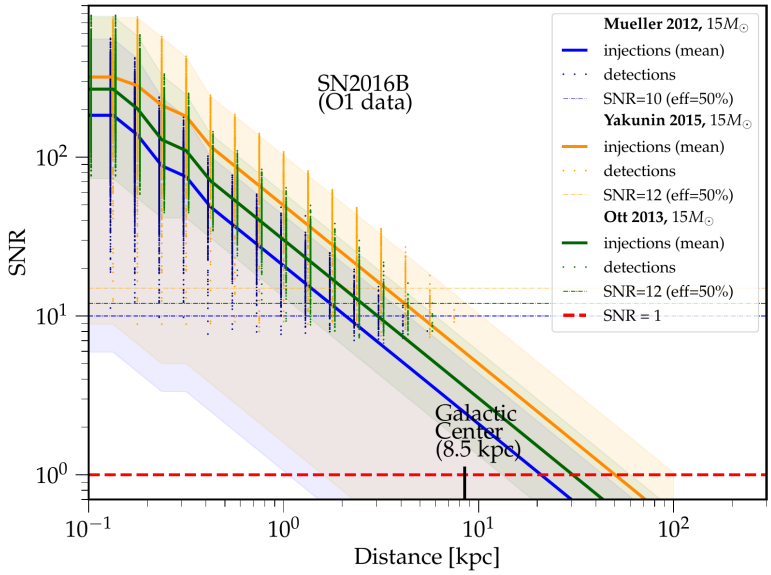

Figure 8.11: Minimum detectable SNR for detecting neutrino driven waveforms.

Right panel in figure 8.12 shows that currently for neutrino driven waveforms (Yakunin and Ott) the distances are few kpc, for magnetorotational driven waveforms (Scheidegger) it is few tens of kpc and finally for extreme emission models: few Mpc.

For a nearby SN we expect a large number of neutrinos, O(100) at 100kpc. There was no SNEWS alert during, so if the event is a SN then only some extreme emission could have produced such an event at distances, to be safe, >1Mpc. If an event was far BH formation and no nu nor EM counterpart present then also only extreme emission models should be considered. A SN with extreme GW emission could be very interesting, but it is rather not realistic.

8.5.2 G274296

Another interesting GraceDB event from the on-line searches happened on Feb 17, 2017 06:05:53 UTC and it was assigned a number G274296. The significance of this event from on-line analysis if FAR = 1.698e-07 Hz (5.36 per year). This trigger also triggered a lot of attention in GW Community.

Panels in figure 8.13 show the reconstructed time series of the event in initial cWB and BW analysis. The reconstructed initial part of this event looks like a GW from The signature of this event looks like GW from a rapidly rotating CCSN assuming optimal equatorial orientation. This signature was reconstructed both in cWB and BW. Additionally BW reconstructed a second part of the trigger that can be explained assuming strong SASI activity or low-T/|W| instability. A question was raised if it is possible that this event is a real GW from CCSN.

To answer this question, few considerations on possible neutrino fluxes and optical observations were performed. We expect O(100) of neutrinos for CCSN at 100kpc, see section 8.5.1. No neutrino flux was observed around the time of this event. No nearby CCSN was observed optically as well. Galactic dust, for example, might cause lack of optical observations. A situation when a very strong asymmetry during a very rapid core collapse and very unfavorable emission of neutrino might support hypothesis that the event is true GW.

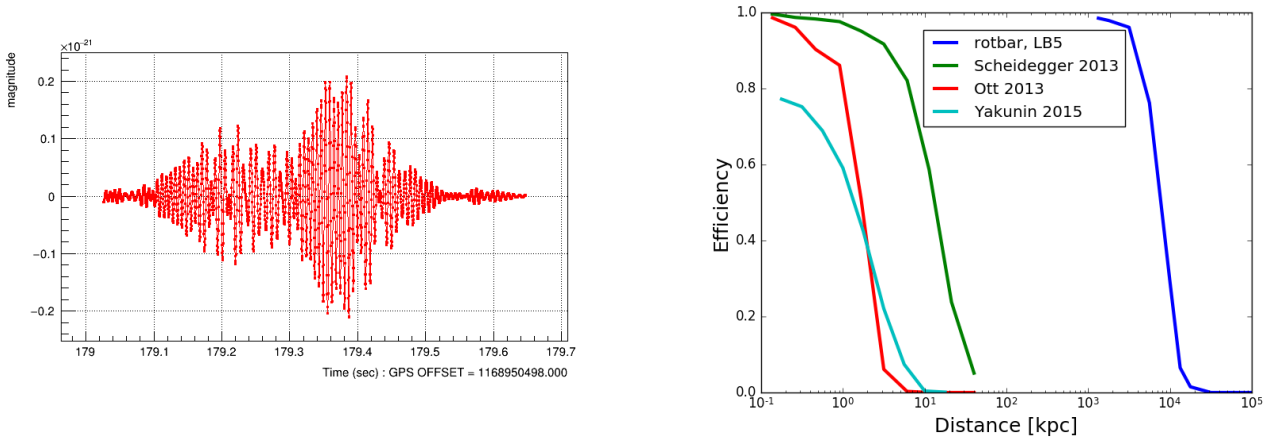

Figure 8.12: G270580 GraveDB event. Left: cWB online, Right: visible distances with O1 data.

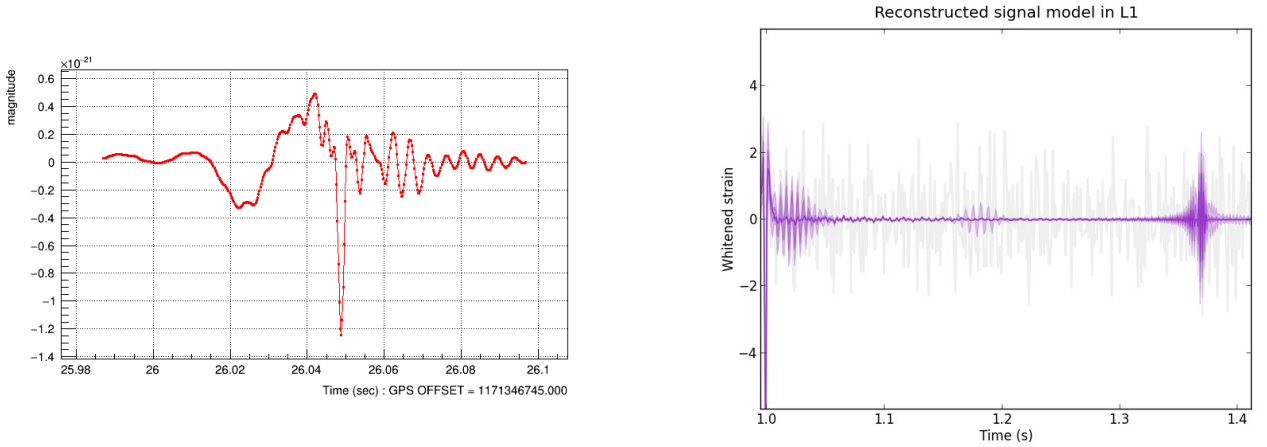

Figure 8.13: G274296 GraceDB event. Left: cWB online, Right: BW preliminary resutls.

Few additional studies were done. Based on SMEE analysis, the signature of the event is consistent with rapidly rotating supernova. However at the same time several glitch types (e.g. blip glitches) are detectable by SMEE as rapidly rotating waveforms.Finally, Q-scans reveal that the most likely this event is formed by coincident blip glitches.

Chapter 9

Detection perspectives with design sensitivities

9.1 Detectability of neutrino driven waveforms

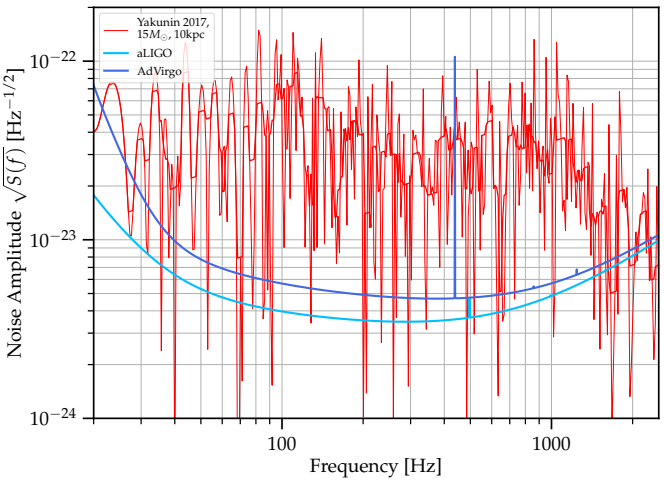

Figure 9.1: aLIGO and C15 waveform at 10kpc.

Data analysis for short GW transients is a well established field of research for compact binary systems (CBC, see e.g. [213, 214]). For CBC GW sources, the evolution of the system for the initial part of the signal (inspiral phase) is dominated by gravity and the equations can be solved with a very high degree of accuracy. Furthermore, the waveforms are deterministic in nature for the whole evolution of the source. The detection and parameter estimation approach for this scenario is matched filtering. GWs from CCSNe have a very different nature since most features are stochastic and the modeling presents several computational challenges. In this situation the default detection apporach is to use what people call, *excess power* methods. In these methods, measures of the unusual amount of energy that happen in a temporal and frequency consistent fashion between different interferometers are employed

to identify interesting candidates. In order to test detectability of the current model, the coherent WaveBurst (cWB) [195] is used.

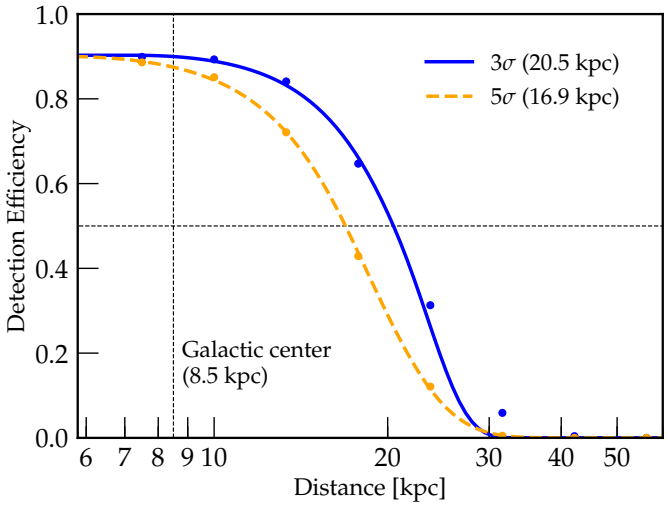

Figure 9.2: Detection efficiency of C15-3D waveform as a function of distance. The significance levels of 3σ and 5σ is calculated based on the background analysis with Gaussian noise recolored to the designed sensitivities of two Advance LIGO detectors and Advance Virgo detector. The 50% detection efficiency is written in the brackets and the distance of the galactic center is introduced with the vertical bar.

In the following analysis, one day of Gaussian noise was adjusted to the designed sensitivities of Advance LIGO detectors in Hanford and Livingston, and the Advance Virgo detector. We also chose the frequency range of the analysis to be $16 - 2048$ Hz that covers the low frequency (SASI, convection) and high frequency (g-mode) components of the C15-3D waveform. We performed two types of analyses: estimation of the background and sensitivity studies. The estimation of the background is realized by artificially shifting the data from one detector with respect to the other (see [17]), and if the temporal shift is longer than the maximum time of flight of the GW between two detectors, the reconstructed events cannot be of astrophysical origin. With this study we estimated the false alarm probability that random fluctuations of the data create triggers that could be confused with GWs. We chose significance level of 3σ and 5σ. We also assumed the presence of a galactic SN whose emitted neutrinos allow us to restrict the window of interest for the presence of a GW esmission to be 10 s.

In the second stage of the analysis we evaluate the sensitivity of the algorithm in detecting the C15-3D model as a function of distance. In this study, the waveform is added in random instances of the detector noise with amplitudes corresponding to the distance of potential supernovae (we call these injections). We use cWB with excess power tuning plus internal checks on the consistency of the reconstructed waveforms among different interferometers. We then calculate *detection efficiency* curves, which represent the fraction of detected CCSNe injections as a function of the distance. Figure 9.2 shows how the detection efficiency changes with respect to the distance at given confidence level. Based on this analysis the 50% detection efficiency for 3σ and 5σ confidence corresponds to 20.5 kpc and 16.9 kpc respectively, which is about two times the distance to the center of Milky Way. An important observation is that the sensitivity does not go up to 100%. This is caused mainly by the fact that the network of GW interferometers are not sensitive in some parts of the sky, making even nearby galactic GWs undetectable. This analysis shows that a reliable detectability of the galactic, C15-3D SN waveforms, corresponds to the Gaussian components of the

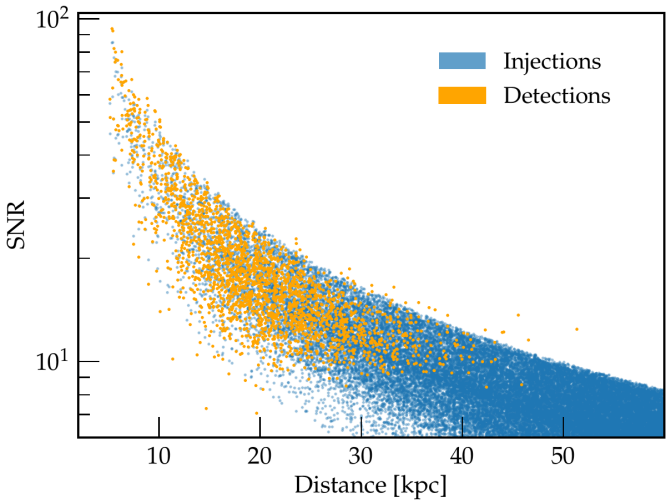

Figure 9.3: SNR of the detected events as a function of distance assuming uniform spatial distribution in the sky and accepting detections above 3σ confidence. The maximum detectable distance that can be reached is around 50 kpc.

noise, assuming it dominates the background statistics. In the future efforts, we will repeat the study for real noise with non-Gaussian transients and, equally important, we will modify the algorithm to preferentionally select events presenting the deterministic features expected in these CCSNe GWs. Such analysis will also be informative for planning future designs of the laser interferometers.

Figure 9.3 depicts how the signal-to-noise ratio (SNR) of the detected triggers changes as a function of the distance. In this study we injected the C15-3D model, assuming uniform spatial distribution in the sky, at the distance range $5 - 60$ kpc. We accepted detected events that are above 3σ confidence. From the plot it can be seen that, for this model, the maximum distance that can be reached is around 50 kpc.

Chapter 10

Galactic Supernova

The next Galactic Supernova will be one of the most important astronomical events of in our century. The event will trigger large attention in scientific community accross different fields and in the public. A nearby supernova will allow to bring new understanding about centers and dynamics of exploding stars. Different messengers will carry different information about the stars (see section 3).

Last Core-Collapse Supernova was visible around four centuries ago. Since that time the optical telescopes, neutrino detectors and GW obseratories were invented. Several studies were conducted that include proposed strategies for observing Galactic supernova [ref,ref]. Most of these plans are related to observation in electromagnetic and neutrino spectra. The observation of GW from CCSN faces a lot of challenges. The plans of detecting GW from CCSN have not reached such a degree of sophistication as for the electromagnetic and neutrino messengers.

In section 10.1 I will present the current LVC plan for searching for GW triggered by SNEWS alert. In section 10.2 I will describe potential content of a detection paper. In section 10.3 I will talk about possible more extensive studies after detection paper is published. In section 10.4 I will talk about special case when data from only one detector is available during the time of SNEWS alert.

10.1 Introduction

As CCSN group chair I have developed and maintained the plan for a nearby CCSN scenario. It is predicted that the supernova will be detected first by the neutrino detectors and a rapid information will be circulated via SuperNova Early Warnig System (SNEWS) alerts.The GW search will be triggered by the neutrino SNEWS alert. The sensitivity of detecting neutrinos from CCSN is around 100kpc. This means that it will cover both Galactic and near extra-Galactic CCSN. The GW search will cover these two scenarios. Upon SNEWS alert the first will be conducted on-line rapid search and then more in-depth off-line search.

SNEWS alert

A nearby CCSN will produce a prominent signal in the global array of neutrino detectors such as Super-Kamiokande [60, 215], Borexino [216, 217], and LVD [218, 219]. In preparation for such an event, the neutrino community has an established alert system known as SNEWS [220]. SNEWS will provide an automated email alert

of "GOLD" events to registered users with an estimated latency of five minutes or less.[1] The best pointing accuracy will be approximately $5^\circ - 20^\circ$ from Super-Kamiokande [221], but this information may not be immediately available at the time of the alert. We therefore envision an all-sky scan for GWs at the rapid-follow-up stage and incorporate directional information in a subsequent offline search.

Observation Scenarios

In the case when data from two or more detectors are available during SNEWS alert the method of assigning the significance of GW candidate will follow the currently developed SN Search methods. In terms of extracting physical information many methods are under development.

SNEWS-triggered search: The goal of the SNEWS-triggered analysis is to provide an online search for a GW burst associated with a galactic or SMC/LMC CCSN. The triggered online search will be carried out. After a SNEWS trigger, we will carry out deeper offline analyses, which will complete within a few days. An important issue for this search is that it is possible that at the time of a SNEWS trigger only one detector will be online. Extreme care will be required to vet detection candidates and to take full statistical advantage of the information provided by SNEWS. However, currently the only statistical advantage we get from the neutrino obseration is the tight on-source window. It is understood that poor quality of the data around the SNEWS trigger will affect the strength of the detection statement. For example if the data contains a large population of unvetoed non-Gaussian glitches the statistical confidence in the detection. Single-detector searches with and without external triggers have been carried out before by Virgo [222, 223] and we will build upon the experience gained by this previous work.

Publication Plan

Publication strategy that will be incorporated in case of a SNEWS alert:

1. Detection Statement paper
2. Follow-up analysis papers

10.2 Detection Statement paper

Main planned content of the detection paper will be:

- detection or non-detection statements along with the significance of the loudest candidate,
- reconstruction of the waveforms with cWB, BW and pipelines that are reviewed at the time of SNEWS alert.

The detection statements will be based on the off-line analysis. We will use an on-source window based on the timing of the core collapse from the SNEWS alert.

[1] The false alarm rate for SNEWS alerts is estimated to be less than one per century [220].

Timeline

The timeline of releasing the paper is estimated to be around 1-3 months It will depend on many factors and this will need to be throughout discussed within LVC collaboration.

SNEWS alerts that will trigger the search will provide crucial information needed for calculating the significance of GW candidate. The information about a nearby supernova will be known immediately from the SNEWS alert and this information will be available publically. The neutrino fluxes will allow to estimate the timing within few miliseconds of the moment of the core collapse. It is a crucial information needed to establish an on-source window used for calculation of the the significance of the GW candidate.

The electromagnetic messeger from a supernova appears usually hours or days after a core collapse when the shock breaks the surface. These optical observations of the supernova might not provide any information that are crucial for the detection statements.

As a reference, the timescale of releasing the first and the second binary black hole detection papers was around 5 months. The reason for such a long timescale was to assure that the GW candidates were GW. In case of binary neutron star detection the timeline was 2 months. This timeline wass an effect of a compromise between GW and Astronomy communities. In case of a narby supernova the crucial ingredients to estimate the significance of the event will be publically available. We predict that the compromise between all communities will allow to publish the detection paper within 1-3 months after SNEWS alert.

On-line analysis

SNEWS trigger will give information about nearby Supernova after few seconds and the alert will be rapidly circulated to the Scientific Communities. The first GW search will be conducted by an online SNEWS-triggered low-latency, rapid-follow-up search for GWs from nearby CCSNe. The motiviation for the on-line search is to provide alerts to the scientific community containing the GW-estimated sky position, ahead of the light emission of SN that is expected up to a day later. This infomration will be important in order to possibly be able to observe a shock breakout.

Off-line analysis

Subsequent to a SNEWS alert with or without GW detection candidate from the online search, we will carry out deeper off-line analyses with cWB. In the case of a SNEWS alert, the cWB analysis will be rerun off-line as needed after any significant changes to calibrations, data quality, or as further information on the supernova is received.

A Galactic CCSN will be an exciting event and the scientific community will want to know as soon as possible if we have a detection. Though pipelines that are not reviewed at the time of SNEWS trigger will not enter the search unless they can provide an important scientific merit that cannot be provided by any other pipeline. In the S5/A5/S6 SN search paper [17] we developed methodolgy on how to combine results of two or more pipelines.

Estimating the GW trigger significance

In order to estiamte the significance GW candidate we calculate the False Alarm Probability, FAP, same way as in the Optically Triggered searches (equation 8.1):

$$FAP = 1 - \exp\left(-T_{\rm on} \times FAR\right) \tag{10.1}$$

where $T_{\rm on}$ is an on-source window and FAR is False Alarm Rate.

The on-source window calculations will come from publically available SNEWS alert. At the first approximation, the on-source window is assumed to be conservative and tentatively we assume it to be $T_{\rm on} = 10$s.

False Alarm Rate is defined as (equation 4.57):

$$FAR = N/T_{\rm bkg}, \tag{10.2}$$

where N is the number of false events and $T_{\rm bkg}$ is the total livetime accumulated by artificially shifting data. The amount of background data used will depend on the significance of the GW candidate we want to achieve. FAP can be approximated as:

$$FAP \approx T_{\rm on}/T_{\rm bkg}. \tag{10.3}$$

For example, the 5σ confidence level corresponds to FAP$\sim 2 \times 10^7$. Assuming that $T_{\rm on} = 10$s the amount of background data needed is $T_{\rm bkg} \sim 1.5$years. In case we have data from two detectors available, then the minimum amount of off-source window data $T_{\rm off}$ can be estimated from equation 4.59. Assuming that $T_{\rm seg} = 600$s and we do one-second long shifts, then we need minimum of $N = 6$ segments that gives $T_{\rm off} = T_{\rm seg} \times N = 1$ hour of data coincident between two detectors. (see section 4.5.1 for more details about lags and super-lag procedures). Assuming 40% coincident duty cycle, the total amount of data around the timeof SNEWS alert is around 3 hours.

Waveform Reconstruction

Upon detection, effort will be directed toward waveform reconstruction and estimating basic signal properties such as central frequency, time-frequency evolution.

Only the pipelines that are reviewed at the time of the SNEWS alert will be included in the first publication, unless they bring a significant contribution to the waveform reconstruction studies.

10.3 Follow-up Studies papers

Following the results from the detection paper, the follow-up studies will be conducted in order to extract physical information from the trigger or placing upper limits on supernova models. In case when a detection gives evidence to answer long awaited Science Questions, like explosion mechanism, or when a GW signature has visible a particular feature, like an evidence of SASI oscillation, then the corresponding papers will be published immediately or within weeks/months after the detection paper. The overall timescale for the follow-up studies is undefined. The observation of the Supernova in the electromagnetic spectrum, better understanding of neutrino fluxes or more sophisticated numerical models of the explosion together with the GW detection will be bringing

more opportunities to advance our knowledge on the nature of exploding stars.

The follow-up studies will be based primarily on the methods that are already developed or that are currently under development for the Optically Triggered Searches and Parameter Estimation. Section 12 summarizes some of the efforts. Each method will used to extract physical information from the GW.

10.4 Single Detector Case

It is very important to address the detectability of a Galactic CCSN in the case of only one detector collecting data at the time of a SNEWS alert. In the next 5 years we have around 20% probability of having only single detector online during SNEWS alert. Therefore, establishing the limits and confidence with which a detection can be claimed in the event of an exploding galactic supernova could be necessary.

The main challenge in establishing a detection with only one interferometer is that no consistency constraints can be applied among different detectors as in the case of a network of two or more interferometers. This allows a population of loud noise glitches to survive in the analysis and as a consequence a possible reduction of statistical significance of GW induced candidate.

The current methodology I am investigating for the LVC Supernova Group uses configuration of cWB for two interferometers with the data of the second interferometer being just a replica of the data from the first. The detection potential of this methodology is not fully explored yet. The drawback of having only one interferometer is that we cannot use consistency tests between interferometers. These tests are important to reduce the population of non-Gaussian glitches. These glitches are statistically unlikely with respect to the Gaussian background and can reduce the statistical significance of an event that is legitimately produced by GW.

For the challenge of increasing the statistical significance off GW candidates we explore two approaches. In both of them we compare populations of the reconstructed interferometer noise transients and the reconstructed injected CCSN waveforms:

- Determining the selection cuts by visually comparing the distributions of the two populations in planes where the axes are morphological parameters (duration, central frequency, corellation, etc) or physical parameters (still under developement). The cuts are supposed to eliminate noise induced events but spare GW induced ones.

- Optimizing the selection cuts using Machine Learning algorithms.

I carrried out preliminary work on the first approach. The specific results show that for a specific waveform family it is viable to claim a detection of GW from a supernova with one detector. These results are described in section 10.4.

In the second approach, we study the distributions of background and simulation triggers that are separated by the Machine Learning algorithm. This approach allows optimizing cuts in a multidimensional paramenter space. The goal is to identify and remove as many possible loud non-Gaussian transients that usually are reduced by consistency checks when more than one interferomteter is collecting data. The application of Machine Learning techniques for the single interferometer scenario is particularly interesting because the morphology of these events is expected to be quite different than those induced by GWs.

At the moment, the analysis is performed only on the strain GW channel. However, when GW is passing through the detector, it leaves traces in the other auxiliary channels. In future development, the method will be using not only reconstructed trigger's properties from using the strain channel, but also their traces in other channels.

Initial Results

At the moment, a cWB approach has been used to carry out the analysis. This coherent method requires data from at least two detectors. In order to overcome this in case of analyzing data from only one detector, we perform a two interferometer search where one data set was the exact copy of the other. For analysis of L1 detector we create a L1L1 network.

In this study I took 5 days of O1 public Science data. The coincident duty cycle is 2.93 days however only data from Livingston detector were used. The time shifts cannot be performed on a single detector data, so the analysis must be performed only on zero lag data. A realistic explosion model, Yakunin 2015 waveform family, were used in this study.

Background and Efficiency The left panel of the figure 10.1 show the False Alarm Rate of the background triggers for a L1L1 network and H1L1 network for comparison. For triggers in single detector mode the effective correlated SNR ρ is practically SNR (the data streams of cloned data is fully coherent, $cc \approx 1$). It is clearly visible that FAR for L1L1 network is orders of magnitudes larger than for a regular L1H1 network. Moreover, the noise triggers are much louder.

The right panel of the figure 10.1 depicts the detection efficiency curves for yak1 waveform for two and single detector networks. From this plot it can be concluded that the detectability of the waveforms for two and single detector networks are comparable. One interesting observation is that the efficiency goes higher for L1L1 network comparing to H1L1 network. Possible reason would be that the events in single detector case are more coherent ($cc \approx 1$) and they are easier detectable

From the figure 10.1 we can conclude that the detectability of GW from a nearby CCSN at a certain significance level will depend greatly from the ability of removing the noise triggers. A great advantage of search for GW triggered by SNEWS alert over blind searches for binary systems, for example, is a very good timing constrain. It allows to accept GW candidates at lower the FAR without loosing their significance.

Triggers distributions After background and simulation for single interferometer were created the next step is to remove the loudest events from the background without decreasing the efficiency curves. We make comparisons between the distributions of the reconstructed events from background and simulation studies. These two distributions are plotted on top over the other and we explore different reconstructed parameters. The panels in figure 10.2 show how these distributions, the backround events are depicted as blue rectangulars and simulation events in depicted as red dots. In this figure four reconstructed properties are considered: duration, bandwidth, central frequency and volume (number of wavelet pixels used for the reconstruction). All of these reconstructed properties are plotted against ρ.

Many background triggers are very loud and at the same time many of them are very narrowband. The loud noise events last also very long, order of even few seconds. The central frequency of the loudest events is estimated to be less than 500Hz.

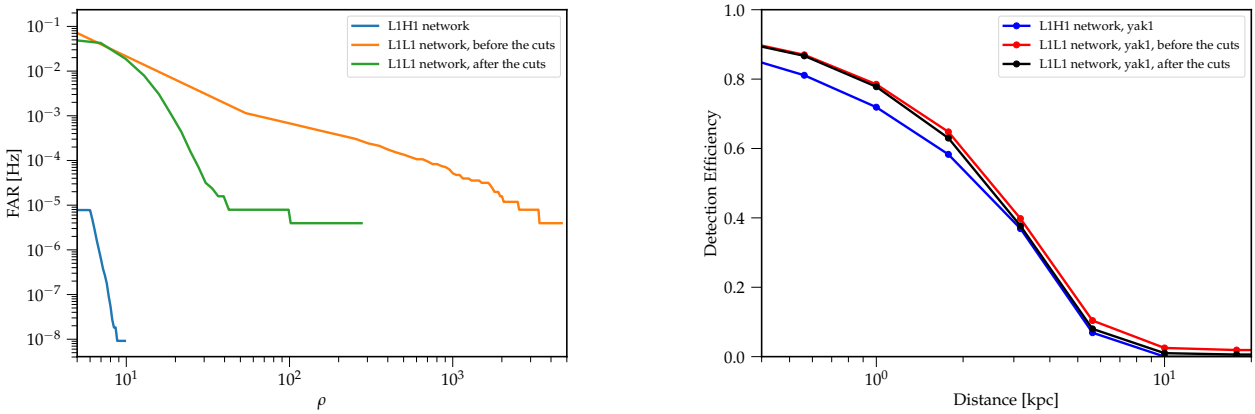

Figure 10.1: Comparison between background (left) and detection efficiency (right) for single detector case analysis and for L1H1 detector network.

On the other hand, the reconstructed properties of the injections depicted as red dots in figure 10.2. Four waveforms of Yakunin 2015 waveform family according. They are broadband and they are and their bandwidth is usually larger than the bandwidth of the loudest noise events. Similar situation can be seen with the peak frequency. The oscillation of proto-neutron star produce the high frequency GW component, above around 500Hz, while the glitches have lower central frequencies. The duration of neutrino driven supernova waveforms used in this study is less than a second. However, a conservative estimatate of their duration is up to 3 seconds, which in turn is still smaller than the duration of the the loudest glitches that can last up to even 30s.

Several other estimated parameters were also considered, such as d1, f1, low0, hgh1, bw0, nrm (see section 4.4 for their description). The distributions of the background and simulation triggers were not as robust as for the described for parameters. However, they will play an important role in the Machine Learning studies described in section 10.4.

Selection cuts The selection cuts set a division between the populations of detector glitches and recontructed GW waveforms. These cuts can be determined experimentally, the GW interferometers are complex instruments and the population of glitches cannot be predicted accurately.

In this study we determine possible cuts by studying visually the reconstructed properties of the two populations in a simple parameter space explained earlier. Based on the plots from Figure 10.2 one possible way to efficiently remove the loud background events is to make the following cuts:

- dominant frequency: frequency[0] $>$ 420 Hz
- duration: duration[1] $<$ 5s

The impact of these cuts can be seeon in figure 10.1. As expected most of the loudest glitches were removed and the FAR went down around two orders of magnitude for $\rho > 20$. At the same time, these cuts did not impact significantly the detection sensitivity for yak1 waveform. Moreover, many falsely detected GW events (events with SNR$<$10 that do not allow efficiency going to zero) were removed with the selected cuts

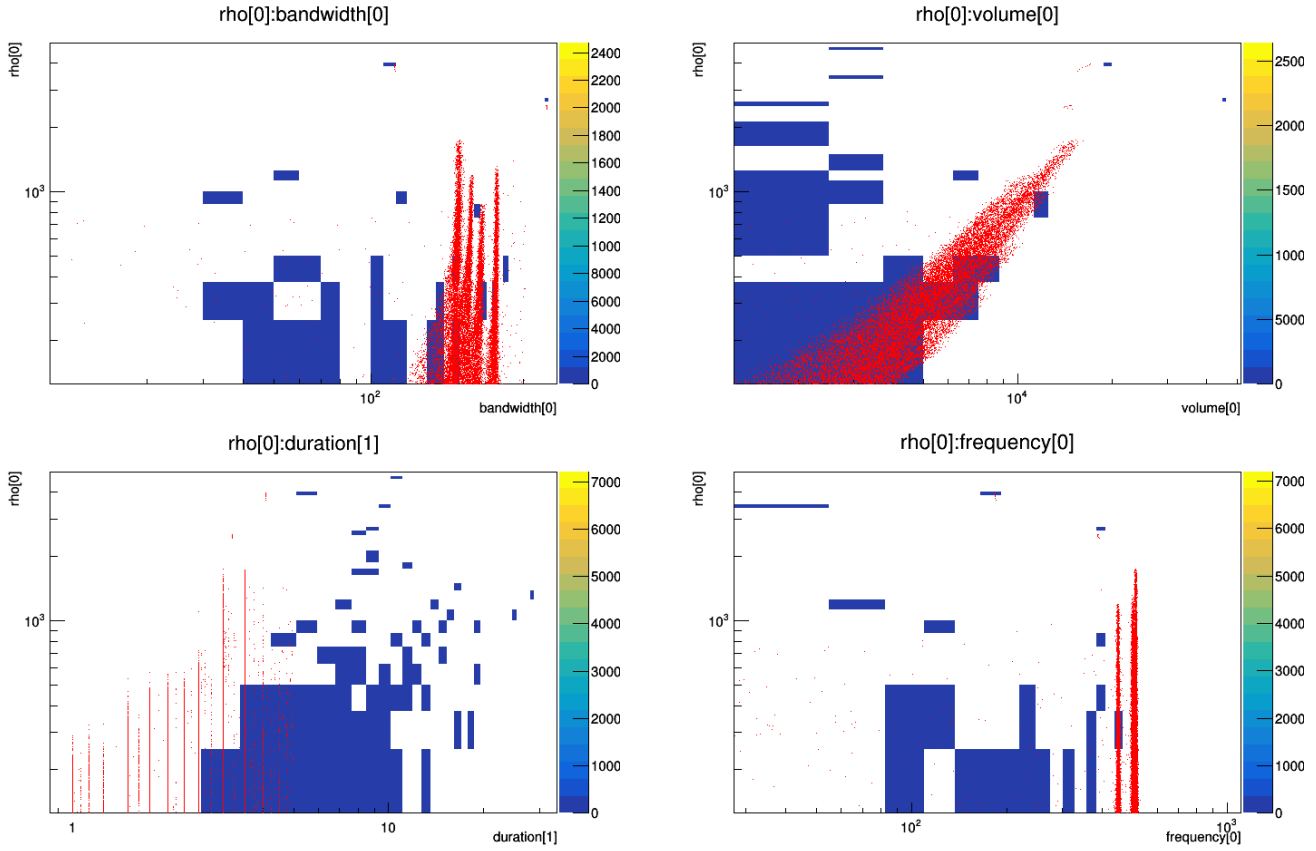

Figure 10.2: Example distributions of the background triggers and reconstructed triggers that were injected at different distances. Different panels compare distributions for different parameters.

L1H1 vs L1L1 performance comparison In order to compare the performance in the detectability of SN waveforms, I analyze visible distance at False Alarm Probability (FAP) at the significance level of 3σ, $FAP(3\sigma) \approx 2.7 \times 10^{-3}$. FAP can be approximated as $FAP = FAR \times T_{\rm on}$, where $T_{\rm on}$ is the duration of an on-source window. Here we assume that $T_{\rm on} = 2$s. The corresponding FAR is then $FAR = FAP/T_{\rm on} \approx 1.4 \times 10^{-3}$Hz. From figure 10.1 we can read that in order to accept detections of GW signals above 3σ confidence, they need to have $\rho \gtrsim 18$.

Table 10.1 shows the results comparing visible distances for L1H1 and L1L1 detector networks, while figure 10.3 shows the detection efficiencies for these two networks. The visible distance is around 30-50% worse in single detector case.

Network	dist@50% [kpc]			
	yak1	yak2	yak3	yak4
H1L1	2.31	2.81	2.91	4.62
L1L1	1.61 (-30.7%)	2.10 (-25.3%)	1.54 (-47.%)	3.00 (-35.0%)

Table 10.1: Comparison of visible distances between for two and signle detector cases at 3σ confidence level assuming $T_{\rm on} = 2$s.

This study demonstrates that given a certain model of explosion, it might be possible to define such selection

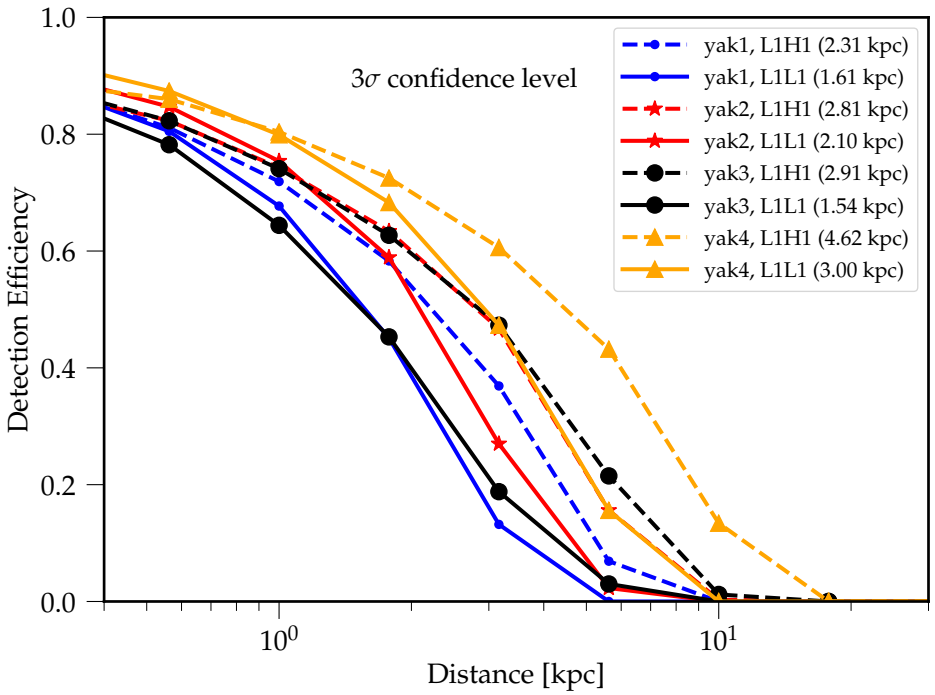

Figure 10.3: Comparison between performance between analysis of detection efficiency at 3σ confidence level for two detector case and single detector case (assuming $T_{\rm on} = 2$s). The visible distance in case for L1L1 network is around 30-50% worse than the corresponding distances for L1H1 network.

cuts that allows notably increase a significance of a GW candidate. The background in single detector case can be significantly reduced if we assume certain emission model Based on this study the the visible distance for single IFO is 30-50% worse in single detector case comparable to the distances for 2-detector network.

This analysis is based on a particular model of GW emission. The final selection cuts are chosen manually and it's choice is not guaranteed to be the most optimal. In case when several different models of emission is used, the situation becomes more complicated.

The next step in the analysis will be to optimize these selection cuts and automatize their choice. With the next step of the development we will be testing the Machine Learning algorithm performance that will help in optimization of the cuts.

Optimizing analysis with Machine Learning

The initial results for single detector case and one waveform family look promissing. The next step in the method development is the optimization of the selection cuts. For this purpose we use Machine Learning algorithms. During the course of writing the dissertation, the method is under development. I am presenting here the results from setting up the baseline for this development.

In order to perform accurate studies with Machine Learning algorithms, it is imporant to use as many triggers as possible for training purposes. A number of few thousands is an generally acceptable number. Unfortunately it

is an issue for the studies with single interferometer data that I will describe in more details.

For this analysis, we used data collected in Hanford detector during O1. The amount of data was choosen to be 4.03 days that corresponds to the on-source window of SN 2016B. It gives direct comparison to the results obtained with the regular two-detector analysis. The amount of data that passed the data quality cuts is 2.01 days.

Background. The data was used to perform the background analysis. Figure 10.4 depicts FAR in terms of ρ that is practically a SNR of the signal. The two days of data allowed to reach $FAR = 5.6 \times 10^{-6}$ for the loudest noise events. The number of noise triggers detected by cWB is 20,264. This number is sufficient to perform the Machine Learning.

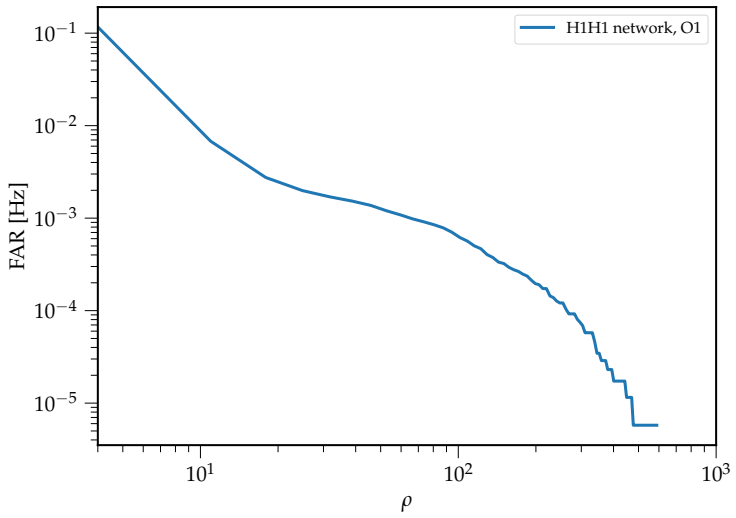

Figure 10.4: Background analysis for single interferometer studies with Machine Learning.

Simulation The production of the reconstructed GW triggers

In this study we considered all waveform families that were used in the O1-O2 Optially Triggered SN Search. A large range of injection distances was used to produce the trigger lists. Table 10.2 shows the detectability ranges for all the waveforms. These distances are estimated without considering the background, all triggers that were detected are included.

Explosion mechanism	Waveform identifier	O1, distance [kpc]
Neutrino driven explosions	yak1/yak2/yak3/yak4	2.33 / 3.13 / 3.21 / 5.03
	ott1	2.05
	mul1/mul2/mul3	1.64 / 0.82 / 0.78
MHD driven explosions	dim1/dim2/dim3	7.22 / 11.2 / 19.5
	sch1/sch2/sch3	0.45 / 30.1 / 35.5
Extereme Emission models	piro1/piro2/piro3/piro4 ($\times 10^3$)	1.38 / 3.55 / 7.80 / 21.0
	lb1/lb2/lb3/lb4/lb5/lb6 ($\times 10^3$)	0.75 / 2.20 / 1.66 / 3.72 / 11.80 / 4.58

Table 10.2: Detectability of SN waveforms for Single Detector Case study before applying any selection cuts.

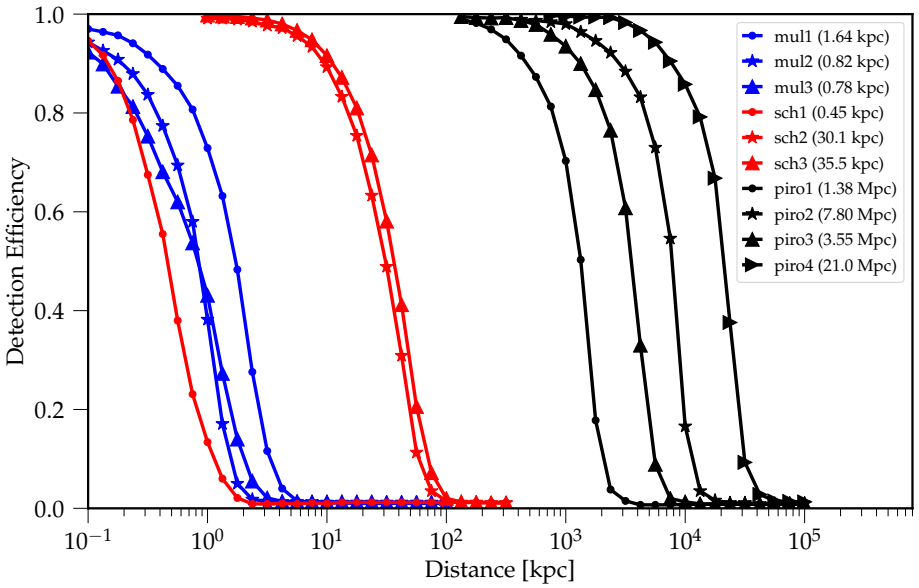

Figure 10.5: Background analysis for single interferometer studies with Machine Learning.

Table 10.2 shows numbers of available triggers at large range of distances. However, in order to find a sufficient number of triggers for training purposes, the number of options is limited. Moreover, the training cannot be biasad to any given morphology - the number of triggers for each waveform needs to be the same.

At small distances many waveforms are too loud that they are whitened out during the search. When the efficiency starts dropping, the triggers are removed (in the next version of triggers this constrain might taken out).

At large distances many of the detected triggers are noise events (the real noise is non-Gaussian producing loud events that imitate GW). Unfortunately they cannot be easily removed - for single detector the coherent tests cannot be performed. It needs to be discussed for the next version of triggers. To quantify the effect, let's take a look at yak4 at 100kpc. There were 1456 injections and there were 8 detected events (all of them are glitches) which is $\sim$0.5%. Looking at some other waveforms, the effect is less than less than $\sim$1%. We want to address it with the next version of triggers (plus address few other issues), but right now we do not have a working solution to solve it.

There is also a large spread in detectability between different waveform families (as expected, given large spread in their energies). Fairly good overlap between all waveform families is at 1kpc.

Assuming that each model morphology had the same chance to be true (the explosion mechanism is unknown), Machine Learning algorithms also assume that all the processed triggers have equal importance. However it is not fully fulfilled with these triggers. For example, the number of ott1 triggers is roughly the same as yak1/yak2/yak3/yak4 combined, sch1/sch2/sch3 combined, dim1/dim2/dim3 combined, mul1/mul2/mul3 combined. This is caused by the way the cWB runs were performed (each waveform family has separate run). This issued needs to be discussed before creating next version of the triggers.

It is crucial to increase the statistics for Machine Learning studies ot obtain robust results. It is especially

D [kpc]	mul1/mul2/mul3	ott1	yak1/yak2/yak3/yak4	sch1/sch2/sch3	dim1/dim2/dim3	Total
0.03	0/1855/1924	0	0/0/0/0	0/0/0	0/0/0	3,779
0.04	0/1848/1905	0	0/0/0/0	1886/0/0	0/0/0	5,646
0.06	0/1833/1891	0	0/0/0/0	1874/0/0	0/0/0	5,598
0.07	1863/1821/1861	5749	0/0/0/0	1849/0/0	0/0/0	13,143
0.10	1850/1793/1820	5740	0/0/0/0	1805/0/0	0/0/0	13,008
0.13	1840/1761/1771	5734	1000/0/0/0	1749/0/0	0/0/0	13,855
0.18	1826/1726/1684	5726	1348/1387/1370/1434	1651/0/0	0/0/0	18,152
0.24	1796/1671/1602	5695	1332/1366/1353/1425	1500/0/0	0/0/0	17,740
0.32	1752/1591/1484	5637	1312/1350/1328/1409	1288/0/0	1849/0/0	19,000
0.42	1696/1471/1343	5567	1282/1326/1309/1398	1058/0/0	1838/1832/0	20,120
0.56	1631/1319/1223	5434	1233/1283/1283/1377	725/0/0	1818/1823/1928	21,077
0.75	1540/1104/1059	5249	1178/1233/1235/1356	440/0/0	1798/1796/1923	19,471
1.00	1391/727/850	5008	1113/1180/1182/1316	255/1884/1967	1761/1772/1914	22,320
1.33	1206/325/539	4601	999/1114/1098/1262	115/1883/1964	1713/1740/1896	20,455
1.78	922/96/276	3798	863/1006/994/1193	41/1880/1962	1646/1706/1872	18,255
2.37	527/36/108	2494	717/896/892/1099	18/1873/1955	1557/1647/1844	15,663
3.16	221/26/42	1256	547/735/745/967	17/1858/1948	1452/1587/1795	13,196
4.22	77/25/27	495	289/521/557/853	19/1848/1931	1292/1510/1747	11,191
5.62	28/24/27	160	88/251/286/672	18/1818/1906	1143/1405/1653	9,479
7.50	22/24/26	85	31/60/80/464	21/1775/1869	931/1258/1539	8,185
10.00	21/22/26	72	20/23/30/193	20/1697/1806	681/1067/1422	7,100
13.34	21/22/26	65	18/13/22/53	22/1584/1719	341/822/1272	6,000
17.78	20/22/26	63	16/8/19/16	22/1434/1597	82/473/1076	4,874
23.71	19/22/26	61	14/7/18/11	22/1204/1410	33/141/830	3,818
31.62	19/22/24	60	14/9/15/8	22/929/1146	21/45/538	2,872
42.17	19/22/24	59	14/9/15/8	22/587/813	20/24/200	1,836
56.23	19/22/24	59	14/9/15/8	22/214/406	19/22/55	908
74.99	19/22/24	59	14/9/15/8	22/67/142	18/22/24	465
100.00	19/22/24	60	14/10/15/8	22/29/40	18/21/20	322
133.35	0/0/0	0	0/0/0/0	22/23/26	18/21/20	130
177.83	0/0/0	0	0/0/0/0	22/22/23	18/20/19	124
237.14	0/0/0	0	0/0/0/0	22/21/21	18/21/19	122
316.23	0/0/0	0	0/0/0/0	22/21/22	17/21/19	122

Table 10.3: Detectability of SN waveforms for Single Detector Case study before applying any selection cuts.

important when the efficiency is small and signals are weak. There are several directions that need to be explored in order to increase statistics. Some of them are:

- Using all O1 data period for ML training purposes.
- Using triggers from both L1 and H1 detectors.
- Making injetions closer (every 10s instead of 30s, for example), but without causing problems with whitening.
- Maximizing further the nearby injections. Repeating injection procedures few times at different unique times. This will pin down the injection rate effectively every 1-2s.

Chapter 11

Hardware Injections of SN signals

Hardware injections (hwinj) are simulated GW signals added physically to the interferometer. During this injection the actuation system displaces the test masses according to certain GW morphology. In comparison, during the software injections the GW signals are added after data is recorded, while for hardware injections, the GW signals are added lively while data is recorded.

Hardware injections give unique opportunities to test several aspects of the GW analysis. The main motivations of doing hardware injections:

- They allow to test on-line anaysis and generation of alerts.
- Measure correctness or validate methods of on-line or off-line search analyses and effect parameter estimation

In this section I will describe the results of hardware injections of SN waveforms that were performed during O2 and perspectives of doing hardware injections in upcoming Science Runs.

11.1 Pcal limitations of injecting SN waveforms

During safety saturation tests it came up that the suggested supernova waveforms cannot be injected at proposed distances. Dominant frequency of SN waveforms is high frequency (above the 400Hz) and the strain must be orders of magnitude smaller than in low frequencies to be safely injected with Photon Calibrator (PCAL). This limitation of PCAL is described [20]. Figure 11.1 shows that the amplitudes of injecting high frequency signals is more limited than in lower frequencies.

A photon calibrator is used to perform injections. The main component of the system that sets limitation is the laser that excites the test mass mirror and the power of that laser. Each waveform that is hardware injected needs to be tested whether they do not require more laser power than is available.

Conversion of the strain to Pcal counts or Pcal counts

In order to inject a waveform into the interferometer, an actuation system of needs to be placed. Currently, a Photon Calibrator (Pcal) is used to inject monochromatic calibration lines and it is also used for making hardware

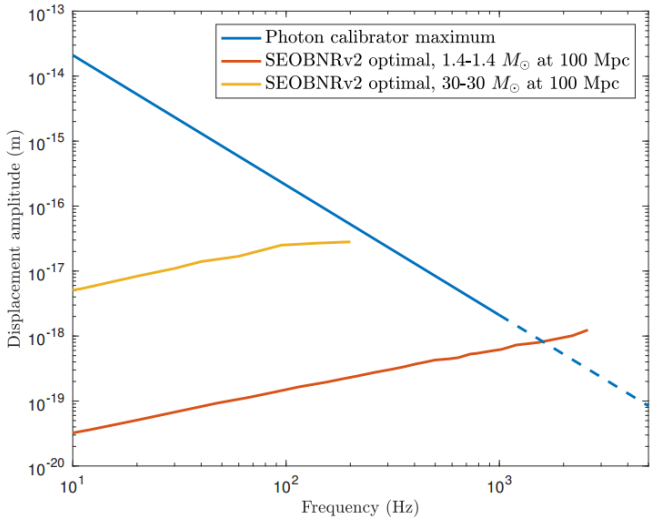

Figure 11.1: PCAL limitations [20]

injections. Pcal excites the test mass mirrors through a laser light and the power of the laser limits the abilities of injecting the GW signals. Before the waveform.

Before the waveform is injected, its strain needs to be converted into amount of light that is required to excite the mirror at each moment of time. It can be measured in *pcal counts*, that are "portions of light", or power. Currently the limit of the Pcal system is determined to be 57,000 counts, but it will be reviewed before O3.

The amount of power required to excite the mirrors grows with the frequency. Though, the injection of waveforms with strong high frequency component is more difficult (large Pcal power) than injecting the waveforms with strong low frequency component. Figure 11.2 shows an example of a rapidly rotating waveform at 10kpc that saturate Pcal.

11.2 Initial injections

The main motivation of doing the hardware injections during before O2 was to estimate the impact of calibration uncertainty on detection efficiencies and parameter estimatation. The main pipelines to be tested were cWB, SMEE and BW. Additionally, these hardware injections would allow to test how well we can distinguish different SN explosion mechanisms.

During Engineering Runs arund O2 we performed the first hardware injections of realistic models of SN explosions. I will describe the preparation process and possible solutions. Unfortunately they were too weak to be detectable.

Choice of waveforms and saturation tests

In order to choose the optimal set of waveforms that can be hardware injected, several factors need to be taken into account. The main aspects are:

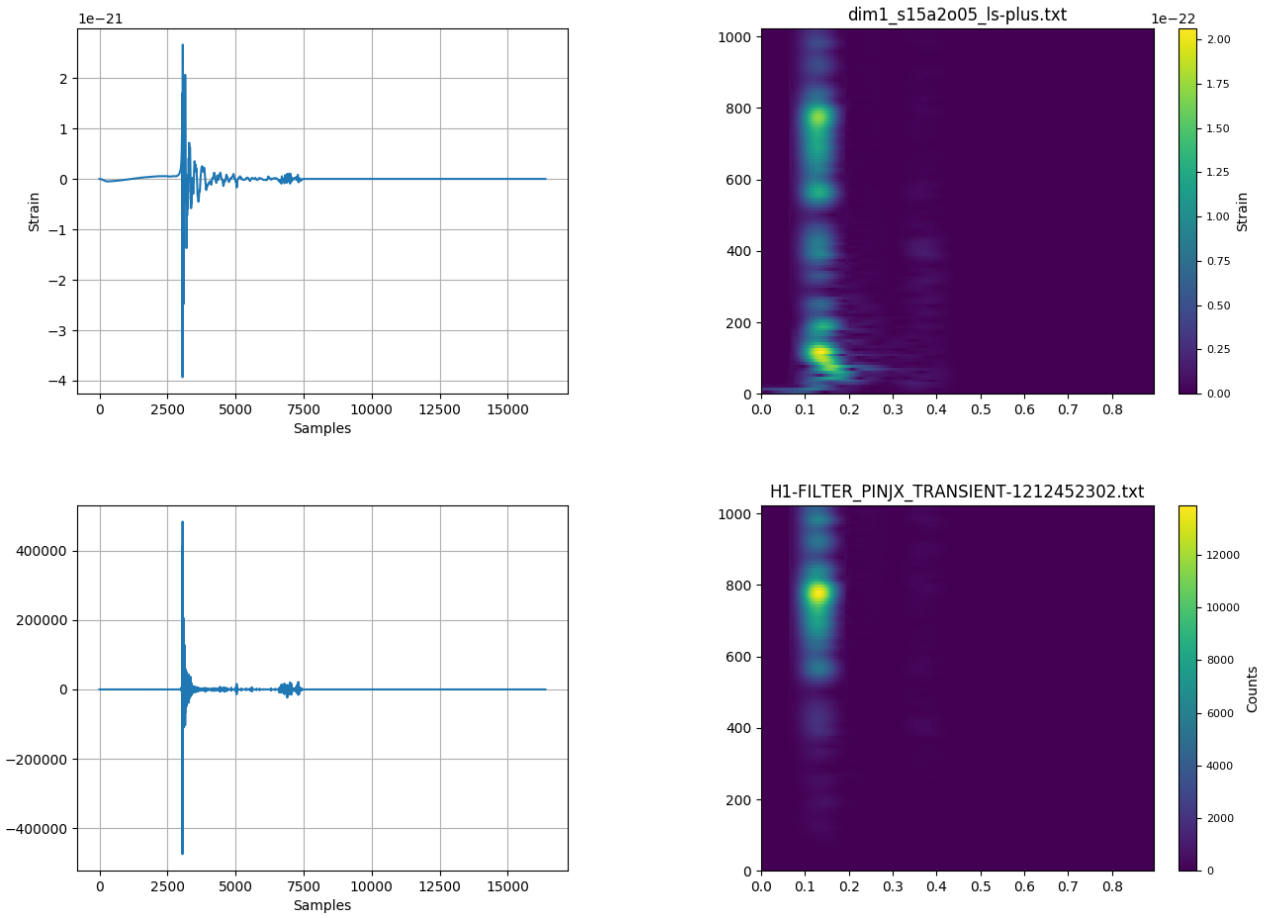

Figure 11.2: Saturation of the photon calibrator. Example with dim1 waveform. Upper panels: original waveform at 10kpc. Lower panels: strain converted into Pcal counts ("portions of light"). Total number of counts for this waveform is 484,403 that exceeds allowed number of counts for LHO Pcal (57,000). High frequency component of the waveform requires largest amount of counts.

- The distance to the source need to be as small as possible to make loud injections. This would allow to estimate accurately the impact of calibration uncertainty.
- In contrary, the SNR of the injected signals cannot be too strong to perform parameter estimation with BW and SMEE pipelines. The computational time grows significantly with increasing SNR.

A compromise is to choose waveforms at distance when SNR$\sim 40-50$. Several SN waveforms of neutrino and magnetorotationally driven explosions were selected. Unfortunately, these waveforms that were initially chosen with desired SNR did not pass the saturation tests. In this situation a distance of the injections was enlarged to be able to inject them safely.

Result of saturation test for three waveform families can be summarized as:

- Scheidegger 2010: these waveforms were produced for rapidly rotating progenitor stars and the dominant frequency for all waveforms is around $\sim$1kHz.

- Yakunin 2015: four waveforms were proposed and tested both in LLO and LHO but none of them passed the saturation test. All of them contain dominant High Frequency component (above 500Hz) corresponding to g-mode.
- Ott 2013: these waveforms does not contain significant HF component due to the fact that the CCSN simulation wave stopped before HF component was developed. However none of the proposed above waveforms produced at 0.5kpc passed the saturation. The distance must has been enlarged and 10kpc was chosen as a safe distance some of the results.

The final set of waveforms comes from Ott 2013 waveform family. The summary of the final set of waveforms along with the Pcal counts can be find in table 11.1.

Results

Table 11.1 presents a summary the injections that were done. Injected SNR is estimated from the software injection studies. It appears that the waveforms are too weak to be detectable. Indeed none of the follow-up studies found the signature of the injected waveforms. The most energetic injection was performed only in Livigston detector and the coincident studies could not be performed.

Waveform name	IFO	Counts	Saturation test	Distance	SNR	Injected time
ott1-nr1	H	34004.25	Passed	10kpc	~ 2	Jun 21, 2017 00:58:22 UTC
ott1-nr2	H	3742.34	Passed	10kpc	< 1	Jun 21, 2017 00:52:22 UTC
ott1-nr3	L	33681.71	Passed	10kpc	$\lesssim 10$	Jun 15, 2017 20:23:19 UTC
ott1-nr1	L	15542.05	Passed	10kpc	~ 2	Jul 26, 2017 16:23:02 UTC
ott1-nr2	L	1798.88	Passed	10kpc	< 1	Jul 26, 2017 16:41:22 UTC

Table 11.1: SN waveforms that were hardware injected.

Data shifted In order to simplify the process of injecting the waveforms it was agreed to make injections non-coincident that is injecting the waveforms one at the time. This approach allows to inject waveforms when only one detector is on-line, this allows to avoid loosing coincident LIGO data. The injections were conducted a months apart (June 21 and July 26) and in order to make the injections coincident the data from one detector. Data from LHO was chosen to be shifted forward in time.

Two possible ways were applied to shift the data:

- according to the time given in the aLog pages, as suggested by HWINJ team
- according to graceDB injection times

For producing the results below the first method method was applied. However none of the two methods produced candidate that can be associated with injected waveforms

A need for new actuating system As pointed in section 2.5 SN waveforms should have a significant HF component (>400Hz). The waveforms that were used for hardware injections do not contain HF part of the

spectrum and using themfor the overall analysis would bias the results of estimating the impact of calibration error on detection and parameter estimation.

In order to be able to perform hardware injection of waveforms with strong high frequency componant it is advisable to use a possibly a different actuation systems

11.3 Further considerations on possibility of injecting SN waveforms

The current main motivation [224] for hardware injecting SN waveforms is to validate method of detecting GW in single detector case. This section describes further this motivation of, the capabilities and limitations of the current hardware injections system to inject SN waveforms.

Motivation

Galactic Supernova will be one of the most interesting astronomical events of the century. The detection of GW from CCSN might solve already a century old problem of what is the explosion mechanism of a supernova. The detection or nulle detection statements will give hints to solve problems in Fundamental Physics, Astronomy or Astrophysics.

If a supernova explodes in our Galaxy in the next 5 years, we have a significant chance that only one detector will be taking data. Therefore, the motivation for doing Hardware Injections during future Engineering Runs:

Validate methodology of detecting GW from a Galactic Supernova
in a situation when only one detector is operating during SNEWS alert.

Search method assigning significance for a GW candidate for burst sources was not yet developed and validated. Objectives of the method:

1. Cleaning the background of the SN search at single-IFO level
2. Develop (better) cuts and vetoes for the search
3. Develop an algorithm to search for interesting triggers at single-IFO level

Questions & Answers

1. *Question:* Can you do the studies only with software injections?
   Answer: Currently we are working on tuning the search using only software injections. Hardware Injections will help validate the method and test possible unforeseen problems that may not be caught with software injections alone. For example, O3 safety studies for developing vetoes and/or background noise reduction in SN searches will make use of information from auxiliary channels. In this situations, hardware injections that simulate how a real signal propagates in the instrument may be crucial to test and validate the methods. Software injections add the simulated GW only to the strain channel. As a SN has not been detected yet, methods for vetoes or noise reduction that we want to validate would benefit from having a signal present in other auxiliary channels. The situation is similar to the situation of CBC and burst searches in the pre-detection era, where hardware injections were used to validate search methods.

2. *Question:* Can you validate the method with hardware injections that were already done?
   Answer: The morphologies of realistic SN waveforms are unique from and much more sophisticated than the waveforms that were injected so far. We think that the injections conducted to date are not sufficient. However we are currently working on quantifying it. The five SN waveforms injected so far (see this page for more details) are too weak to be detectable. In addition, we expect the characteristics of the noise in O3 to be different than in previous runs due to instrumental changes in the detector (new classes of glitches, different background floor, noise lines...). Validation of the methods with pre-O3 injections would likely not produce accurate results.

3. *Question:* How many injections do you need?
   Answer: A number of injections of the order of ten would be sufficient for currently planned tests.

Remarks

1. We propose making hardware injections during the times when only one detector is in Science Mode - we do not lose any Science data even if the injections are made during Engineering Run.

2. In a long perspective when we develop a method making use of the In long perspective we plan to develop a method making use of information from auxiliary channels, we plan to use proposed hardware injections to validate that method as well.

Supernova waveforms that could be hardware injected

We tested all Supernova waveform morphologies used in the O1-O2 Optically Triggered SN Search paper. Figure 11.3 and Figure 11.4 shows the detection efficiencies of detecting particular waveforms at different distances (black curves). The efficiencies are produced with cWB in Single Detector Mode. These Figures also compare the capabilities of the Photon Calibrator to inject particular Supernova waveforms (red curves).

From this plots it is visible that 2 out of 5 waveform families can be injected at detectability larger than 50% without saturation the Pcal - Mueller 2012 and Ott 2013. These waveforms have dominant low frequency component.

On the other side, 3 waveform families, Yakunin 2015, Dimmelmeier 2008 and Scheidegger 2010, could be injected without saturating Pcal at distances, where they are too weak to be detectable. These waveforms have a strong high frequency componant.

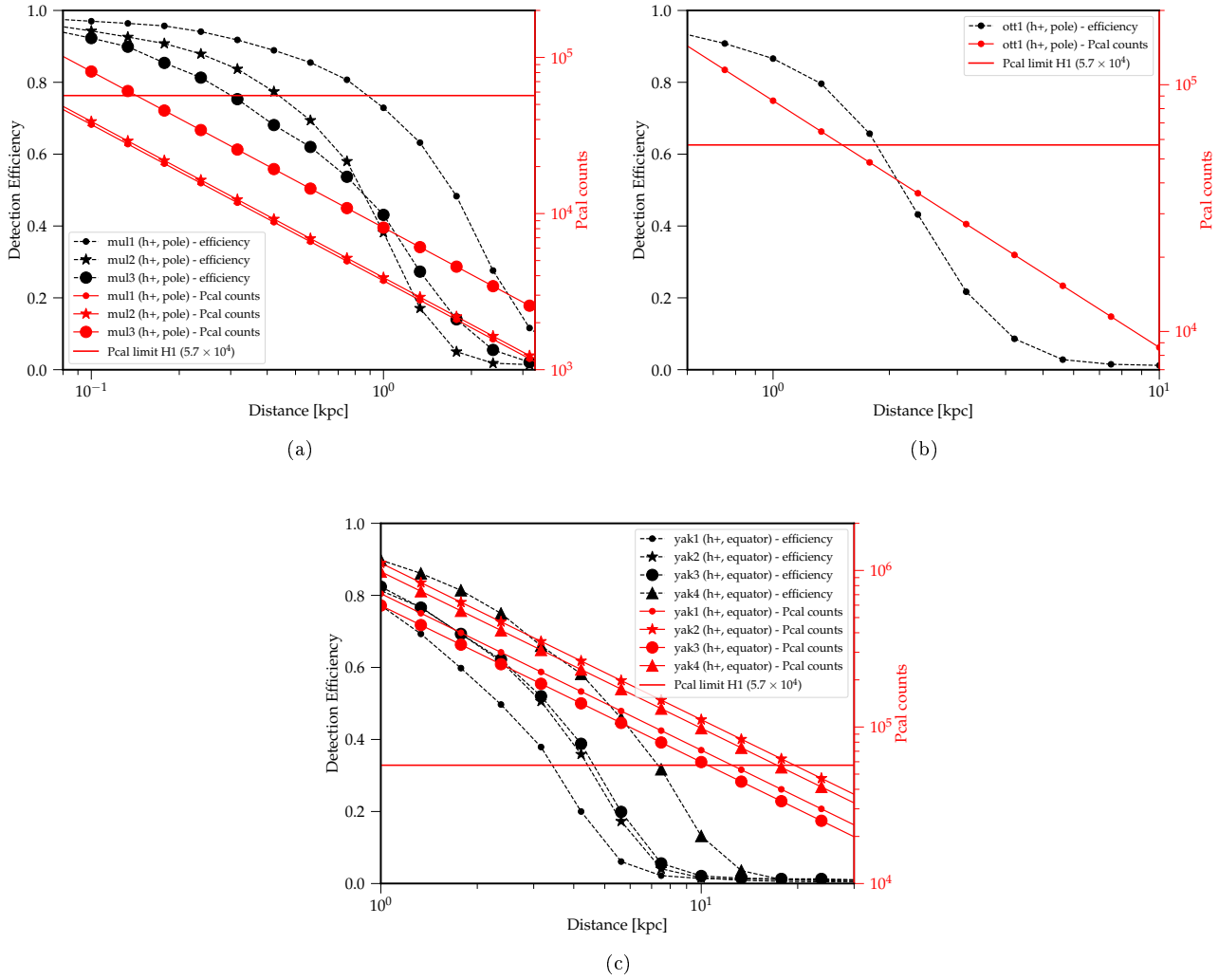

Figure 11.3: Saturation tests for slowly rotating SN explosions. Upper left: Mueller 2012 waveform family. Upper right: Ott 2013 waveform family. Down: Yakunin 2015 waveform family.

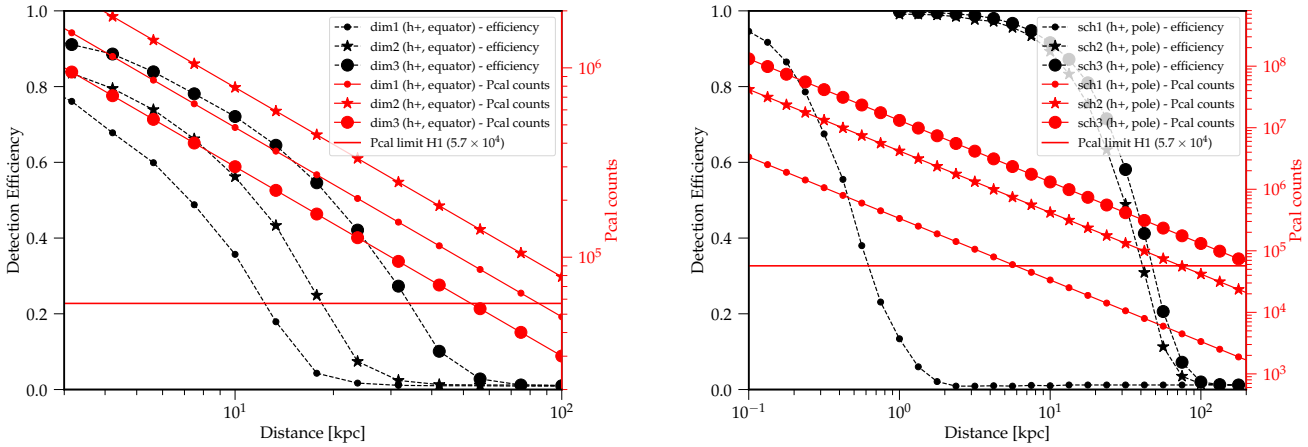

Figure 11.4: Saturation tests for rapidly rotating SN explosions. Left: Dimmelmeier 2008 waveform family. Right: Scheidegger 2010 waveform family.

Chapter 12

Supernova Parameter Estimation

If a detection is achieved the next step is to extract the waveform from interferometer data and/or extract physical parameters. cWB is a general algorithm for GW transients, which loads the data, identifies candidate events and performs a constrained likelihood waveform reconstruction. The cWB structure, as well as the data analysis overall approach, is modular. Some modules can also be devoted to parameter estimation and in that regard, several efforts I contribute to several efforts in improving specific aspects of the pipeline and follow up of the events with the goal of extracting physical information. For example:

1. Coherent Event Display (CED) is the first tool to extract the waveforms through cWB. I am collaborating for facilitating the extraction of SN features with the CED, for example, specialized wavelet packets customization to the extraction of g-mode feature. No paper on this topic is expected to be completed by the proposed defence time, but some descriptive text will be provided in the thesis.

2. Supernova Model Evidence Extractor [29] - this follow-up algorithm uses Principal Component decomposition of CCSN waveform families to reconstruct the waveform from the search pipeline triggers and estimate physical parameters. This work will need to evolve in order to test the reconstruction with respect to source orientation especially for rapidly rotating progenitors however [225] This analysis and the results will be summarized in the thesis.

3. Bayesian approach [30] - this approach uses BayesWave pipeline [226]. The algorithm estimates and compares the probability a transient identified by cWB is a GW, a Gaussian noise induced event or a non Gaussian glitch. Priors on the polarization, sky location and ellipticity are used to evaluate probability to distinguish GW events from noise events. It might allow to reduce the number of false alarm and enhance the detectability of CCSN waveforms at a fixed false alarm probability. I am co-author of a submitted to PRD paper on this topic and I am not planning further work before the defense.

4. Machine Learning (ML) - these techniques are used as a follow-up on the events produced by the search pipeline to veto and classify events. My contribution here has been in providing triggers to test the performance of ML for CCSN searches.

5. Two Step Denoising [227] - in this method of noise reduction, the Harmonic Regeneration Noise Reduction

is used. Method is in the development stage. The algorithm is written and I test its performance on initial LIGO and O1 data.

The elucidation of the parameter space of the GW emitting CCSNe progenitors is an on going process. The identification of the relevant parameters that should be used as key degrees of freedom in characterizing the progenitors is under consideration from both the numerical simulation and data analysis communities. For example the mass and the total angular momentum are considered important while other figures of merit like the compactness are under debate (for predicting the explodability of a progenitor). It is also important to understand what controls the onset of features like the SASI and in general the production of a large set of reliable GWs waveforms that explores the parameter space will take years even just because of computational constaints.

12.1 Supernova Parameters

As mentioned in section 3.4 a possible way of extracting the physical parameters from a SN candidate can be implemented through a two step approach:

1. model selection,
2. parameter extaction within the model.

Below I enlist examples of parameter that can be extracted from a supernova trigger.

Neutrino Driven explosions models The neutrino driven explosions are caused by neutrinos heating the star sufficiently enough to drive an explosion. Some of the parameters that can be used to characterize the waveforms:

- PNS parameters: radius, mass, temperature
- SASI/convection parameters: shock radius dynamics
- Accretion rate

Magnetorotationally Driven explosions models These explosions are caused by a strong magnetic field and rapid rotation of a progenitor star.

- PNS parameters: radius, mass, temperature
- Low T/W instability: rotational rate
- Initial core-collapse and bounce: angular momentum

BH formation and collapsar models Parameters:

- PNS: radius, mass, temperature
- BH: time of the formation

Extreme Emission Models Possible parameters:

- Collapsars/hypernova: radius,
- Longbar: rotational rate, degree of deformation,
- Torus defragmentation instability: mass of central black hole, M_{BH} vs M_{fall},
- Phase Transition: degree of the transition.

12.2 Coherent Event Display

Coherent Event Display (CED) is a cWB tool that provides a detailed characterization of the GW candidates. As mentioned in section 4, cWB by default does not reconstruct GW triggers, this reconstruction of the triggers is done separately. CED provides reconstructed waveforms in time, frequency and time-frequency domains along with other detailed statistics. In this section I will describe its main components.

As an illustration I will use a Yakunin 2015 waveform of a $12M_{\odot}$ progenitor star explosion (yak1) injected at distance 1.25kpc. I will consider network of 2 detectors, L1 and H1, and a Gaussian noise recolored to O1 sensitivity.

Event paramenters

The most important information about the event and the network at the time of this event can be summarized as follows (the relevant values considered example are in the brackets):

- GPS time of an event,
- SNR - reconstructed network signal-to-noise ratio (20.3),
- ρ - effective correlated SNR (12.2),
- cc - correlation coefficient (0.80),
- ED - network energy disbalance describing how different is the noise floor between detctors (0.01),
- (ϕ, θ) - reconstructed sky localization.

Time-Frequency Maps

After data is prepared (whitened, lines removed etc.) then cWB decomposes the time series into time-frequency maps. They allow to track the signal's frequencies change over time. The search for the triggers is performed in these maps.

There are two types of time-frequency maps that visualize the data around the event:

- Spectrograms - this is a decomposition based on Short Fourier Transform.
- Scalograms - a representation displaying wavelet coefficients of a Wavelet Transform.

The event is relatively strong (SNR∼20) and visible. However there are strong features visible in the time-frequency maps around the event. In this example the data used is Gaussian. The non-Gaussian data contains more and stronger misleading features. The next step will be to create time-frequency maps depicting coincident energy.

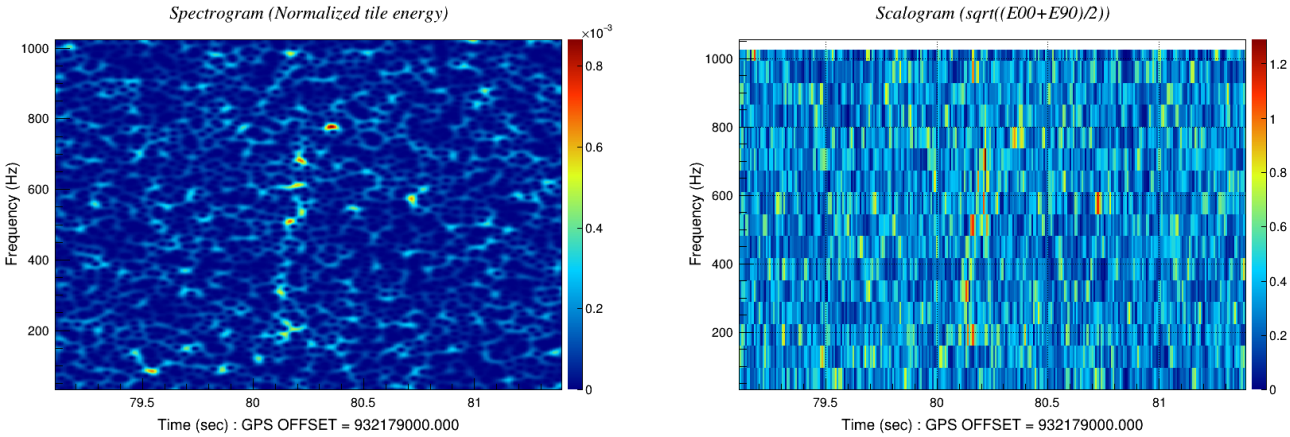

Figure 12.1: Time-frequency decompositions of the data for H1 detector. Left: Spectrogram (Short Fourier Transform). Right: Scalogram (WDM Wavelet Transform).

Likelihood Time-Frequency Maps

The spectrograms and scalograms show the energy distributions for each detector separately. In the excess power methods the GW candidates are created by combining the data from multiple detectors to find a coincident energy excess. The Likelihood TIme-Frequency maps visualize the distribution of coincident energy in time and frequency.

Two types of maps are distinguished:

- Likelihood - a scalogram with the identified pixels that contribute to the event. These pixels create a cluster and they are used later for the reconstruction and estimating event parameters, like SNR.
- Null stream - when an event is reconstructed, then the next step is to subtract it from the data. The leftover energy, or *residual energy* describes how well algorithm was able to reconstruct the event. If the event is a real GW then the signature should match between detectors and the residual energy is small. On the other side, if the event is a coincident glitch, then the signature in the detectors do not match and leaving relatively large amount of energy. This gives a powerfull tool to distinguish GW and noise events. The Null stream is a scalogram that depicts time and frequency distribution of of residual energy.

Left panel of figure 12.2 shows an example of the Likelihood Time-Frequency map of yak1 waveform. Two element are visible in this event. The first one is the low frequency GW signal from SASI/convection emission processes. The second contribution is the higher frequency PNS oscillation, g-mode. The growing peak frequency shows the evolution of PNS. The right panel of figure 12.2 depicts the Null stream for this event. The shape follows

the likelihood, however the amplitude is significantly smaller. The Null stream energy is around 10% of the total event energy.

It is also visible, that the pixels in the Likelihood cluster are not even. This is a result of multi-resolution decomposition of the data.

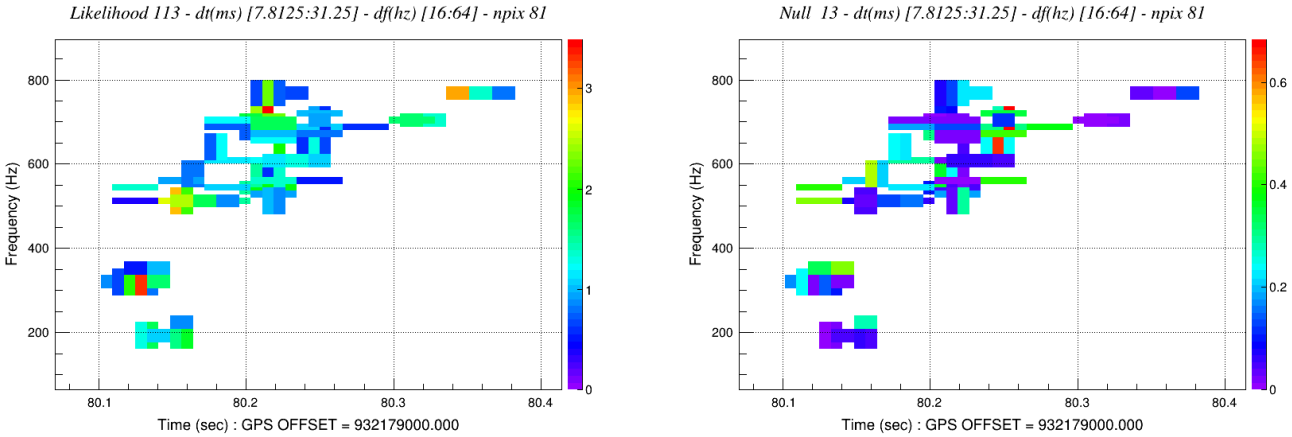

Figure 12.2: Likelihood Time-frequency Maps. Left: Likelihood. Right: Null energy.

Reconstructed waveforms

As mentioned earlier, the event is reconstructed using the cluster of pixels in Likelihood time-frequency map. Figure 12.3 shows a comparison between the injected and reconstructed event in time, frequency and time-frequency domains.

Upper right panel of figure 12.3 compares the injected and reconstructed waveform in time domain. The time domain of a waveform is rectreated through inverse Wavelet Transform of the pixels in the cluster. The most energetic components of the waveform are reconstructed, however the weaker features (like the initial part of PNS convection) are not.

The frequency domain of injected and reconstructed waveforms are depicted in upper left panel of figure 12.3. The reconstruction in frequency domain is also realized by an inverse Wavelet Transform of the pixels in the cluster. In this example, the injected waveform is broadband (black dots) with peak frequency around 700Hz. The reconstructed waveform matches the injected one in certain bands while some in few bands the signal was not detected. It is especially visible in low frequency region, where the detector noise becomes a dominant factor.

The lower panels of figure 12.3 compare the scalograms of the injected and reconstructed waveforms. The injected waveform is relatively long and broadband. The energy is distributed on a large area of the time-frequency map. It brings a challenge. It is difficult to create a cluster when the energy is spread in time and frequency. The signal needs to be relatively strong to be detectable. The scalogram of the reconstructed event depicts this challenge. Only the loudest time-frequency regions were detected. The weak parts were undetected. One of the possible solutions to this challenge is to change the clusterization algorithm, for example use pattern=10 (see section 4.3.6) that has an advantage of better collecting coincident pixels for long and broadband events (see section 8.2.3 for more detailed results).

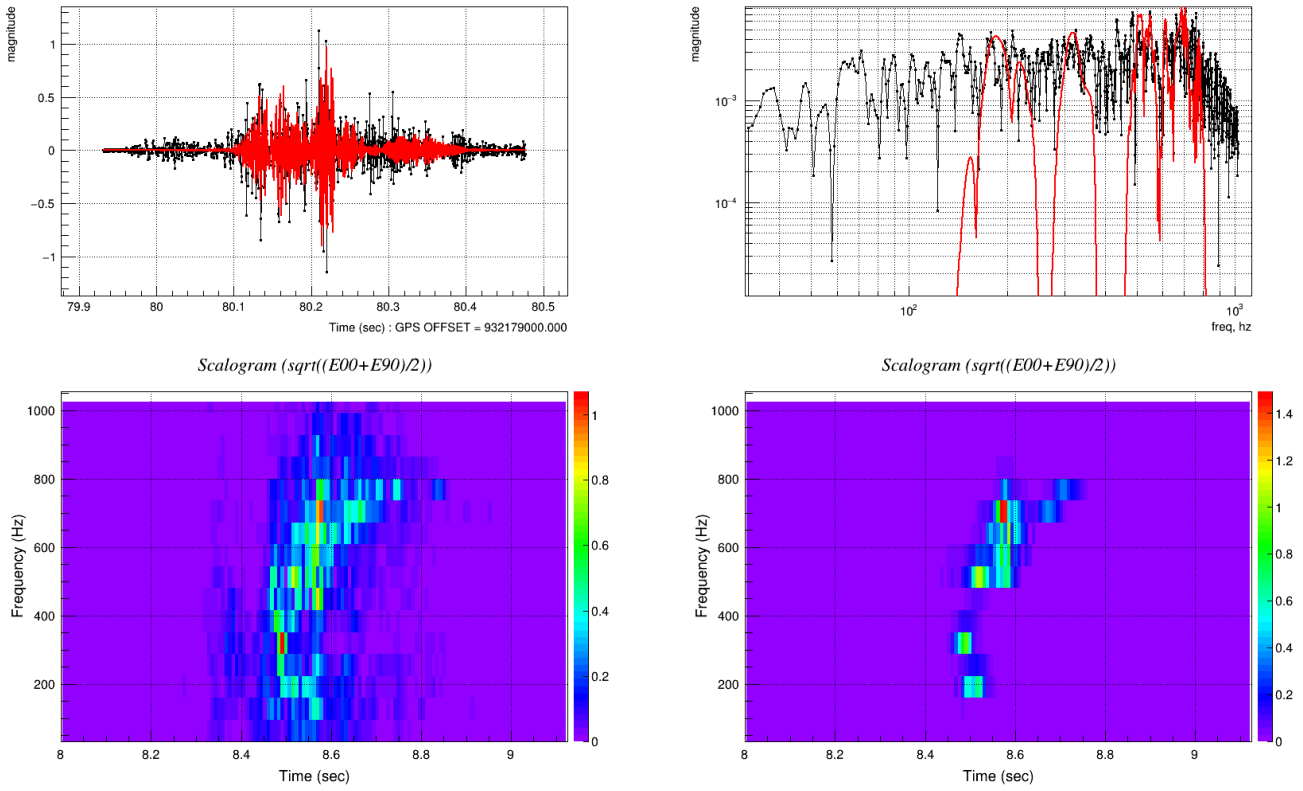

Figure 12.3: Comparison between reconstructed and injected Upper left: Time domain (injected - black, reconstructed - red). Upper right: Frequency domain (injected - black, reconstructed - red). Lower left: Scalogram of an injected waveform in Hanford detctor. Lower right: Scalogram of a reconstructed waveform in Hanford detector.

Skymaps

The skymaps depict various quantities that help in localizing the source of GW. They are depicted in the Earth based coordinate system.

Figure 12.4 shows an example of the distribution of probability of sky locations.

12.3 Evolution of Proto-Neutron Star

Afte the collapse, during the deleptonization, the size of proton-neutron star decreases over time stiffening the matter. In turn, the accreting matter excites proton-neutron star. The peak frequency of this excitation grows over time. Three main modes of the oscillation of the proto-neutron star can be distinguished: g-mode (gravity is a restoring force), p-modes (pressure) and f-modes (surface).

Figure 12.5 presents spectrograms of example GW signals with visible g-mode [33, 228, 38]. This robust information for these waveforms allows to tune the search specifically and increase the significance of the detected events. I performed test with the detectability of Yakunin et al 2015 waveforms using wavelet packets (see section 4.3.6). First part of the analysis consists a detection sensitivity study using single pixel mode (pattern=0) and in the

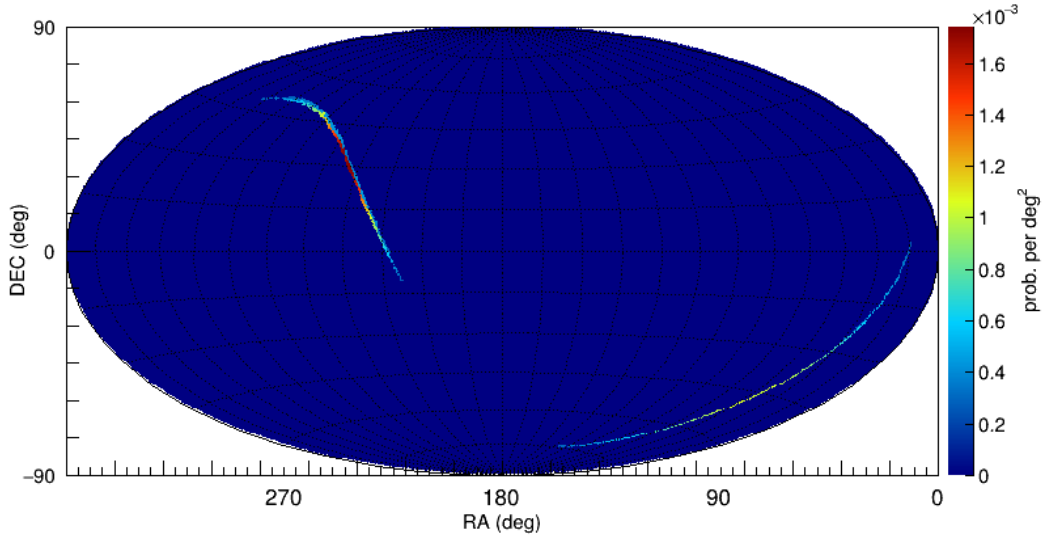

Figure 12.4: Sky location probabilities, an example.

second part the ring-up wavelet packet pattern was used (pattern=5). In both cases the False Alarm Rate is fixed (1.0×10^{-6}Hz). After comparing the visible distance there is a 30% increase in detection distance when ring-up pattern is used.

Moreover, the growing peak frequency carries also information about the evolution of proto-neutron star. Following [229] the evolution of peak frequecy, f_p, can be described as:

$$f_p \approx \frac{1}{2\pi}\frac{GM}{R^2}\sqrt{1.1\frac{m_n}{< E_{\bar{\nu}_e} >}}\left(1-\frac{GM}{Rc^2}\right)^2, \tag{12.1}$$

where G is gravity constant, M and R are proton-neutron star mass and radius, m_n neutron mass and $< E_{\bar{\nu}_e} >$ an average energy of electron antineutrino. The evolution of proto-neutron star ranges typically from 1.4 to 2.0 $M_\odot$ and the average neutrino energy is around 10-15MeV. This allows in the first approximation to parametrize the peak frequency as:

$$f_p \approx K/R^2, \tag{12.2}$$

where $K \approx 1.1 \times 10^{12} m^2 s^{-1}$.

12.4 Supernova Model Evidence Extractor

A "supernova problem" of finding a dominant explosion mechanism driving supernova explosions is decades old problem. Addressing this dilemma requires direct measurement of the dynamics during core collapse. Gravitational Waves are the main source of information, the neutrino signals provide main thermodynamical information and the electromagnetic spectrum is visible long after the initial collapse. Several explosion models were proposed so far and all of them require experimental evience.

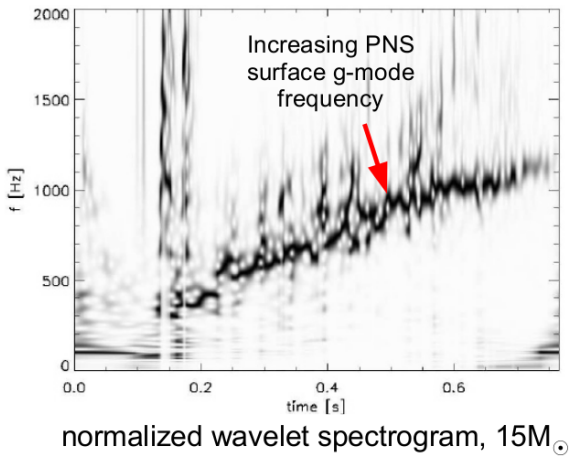

(a)

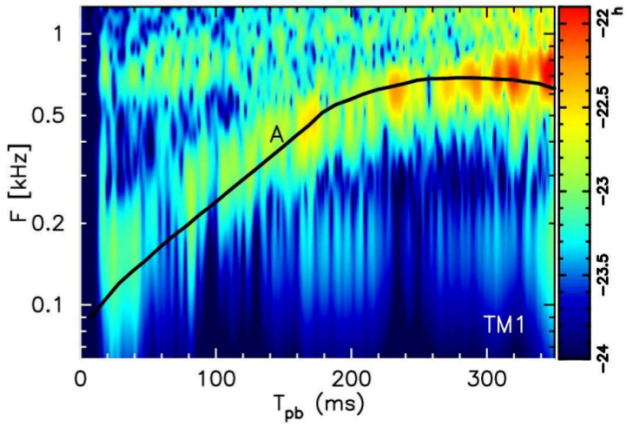

(b)

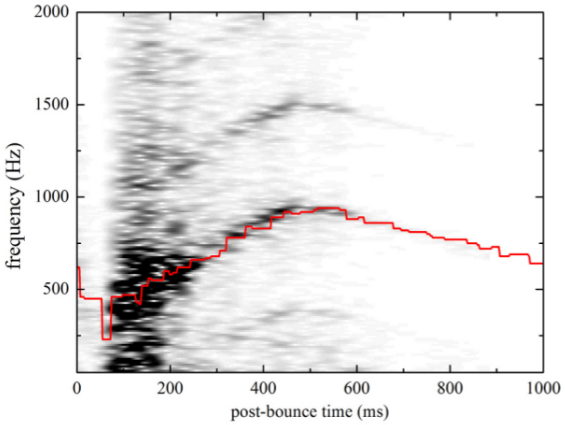

(c)

Figure 12.5: Examples of the supernova waveforms with growing peak frequency, rump-up of g-mode. Upper left: Mueller et al 2012. Upper right: Kuroda et al 2016. Bottom: Yakunin et al 2012.

Supernova Model Evidence Extractor (SMEE) is an algorithm designed to distinguish different models for a given GW candidate. In the Powell et al [29] we explore the ability of the algorithm to distinguish between neutrino driven mechanism, magnetorotationally driven explosion and noise artifacts that imitate real GW signals. Below I present basics of the methodology and some results.

12.4.1 SMEE

Bayesian Inference

The Bayes' theorem gives a *posterior* probability $p(\theta|x, M)$ for a parameter θ in a given model M (e.g. GW signal and glitch), after data x is collected:

$$p(\theta|x, M) = \frac{p(x|\theta, M) \times p(\theta|M)}{p(x|M)}. \tag{12.3}$$

Likelihood $p(x|\theta, M)$ is a conditional probability distribution of the data x for a paramenter θ.

Prior $p(\theta|M)$ is a probability describing the distribution of parameter θ when no data is present.

Evidence $p(x|M)$ is a normalization factor used for Bayesian model selection. It is obtained by integrating the product of its likelihood probability and prior across all model parameter values θ:

$$p(x|M) = \int_\theta p(\theta|M)p(x|\theta, M)\mathrm{d}\theta. \tag{12.4}$$

Bayesian Model Selection

We employ Bayesian Model Selection to distinguish competing models. We defne Bayes factor B_{ij} as a ratio of evidences:

$$B_{ij} = \frac{p(x|M_i)}{p(x|M_j)}, \tag{12.5}$$

where i and j correspond to glitch or signal models. For convenience we define the log of the Bayes factor:

$$\log B_{ij} = \log p(x|M_i) - \log p(x|M_j). \tag{12.6}$$

When $\log B_{ij} > 0$ then model M_i is preferred over model M_j.

Principal Component Analysis

Principal Componant Analysis (PCA) is a procedure of transforming data set into an ortogonal principal components (PCs) that are eigenvectors of the data set. To perform a decomposition, a catalog of m waveforms with uniform length n is used to create a $n \times m$ matrix $\mathbf{A}$ that is factored as:

$$\mathbf{A} = \mathbf{U}\mathbf{\Sigma}\mathbf{V}^T, \tag{12.7}$$

where $\mathbf{U}$ is an $n \times n$ matrix with columns corresponding to the eigenvectors of $\mathbf{A}\mathbf{A}^T$, $\mathbf{V}$ is an $m \times m$ matrix with columns corresponding to the eigenvectors of $\mathbf{A}^T\mathbf{A}$ and $\mathbf{\Sigma}$ is an $n \times m$ matrix with values corresponding to the square root of the eigenvalues. A waveform h_i from a catalog can be approximated by k first PCs:

$$h_i \approx \Sigma_{j=1}^{k} U_j \beta_j, \tag{12.8}$$

where U_j is jth PC from $\mathbf{U}$.

Signal and Noise Models

Two signal models were created corresponding to the explosion mechanism: neutrino and magnetorotational. For creating a signal model for magnetorotationally driven explosions the waveforms from rapidly rotating progenitor star simulations of Scheiddegger et al [40] were used. The main feature in these waveforms is a very strong signal from the core collapse and bounce. As for neutrino driven explosions, the PCs are created from the 3-dimensional

simulations of Kuroda et al [228], Mueller et al [33] and Andresen et al [230]. For these waveforms the main components are turbulent features of SASI and convection.

For a real astrophysical event the signal should be coherent between two or more detectors. In order to distinguish noise transients from GW sources we perform Bayesian coherence test. If the trigger passes the coherence test then we determine an explosion mechanism.

12.4.2 Results

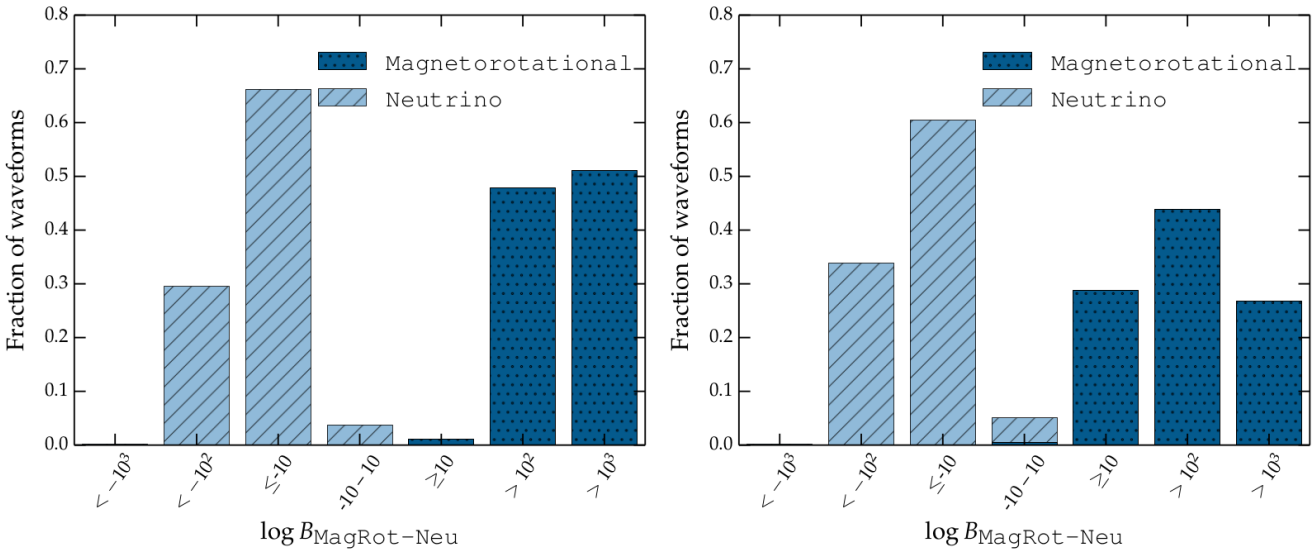

Figure 12.6: Distringuishing explosion mechanism. Left: L1H1V1 detector network. Right: L1 detector only.

The signal models are created based on the predicted GW waveforms and they need to be tested for triggers that are detector noise. For this purpose 1000 of Gaussian noise transients and 1000 real recolored noise transients recolored to Advanced detectors sensitivity were used. The log Bayes factor of the signal vs noise models for neutrino and magnetorotational mechanisms are centered around 0. However, due to the spread, in order to be conservative, we assume that the signal is detected when $\log B_{S/N} > 10$.

After the trigger is classified as signal, the next step is to determine an explosion mechanism. To test the ability of distinguising the two explosion mechanisms we performed analysis with cWB and used SMEE as a follow-up of the detected triggers. We injected Mueller et al waveforms at the distance of 2kpc and Scheidegger et al at 10kpc. The magnetorotationally driven explosions are more energetic, and they can be detectable at larger distances.

Figure 12.6 shows Bayes factors of the triggers for L1H1V1 detector network (left) and only L1 detector (right). The signal is considered to be considered to be coming from an magnetorotationally driven explosion if $\log B_{MagRot-Neu} > 10$ and neutrino driven explosion when $\log B_{MagRot-Neu} < -10$. For three detector network, 100% of Scheiddegger et al waveforms were correctly classified as magnetorotationally driven explosions at 10kpc, while 95% of Mueller et al waveforms were classified correctly as neutrino driven explosions at 2kpc. Similar results were obtained also in case of injections in L1.

12.5 BayesWave

12.5.1 Introduction

In this study, we use a sample of four days of S5 data considering two-detector network, LIGO Hanford H1 and Livingston L1. In the analysis, we create lists of potential GW triggers using cWB and then we use BW as a follow-up to constrain the number of triggers by removing further the noise events. We perform two kinds of analyses: background and simulation. In the background analysis, we follow standard procedure of excess power methodology of artificially shifting data between detectors [231]. This part gives us information of how often the noise of GW data creates triggers that falsely look alike GW waveforms. cWB ranks the triggers with network signal-to-noise ratio denoted as ρ and the created list of noise triggers we use to establish False Alarm Rate (FAR) with respect to ρ. In the simulation stage we calculate sensitivity of the algorithms to detect particular emission model. Supernova waveforms are added to GW data with various amplitudes corresponding to different simulated source distances. We test sensitivity of the cWB by testing how sensitive the pipeline is to detect supernova waveforms injected at different distances. After establishing the list of noise triggers and GW triggers we pass them to BW pipeline.

In order to compare the performance of cWB and cWB+BW, we need to establish the sensitivity of those approaches at fixed FAR. It can be accomplished by plotting Receiving Operating Characteristic (ROC) curves that compare sensitivities of cWB and cWB+BW across different FARs. Based on background analysis we can read the corresponds ρ thresholds of false triggers at given FARs. Those ρ values are used as thresholds in the simulation stage, by this we mean that we accept SN triggers above certain FAR. The ROC curves give sensitivity of detecting SN signals above range of FARs. Using BW as a follow up of cWB allows to eliminate noise triggers and reduce FAR without losing detection sensitivity.

12.5.2 BayesWave (BW)

BayesWave (BW), however, acts more as a post-processing pipeline for detecting and characterizing GW bursts working within the framework of Bayesian statistics [232] on triggers provided by cWB [233, 234]. BW is effective in distinguishing GW signals from non-Gaussian noise artifacts (glitches), which enables the combination of the cWB and BW to achieve high-confidence detections across a range of binary system waveform morphologies [235, 236]. Most Burst search algorithms, such as cWB, apply selection cuts to remove glitches, and then rank the remaining signals with a statistic proportional to signal-to-noise ratio (SNR). BW instead attempts to fit the data with both a GW signal model and a glitch model, and then calculates the Bayesian evidence ratio (BayesFactor) between the two competing hypotheses. The ratio of the Bayesfactor is then used to compute the glitch-to-gravitational wave BayesFactor whereas cWB uses a detection statistic that scales linearly with SNR. Recognized glitches with significant time-frequency structures that require multiple wavelets to reconstruct, however, are extremely unlikely to have the same time-frequency structure present in both detectors. BW uses this feature of the data inputted in order to assign a high detection confidence with these signals belonging to complex time-frequency structures and low detection confidence to signals with simple time-frequency structures, while complex glitches are rejected due to a lack of coherence between the online detectors. While cWB ranks events by coherent SNR, BW brings a complimentary addition by using morphology information as a secondary follow-up to rank the same events passed through cWB.

12.5.3 Understanding the BW Model through Bayes Factors

The two Bayes Factors to determine candidate or glitch classification are the signal-to-glitch ($\ln B_{SG}$) and the signal-to-noise ($\ln B_{SN}$), where $\ln B_{SN}$ scales with the square of the signal to noise ratio (SNR). lnB_{SG} is calculated in a framework that directly compares a signal model with a glitch model. If either lnB_{SN} or $lnB_{SG} > 0$, then the signal model is preferred and the a candidate GW signal is identified. If either lnB_{SN} or $lnB_{SG} < 0$, then the glitch model is preferred and the data is a product of instrumental noise. The introduction of a Bayesian framework with evidence ratios, specifically *Bayes Factors*, brings in the possibility of selecting between either a glitch, signal, or a noise model. The Bayesian approach to model selection is a welcomed supplement to thresholding as it relies only on the current data being processed instead of imposing pre-existing behavioral assumptions on the data. Bayes Factors represent a detection statistic where it compares the relative probability that a data set contains a strain due to a GW to the probability that the data only contains noise. It is important to note that the Bayesian approach does not yield a fixed signal-to-noise threshold in which a signal will become detectable if it passes this set threshold. Instead, the signal-to-noise ratio is introduced to analyze signals in a given noise that may become detectable for that individual, analyzed case. The identified GW signal (h) would be clustered in time-frequency power, coherent across the network in time, frequency, and morphology, as well as being composed of a single set of wavelets that are projected onto the detector network. Identified glitches (g) are also clustered in time-frequency power, incorporates known glitch morphologies [237], but instead is localized to each detector and reconstructs data independently in each detector. Integrating such an approach on-top of pre-existing pipelines, such as cWB, and running an analysis on potential GW signals will result in further separation of the non-Gaussian noise artifacts (glitches) belonging in the background enables a possibility of achieving high-confidence detections across a range of CCSNe.

12.5.4 Sky-Location Prior

An important advantage known to the targeted SN search is knowing the sky location of the SN trigger via electromagnetic information provided to us by our astronomer counterparts. A SN-driven GW source is characterized by a set of five angles (θ, Φ, ψ) that describe the sky location and polarization of the source, while (ι, ϕ) describe the internal orientation of the source relative to the observer's line of sight. Since it's not possible to pinpoint the inclination angle, ι, and the azimuthal angle, ϕ, we compensate by injecting CCSNe signals with many different (ι, ϕ) in order to average over all internal source orientations [142]. cWB reconstructs the direction of the source in the sky based on triangulation and coherent network analysis methods [238]. For the two detector network, the time delay of a passing GW between detectors specifies a ring of possible sky locations. cWB calculates likelihood across the ring and the reconstructed sky location is chosen based on area in the sky with largest likelihood value. The direction of GW waveforms tend to have better reconstructed sky localization than noise triggers, and so this information is then used to discard noise triggers. In the simulation stage of the analysis, the SN waveforms are injected into the detector noise with fixed sky location. The analysis specific to this ring skymask is defined around a circular radial area of 5° of the SN trigger of interested. Any possible triggers falling outside of this skymask are discarded. BW, on the other hand, produces a skymap that defines the posterior probability density function of the GW source location expressed as a function of right ascension and declination, denoted by $\mathrm{p_{sky}}(\alpha, \delta)$. The angular distance between the maximum of $\mathrm{p_{sky}}$ and the true location of the injected signal is defined as the angular

offset, ($\delta\theta$). The distribution of $\delta\theta$ values peaks at $\cos(\delta\theta) = 1$, which corresponds to BW reconstructing the most probable location of the source close to the actual source location. A smaller peak occurs at $\cos(\delta\theta) = -1$, which illustrates that BW may also reconstruct the opposite direction of the sky compared to the actual location of the injected signal than a direction perpendicular to the injected signal's locations as opposite directions cannot be currently distinguished using the network antenna pattern due to the near co-alignment of the H1 and L1 detectors. But, noting that the peak at $\cos(\delta\theta) = -1$ is smaller than the distributed peak at $\cos(\delta\theta) = 1$, this physically indicates that opposing directions of source reconstruction occur only by the triangulation ring when the source is right above or below the detector network [239]. Taking this into account, this paper bypassed this feature for now by pre-defining the location of the SN analyzed as future modifications will be introduced to optimize CCSNe sky location reconstruction.

12.6 Machine Learning

Machine Learning is a branch of Artificial Intelligence field of Computational Sciences. In these techniques, the algorithms are "learned" to set of data to be able to perform a specific task. Machine Learning approaches are used for the massive computation and for pattern recognition purposes.

In these studies we use Machine Learning algorithms as a follow-up of cWB. The Machine Learning algorithms are used to to distinguish background noise triggers from simulation triggers. The algorithms are first trained on test sets of cWB background and simulation triggers, and then these algorithms are used to distinguish a background and simulation triggers on a proper large set.

12.6.1 Genetic Programming

Introduction to GP

Genetic Programming (GP) is a techinque using evolutionary algorithms. KarooGP is used.

A note about the vocabulary differences between GW community and communities using GP:

- cWB parameter - in GP community these are called "feature"
- triggers - GP cummunity uses term "data points"

In this dissertation we will be using consequently GW community vocabulary.

Triggers

The following cWB parameters (full description of cWB parameters in section 4.4) were used in this study:

$$\text{rh1}, \text{cc0}, \text{cc1}, \text{cc2}, \text{cc3}, \text{vol}, \text{d0}, \text{d1}, \text{f0}, \text{f1}, \text{df}, \text{low}, \text{hgh},$$
$$\text{bw0}, \text{bw1}, \text{dbw}, \text{nrm}, \text{pty}, \text{eA1...eA9}, \text{nu0}, \text{nu1}, \text{ni0}, \text{ni1}, \text{ecr},$$

The initial sets were trained on the same number of background and simulation triggers. We binned the triggers according to the rho values:

1. only yak1
2. BKG: 5000 triggers
3. SIM:
3.1. rho=4-5: 5000 triggers
3.2. rho=5-6: 2708 triggers
3.3. rho=6-7: 1866 triggers
3.4. rho=7-8: 1471 triggers
3.5. rho=8-9: 1355 triggers

Multivariate expression A multivariate expression evolved by GP from machine learning algorithm that differentiate noise from signal in the best possible way:

$$\begin{aligned} f = & -bw1 + bw1/d0 + 2 * cc2 - d1 * eA9 * hgh + dbw * ecr * pty * rh1 \\ & - df * eA3 - eA4 + eA6 - eA7 * hgh + ecr - f0 + f1 - vol \\ & + eA6/cc1^2 - vol/cc0 - cc2/bw0 \end{aligned} \tag{12.9}$$

For each triggers the value of this expression tells us how much the triggers is a real GW triggers. Different thresholds can be chosen in order to differentiate between bkg and sim triggers. In this study we assume that all triggers fullfiling the condition:

$$f > 0 \tag{12.10}$$

are GW triggers.

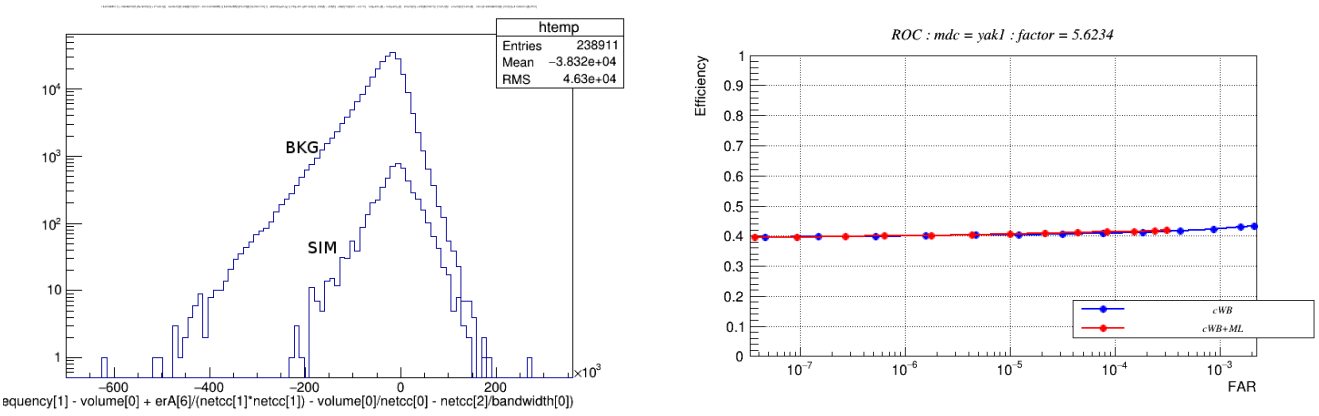

Figure 12.7: GP studies. Left: distribution of bkg and sim triggers according to the multivariate expression. Right: Impact of using the expression on ROC curve.

Figure ref shows the dirstibution of the multivariate expression for both bkg and sim triggers. The expression gives 80% accuracy of differentiating bkg and sim triggers. The expression removes majority of bkg triggers. However, it also removes many of sim triggers. In the Figure ref the ROC is shown before applying the multivariate expression and after. The FAR decreases one order of magnitude and at the same time efficiency drops not too much.

Unfortunately, the improvement in ROC curve is marginal. The studies are preliminary, and several improvements can be done. Possible future directions:

- Non-flat ROC - curretly the method is used in a situation, when the ROC cures are flat, i.e. the efficiency does not change significantly over several orders of magnitude in FAR.Given that GP removes the a large population of noise triggers, it might give positive results in the situation detection efficiency changes significantly with FAR.
- Improve the accuracy of multivariate expression - the expression 12.9 gives accuracy of $\sim 82\%$ in distinguishing noise and simulation triggers. Further studies has shown that higher accuracies are possible to achieve. I will study this.
- Threshold on the multivariate expression - by default the threshold is set to zero, $f > 0$. However, this threshold can be chosen manually to give optimal performance on ROC. It can be chosen in such a way that it save more simulation triggers, for example.
- Increase of the number of triggers - the better performance is expected when the number of triggers for training increases. This can be done in case of the background triggers by increasing number of lags (see section 4.5.1). The number of injections can be done by making injections more frequent, for example.
- Choosing differnt paramters for creating multivariate expressions.

The method so far does not show benefits to the search. However it has imporant potential computational benefits. The method requires a large number of triggers for the training stage to be able to increase accuracy in differentiating bkg from sim triggers. It gives an important potential to remove larger sets of noise events. In this regard it has an advantage over BW or SMEE follow-up that require several hours to days to analyze a single loud event.

12.7 Two Step Denoising

Noise reduction can be viewed as an estimation problem, where an unknown signal is to be estimated in the presence of noise, where only the noisy observation is available. In the Two Step Denoising (TSD) algorithm, by exploiting the spectral diversity between the signal and the noise, along with the high degree of the nonstationarity of the signal. The algorithm is based on previous work by [240, 241, 242, 243, 244, 245]. A first implementation of the method in the context of detection of GW from SN has been described in [246]. For the sake of brevity, we do not repeat the mathematical steps here.

12.7.1 Data used

The analysis presented in this article was performed in presence od LIGO fifth science run (S5 [247]) data. The real-time sampling rate of 16384Hz was downsampled to 4096Hz to lower the computational cost. The frequency band of this study is based on GW emission processes in a supernova. In low frequencies the dominant source of gravitational radiation is so called Standing Accretion Shock Instability (SASI with typical frequency of 100Hz and in high frequencies the extreme emission models can produce GW up to 2kHz. Though the frequency band

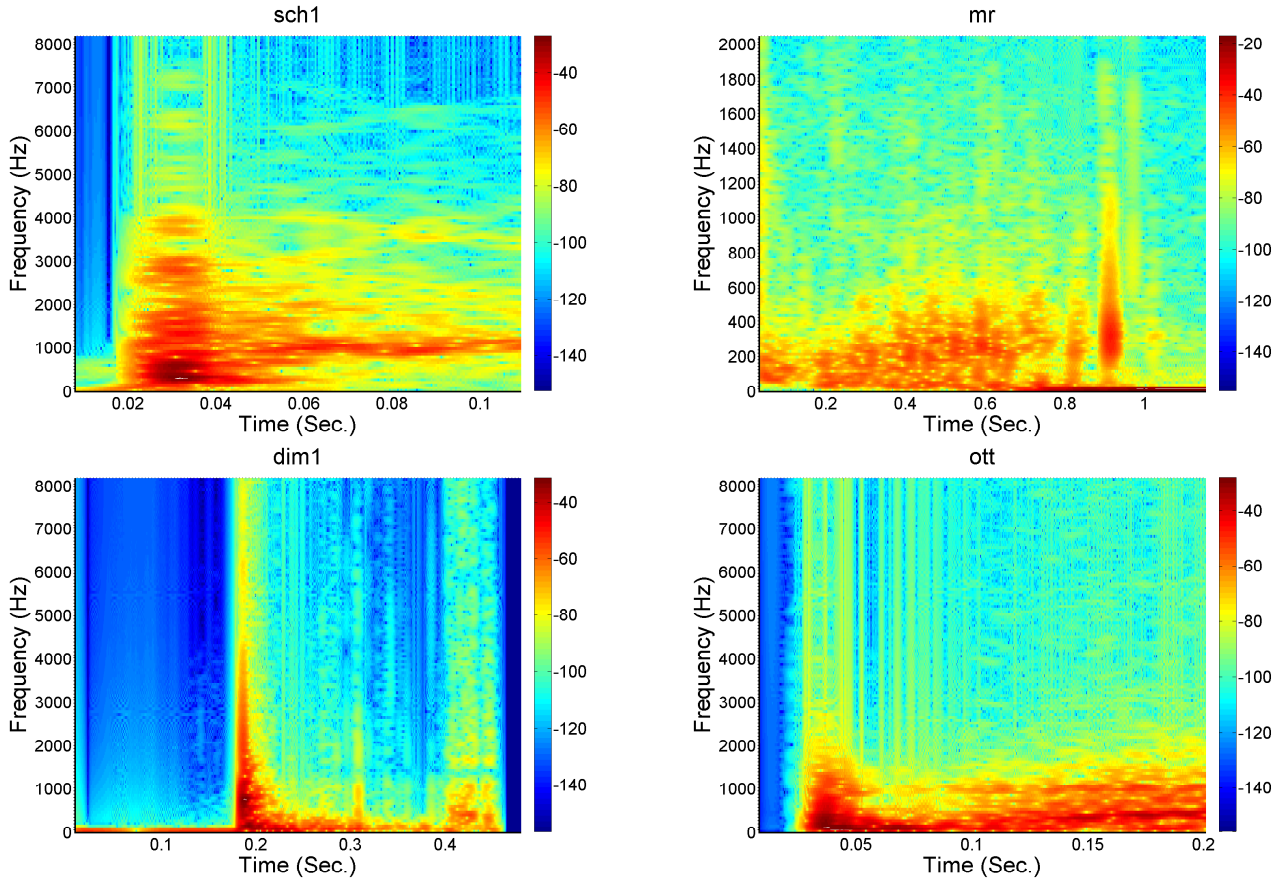

Figure 12.8

we astrophysically motivate is ranging from 64Hz to 2048Hz. The GW detector data is non-stationary with many enviromental and instrumental artifacts so the data used to test TSD filter was taken during time when the detector was locked in proper configuration and the times of well understood instrumental problems or during hardware injections were removed.

12.7.2 Results

In this section the results of using TSD algorithm are described. Table 12.1 and 12.2 summarize advantages of using TSD algorithm across different waveform morphologies, both generic and realistic. Table 12.3 sums up two tests of using the TSD filter that potentially might affect supernova searches - these results also show positive impact of using the filter. All results are produced in context of searching fot GW from core-collapse supernovae.

Emission type	Identifier	Ref	FAR [Hz]	Eff cWB	Eff cWB+TSD	Eff increment
Generic morphology	GA2d500	-	1.0e-8	38.0%	52.0%	14.0%
			1.0e-7	41.0%	55.0%	14.0%
			1.0e-6	43.0%	58.0%	14.0%
	SG361Q8d9	-	1.0e-8	38.0%	56.0%	18.0%
			1.0e-7	40.0%	60.0%	20.0%
			1.0e-6	44.0%	62.0%	18.0%
Extreme emission model	M0p2f1000t1000	[248]	1.0e-7	40.0%	60.0%	20.0%
			1.0e-6	47.0%	64.0%	17.0%
			1.0e-5	54.0%	67.0%	13.0%

Table 12.1: Advantage of using TSD filter for generic morphology and extreme emission model waveforms.

Emission type	Identifier	Ref	FAR [Hz]	Eff cWB	Eff cWB+TSD	Eff increment
Magnetorotationally driven explosion	sch1	[40]	1.0e-6	36.9%	45.9%	9.0%
			1.0e-5	37.4%	46.7%	9.3%
			1.0e-4	38.2%	47.5%	9.3%
	sch2	[40]	1.0e-6	62.9%	65.8%	2.9%
			1.0e-5	63.1%	65.8%	2.7%
			1.0e-4	64.2%	66.6%	2.4%
	sch3	[40]	1.0e-6	61.3%	70.8%	9.5%
			1.0e-5	61.5%	71.1%	9.4%
			1.0e-4	61.5%	71.1%	9.4%
	dim1	[39]	1.0e-6	33.7%	41.7%	8.0%
			1.0e-5	34.4%	42.4%	8.0%
			1.0e-4	35.3%	43.0%	7.7%
	dim2	[39]	1.0e-6	45.4%	50.7%	5.3%
			1.0e-5	45.9%	51.2%	5.3%
			1.0e-4	46.1%	51.7%	5.6%
	dim3	[39]	1.0e-6	63.1%	71.6%	8.5%
			1.0e-5	63.4%	72.1%	8.8%
			1.0e-4	63.9%	72.1%	8.2%
Neutrino driven explosion	mur	[249]	1.0e-6	42.0%	46.0%	9.5%
			1.0e-5	46.5%	52.5%	12.9%
			1.0e-4	53.5%	60.0%	12.1%
	ott	[140]	1.0e-6	41.1%	46.7%	5.6%
			1.0e-5	41.6%	46.9%	5.3%
			1.0e-4	42.4%	47.5%	5.0%

Table 12.2: Improvements of using TSD algorithm for magnetorotationaly and neutrino driven explosion models. The improvement is consistet across those models.

Generic morphologies

The first results shown in this paper are regarding generic morphology waveforms. The generic waveforms are used in different searches [17, 18]. Specifically in the initial LIGO/Virgo optically triggered supernova search [18] the sine-Gaussian waveforms were used to state upper limit on GW energy emitted with supernova explosion based on SN 2007gr and SN 2011dh. Table 12.1 shows an increment in efficiency for fixed FAR at different FAR levels.

Extreme emission model waveforms

Based on the initial LIGO/Virgo optically triggered supernova search paper [18] it is expected to exclude some of the most extreme emission models. Table 12.1 presents improvement in detecting extreme emission model by Fryer et al [248] using the TSD filter. This waveform family is morphologically similar to the waveforms used in supernova search.

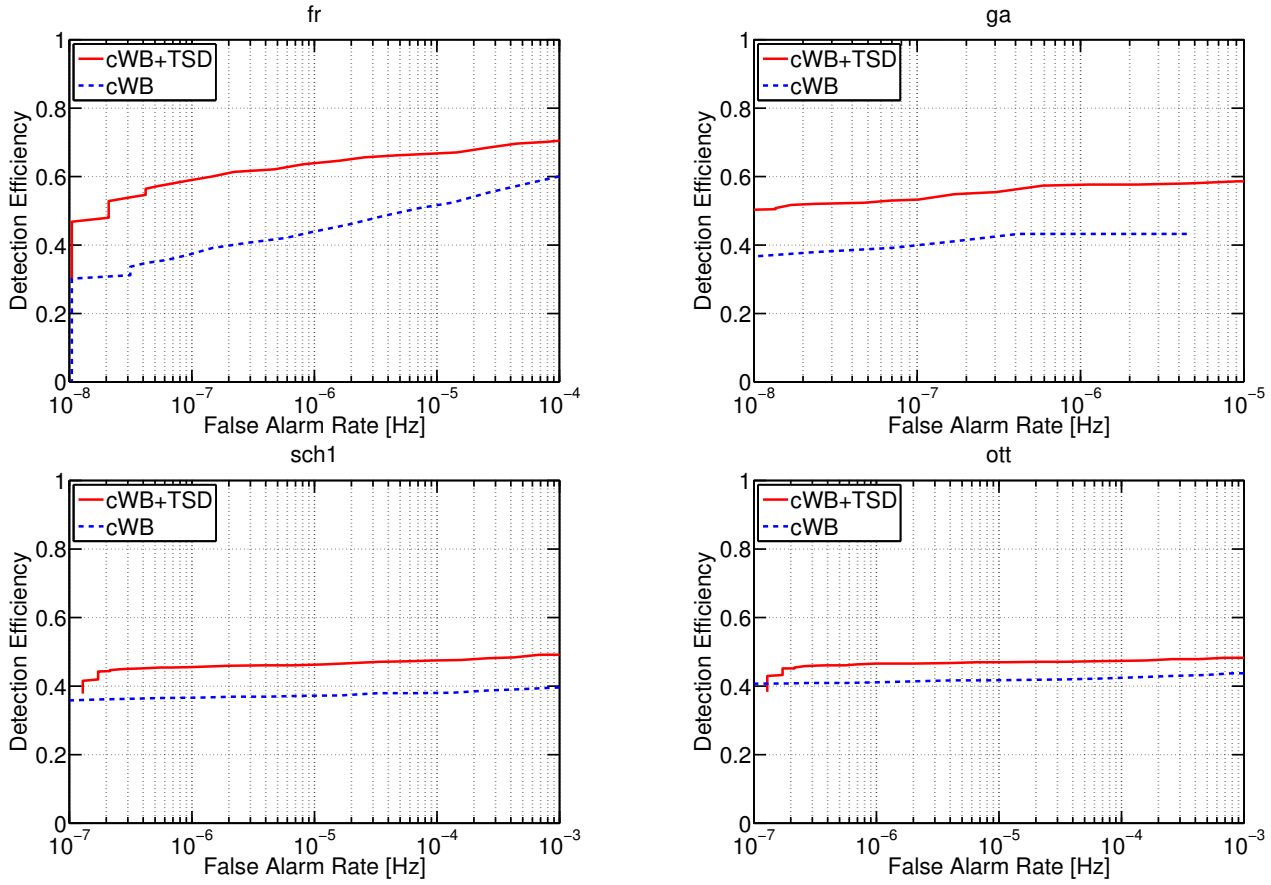

Figure 12.9

Magnetorotationally driven explosions

Magnetorotational driven explosion happens when the progenitor star rotates rapidly and there is a seed magnetic field that is greatly magnified under fast collapse and rapid rotation. Table 12.2 summarizes results for two waveform families. It is visible that the improvement in sensitivity is present across those waveform families.

Nautrino driven explosions

In this study we consider two waveform families and table 12.4 sums up the advantage of using TSD filter.

Various tests

In this section we show two tests of TSD algorithm performance that might have impact in the supernova searches. 12.3 summarizes the results.

In the first test the impact of using skymask on the search is presented. This is particularly important to supernova triggered searches where we have optical information on sky location of the supernova. Two detector network (LIGO Hanford and LIGO Livingston), skymask of 5deg radius and realistic magnetorotationally driven explosion waveform is used in this study. As pointed for this example in Table 12.3 the TSD filter has positive

Test	Variation	FAR [Hz]	Eff cWB	Eff cWB+TSD	Eff increment
Impact on the skymask (dim2)	No skymask	1.0e-6	45.4%	50.7%	5.3%
		1.0e-5	45.9%	51.2%	5.3%
		1.0e-4	46.1%	51.7%	5.6%
	Circular skymask	1.0e-7	41.6%	49.6%	8.0%
		1.0e-6	41.9%	49.3%	7.4%
		1.0e-5	42.2%	49.6%	7.4%
Polarization of the waveforms (sch1)	Linearly polarized	1.0e-6	34.0%	43.0%	8.0%
		1.0e-5	35.0%	44.8%	9.8%
		1.0e-4	35.8%	45.9%	10.1%
	Non-linearly polarized	1.0e-6	36.9%	45.9%	9.0%
		1.0e-5	37.4%	46.7%	9.3%
		1.0e-4	38.2%	47.5%	9.3%

Table 12.3: Results summarizing tests of using TSD algorithm when skymask is present and ROC improvements for various tests

impact on sensitivity.

The second test considered here relates to the impact of the TSD filter on the linear and non-linear waveforms. In this example 3D Scheidegger et al waveform is used. For this waveform family the initial part of the core-collapse and bounce is linarly polarized and the polarization of the latter part has random phase. Table 12.3 indicates that the TSD filter does not affect detection efficiency when the non-linear component is present.

It is important to notice that the improvements shown in the tables are consistent across different False Alarm Rates, ranging from 1.0e-4Hz and 1.0e-8Hz.

Emission type	Identifier	Ref	FAR [Hz]	Eff cWB	Eff cWB+TSD	Eff increment
Magnetorotationally driven explosion	sch1	[40]	1.0e-6	36.9%	45.9%	9.0%
			1.0e-5	37.4%	46.7%	9.3%
			1.0e-4	38.2%	47.5%	9.3%
	sch2	[40]	1.0e-6	62.9%	65.8%	2.9%
			1.0e-5	63.1%	65.8%	2.7%
			1.0e-4	64.2%	66.6%	2.4%
	sch3	[40]	1.0e-6	61.3%	70.8%	9.5%
			1.0e-5	61.5%	71.1%	9.4%
			1.0e-4	61.5%	71.1%	9.4%
	dim1	[39]	1.0e-6	33.7%	41.7%	8.0%
			1.0e-5	34.4%	42.4%	8.0%
			1.0e-4	35.3%	43.0%	7.7%
	dim2	[39]	1.0e-6	45.4%	50.7%	5.3%
			1.0e-5	45.9%	51.2%	5.3%
			1.0e-4	46.1%	51.7%	5.6%
	dim3	[39]	1.0e-6	63.1%	71.6%	8.5%
			1.0e-5	63.4%	72.1%	8.8%
			1.0e-4	63.9%	72.1%	8.2%
Neutrino driven explosion	mur	[249]	1.0e-6	42.0%	46.0%	9.5%
			1.0e-5	46.5%	52.5%	12.9%
			1.0e-4	53.5%	60.0%	12.1%
	ott	[140]	1.0e-6	41.1%	46.7%	5.6%
			1.0e-5	41.6%	46.9%	5.3%
			1.0e-4	42.4%	47.5%	5.0%

Table 12.4: Improvements of using TSD algorithm for magnetorotationaly and neutrino driven explosion models. The improvement is consistet across those models.

Part IV

Future Generation Detectors

Chapter 13

GW Detection Perspectives with Future Detectors

While there are extensive studies of detectability of binary systems with future interferometers, the studies regarding detectability of CCSNe are not at the same level of maturity. The reasons reside both in the on-going work for completness of the waveforms as well as the optimization of the detection methodologies. For the first generation detectors and original excess power data analysis methodologies, the visible distance of SN signals was less then 1kpc for the most realistic waveforms computed for slowly rotating progenitors [17]. The designed sensitivities of Advanced Interferometers will be more than 10 times more sensitive in high frequency ($\sim 500-800$Hz) where we expect to detect majority of GW energy. They will give us visible distances for detecting CCSN of about O(10) kpc (Yakunin et al. in prep). Given that the aimed sensitivities of ET and CE will be around 10 times better than the sensitivities of Advanced Detectors, the visible ranges for detecting GW from slowly rotating progenitor CCSNe are expected to be O(100) kpc. Unfortunately, the SN rate at the distance of ∼100kpc is very small. The interesting ranges are when the sensitivity reaches starburst galaxies (starting at ∼3Mpc), Virgo Cluster (∼10-15Mpc) where we expect one SN per year and ∼20Mpc where we expect to see around 4 supernovae per year (Gill et al. in prep, section 7). In this regard, two orders of magnitude in visible distance are needed to achieve regular GW detections.

Understanding the perspectives is, however, complicateds because of a number of factors. For example, rapidly rotating progenitors, even if rare, are expected to produce more energetic waveforms than slowly rotating ones. Furthermore, the available waveforms are mostly incomplete. Another factor is the constant evolution of the pipelines. Finally, the improvement of the hardware for high frequency signals is a current topic of research.

13.1 Science Case

In my considerations of the detectability of GW from CCSN with the future GW detectors I will keep the supernova problem as my reference:

Why do the massive stars explode?

This problem can also be expressed in several different ways, like what the main explosion mechanism of a CCSN

is, what revives the shock that blows the stars or where the asymmetry of the explosion come from. There is a large spectrum of the questions associated with CCSN explosions (see section 2.3.1) from Fundamental Physics, Astrophysics etc. In the quest of answering the supernova problem, many of other supernova related problems from that spectrum can be addressed. One of them is the understand the timing of GW and neutrino messengers. It will possibly lead us to understanding the speed of neutrinos, their distribution that depends on still unknown neutrino mass hierarchy. In case when the star fails to explode and we get BH formation we will observe an unique neutrino and GW signatures. Spotting BH formation at its birth with help us to explore the formation of the event horizon or even test the no-hair theorem.

To address the supernova problem we need to be able to measure GW and their detectability depends mainly on their energies and frequency content. The difference between explosion mechanisms depends mainly on the progenitor star initial rotation: neutrino driven explosions for slow rotation and magnetorotatinally driven explosions for rapid rotation. GW observations or the lack of GW observations from nearby supernovae should shed light on the dominant explosion mechanism. The detectability of SN waveforms greatly depends on the frequency content. The detector's sensitivities are frequency dependent and it's important to design such an interferometer that is most sensitive in the frequency range where we expect to detect majority of GW energy.

13.2 Future Detectors

GWs from binary systems detected so far and the fact that the number of detectable events grows like cube with the distance provide great motivation to design and build GW detectors with greater sensitivities. Future detectors can be built either in new locations that allow making the interferometer arms longer or the new detectors can be built in the current facilities.

13.2.1 Einstein Telescope and Cosmic Explorer

Currently there are two main proposals for the next generation interferometers, Cosmic Explorer (CE, [250]) and Einstein Telescope (ET, [251]). CE is an American proposal with L-shape interferometer of 40km arm lengths while ET is an European proposal with triangular shape of 10km arm lengths that is supposed to be underground. The sensitivities of these detectors will be around an order of magnitude better than sensitivities of the Advanced Interferometers.

Figure 13.1 compares supernova waveforms produced at 10kpc referenced interferometer sensitivities. It shows an initial LIGO S5 sensitivity for SN 2007gr. The design sensitivities of Advanced Detectors are plottes in the shades of blue color. The bandwidth is wider and the predicted improvement in high frequency ~ 600Hz is better than in lower frequencies $\sim 100 - 200$Hz, while KAGRA has the best sensitivity in low frequency. The predicted sensitivities of Einstein Telescope and Cosmic Explorer are plotted as black and grey, respectively. The noise floor is lowered around a order of magnitude in comparison to the Advanced detectors, as well as the noise floor below ~ 30Hz is predicted to improve significantly better. Cosmic Explorer is designed to have arms 40km long. For such a arm length the long wavelength approximation is an issue at GW frequencies around 3.5kHz. At that frequency an average time of light circulation in the detector arms matches the period of GWs. This problem is visible on the plot as a peak at thisfrequency.

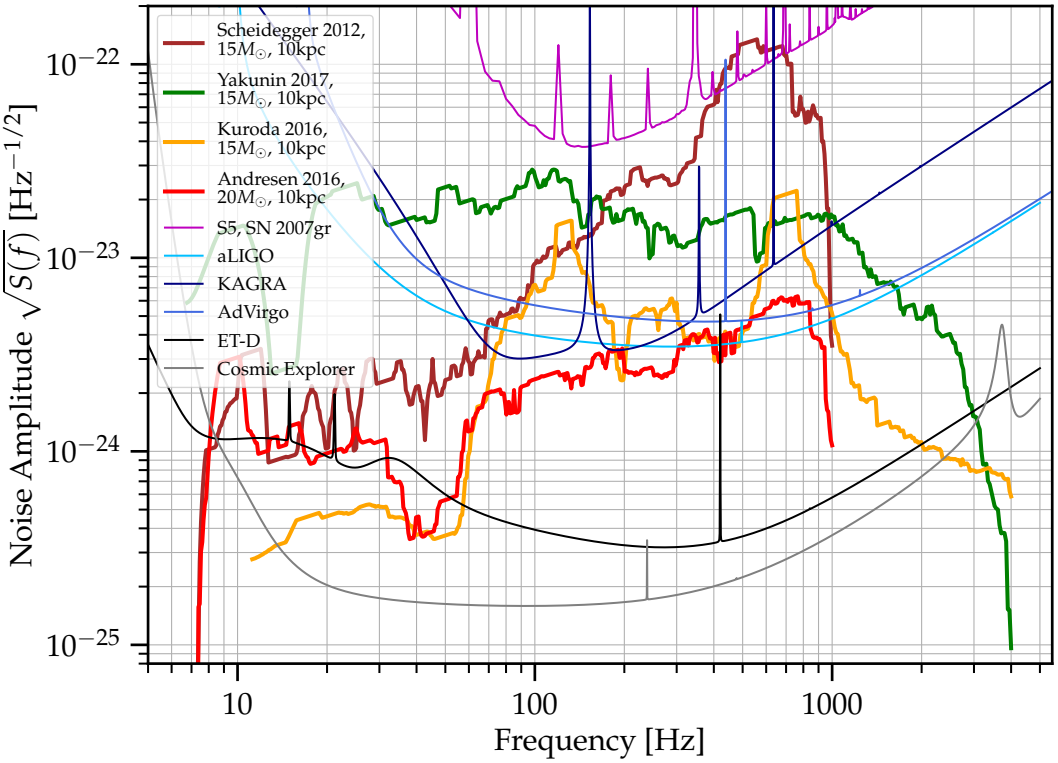

Figure 13.1: The comparison between noise floors between iLIGO/Virgo, designed Advanced Detectors and example Future Detectors. The plot also illustrates the spectras of the 3 neutrino driven waveforms.

Figure 13.1 shows also waveforms coming from the slowly rotating $15-20M_\odot$ progenitor stars supernova simulations of neutrino driven explosions: Yakunin et al 2017 [28], Kuroda et al 2016 [228] and Andresen et al [230]. The features that can be distinguished in the morphologies can be split into low and high frequency components that can be explained by SASI/convection and proto-neutron star oscillation respectively. It is particularly visible in for Yakunin et al 2017 and Kuroda et al 2016 waveforms, while the low frequency component is relatively weak for Andresen et al waveform. If a supernova explodes in the center of Milky Way (~ 8.5kpc) then for each of these models some parts of the waveforms stand above the noise floor stand above the noise floor for designed Advanced detectors. For an extragalactic supernova explosion (e.g. at the distance of SN 1987A in Large Magellanc Cloud, ~ 51kpc), we might be able to see some signal for each model for Future interferometer.

13.2.2 Specialized Detectors

Along with designing interferometers with longer arms in new facilities, the parrallel effort might be devoted to design detectors that maximize the capabilities of current facilities. Several proposals are currently under consideration and the research is in progress. I will consider detectability of SN waveform with few of the proposed designs.

One of the main astrophysical motivations for this efforts is to allow detection of the Binary Neutron Star merger phase at high frequencies [252]. This will shed light on understanding still unknown Nuclear Equation of State.

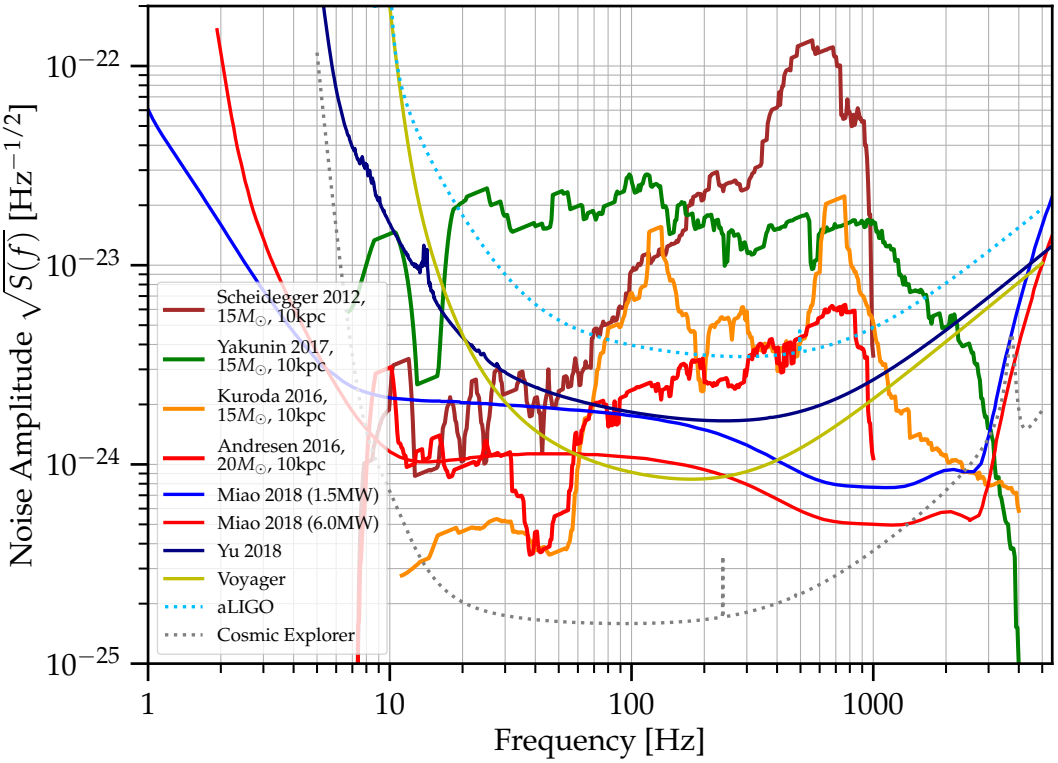

Figure 13.2: The comparison between noise floors for different proposals of redisigning the Advanced detectors to maximize the capabilities of current facilities. The plot also illustrates the spectras of the 3 neutrino driven waveforms.

High frequencies are also of great interest for detection of GW from CCSN. Another astrophysical motivation is the detection of GW memory from binary systems [253] or high mass binary systems [254]. GW from these sources are at very low frequencies $\sim$ 10Hz. This goal is also of interest for Supernova research. During the collapse, a massive flux of neutrinos are leaving proto-neutron star and asymmetry of this flux produce low frequency GW with peak frequency typically below $\sim$ 10Hz. Also, large asymmetries of the explosion (e.g. pulsar kicks) can also produce very low frequency GW signals. Although, there are debates on the strength of GW at very low frequencies, it is worth estimating the detectability of these effects for the proposed sensitivities.

Figure 13.2 presents different proposed designs that can be used to replace the interferometers in the current facilities. After the design sensitivity is reached, then the Advanced detectors are planned to be upgraded to A+ [255] with factor of two in beyond aLIGO. Several new technologies, like 6dB squeezing will be implemented and improved mirror coatings. After A+ the next upgrade is called Voyager [256] and it will require major modifications. The current mirrors will be replaced with $\sim 150-200$kg silicon mirrors and the suspension system will must be replaced. The mirrors will have new coatings implemented, they will be operating in low temperatures ($\sim$ 124K). The new pre-stabilized 200W laser with $\sim$ 2000nm wavelength will be implemented and $\sim$ 10dB squeezed light is planned to be used.

Beyond these plans, there are also other proposals of improving the noise floor of the interferometers. Figure 13.2 presents them and compare with the currently planned upgrades. A proposal, reffered as LIGO-LF, of upgrading

the low frequency part of spectrum at $\sim 5-30$Hz was proposed by Yu et al [254]. Several sources of non-stationary technical noises are limiting sensitivity at low frequencies that possibly can be minimized. Miao et al [252] proposes to limit the high frequency quantum noise at high frequencies with detuning signal recycling with an active optomechanical filter, frequency depending squeezing and high power laser.

13.3 Initial Studies

13.3.1 Initial Visible Distance Estimate

A simple estimate of predicted visible distance to detect GW from CCSN is rescaling the detection sensitivity curves according to the planned future hardware and algorithm improvements. We can do it because the visible distance and signal-to-noise ratio scale like $1/r$. We start from assuming that the following improvements might be possible in the future:

- $\times 1.5$ - algorithm development
- $\times 30$ - iLIGO to aLIGO improvement in High Frequncy
- $\times 10$ - aLIGO to vanilia ET/CE improvement
- $\times 5$ - improvement due to detection of population of GW.

The total improvement is 2250. These assumptions will need to be revisited.

Figure 13.3 show detection sensitivity curves taken from the iLIGO/Virgo Optically Triggered Search [17]. The dashed color curves correspond to different SN emission models for SN 2007gr. Black curves correspond to the potential improvements given in the previous paragraph for one of the emission models [58]. The visible distance for this model is ~ 1.65kpc and predicted detection range is estimated to be around $3-4$Mpc. This is important to highlight that at this distance the starburst galaxies host CCSNe frequently.

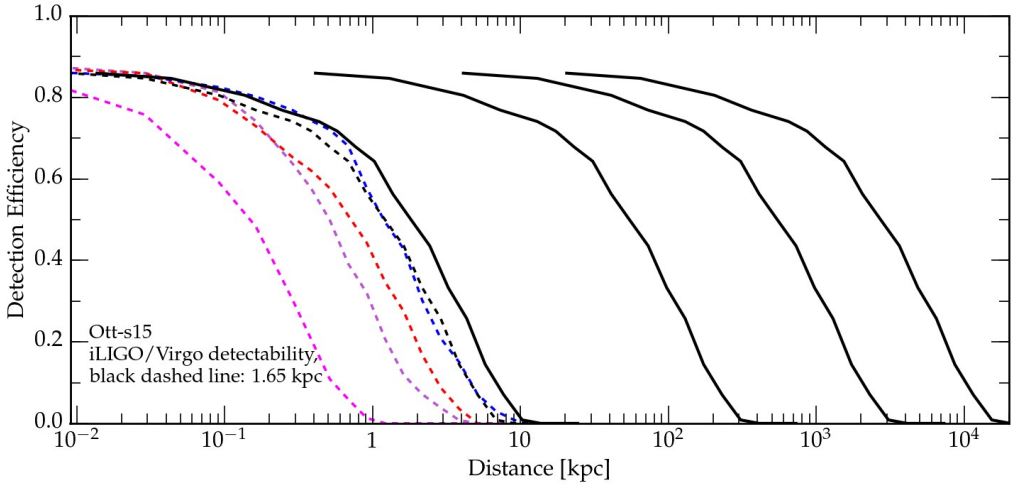

Figure 13.3: Initial considerations on the detectability of SN waveforms with the future detectors assuming certain hardware and algorithm improvements (see text for more details).

13.3.2 GW Detection Rate

The next step in estimating the detectability of GW from CCSNe is the detection rate as a distance of distance. Detection Rate is the estimated number of possible gravitational waves (GW) detection for a given period of time based mainly on the differential rate of CCSN and sensitivity curve of for a given emission model. We assume a Standard Candle approach where we assume that the considered emission model is dominant.

The detection rate n for a particular GW emission model is defined as follows:

$$n = \int_0^\infty \frac{\mathrm{d}R(r)}{\mathrm{d}r}\epsilon(r)\mathrm{d}r, \tag{13.1}$$

where $\frac{\mathrm{d}R(r)}{\mathrm{d}r}$ is a differential supernova rate as a function of distance r (from Gill et al in prep) and $\epsilon(r)$ efficiency as a function of distance r. At the small distances, n is small (or zero) because the supernova rate is very small. The detection rate grows with the distance as the rate grows, but when the detection efficiency goes to zero, the detection rate also goes to zero.

Figure 13.4 shows how the detection rate grows with the improvement in the sensitivity of the visible distance α. Few SN explosion models are considered: Dimmelmeier et al [39] (Dim1, Dim2, Dim3), Ott et al [58] (Ott-s15) and Yakunin et al [132] (Yak-s15). For the predicted earlier improvement of $\alpha = 2250$ the detection rate is either close to zero or closer to 1 per year for the most energetic Dim3 and Ott-s15 models. The detection rate grows rapidly above $\alpha = 2250$, additional factor of 2 might be within reach. It seems that for the maximum possible hardware and algorithm improvements it might be possible to have regular detections.

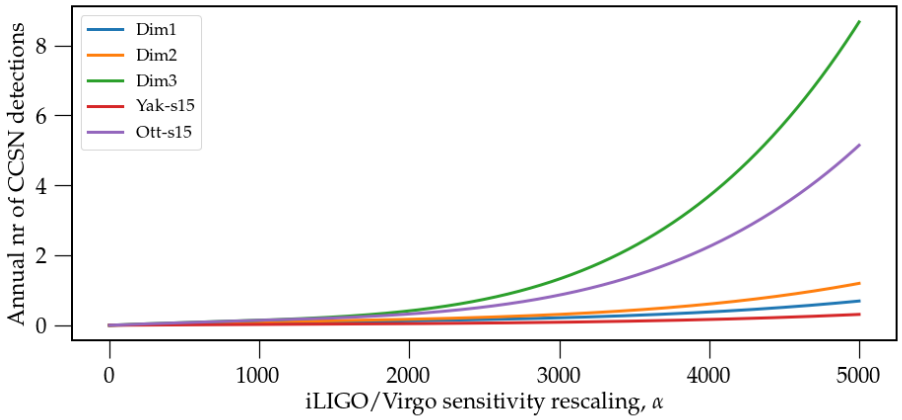

Figure 13.4: Detection rate for few emission models.

13.4 Detection ranges

Next step in the consideration of detectability of the SN waveforms is the estimation of the visible distances taking into account the predicted improvement in the interferometers noise floor. In this study, the O1 data was recolored to the designed sensitivities of some planned future detectors: A+, Voyager, ET_D, CE_wb. Two

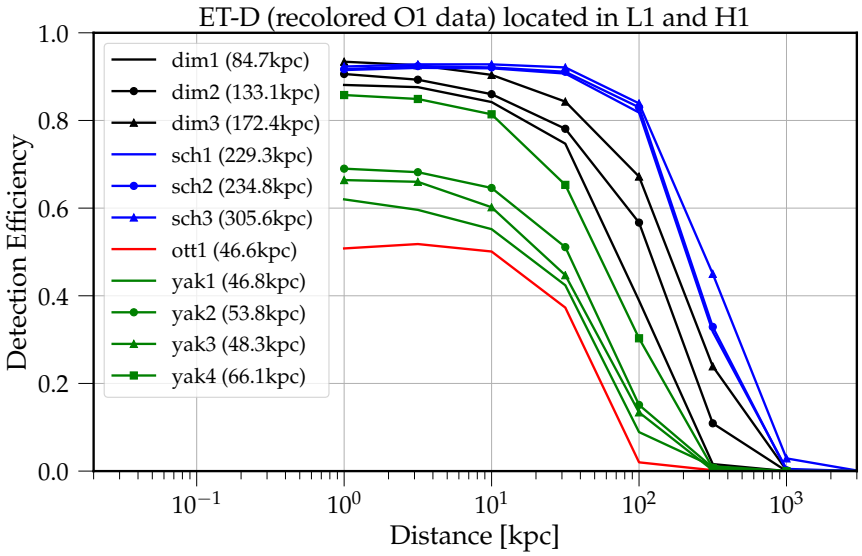

Figure 13.5: Visible detection ranges for the network of future detectors assuming two detctors located at the L1 and H1 sites with ET_D designed sensitivities.

interferometer networks are created for each planned detector that are placed in L1 and H1 locations. Note that the Einstein Telescope is a detector made out of 3 interferometers, but in this study we calculate the visible distance assuming only one interferometer for ET.

Figure 13.5 and figure 13.6 presents the detection efficiencies for Einstein Telescope and Cosmic Explorer, respectively. Detection efficiencies are calculated for four supernova waveforms from the iLIGO/Virgo search [17]. The numbers in the brackets are the distances at which the efficiencies equals 50% of its asymptotic value at small distances For Einstein Telescope the reach for the neutrio riven waveforms (ott1, yak1, yak2, yak3, yak4) is around 50 kpc, while the distance for magnetorotatinally driven waveforms goes up even to 300 kpc (dim1, dim2, dim3, sch1, sch2, sch3). In both cases we should see Supernovae beyond Milky Way. For a network of Cosmic Explorer detectors the visible distances roughly double for both explosion mechanisms.

Table 13.1 summarizes the results for different planned detectors. The planned improvement between O1 and A+ is around an order of machitude. Voyager cofiguration will give additional improvement in range of around 50%. Einstein Telescope sensitivity (one interferometer) will bing factor of 3 in the ranges. A network of two Cosmic Explorers will give an additional factor of 2. In ths study, none of the waveforms reaches the distance of Virgo cluster (10-15 Mpc) where the cummulative rate is about 1 CCSN per year. For slowly rotating neutrino driven explosions, two orders of magnitude are needed to reach the rate of annual detection.

13.5 Review of Different Aspects of GW SN Research

Although the visible distance for the current SN waveforms for slowly rotating progenitor stars is of an order of few hundreds of kpc where the rate of SNe is very small, it is worth persuing further considerations of the possibility of detecting GW from CCSN in case of exploring the long term potentials of different branches of research related

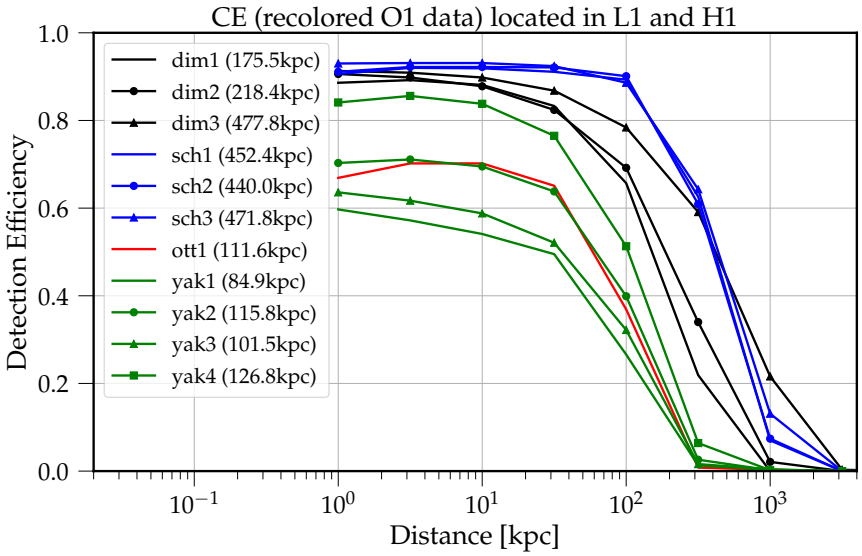

Figure 13.6: Visible detection ranges for the network of future detectors assuming two detctors located at the L1 and H1 sites with CE_wb designed sensitivities.

to the GW Multimessenger Astronomy.

13.5.1 Numerical Simulations

Simulating Core-Collapse Supernovae is a multi-scale multi-physics computational challenge. All fundamental forces are involoved and play important roles in creating explosions. The micro-physics has an impact on macro-physica phenomena and vice versa. Particularly, the Neutrino Physics require special attention. Raliable modeling is computationally extremely challenging and require milions of CPU hours and many months to produce less than a second of a supernova explosion and the GW waveforms.

In the recent decades significant progress was made to produce a succesfull explosions[257]. Robust explosions

Waveform	Visible Distance [kpc]				
	O1	A+	Voyager	ET_D	CE_wb
yak1	1.6	11.1	16.0	46.8	84.9
yak2	1.7	12.6	18.2	53.8	115.8
yak3	1.9	12.8	18.0	48.3	101.5
yak4	2.9	15.6	21.0	66.1	126.8
ott1	1.8	11.9	17.5	46.6	111.6
sch1	8.3	54.5	71.3	229.3	452.4
sch2	8.4	51.6	77.1	234.8	440.0
sch3	9.5	59.7	83.7	305.6	471.8
dim1	3.4	17.4	34.5	84.7	175.5
dim2	4.4	28.8	43.1	133.1	218.4
dim3	6.7	41.8	67.4	172.4	477.8

Table 13.1: Visible distances for ddifferent designed noise floors of the future planned detectors.

were achieved in 2D models with qualitative agreement between groups. First explosions were accomplished in 3D.

However, several challenges are still waiting to be solved. At the current state-of-the-art the community simulating CCSNe is transitioning from 2D to 3D models. Including initial star rotation is a natural next step which is not yet included into the most sophisticated neutrino driven models. Similarly, the magnetic field is not fully implemented yet. Moreover, different groups simulating supernovae use different progenitor star, different approximations or different physics components, which makes the comparison between models a difficult task.

The modeling will remain a huge challenge for the next many years or decades. Along with including more physics into the models and computational demands, there are many limitations to improve the models. The next decade will bring new peta and exascale machines that will provide necessary computational power to allow improving the models. However, the architecture of these super computers will be radically different and all the current codes will have to be rewritten. Many parameters in the vast supernova parameter space cannot be reliably constrained through the astrophysical observations making the modeling even more difficults.

The detection of GW from CCSN will allow to greatly improve the models, teach us about the dynamics of the supernova explosion and shed new light on the supernova problem. Similarly a null detection will allow us to bring new understanding of the core-collapse supernovae. The tight cooperation between Supernova Modelers and GW Astronomers might allow systematically explore nature of exploding stars and get ready for the next Galactic supernova.

13.5.2 Interferometer R&D

The SN waveforms are predicted to be broadband, but the majority of the energy is associated with high frequency proto-neutron star oscillation, $\sim 500 - 800$ Hz. In the lower frequencies, below 50 Hz, the SN models do not predict a significant amount of radiated GW, while the peak frequency from the GW Memory is estimates to be below 10 Hz where hardware improvement is extremely challenging. In this regard, the focus on improving the GW detector for detecting SN sources should be centered around improvements in high frequencies.

The high frequencies are limited by the photon shot noise and there are few methods of decreasing it. Main method would be increasig the laser power circulating in the detector arms. This allows decreasing the noise in high frequencies, but for paying the price of significantly decreasing the sensitivity in the low frequencies. Another method that is a subject of the current R&D is squeezing. This method is predicted to give few factors improvement in interferometer sensitivity. Additionally, increasing wavelength of the laser light allows improving the sensitivity. Currently, the detectors oparate with 1064nm lasers but an active research is deveted to use ~2000nm lasers. The research on designing interferometer for detecting SN sources is on-going.

13.5.3 Neutrino Observations

An important role in detecting GW from CCSN lays in understanding the timing of GW from detection neutrino fluxes. The initial flux of neutrinos leaves the core within the first second of the GW, while most of the neutrinos leave the core during the first 10s [258]. These stringent timing constraints can be used to more efficiently search for a GW signal. An important scenario is the search for GW from a Galactic supernova triggered by neutrino detections and communicated with a SNEWS alert. In this scenario, the flux of neutrinos is estimated to be very strong (O(10,000) of detected neutrinos for Galactic Supernova).

The current neutrino detectors, primarily Super Kamiokande, are able to detect neutrinos from a CCSN events up to several hundreds of kpc. The next generation of the Japanese/Korean neutrino detectors, Hyper Kamiokande, might be able to detect extragalactic CCSN up to several Mpc [9]. This kind of instrument would allow to detect neutrino fluxes from nearby starburst galaxies. Figure 13.7 shows a predicted sensitivity of Hyper-Kamiokande. The neutrino signal from supernovae few Mpc away might be very weak, but they can become essential in the search for GW.

Furthermore this distance can be improved by creating a network of neutrino detectors [27]. The work of planning/creating/coordinating a network of current neutrino detectors is on-going in the scientific community.

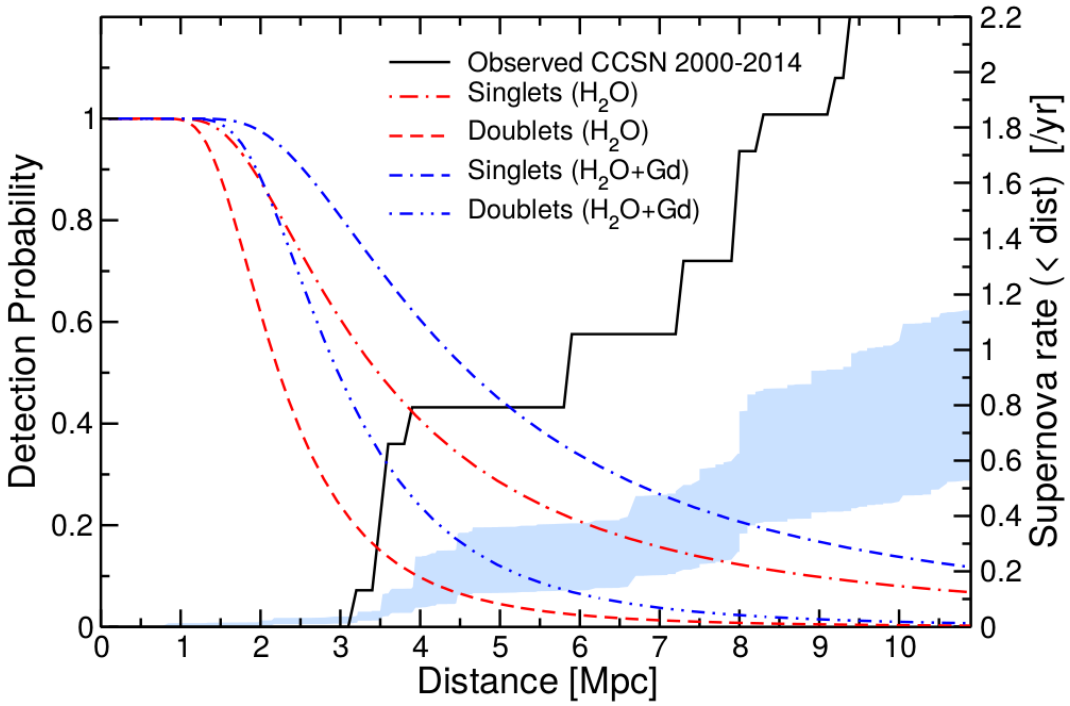

Figure 13.7: The predicted sensitivity of Hyper-Kamiokande detector (image source [9]).

13.5.4 Astronomical Observations

All CCSNe that we know nowadays were detected in electromagnetic spectrum. Astronomical observations give us many information about supernovae, that will allow increase significance of GW candidates (on-source window), removing noise transients in GW detectors (e.g. sky location) or constraining the explosion models (e.g. distance). See section 3 for more details. For the neutrino triggered GW search (in particularly SNEWS triggered search) the optical observations do not bring crucial informations for the GW detection purposes, they are very important for constraining the SN models. The amount of discovered supernovae is growing over the decades and improved astronomical survays searching for supernovae will allow us systematic constraining the central engine of the supernova explosion.

13.5.5 GW Data Analysis

The search of GW from CCSNe is a challenging task given non-deterministic nature of the waveforms. However, there are certain advantages of that search over a blind search. Neutrino and optical observations give us prior information that will allow us to increase significance of the GW candidates. Some of these advantages are listed in section 3. Particularly crucial information is the timing of the moment of the collapse from the neutrino observations of an order of seconds or even less. Having such a constrained on-source window, can we accept very weak GW candidates? Currently, the minimum detectable signal-to-noise ratio (SNR) is around 10-30, and there is an on-going work on understanding feasibility of detecting GW signals at SNR$\sim 2-3$.

One problem that might emerge with detecting GW from CCSNe is the large amount of GWs from binary systems in the future generation detectors. These GWs will overlap with GWs coming from supernovae. It will be important to develop algorithms that could separate effectively the binary systems from other types of GW souces.

Chapter 14

SNR Distributions

In this chapter I investigate the SNR distributions for different GW signals from CCSNe. for depends on the distance below currently detectable SNR limits and the maximum ranges where SNR>1. The information about the timing of a collapsing core based on detection of neutrino fluxes has the potential of increasing the visible range by an order of magnitude. The investigation of developing methodologies that would allow detecting very weak signals (SNR>1) is beyond the scope of this thesis.

Matched filtering SNR is a standard measure of the strength the signal that is independent from the method and the pipeline used. In these studies the SNR values are obtained by calculating matched filtering SNR using injections of cWB.

14.1 Signal-to-Noise Ratio

Matched Filtering SNR Matched Filtering Signal-to-Noise Ratio (SNR) is a measure of how much the signal stands above the noise assuming optimal method of matched fltering. The SNR is defined as (see also section 4.2.2):

$$SNR = \sqrt{4 \int_0^\infty df \frac{|\widetilde{h}(f)|^2}{S_n(f)}}, \tag{14.1}$$

where $\widetilde{h}(f)$ is a Fourier Transform of the GW strain $h(t)$:

$$\widetilde{h}(f) = \int_{-\infty}^{+\infty} dt h(t) e^{+ift}, \tag{14.2}$$

and $S_n(f)$ is Amplitude Spectral Density of the detector noise. It is worth mentioning that given that the GW strain decreases like $1/r$, the SNR will also decrease as $1/r$. When a SN is placed at the distance of 10kpc and the SNR at that distance is $SNR(10\text{kpc})$, then the SNR value for a SN placed at distance r is:

$$SNR(r) = \frac{10\text{kpc}}{r} SNR(10\text{kpc}). \tag{14.3}$$

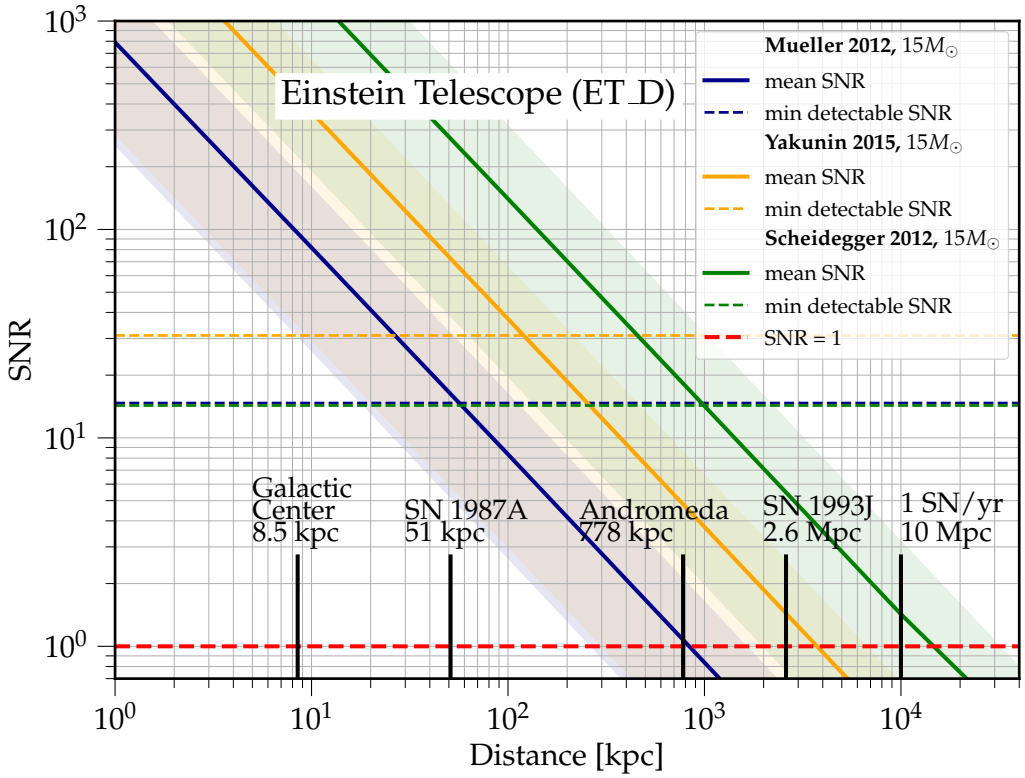

Figure 14.1: SNR versus distance dependance and minimum detectable SNR for ET-D and magnetorotatinally driven waveforms.

This dependance is visible in plots of this chapter as a linear trend in logarithmic plots. Notice, that in some literature the matched filtering SNR is denoted as ρ. However, ρ throughout this thesis is reserved as coherent SNR, not matched filtering SNR.

Network SNR For a network of GW detectors, the total SNR increases with the number of detectors in the network. The network SNR is defined as:

$$SNR_{net} = \sqrt{\sum_{i=0}^{K} SNR_i}, \tag{14.4}$$

where K is a number of detectors in the network. For K detectors with similar noise floor, the total SNR is proportional to $\sqrt{K}$. Further on, the SNR_{net} is denoted simply as SNR, unless stated otherwise.

Minimum Detectable SNR The minimum detectable SNR is reffered as a SNR at 50% detection efficiency. More details can be found in section 8.4.5. The potential capabilities of detecting very weak event with SNR$\sim 2-3$ will require research and it is not scope of this dissertation.

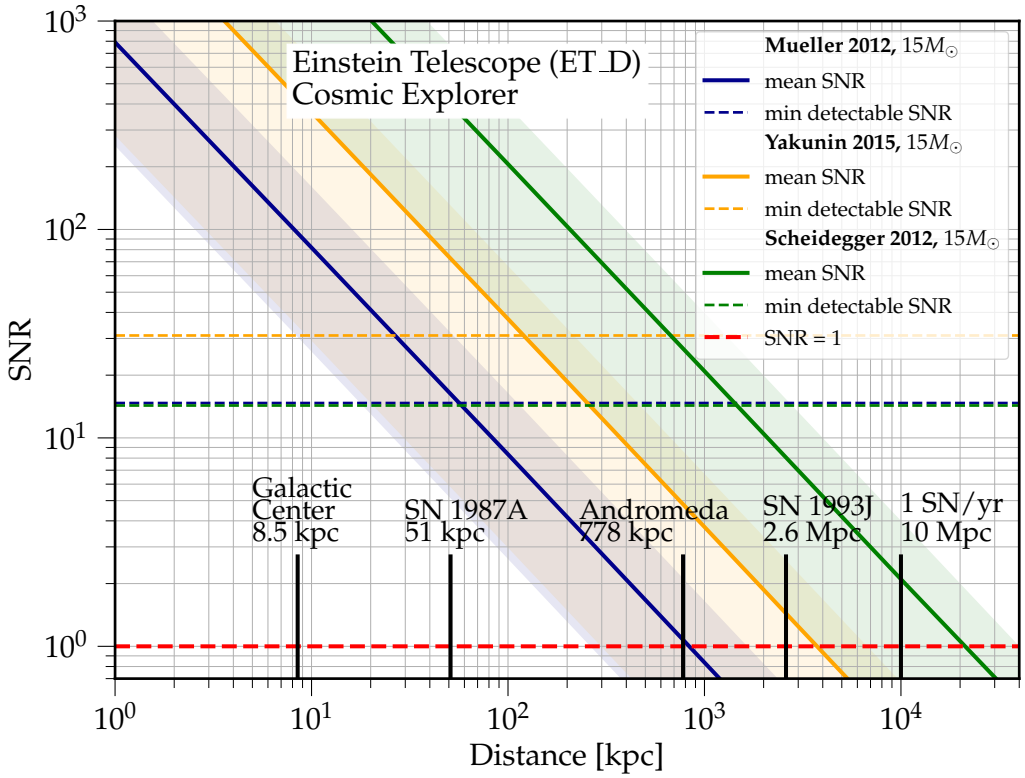

Figure 14.2: SNR versus distance dependance and minimum detectable SNR for ET/CE network and magnetorotatinally driven waveforms.

14.2 Future Detectors

This section describes the detctable SNR distributions as functions of the distance for the networks of planned future detectors. Figure 14.1 and 14.2 depict the SNR distribution as a function of distance for three waveform families: two neutrino driven for slowly rotating progenitors (Mueller et al 2012 and Yakunin et al 2015) and one for magnetorotatinally driven explosions for rapidly rotating progenitors (Scheidegger et al 2010). The plot shows the average SNR as a function of time and the shaded regions contain the SNR values between the minimum and maximum predicted SNR (the spread is mostly due to the antenna pattern of the detector). As pointed earlier, the SNR decreases as $1/r$ and in the logarithmic plot they are straight lines.

Figure 14.1 and 14.2 point out few distances as references for the GW detectability:

- 8.5 kpc - Galactic Center,
- 51 kpc - SN 1987A,
- 778 kpc - Andromeda, the closest spiral galaxy similar to Milky Way,
- 2.6 Mpc - SN 1993J, the second closest supernova of the last century, after SN 1987A,
- 10 Mpc - range where we expect to see optially 1 SN per yer.

In practice, in the distance range between 2.6 Mpc and 10 Mpc we observe and we expect realistically to observe optically a core-collapse supernova. The enclosed volume includes also some starburst galaxies producing CCSNe at the higher rate than regular galaxies. Beyond 10 Mpc the rate of supernovae grows like cube with the distance and reaching distances beyond 10 Mpc is very desirable. At small distances, $\lesssim$ 2.6 Mpc the CCSNe are expeced to very rare, but they will atract a particular interest, like SN 1987A or SN 1993J.

The plots shows also the minimum detectable SNR (see also section 8.4.5) as a reference. The detectable SNR for realistic models ranges between 10 and 30. Reaching SNR$\sim$ 1 would extend the distance one order of magnitude.

Table 14.1 and 14.2 present the expected SNR values for few reference distance and several waveform families. The waveform models cover the following core-collapse scenarios:

- simulations of slowly rotating progenitor stars: Mueller et al 2012 [33], Ott et al 2013 [140], Yakunin et al 2015 [38], Andresen et al 2017 [230], Kuroda et al 2016 [228], Kuroda et al 2017 [259],
- simulations of rapidly rotating progenitor stars: Scheidegger et al 2010 [40], Dimmelmeier et al 2008 [39],
- Black Hole formation with rapid rotation: Cerda-Duran et al 2013 [26], Ott et al 2010 [260].

The tables show average values of the SNR values and standard deviations of these values.

14.2.1 Einstein Telescope alone

Einstein Telescope is designed to be a triangular-shape detector made of three interferometers rotated 60^o degrees Einstein Telescope will be able to detect GWs alone, without a network of other interferometers spacially separated. However, ET will not be able to estimate robustly the sky locations of GW sources. The total SNR of the whole ET will be $\sqrt{3}$ larger than the SNR coming from a single ET interferometer.

Figure 14.1 and table 14.1 presents the SNR distributions for Einstein Telescope alone. We should be able to detect GWs beyond the distance of SN 1987A. However, at the distance of Andromeda we have little change to measure any GW signal assuming the most realistic models. However, we should be able to start constraining some of the more extreme emission models.At the distance of SN 1993J and at 10Mpc the SNR goes below 1, so we do not expect detecting any GWs.

14.2.2 Einstein Telescope and Cosmic Telescope Network

The sensitivity of CE alone will be better than sensitivity of a single ET interferometer. However, the sensitivity of the network of ET and CE will not be much larger than sngle ET. The network will allow to better localize the source. Figure 14.2 and table 14.2 shows the SNR distributions. GW from sueprnovae will be detectable up to 51kpc for all models. Sueprnovae at the distance of SN 1993J might be able to detect GW from assuming more energetic emission process.

Waveform Family	Model	8.5 kpc GC	51 kpc SN 1987A	778 kpc Andromeda	2.6 Mpc SN 1993J	10 Mpc 1 SN/year
Mueller et al 2012 [33]	L15-3	55 ± 15	9.4 ± 2.5	0.6 ± 0.2	0.2 ± 0.1	0.05 ± 0.01
	N20-2	33 ± 8	5.6 ± 1.3	0.4 ± 0.1	0.11 ± 0.03	0.03 ± 0.01
	W15-4	39 ± 11	6.5 ± 1.9	0.4 ± 0.1	0.13 ± 0.04	0.03 ± 0.01
Ott et al 2013 [140]	s27fheat1p05	85 ± 23	14 ± 4	0.9 ± 0.3	0.3 ± 0.1	0.07 ± 0.02
Yakunin et al 2015 [38]	B12-WH07	176 ± 47	30 ± 8	2.0 ± 0.5	0.6 ± 0.2	0.15 ± 0.04
	B15-WH07	250 ± 65	42 ± 11	2.8 ± 0.7	0.8 ± 0.2	0.22 ± 0.06
	B20-WH07	218 ± 69	37 ± 12	2.4 ± 0.8	0.7 ± 0.2	0.19 ± 0.06
	B25-WH07	343 ± 102	58 ± 17	3.8 ± 1.2	1.2 ± 0.3	0.30 ± 0.09
Andresen et al 2017 [230]	s11	24 ± 8	4.0 ± 1.3	0.3 ± 0.1	0.08 ± 0.002	0.02 ± 0.01
	s20	57 ± 19	9.5 ± 3.2	0.6 ± 0.2	0.2 ± 0.1	0.05 ± 0.02
	s20s	102 ± 34	17 ± 6	1.1 ± 0.4	0.3 ± 0.1	0.09 ± 0.03
	s27	40 ± 13	6.8 ± 2.2	0.4 ± 0.1	0.13 ± 0.04	0.03 ± 0.01
Yakunin et al 2017 [28]	C15	352 ± 112	60 ± 19	3.9 ± 1.3	1.2 ± 0.4	0.3 ± 0.1
Kuroda et al 2016 [228]	SFHx	208 ± 67	35 ± 11	2.3 ± 0.8	0.7 ± 0.2	0.18 ± 0.06
	TM1	146 ± 47	25 ± 8	1.6 ± 0.5	0.5 ± 0.2	0.13 ± 0.04
Kuroda et al 2017 [259]	S11d2	404 ± 138	69 ± 23	4.6 ± 1.6	1.4 ± 0.5	0.4 ± 0.1
	S15d0	97 ± 33	16 ± 5	1.1 ± 0.4	0.3 ± 0.1	0.08 ± 0.03
Scheidegger et al 2010 [40]	R1E1CA$_L$	24 ± 11	4.0 ± 1.8	0.27 ± 0.12	0.08 ± 0.04	0.02 ± 0.01
	R3E1AC$_L$	1606 ± 707	273 ± 120	18 ± 8	5.4 ± 2.4	1.4 ± 0.6
	R4E1FC$_L$	1584 ± 644	270 ± 110	18 ± 7	5.4 ± 2.2	1.4 ± 0.6
Dimmelmeier et al 2008 [39]	s15A2O05ls	345 ± 120	59 ± 21	3.9 ± 1.4	1.2 ± 0.4	0.3 ± 0.1
	s15A2O09ls	583 ± 207	99 ± 35	6.6 ± 2.4	2.0 ± 0.7	0.5 ± 0.2
	s15A3O15ls	618 ± 230	105 ± 39	7.0 ± 2.6	2.1 ± 0.8	0.5 ± 0.2
Cerda-Duran et al 2013 [26]	slow	2428 ± 915	415 ± 156	28 ± 11	8.4 ± 3.2	2.2 ± 0.8
	fiducial	1477 ± 542	253 ± 93	17 ± 6	5.1 ± 1.9	1.3 ± 0.5
Ott et al 2010 [260]	u75rot1	1107 ± 389	190 ± 67	13 ± 5	3.8 ± 1.4	1.0 ± 0.4
	u75rot1.5	2077 ± 735	357 ± 126	24 ± 9	7.3 ± 2.6	1.9 ± 0.7
	u75rot2	2552 ± 941	436 ± 161	30 ± 11	9.0 ± 3.3	2.3 ± 0.9

Table 14.1: SNR distribution for Einstein Telescope (ET_D) alone.

Waveform Family	Model	8.5 kpc GC	51 kpc SN 1987A	778 kpc Andromeda	2.6 Mpc SN 1993J	10 Mpc 1 SN/year
Mueller et al 2012 [33]	L15-3	96 ± 28	16 ± 5	1.1 ± 0.3	0.3 ± 0.1	0.08 ± 0.02
	N20-2	62 ± 18	10 ± 3	0.7 ± 0.2	0.21 ± 0.06	0.05 ± 0.02
	W15-4	67 ± 20	11 ± 3	0.7 ± 0.2	0.22 ± 0.07	0.06 ± 0.02
Ott et al 2013 [140]	s27fheat1p05	149 ± 40	25 ± 7	1.7 ± 0.5	0.5 ± 0.1	0.13 ± 0.03
Yakunin et al 2015 [38]	B12-WH07	302 ± 95	51 ± 16	3.4 ± 1.1	1.0 ± 0.3	0.26 ± 0.08
	B15-WH07	429 ± 132	73 ± 22	4.8 ± 1.5	1.4 ± 0.4	0.37 ± 0.12
	B20-WH07	386 ± 118	65 ± 20	4.3 ± 1.3	1.3 ± 0.4	0.34 ± 0.10
	B25-WH07	581 ± 185	99 ± 32	6.5 ± 2.1	2.0 ± 0.6	0.51 ± 0.16
Andresen et al 2017 [230]	s11	37 ± 8	6.2 ± 1.3	0.41 ± 0.09	0.12 ± 0.03	0.03 ± 0.01
	s20	85 ± 18	14 ± 3	0.9 ± 0.2	0.3 ± 0.1	0.08 ± 0.02
	s20s	159 ± 31	27 ± 5	1.8 ± 0.3	0.5 ± 0.1	0.14 ± 0.03
	s27	63 ± 13	11 ± 2	0.7 ± 0.1	0.21 ± 0.04	0.05 ± 0.01
Yakunin et al 2017 [28]	C15	598 ± 130	102 ± 22	6.7 ± 1.5	2.0 ± 0.4	0.5 ± 0.1
Kuroda et al 2016 [228]	SFHx	315 ± 74	53 ± 13	3.5 ± 0.8	1.1 ± 0.3	0.27 ± 0.07
	TM1	218 ± 41	37 ± 7	2.4 ± 0.5	0.73 ± 0.14	0.19 ± 0.04
Kuroda et al 2017 [259]	S11d2	624 ± 160	106 ± 27	7.0 ± 1.8	2.1 ± 0.5	0.5 ± 0.1
	S15d0	154 ± 34	26 ± 6	1.7 ± 0.4	0.5 ± 0.1	0.13 ± 0.03
Scheidegger et al 2010 [40]	R1E1CA$_L$	35 ± 12	5.9 ± 2.1	0.39 ± 0.14	0.12 ± 0.04	0.03 ± 0.01
	R3E1AC$_L$	2355 ± 844	401 ± 144	27 ± 10	8.1 ± 2.9	2.1 ± 0.8
	R4E1FC$_L$	2366 ± 776	403 ± 132	27 ± 9	8.1 ± 2.7	2.1 ± 0.7
Dimmelmeier et al 2008 [39]	s15A2O05ls	534 ± 176	91 ± 30	6.0 ± 2.0	1.8 ± 0.6	0.5 ± 0.2
	s15A2O09ls	857 ± 259	146 ± 44	9.7 ± 3.0	2.9 ± 0.9	0.75 ± 0.23
	s15A3O15ls	1095 ± 405	186 ± 69	12 ± 5	3.7 ± 1.4	1.0 ± 0.4
Cerda-Duran et al 2013 [26]	slow	3653 ± 1140	623 ± 189	42 ± 13	13 ± 4	3.2 ± 1.0
	fiducial	2264 ± 689	389 ± 117	26 ± 8	7.9 ± 2.4	2.0 ± 0.6
Ott et al 2010 [260]	u75rot1	1773 ± 604	304 ± 101	21 ± 7	6 ± 2	1.6 ± 0.5
	u75rot1.5	3274 ± 1066	561 ± 185	38 ± 13	12 ± 4	3.0 ± 1.0
	u75rot2	4092 ± 1394	707 ± 243	48 ± 17	15 ± 5	3.8 ± 1.3

Table 14.2: SNR distribution for Einstein Telescope (ET_D) and Cosmic Explorer (CE_wb) network.

Chapter 15

Distributional Tests

Since the advanced Laser Interferometer Gravitational-wave Observatory (aLIGO) became operational in 2015, many new and exciting astrophysical phenomena have been discovered from their gravitational waves, such binary blackhole systems. One of the current goals of aLIGO is to detect gravitational waves from supernova sources in order to explore the mechanisms of collapse and explosion. However, simulated supernovae signals have been shown to be weak in comparison with other events detected by aLIGO. Currently, potential gravitational wave candidates that could be supernovae are analyzed with the coherent Waveburst pipeline (cWB) and rely only on the loudest event statistics, where the loudest energy, known as a trigger, is considered and the rest of the triggers are discarded. A study on this method has shown that with realistic supernova simulations, 40% of supernova triggers are lost in the background noise, and all the triggers have extremely high energies. Further, there are only few supernovae per year predicted to occur in the range that aLIGO can detect (see section 7), thus making it imperative that a new detection method be implemented.

One such detection method is that of distributional tests, which compare a background of noise triggers to that of a foreground with potential gravitational wave candidates and determine if the two come from a common population, or rather that both are merely noise. Additionally, there are two types of distributional tests: parametric, which assume that the background is of a known shape such as a Gaussian or Poissonian; and nonparametric, which make no assumptions on the shape of the background. Since the background in aLIGO is a random distribution of noise triggers, nonparametric tests are prefered. Those examined were chosen from common statistical methods and from convention for tests with large data, and include the Kolmogorov-Smirnov two-sample test, the Anderson-Darling two-sample test, the Mann-Whitney U test, and the Chi Squared test.

15.1 Methodology

The cWBpipeline uses many detection statistics in its analysis. To test the viability of using distributional tests, the network signal-to-noise ratio statistic ρ is used (see section 4). It is a scalar measure, but cannot be combined over different on-source windows. Each test iss chosen based on its conventional use in analyzing large sets of data. Typically, these tests are used in analyzing data from social experiments and involve continuous or binned data. However, each test has limitations. Here, the foreground is denoted as F, and the background as B.

We use L1 and H1 data from LIGO Scientific Run 6 (S6) recolored to O1 noise level. The background is created based on the time shifting the data from one detector with respect to the other, lags. We use 300 lages to create the background, and we use each lag as an simulated foreground. Figure 15.1 shows the False Alarm Rate of the background and a random time slide lag, which is an example of a foreground.

The results of each test are compared using the p-value (p), which is the probability that the foreground and background are from the same population. A 5% confidence level is used, meaning that for a detection to occur, $p \leq 0.05$. The null hypothesis in each case is that the distributions come from the same population, and the alternative hypothesis in each case is that the two distributions come from different populations.

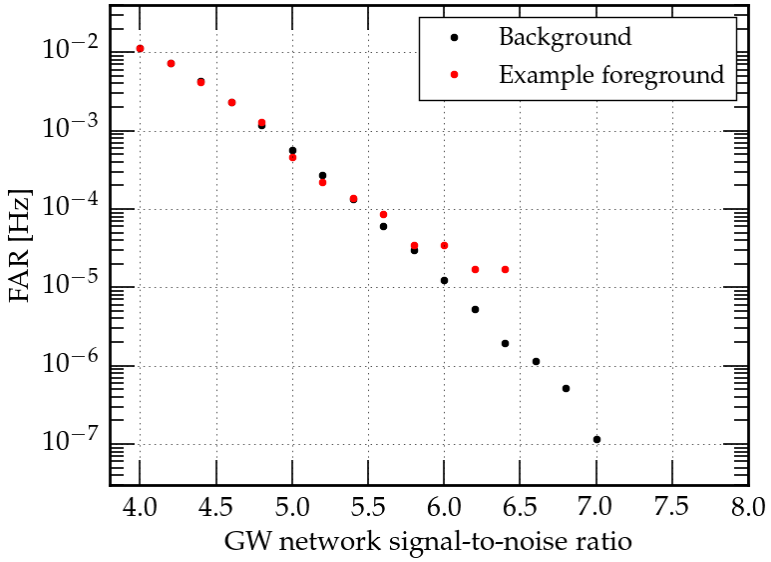

Figure 15.1: Background and an example of a foregrond. Distributional tests quantify the probability of how the distributions are similar are the two distributions.

15.1.1 Kolmogorov-Smirnov Two-Sample Test

The Kolmogorov-Smirnov two-sample test is one of the most well-known and widely used distributional tests. It relies on continuous data and a sample size of greater than 30. First, the background and foreground are ranked from lowest to highest ρ values, and each ρ value given a rank from 1 to the total number of triggers in the distribution. The ranks are then divided by the total number of triggers, giving the cumulative distribution function. When compared, the difference between cumulative distribution functions for the foreground and the background is found - this is the Kolmogorov-Smirnov test statistic D:

$$D = max(|B - F|) \tag{15.1}$$

This value of D is then converted into a p-value:

$$P(D) = Q_{ks}([\sqrt{N_e} + 0.12 + \frac{0.11}{\sqrt{N_e}}]D) \tag{15.2}$$

The value of Q_{ks} is given by the cumulative distribution function:

$$Q_{ks}(z) = 2\sum_{j=1}^{\infty}(-1)^{j-1}e^{-2j^2z^2}. \tag{15.3}$$

And the value N_e is given as:

$$N_e = \frac{N_F N_B}{N_F + N_B} \tag{15.4}$$

This test is most sensitive near the median of the distributions, and less sensitive at extremely low ρ values or extremely high ρ values.

15.1.2 Anderson-Darling Two-Sample Test

The Anderson-Darling two-sample test is a variation of the Kolmogorov-Smirnov test that is more sensitive at the extremes, but less so towards the median. It involves the use of a weighted test statistic, $D*$, and still uses continous data.

$$D* = \frac{1}{N}\sum_{i=1}^{k}\frac{1}{n_i}\sum_{j=1}^{N-1}\frac{(NM_{ij} - jn_i)^2}{j(N-j)} \tag{15.5}$$

Here, M_{ij} is the number of observations in the ith sample not greater than the jth pooled ordered sample between the distributions, and N is the number of all pooled observations.

15.1.3 Mann-Whitney U Test

The Mann-Whitney U test, otherwise known as the Wilcoxon-Mann-Whitney test, is another widely accepted distributional test that relies on continuous data, but is less powerful than the Kolmogorov-Smirnov test and its variations in that it assumes the foreground and background have the same shape. Here, the foreground and background distributions are combined and ranked together. Each value is given a rank between 1 and the total number of ρ values in both the background and foreground. The distributions are then separated, and the values of the ranks summed for each. The hypothesis is that if the sum of the ranks is roughly equivalent, then the ρ values were evenly distributed when combined and thus the two distributions come from the same population; if there is a large discrepancy in the sum of the ranks, then the ρ values were clustered at the extremes and thus the two distributions come from different populations. The test statistic U is given as:

$$U = N_F N_B + \frac{N_B(N_B+1)}{2} - \sum_{i=1}^{N} rank_B \tag{15.6}$$

The U statistic is then converted into a z-value, and later can be converted into a p-value by well-established methods.

$$z = \frac{U - \frac{N_F N_B}{2}}{\sqrt{\frac{N_F N_B (N_F + N_B + 1)}{12}}} \tag{15.7}$$

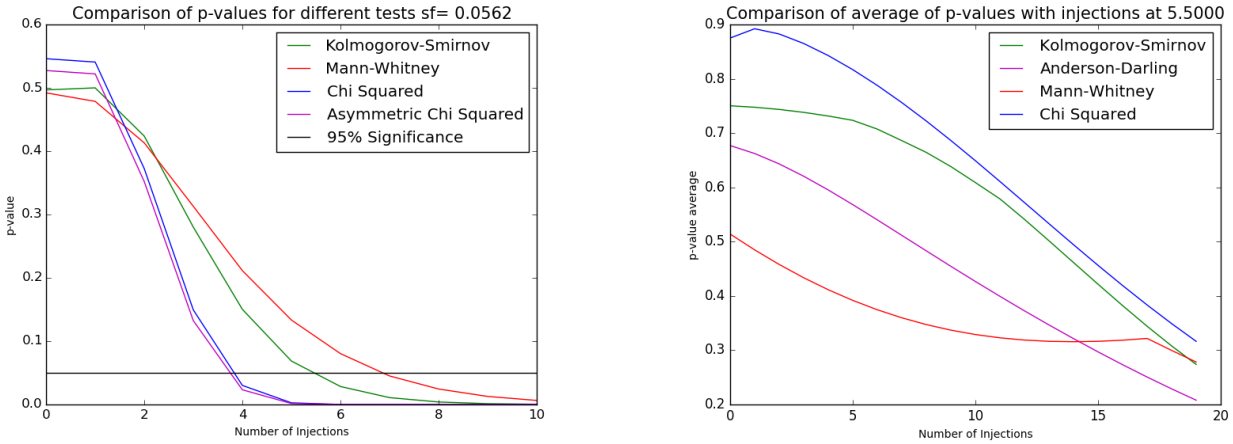

Figure 15.2: Examples of comparing of performence between different non-parametric tests. *Left*: Injections at distance of 178kpc. *Right*: Injections with average ρ=5.5.

15.1.4 Chi Squared Test

The last well-established test used is the Chi Squared test. This differs from the other tests in that it requires binned data. The background is binned first and evenly so that each bin is the same width in order to preserve the shape of the background. The foreground is then binned with the same bins and the number of counts in each bin for each distribution is compared. The test statistic, χ^2, can be calculated as follows:

$$\chi^2 = \sum_i \frac{(\sqrt{\frac{\sum_i F_i}{\sum_i B_i}} B_i - \sqrt{\frac{\sum_i B_i}{\sum_i F_i}} F_i)^2}{B_i + Fi} \tag{15.8}$$

The χ^2 statistic can then be converted into a p-value using the standard χ^2 distribution.

15.1.5 Gravitational wave population

For the purposes of this study, a rotary bar waveform (lb5, see section 5.5.3) is used to simulate the gravitational wave candidates from supernovae, which his is an extreme emission model. Further, only supernovae occuring up to 25Mpc are considered as this is considered the upper bound of aLIGO range. As in the opticallytargeted searches (section 5 and 8), we assume standard candle approach. We inject waveforms according to the distance or the ρ value. We consider subthreshold events, which do not exceed 3σ confidence.

15.2 Results and discussion

To compare the efficiency of the tests, each is compared to the other with various background and foreground data.Figure 15.2 shows examples of comparison of performance between different distributional tests. Both plots present the p-values as functions of how many waveforms are added to the foreground. We average the results based on the results of 300 foregrounds. In the left panel we consider injections at fixed distance of 178kpc. The

injections have relatively large ρ values and only several injections are enough to reach 95% significance level that the two distributions are different. On the right panel we inject waveforms with average $\rho = 5.5$ value. In this case the injections are weaker and even 20 injections are not enough to reach 95% confidence level. In the two cases we use different background samples and the initial p-values vary.

Notice also that the performence for each test depend on the data used. These results show that the growing number of injections indeed make the background and foreground distributions to vary, however more studies are needed to find which test performs gives better results and in what conditions.

Bibliography

[1] Crab nebula - a sn 1054 remnant. https://en.wikipedia.org/wiki/Crab_Nebula#/media/File:Crab_Nebula.jpg. Accessed: 2018-07-20.

[2] S. E. Gossan, P. Sutton, A. Stuver, M. Zanolin, K. Gill, and C. D. Ott. Observing gravitational waves from core-collapse supernovae in the advanced detector era. *Phys. Rev. D*, 93:042002, Feb 2016.

[3] M. J. Szczepańczyk and C. D. Ott. Expressing gravitaional waves energy in terms of quadrupole moment. *LIGO Document Control Center*, (LIGO-T1500586), November 2015.

[4] Spacetime curvature. https://commons.wikimedia.org/wiki/File:Spacetime_curvature.png. Accessed: 2018-07-07.

[5] Spiral dance of black holes. https://www.ligo.caltech.edu/image/ligo20160615f. Accessed: 2018-07-07.

[6] Mengyao Wang, Haixing Miao, Andreas Freise, and Yanbei Chen. Sensitivity of intracavity filtering schemes for detecting gravitational waves. *Physical Review D*, 89(6), mar 2014.

[7] What is an interferometer? https://www.ligo.caltech.edu/WA/page/what-is-interferometer. Accessed: 2018-07-01.

[8] Ligo hanford. https://www.ligo.caltech.edu/WA/image/ligo20150731f. Accessed: 2018-07-01.

[9] Ko Nakamura, Shunsaku Horiuchi, Masaomi Tanaka, Kazuhiro Hayama, Tomoya Takiwaki, and Kei Kotake. Multimessenger signals of long-term core-collapse supernova simulations: synergetic observation strategies. *Monthly Notices of the Royal Astronomical Society*, 461(3):3296–3313, jun 2016.

[10] V Necula, S Klimenko, and G Mitselmakher. Transient analysis with fast wilson-daubechies time-frequency transform. *Journal of Physics: Conference Series*, 363:012032, jun 2012.

[11] S Klimenko and G Mitselmakher. A wavelet method for detection of gravitational wave bursts. *Classical and Quantum Gravity*, 21(20):S1819–S1830, sep 2004.

[12] H. Grote, K. Danzmann, K. L. Dooley, R. Schnabel, J. Slutsky, and H. Vahlbruch. First Long-Term Application of Squeezed States of Light in a Gravitational-Wave Observatory. *Phys. Rev. Lett.*, 110(18):181101, May 2013.

[13] S. Klimenko, I. Yakushin, A. Mercer, and G. Mitselmakher. A coherent method for detection of gravitational wave bursts. *Class. Quantum Grav.*, 25:114029, June 2008.

[14] P. J. Sutton, G. Jones, S. Chatterji, P. Kalmus, I. Leonor, S. Poprocki, J. Rollins, A. Searle, L. Stein, M. Tinto, and M. Was. X-Pipeline: an analysis package for autonomous gravitational-wave burst searches. *N. J. Phys.*, 12:053034, May 2010.

[15] Michal Was, Patrick J. Sutton, Gareth Jones, and Isabel Leonor. Performance of an externally triggered gravitational-wave burst search. *Phys. Rev.*, D86:022003, 2012.

[16] B P Abbott, others, LIGO Scientific Collaboration, and Virgo Collaboration. Characterization of transient noise in advanced ligo relevant to gravitational wave signal gw150914. *Classical and Quantum Gravity*, 33(13):134001, 2016.

[17] B. P. Abbott et al. First targeted search for gravitational-wave bursts from core-collapse supernovae in data of first-generation laser interferometer detectors. *Phys. Rev. D*, 94:102001, Nov 2016.

[18] B. P. Abbott et al. All-sky search for short gravitational-wave bursts in the first advanced LIGO run. *Physical Review D*, 95(4), feb 2017.

[19] B. P. Abbott et al. Observation of gravitational waves from a binary black hole merger. *Phys. Rev. Lett.*, 116:061102, Feb 2016.

[20] C. Biwer, D. Barker, J. C. Batch, J. Betzwieser, R. P. Fisher, E. Goetz, S. Kandhasamy, S. Karki, J. S. Kissel, A. P. Lundgren, D. M. Macleod, A. Mullavey, K. Riles, J. G. Rollins, K. A. Thorne, E. Thrane, T. D. Abbott, B. Allen, D. A. Brown, P. Charlton, S. G. Crowder, P. Fritschel, J. B. Kanner, M. Landry, C. Lazzaro, M. Millhouse, M. Pitkin, R. L. Savage, P. Shawhan, D. H. Shoemaker, J. R. Smith, L. Sun, J. Veitch, S. Vitale, A. J. Weinstein, N. Cornish, R. C. Essick, M. Fays, E. Katsavounidis, J. Lange, T. B. Littenberg, R. Lynch, P. M. Meyers, F. Pannarale, R. Prix, R. O'Shaughnessy, and D. Sigg. Validating gravitational-wave detections: The advanced LIGO hardware injection system. *Physical Review D*, 95(6), mar 2017.

[21] B. P. Abbott et al. Gw170817: Observation of gravitational waves from a binary neutron star inspiral. *Phys. Rev. Lett.*, 119:161101, Oct 2017.

[22] S. Scheidegger, R. Käppeli, S. C. Whitehouse, T. Fischer, and M. Liebendörfer. The influence of model parameters on the prediction of gravitational wave signals from stellar core collapse. *Astronomy and Astrophysics*, 514:A51, may 2010.

[23] Tomoya Takiwaki, Kei Kotake, and Yudai Suwa. Three-dimensional simulations of rapidly rotating core-collapse supernovae: finding a neutrino-powered explosion aided by non-axisymmetric flows. *Monthly Notices of the Royal Astronomical Society: Letters*, 461(1):L112–L116, may 2016.

[24] Anthony L. Piro and Eric Pfahl. Fragmentation of collapsar disks and the production of gravitational waves. *The Astrophysical Journal*, 658(2):1173–1176, apr 2007.

[25] C. D. Ott, C. Reisswig, E. Schnetter, E. O'Connor, U. Sperhake, F. Löffler, P. Diener, E. Abdikamalov, I. Hawke, and A. Burrows. Dynamics and gravitational wave signature of collapsar formation. *Physical Review Letters*, 106(16), apr 2011.

[26] Pablo Cerdá-Durán, Nicolas DeBrye, Miguel A. Aloy, José A. Font, and Martin Obergaulinger. Gravitational wave signatures in black-hole-forming core collapse. *The Astrophysical Journal*, 779(2):L18, dec 2013.

[27] C. Casentini, G. Pagliaroli, C. Vigorito, and V. Fafone. Pinpointing astrophysical bursts of low-energy neutrinos embedded into the noise, 2018.

[28] K. N. Yakunin, E. Endeve, A. Mezzacappa, M. Szczpanczyk, M. Zanolin, P. Marronetti, E. J. Lentz, S. W. Bruenn, W. R. Hix, O. E. B. Messer, J. M. Blondin, and J. A. Harris. Gravitational wave signals from multi-dimensional core-collapse supernova explosion simulations, 2017.

[29] Jade Powell, Marek Szczepanczyk, and Ik Siong Heng. Inferring the core-collapse supernova explosion mechanism with three-dimensional gravitational-wave simulations. *Phys. Rev. D*, 96:123013, Dec 2017. arXiv:1709.00955.

[30] Kiranjyot Gill, Wenhui Wang, Oscar Valdez, Marek Szczepanczyk, Michele Zanolin, and Soma Mukherjee. Enhancing the sensitivity of searches for gravitational waves from core-collapse supernovae with a bayesian classification of candidate events, 2018. arXiv:1802.07255.

[31] C. Reisswig, C. D. Ott, U. Sperhake, and E. Schnetter. Gravitational wave extraction in simulations of rotating stellar core collapse. *Physical Review D*, 83(6), mar 2011.

[32] Michele Maggiore. *Gravitational Waves : Volume 1: Theory and Experiments.* Oxford University Press, Oxford, 2007.

[33] E. Müller, H.-T. Janka, and A. Wongwathanarat. Parametrized 3D models of neutrino-driven supernova explosions. Neutrino emission asymmetries and gravitational-wave signals. *Astron. Astrophys.* , 537:A63, January 2012.

[34] S. Scheidegger, R. Käppeli, S. C. Whitehouse, T. Fischer, and M. Liebendörfer. The influence of model parameters on the prediction of gravitational wave signals from stellar core collapse. *Astron. Astrophys.* , 514:A51, May 2010.

[35] P. J. Sutton. A Rule of Thumb for the Detectability of Gravitational-Wave Bursts. *arXiv:1304.0210*, 2013.

[36] Charles Misner. *Gravitation.* Princeton University Press, Princeton, N.J, 2017.

[37] Anjasha Gangopadhyay, Kuntal Misra, A. Pastorello, D. K. Sahu, L. Tomasella, L. Tartaglia, Mridweeka Singh, Raya Dastidar, S. Srivastav, P. Ochner, Peter J. Brown, G. C. Anupama, S. Benetti, E. Cappellaro, Brajesh Kumar, Brijesh Kumar, and S. B. Pandey. Sn 2015as: A low luminosity type iib supernova without an early light curve peak. 2018.

[38] K. N. Yakunin, A. Mezzacappa, P. Marronetti, S. Yoshida, S. W. Bruenn, W. R. Hix, E. J. Lentz, O. E. B. Messer, J. A. Harris, E. Endeve, J. M. Blondin, and E. J. Lingerfelt. Gravitational Wave Signatures of Ab Initio Two-Dimensional Core Collapse Supernova Explosion Models for 12-25 Solar Masses Stars. *Submitted to Phys. Rev. D.; arXiv:1505.05824*, May 2015.

[39] H. Dimmelmeier, C. D. Ott, A. Marek, and H.-T. Janka. Gravitational wave burst signal from core collapse of rotating stars. *Phys. Rev. D.*, 78:064056, 2008.

[40] S. Scheidegger, S. C. Whitehouse, R. Käppeli, and M. Liebendörfer. Gravitational waves from supernova matter. *Class. Quantum Grav.*, 27:114101, June 2010.

[41] A. L. Piro and E. Pfahl. Fragmentation of Collapsar Disks and the Production of Gravitational Waves. *Astrophys. J.*, 658:1173, April 2007.

[42] Jon C. Mauerhan, G. Grant Williams, Douglas C. Leonard, Paul S. Smith, Alexei V. Filippenko, Nathan Smith, Jennifer L. Hoffman, Leah Huk, Kelsey I. Clubb, Jeffrey M. Silverman, S. Bradley Cenko, Peter Milne, Avishay Gal-Yam, and Sagi Ben-Ami. Spectropolarimetry of SN 2011dh in m51: geometric insights on a type IIb supernova progenitor and explosion. *Monthly Notices of the Royal Astronomical Society*, 453(4):4468–4485, sep 2015.

[43] D. C. Leonard. ASTRONOMY: A supernova riddle. *Science*, 315(5809):193–194, jan 2007.

[44] S. E. Boggs, F. A. Harrison, H. Miyasaka, B. W. Grefenstette, A. Zoglauer, C. L. Fryer, S. P. Reynolds, D. M. Alexander, H. An, D. Barret, F. E. Christensen, W. W. Craig, K. Forster, P. Giommi, C. J. Hailey, A. Hornstrup, T. Kitaguchi, J. E. Koglin, K. K. Madsen, P. H. Mao, K. Mori, M. Perri, M. J. Pivovaroff, S. Puccetti, V. Rana, D. Stern, N. J. Westergaard, and W. W. Zhang. 44ti gamma-ray emission lines from SN1987a reveal an asymmetric explosion. *Science*, 348(6235):670–671, may 2015.

[45] K. Asakura, A. Gando, Y. Gando, T. Hachiya, S. Hayashida, H. Ikeda, K. Inoue, K. Ishidoshiro, T. Ishikawa, S. Ishio, M. Koga, S. Matsuda, T. Mitsui, D. Motoki, K. Nakamura, S. Obara, T. Oura, I. Shimizu, Y. Shirahata, J. Shirai, A. Suzuki, H. Tachibana, K. Tamae, K. Ueshima, H. Watanabe, B. D. Xu, A. Kozlov, Y. Takemoto, S. Yoshida, K. Fushimi, A. Piepke, T. I. Banks, B. E. Berger, B. K. Fujikawa, T. O'Donnell, J. G. Learned, J. Maricic, S. Matsuno, M. Sakai, L. A. Winslow, Y. Efremenko, H. J. Karwowski, D. M. Markoff, W. Tornow, J. A. Detwiler, S. Enomoto, and M. P. Decowski and. KamLAND SENSITIVITY TO NEUTRINOS FROM PRE-SUPERNOVA STARS. *The Astrophysical Journal*, 818(1):91, feb 2016.

[46] Salvatore Vitale and Michele Zanolin. Application of asymptotic expansions for maximum likelihood estimators' errors to gravitational waves from inspiraling binary systems: The network case. *Physical Review D*, 84(10), nov 2011.

[47] S. Klimenko, G. Vedovato, M. Drago, F. Salemi, V. Tiwari, G. A. Prodi, C. Lazzaro, K. Ackley, S. Tiwari, C. F. Da Silva, and G. Mitselmakher. Method for detection and reconstruction of gravitational wave transients with networks of advanced detectors. *Physical Review D*, 93(4), feb 2016.

[48] M. Drago. *Search for transient gravitational wave signals with unknown waveform in the LIGO Virgo network of inteferometric detectors using a fully coherent algorithm.* PhD thesis, University of Padova, 2011.

[49] S. Klimenko, S. Mohanty, M. Rakhmanov, and G. Mitselmakher. Constraint likelihood analysis for a network of gravitational wave detectors. *Physical Review D*, 72(12), dec 2005.

[50] B. P. Abbott et al. LIGO: the Laser Interferometer Gravitational-Wave Observatory. *Rep. Prog. Phys.*, 72(7):076901, July 2009.

[51] H. Grote. The GEO 600 status. *Class. Quantum Grav.*, 27:084003, April 2010.

[52] T. Accadia, F. Acernese, M. Alshourbagy, P. Amico, F. Antonucci, S. Aoudia, N. Arnaud, C. Arnault, K. G. Arun, P. Astone, and et al. Virgo: a laser interferometer to detect gravitational waves. *Journal of Instrumentation*, 7:3012, March 2012.

[53] Harvard/CFA List of Supernovae.

[54] Maurice H. P. M. van Putten. Directed searches for broadband extended gravitational wave emission in nearby energetic core-collapse supernovae. *The Astrophysical Journal*, 819(2):169, 2016.

[55] J. Aasi et al. Advanced LIGO. *Class. Quantum Grav.*, 32:074001, 2015.

[56] F. Acernese et al. Advanced Virgo: a second-generation interferometric gravitational wave detector. *Class. Quant. Grav.*, 32(2):024001, 2015.

[57] Yoichi Aso, Yuta Michimura, Kentaro Somiya, Masaki Ando, Osamu Miyakawa, Takanori Sekiguchi, Daisuke Tatsumi, and Hiroaki Yamamoto. Interferometer design of the kagra gravitational wave detector. *Phys. Rev. D*, 88:043007, Aug 2013.

[58] C. D. Ott. TOPICAL REVIEW: The gravitational-wave signature of core-collapse supernovae. *Class. Quantum Grav.*, 26:063001, March 2009.

[59] G. Pagliaroli, F. Vissani, E. Coccia, and W. Fulgione. Neutrinos from Supernovae as a Trigger for Gravitational Wave Search. *Phys. Rev. Lett.*, 103(3):031102, July 2009.

[60] M. Ikeda et al. Search for Supernova Neutrino Bursts at Super-Kamiokande. *Astrophys. J.*, 669:519, 2007.

[61] I. Leonor, L. Cadonati, E. Coccia, S. D'Antonio, A. Di Credico, V. Fafone, R. Frey, W. Fulgione, E. Katsavounidis, C. D. Ott, G. Pagliaroli, K. Scholberg, E. Thrane, and F. Vissani. Searching for prompt signatures of nearby core-collapse supernovae by a joint analysis of neutrino and gravitational wave data. *Class. Quantum Grav.*, 27:084019, April 2010.

[62] Ko Nakamura, Shunsaku Horiuchi, Masaomi Tanaka, Kazuhiro Hayama, Tomoya Takiwaki, and Kei Kotake. Multimessenger signals of long-term core-collapse supernova simulations: synergetic observation strategies. *Monthly Notices of the Royal Astronomical Society*, 461(3):3296–3313, 2016.

[63] A. V. Filippenko. Optical Spectra of Supernovae. *Ann. Rev. Astron. Astrophys.*, 35:309, 1997.

[64] S. J. Smartt. Progenitors of Core-Collapse Supernovae. *Ann. Rev. Astron. Astroph.* , 47:63, September 2009.

[65] M. D. Kistler, W. C. Haxton, and H. Yüksel. Tomography of Massive Stars from Core Collapse to Supernova Shock Breakout. *Astrophys. J.*, 778:81, November 2013.

[66] C. D. Matzner and C. F. McKee. The Expulsion of Stellar Envelopes in Core-Collapse Supernovae. *Astrophys. J.*, 510:379, January 1999.

[67] V. Morozova, A. L. Piro, M. Renzo, C. D. Ott, D. Clausen, S. M. Couch, J. Ellis, and L. F. Roberts. Light Curves of Core-collapse Supernovae with Substantial Mass Loss Using the New Open-source SuperNova Explosion Code (SNEC). *Astrophys. J.*, 814:63, November 2015.

[68] M. C. Bersten, O. G. Benvenuto, K. Nomoto, M. Ergon, G. Folatelli, J. Sollerman, S. Benetti, M. T. Botticella, M. Fraser, R. Kotak, K. Maeda, P. Ochner, and L. Tomasella. The Type IIb Supernova 2011dh from a Supergiant Progenitor. *Astrophys. J.*, 757:31, September 2012.

[69] D. Kasen and S. E. Woosley. Type II Supernovae: Model Light Curves and Standard Candle Relationships. *Astrophys. J.*, 703:2205–2216, October 2009.

[70] A. M. Soderberg, E. Berger, K. L. Page, P. Schady, J. Parrent, D. Pooley, X.-Y. Wang, E. O. Ofek, A. Cucchiara, A. Rau, E. Waxman, J. D. Simon, D. C.-J. Bock, P. A. Milne, M. J. Page, J. C. Barentine, S. D. Barthelmy, A. P. Beardmore, M. F. Bietenholz, P. Brown, A. Burrows, D. N. Burrows, G. Byrngelson, S. B. Cenko, P. Chandra, J. R. Cummings, D. B. Fox, A. Gal-Yam, N. Gehrels, S. Immler, M. Kasliwal, A. K. H. Kong, H. A. Krimm, S. R. Kulkarni, T. J. Maccarone, P. Mészáros, E. Nakar, P. T. O'Brien, R. A. Overzier, M. de Pasquale, J. Racusin, N. Rea, and D. G. York. An extremely luminous X-ray outburst at the birth of a supernova. ??*jnlNature*, 453:469, May 2008.

[71] S. Gezari, L. Dessart, S. Basa, D. C. Martin, J. D. Neill, S. E. Woosley, D. J. Hillier, G. Bazin, K. Forster, P. G. Friedman, J. Le Du, A. Mazure, P. Morrissey, S. G. Neff, D. Schiminovich, and T. K. Wyder. Probing Shock Breakout with Serendipitous GALEX Detections of Two SNLS Type II-P Supernovae. *Astrophys. J. Lett.*, 683:L131, August 2008.

[72] D. F. Cowen, A. Franckowiak, and M. Kowalski. Estimating the explosion time of core-collapse supernovae from their optical light curves. *Astropart. Phys.*, 33:19, February 2010.

[73] R. P. Kirshner and J. Kwan. Distances to extragalactic supernovae. *Astrophys. J.*, 193:27, October 1974.

[74] L. Dessart and D. J. Hillier. Distance determinations using type II supernovae and the expanding photosphere method. *Astron. Astrophys.* , 439:671, August 2005.

[75] D. Madison and W. Li. Supernova 2007gr in NGC 1058. *Central Bureau Electronic Telegrams*, 1034:1, August 2007.

[76] A. V. Filippenko, W. D. Li, R. R. Treffers, and M. Modjaz. The Lick Observatory Supernova Search with the Katzman Automatic Imaging Telescope. In B. Paczynski, W.-P. Chen, and C. Lemme, editors, *IAU Colloq. 183: Small Telescope Astronomy on Global Scales*, volume 246 of *Ast. Soc. Pac. Conf. Ser.*, page 121, 2001.

[77] R. M. Crockett, J. R. Maund, S. J. Smartt, S. Mattila, A. Pastorello, J. Smoker, A. W. Stephens, J. Fynbo, J. J. Eldridge, I. J. Danziger, and C. R. Benn. The Birth Place of the Type Ic Supernova 2007gr. *Astrophys. J. Lett.*, 672:L99, January 2008.

[78] P. A. Mazzali, I. Maurer, S. Valenti, R. Kotak, and D. Hunter. The Type Ic SN 2007gr: a census of the ejecta from late-time optical-infrared spectra. *Mon. Not. Roy. Astron. Soc.* , 408:87–96, October 2010.

[79] J. J. Eldridge, M. Fraser, S. J. Smartt, J. R. Maund, and R. M. Crockett. The death of massive stars - II. Observational constraints on the progenitors of Type Ibc supernovae. *Mon. Not. Roy. Astron. Soc.* , 436:774, November 2013.

[80] J. Chen, X. Wang, M. Ganeshalingam, J. M. Silverman, A. V. Filippenko, W. Li, R. Chornock, J. Li, and T. Steele. Optical Observations of the Type Ic Supernova 2007gr in NGC 1058. *Astrophys. J.*, 790:120, August 2014.

[81] B. P. Schmidt, R. P. Kirshner, R. G. Eastman, M. M. Phillips, N. B. Suntzeff, M. Hamuy, J. Maza, and R. Aviles. The distances to five Type II supernovae using the expanding photosphere method, and the value of H_0. *Astrophys. J.*, 432:42, September 1994.

[82] N. A. Silbermann, P. Harding, B. F. Madore, R. C. Kennicutt, Jr., A. Saha, P. B. Stetson, W. L. Freedman, J. R. Mould, J. A. Graham, R. J. Hill, A. Turner, F. Bresolin, L. Ferrarese, H. Ford, J. G. Hoessel, M. Han, J. Huchra, S. M. G. Hughes, G. D. Illingworth, R. Phelps, and S. Sakai. The Hubble Space Telescope Key Project on the Extragalactic Distance Scale. VI. The Cepheids in NGC 925. *Astrophys. J.*, 470:1, October 1996.

[83] R. Chornock, A. V. Filippenko, W. Li, R. J. Foley, A. Stockton, E. C. Moran, J. Hodge, and K. Merriman. Supernova 2008ax in NGC 4490. *Central Bureau Electronic Telegrams*, 1298:1, March 2008.

[84] R. Mostardi, W. Li, and A. V. Filippenko. Possible Supernova in NGC 4490. *Central Bureau Electronic Telegrams*, 1280:1, March 2008.

[85] R. Arbour. Supernova 2008ax in NGC 4490. *Central Bureau Electronic Telegrams*, 1286:2, March 2008.

[86] R. Chornock, A. V. Filippenko, W. Li, G. H. Marion, R. J. Foley, M. Modjaz, M. Rafelski, G. D. Becker, W. H. de Vries, P. Garnavich, R. A. Jorgenson, D. K. Lynch, A. L. Malec, E. C. Moran, M. T. Murphy, R. J. Rudy, R. W. Russell, J. M. Silverman, T. N. Steele, A. Stockton, A. M. Wolfe, and C. E. Woodward. The Transitional Stripped-envelope SN 2008ax: Spectral Evolution and Evidence for Large Asphericity. *Astrophys. J.*, 739:41, September 2011.

[87] R. M. Crockett, J. J. Eldridge, S. J. Smartt, A. Pastorello, A. Gal-Yam, D. B. Fox, D. C. Leonard, M. M. Kasliwal, S. Mattila, J. R. Maund, A. W. Stephens, and I. J. Danziger. The type IIb SN 2008ax: the nature of the progenitor. *Mon. Not. Roy. Astron. Soc.* , 391:L5, November 2008.

[88] G. Folatelli, M. C. Bersten, H. Kuncarayakti, O. G. Benvenuto, K. Maeda, and K. Nomoto. The Progenitor of the Type IIb SN 2008ax Revisited. *Astrophys. J.in press; arXiv:1509.01588*, September 2015.

[89] A. Pastorello, M. M. Kasliwal, R. M. Crockett, S. Valenti, R. Arbour, K. Itagaki, S. Kaspi, A. Gal-Yam, S. J. Smartt, R. Griffith, K. Maguire, E. O. Ofek, N. Seymour, D. Stern, and W. Wiethoff. The Type IIb SN 2008ax: spectral and light curve evolution. *Mon. Not. Roy. Astron. Soc.* , 389:955, September 2008.

[90] L. A. G. Monard. Supernova 2008bk in NGC 7793. *Central Bureau Electronic Telegrams*, 1315:1, March 2008.

[91] N. Morrell and M. Stritzinger. Supernovae 2008bk and 2008br. *Central Bureau Electronic Telegrams*, 1335:1, April 2008.

[92] D. A. Howell, M. Sullivan, K. Perrett, T. J. Bronder, I. M. Hook, P. Astier, E. Aubourg, D. Balam, S. Basa, R. G. Carlberg, S. Fabbro, D. Fouchez, J. Guy, H. Lafoux, J. D. Neill, R. Pain, N. Palanque-Delabrouille, C. J. Pritchet, N. Regnault, J. Rich, R. Taillet, R. Knop, R. G. McMahon, S. Perlmutter, and N. A. Walton. Gemini Spectroscopy of Supernovae from the Supernova Legacy Survey: Improving High-Redshift Supernova Selection and Classification. *Astrophys. J.*, 634:1190, December 2005.

[93] L. Dessart. private communication, 2011.

[94] M. Hamuy, G. Pignata, J. Maza, A. Clocchiatti, J. Anderson, M. Bersten, G. Folatelli, F. Forster, C. Gutiérrez, J. Quinn, M. Stritzinger, and P. Zelaya. The CHilean Automatic Supernova sEarch . *Mem. Societa Astronomica Italiana*, 83:388, 2012.

[95] J. R. Maund, S. Mattila, E. Ramirez-Ruiz, and J. J. Eldridge. A new precise mass for the progenitor of the Type IIP SN 2008bk. *Mon. Not. Roy. Astron. Soc.* , 438:1577, February 2014.

[96] S. D. Van Dyk, T. J. Davidge, N. Elias-Rosa, S. Taubenberger, W. Li, E. M. Levesque, S. Howerton, G. Pignata, N. Morrell, M. Hamuy, and A. V. Filippenko. Supernova 2008bk and Its Red Supergiant Progenitor. *Astron. J.*, 143:19, January 2012.

[97] S. Mattila, S. J. Smartt, J. J. Eldridge, J. R. Maund, R. M. Crockett, and I. J. Danziger. VLT Detection of a Red Supergiant Progenitor of the Type II-P Supernova 2008bk. *Astrophys. J. Lett.*, 688:L91, December 2008.

[98] W. Li, S. D. van Dyk, A. V. Filippenko, R. J. Foley, G. Pignata, M. Hamuy, J. Moza, D. Reichart, K. Ivarsen, A. Crain, D. Foster, M. Nysewander, and A. Lacluyze. Supernova 2008bk in NGC 7793. *Central Bureau Electronic Telegrams*, 1319:1, March 2008.

[99] G. Pietrzyński, W. Gieren, M. Hamuy, G. Pignata, I. Soszyński, A. Udalski, A. Walker, P. Fouqué, F. Bresolin, R.-P. Kudritzki, A. Garcia-Varela, O. Szewczyk, M. Szymański, M. Kubiak, and Ł. Wyrzykowski. The Araucaria Project: First Cepheid Distance to the Sculptor Group Galaxy NGC 7793 from Variables Discovered in a Wide-field Imaging Survey. *Astron. J.*, 140:1475, November 2010.

[100] B. A. Jacobs, L. Rizzi, R. B. Tully, E. J. Shaya, D. I. Makarov, and L. Makarova. The Extragalactic Distance Database: Color-Magnitude Diagrams. *Astron. J.*, 138:332–337, August 2009.

[101] M. G. Lee, W. L. Freedman, and B. F. Madore. The Tip of the Red Giant Branch as a Distance Indicator for Resolved Galaxies. *Astrophys. J.*, 417:553, November 1993.

[102] T. Griga, A. Marulla, A. Grenier, G. Sun, X. Gao, S. Lamotte Bailey, R. A. Koff, H. Mikuz, B. Dintinjana, J. M. Silverman, S. B. Cenko, A. V. Filippenko, W. Li, M. Yamanaka, R. Itoh, A. Arai, M. Nagashima, and K. Kajiawa. Supernova 2011dh in M51 = Psn J13303600+4706330. *Central Bureau Electronic Telegrams*, 2736:1, June 2011.

[103] G. H. Marion, J. Vinko, R. P. Kirshner, R. J. Foley, P. Berlind, A. Bieryla, J. S. Bloom, M. L. Calkins, P. Challis, R. A. Chevalier, R. Chornock, C. Culliton, J. L. Curtis, G. A. Esquerdo, M. E. Everett, E. E. Falco, K. France, C. Fransson, A. S. Friedman, P. Garnavich, B. Leibundgut, S. Meyer, N. Smith, A. M. Soderberg, J. Sollerman, D. L. Starr, T. Szklenar, K. Takats, and J. C. Wheeler. Type IIb Supernova SN 2011dh: Spectra and Photometry from the Ultraviolet to the Near-infrared. *Astrophys. J.*, 781:69, February 2014.

[104] M. Ergon, J. Sollerman, M. Fraser, A. Pastorello, S. Taubenberger, N. Elias-Rosa, M. Bersten, A. Jerkstrand, S. Benetti, M. T. Botticella, C. Fransson, A. Harutyunyan, R. Kotak, S. Smartt, S. Valenti, F. Bufano, E. Cappellaro, M. Fiaschi, A. Howell, E. Kankare, L. Magill, S. Mattila, J. Maund, R. Naves, P. Ochner, J. Ruiz, K. Smith, L. Tomasella, and M. Turatto. Optical and near-infrared observations of SN 2011dh - The first 100 days. *Astron. Astrophys.* , 562:A17, February 2014.

[105] A. Horesh, C. Stockdale, D. B. Fox, D. A. Frail, J. Carpenter, S. R. Kulkarni, E. O. Ofek, A. Gal-Yam, M. M. Kasliwal, I. Arcavi, R. Quimby, S. B. Cenko, P. E. Nugent, J. S. Bloom, N. M. Law, D. Poznanski, E. Gorbikov, D. Polishook, O. Yaron, S. Ryder, K. W. Weiler, F. Bauer, S. D. Van Dyk, S. Immler, N. Panagia, D. Pooley, and N. Kassim. An early and comprehensive millimetre and centimetre wave and X-ray study of SN 2011dh: a non-equipartition blast wave expanding into a massive stellar wind. *Mon. Not. Roy. Astron. Soc.* , 436:1258, December 2013.

[106] rochesterastronomy.org: SN 2011dh.

[107] S. D. Van Dyk, W. Zheng, K. I. Clubb, A. V. Filippenko, S. B. Cenko, N. Smith, O. D. Fox, P. L. Kelly, I. Shivvers, and M. Ganeshalingam. The Progenitor of Supernova 2011dh has Vanished. *Astrophys. J. Lett.*, 772:L32, August 2013.

[108] J. Vinkó, K. Takáts, T. Szalai, G. H. Marion, J. C. Wheeler, K. Sárneczky, P. M. Garnavich, J. Kelemen, P. Klagyivik, A. Pál, N. Szalai, and K. Vida. Improved distance determination to M 51 from supernovae 2011dh and 2005cs. *Astron. Astrophys.* , 540:A93, April 2012.

[109] S. D. Van Dyk, W. Li, S. B. Cenko, M. M. Kasliwal, A. Horesh, E. O. Ofek, A. L. Kraus, J. M. Silverman, I. Arcavi, A. V. Filippenko, A. Gal-Yam, R. M. Quimby, S. R. Kulkarni, O. Yaron, and D. Polishook. The Progenitor of Supernova 2011dh/PTF11eon in Messier 51. *Astrophys. J. Lett.*, 741:L28, November 2011.

[110] K. Sárneczky, N. Szalai, M. Kun, T. Szalai, K. Takáts, and J. Vinkó. Precise astrometric position of SN2011dh/PTF11eon in M51. *The Astronomer's Telegram*, 3406:1, June 2011.

[111] J. J. Feldmeier, R. Ciardullo, and G. H. Jacoby. Planetary Nebulae as Standard Candles. XI. Application to Spiral Galaxies. *Astrophys. J.*, 479:231, April 1997.

[112] J. L. Tonry, A. Dressler, J. P. Blakeslee, E. A. Ajhar, A. B. Fletcher, G. A. Luppino, M. R. Metzger, and C. B. Moore. The SBF Survey of Galaxy Distances. IV. SBF Magnitudes, Colors, and Distances. *Astrophys. J.*, 546:681–693, January 2001.

[113] R. B. Tully. *Nearby Galaxies Catalog.* Cambridge University Press, Cambridge, UK, April 1988.

[114] B. P. Abbott et al. (LIGO Scientific Collaboration). Search for gravitational-wave bursts in the first year of the fifth LIGO science run. *Phys. Rev. D.*, 80(10):102001, November 2009.

[115] J. Aasi et al. The characterization of Virgo data and its impact on gravitational-wave searches. *Class. Quantum Grav.*, 29(15):155002, August 2012.

[116] J. Aasi et al. Characterization of the LIGO detectors during their sixth science run. *Class. Quantum Grav.*, 32(11):115012, June 2015.

[117] J. McIver. Data quality studies of enhanced interferometric gravitational wave detectors. *Class. Quantum Grav.*, 29(12):124010, June 2012.

[118] K. Kotake. *Comptes Rendus Physique*, 14:318, April 2013.

[119] C. Fryer and K. C. B. New. Gravitational waves from gravitational collapse. *Liv. Rev. Rel.*, 14:1, 2011.

[120] J. Abadie et al. All-sky search for gravitational-wave bursts in the first joint ligo-geo-virgo run. *Phys. Rev. D*, 81(10):102001, May 2010.

[121] Shourov Chatterji, Albert Lazzarini, Leo Stein, Patrick J. Sutton, Antony Searle, and Massimo Tinto. Coherent network analysis technique for discriminating gravitational-wave bursts from instrumental noise. *Phys. Rev. D*, 74:082005, Oct 2006.

[122] Antony C Searle, Patrick J Sutton, Massimo Tinto, and Graham Woan. Robust Bayesian detection of unmodelled bursts. *Class. Quantum Grav.*, 25:114038, 2008.

[123] A. C. Searle, P. J. Sutton, and M. Tinto. Bayesian detection of unmodeled bursts of gravitational waves. *Class. Quantum Grav.*, 26:155017, August 2009.

[124] E. Müller. Gravitational radiation from collapsing rotating stellar cores. *Astron. Astrophys.* , 114:53, October 1982.

[125] T. Zwerger and E. Müller. Dynamics and gravitational wave signature of axisymmetric rotational core collapse. *Astron. Astrophys.* , 320:209, April 1997.

[126] H. Dimmelmeier, J. A. Font, and E. Müller. Relativistic simulations of rotational core collapse II. Collapse dynamics and gravitational radiation. *Astron. Astrophys.* , 393:523, October 2002.

[127] K. Kotake, S. Yamada, and K. Sato. Gravitational radiation from axisymmetric rotational core collapse. *Phys. Rev. D.*, 68:044023, August 2003.

[128] C. D. Ott, A. Burrows, E. Livne, and R. Walder. Gravitational waves from axisymmetric, rotating stellar core collapse. *Astrophys. J.*, 600:834, 2004.

[129] C. D. Ott, H. Dimmelmeier, A. Marek, H.-T. Janka, I. Hawke, B. Zink, and E. Schnetter. 3D Collapse of Rotating Stellar Iron Cores in General Relativity Including Deleptonization and a Nuclear Equation of State. *Phys. Rev. Lett.*, 98:261101, June 2007.

[130] E. Abdikamalov, S. Gossan, A. M. DeMaio, and C. D. Ott. Measuring the angular momentum distribution in core-collapse supernova progenitors with gravitational waves. *Phys. Rev. D.*, 90(4):044001, August 2014.

[131] J. M. Lattimer and F. D. Swesty. A Generalized Equation of State for Hot, Dense Matter. *Nucl. Phys. A*, 535:331, 1991.

[132] K. N. Yakunin, P. Marronetti, A. Mezzacappa, S. W. Bruenn, C.-T. Lee, M. A. Chertkow, W. R. Hix, J. M. Blondin, E. J. Lentz, B. Messer, and S. Yoshida. Gravitational waves from core collapse supernovae. *Class. Quantum Grav.*, 27:194005, October 2010.

[133] E. Müller and H.-T. Janka. Gravitational radiation from convective instabilities in Type II supernova explosions. *Astron. Astrophys.* , 317:140, January 1997.

[134] E. Müller, M. Rampp, R. Buras, H.-T. Janka, and D. H. Shoemaker. Toward Gravitational Wave Signals from Realistic Core-Collapse Supernova Models. *Astrophys. J.*, 603:221, March 2004.

[135] K. Kotake, N. Ohnishi, and S. Yamada. Gravitational Radiation from Standing Accretion Shock Instability in Core-Collapse Supernovae. *Astrophys. J.*, 655:406, January 2007.

[136] J. W. Murphy, C. D. Ott, and A. Burrows. A Model for Gravitational Wave Emission from Neutrino-Driven Core-Collapse Supernovae. *Astrophys. J.*, 707:1173, December 2009.

[137] K. Kotake, W. Iwakami, N. Ohnishi, and S. Yamada. Stochastic Nature of Gravitational Waves from Supernova Explosions with Standing Accretion Shock Instability. *Astrophys. J. Lett.*, 697:L133, June 2009.

[138] A. Marek, H.-T. Janka, and E. Müller. Equation-of-state dependent features in shock-oscillation modulated neutrino and gravitational-wave signals from supernovae. *Astron. Astrophys.* , 496:475, March 2009.

[139] B. Müller, H.-T. Janka, and A. Marek. A New Multi-dimensional General Relativistic Neutrino Hydrodynamics Code of Core-collapse Supernovae. III. Gravitational Wave Signals from Supernova Explosion Models. *Astrophys. J.*, 766:43, March 2013.

[140] C. D. Ott, E. Abdikamalov, P. Mösta, R. Haas, S. Drasco, E. P. O'Connor, C. Reisswig, C. A. Meakin, and E. Schnetter. General-relativistic Simulations of Three-dimensional Core-collapse Supernovae. *Astrophys. J.*, 768:115, May 2013.

[141] Tomoya Takiwaki, Kei Kotake, and Yudai Suwa. Three-dimensional simulations of rapidly rotating core-collapse supernovae: finding a neutrino-powered explosion aided by non-axisymmetric flows. *Monthly Notices of the Royal Astronomical Society: Letters*, 461(1):L112–L116, 2016.

[142] S. E. Gossan, P. Sutton, A. Stuver, M. Zanolin, K. Gill, and C. D. Ott. Observing Gravitational Waves from Core-Collapse Supernovae in the Advanced Detector Era. *Phys. Rev. D.*, 93:042002, November 2016.

[143] A. Burrows, E. Livne, L. Dessart, C. D. Ott, and J. Murphy. A New Mechanism for Core-Collapse Supernova Explosions. *Astrophys. J.*, 640:878, April 2006.

[144] A. Burrows, E. Livne, L. Dessart, C. D. Ott, and J. Murphy. Features of the Acoustic Mechanism of Core-Collapse Supernova Explosions. *Astrophys. J.*, 655:416, January 2007.

[145] C. D. Ott, A. Burrows, L. Dessart, and E. Livne. A New Mechanism for Gravitational-Wave Emission in Core-Collapse Supernovae. *Phys. Rev. Lett.*, 96:201102, May 2006.

[146] A. Marek and H.-T. Janka. Delayed Neutrino-Driven Supernova Explosions Aided by the Standing Accretion-Shock Instability. *Astrophys. J.*, 694:664, March 2009.

[147] D. Lai and S. L. Shapiro. Gravitational radiation from rapidly rotating nascent neutron stars. *Astrophys. J.*, 442:259, 1995.

[148] J. D. Brown. Rotational Instabilities in post-Collapse Stellar Cores. In *AIP Conf. Proc. 575: Astrophysical Sources for Ground-Based Gravitational Wave Detectors*, page 234, 2001.

[149] M. Shibata and Y.-I. Sekiguchi. Three-dimensional simulations of stellar core collapse in full general relativity: Nonaxisymmetric dynamical instabilities. *Phys. Rev. D.*, 71:024014, January 2005.

[150] M. Rampp, E. Müller, and M. Ruffert. Simulations of non-axisymmetric rotational core collapse. *Astron. Astrophys.* , 332:969, April 1998.

[151] C. D. Ott, S. Ou, J. E. Tohline, and A. Burrows. One-armed Spiral Instability in a Low-T/|W| Postbounce Supernova Core. *Astrophys. J.*, 625:L119, June 2005.

[152] C.L. Fryer, D.E. Holz, and S.A. Hughes. Gravitational Wave Emission from Core Collapse of Massive Stars. *Astrophys. J.*, 565:430, 2002.

[153] C. D. Ott. GWs from Barmode Instabilities. Technical Report LIGO-T1000553-v2, LIGO Scientific Collaboration, 2010.

[154] L. Santamaria and C. D. Ott. GWs from Accretion Disk Instabilities. Technical Report LIGO-T1100093-v2, LIGO Scientific Collaboration, 2011.

[155] J. Abadie et al. All-sky search for gravitational-wave bursts in the second joint ligo-virgo run. *Phys. Rev. D*, 85:122007, Jun 2012.

[156] J. Abadie et al. (LIGO Scientific Collaboration and Virgo Collaboration). All-sky search for gravitational-wave bursts in the second joint LIGO-Virgo run. *Phys. Rev. D.*, 85(12):122007, June 2012.

[157] Marc Paterno. Calculating efficiencies and their uncertainties. Technical Report FERMILAB-TM-2286-CD, 2004.

[158] B. P. Abbott et al. (LIGO Scientific Collaboration). Search for high frequency gravitational-wave bursts in the first calendar year of LIGO's fifth science run. *Phys. Rev. D.*, 80:102002, November 2009.

[159] J. Abadie et al. Calibration of the ligo gravitational wave detectors in the fifth science run. *Nuc. Inst. Meth. Phys. Res. A*, 624(1):223, 2010.

[160] F. Marion, B. Mours, and L. Rolland. "h(t) reconstruction for vsr1; version 2 and 3.". Technical Report VIR-0078A-08, 2010.

[161] J. M. Lattimer and M. Prakash. Neutron Star Structure and the Equation of State. *Astrophys. J.*, 550:426, March 2001.

[162] F. Vissani. Comparative analysis of SN1987A antineutrino fluence. *J. Phys. G, Nuc. Phys.*, 42(1):013001, January 2015.

[163] P. Kalmus, M. Zanolin, and S. Klimenko. Excluding Source Models with Multiple Astrophysical Observations. *LIGO Document Control Center*, (LIGO-P1300018-v2), February 2013.

[164] B. P. Abbott, R. Abbott, T. D. Abbott, M. R. Abernathy, F. Acernese, K. Ackley, C. Adams, T. Adams, P. Addesso, R. X. Adhikari, and et al. Prospects for Observing and Localizing Gravitational-Wave Transients with Advanced LIGO and Advanced Virgo. *Living Reviews in Relativity*, 19, February 2016.

[165] Pietro Antonioli, Richard Tresch Fienberg, Fabrice Fleurot, Yoshiyuki Fukuda, Walter Fulgione, Alec Habig, Jaret Heise, Arthur B McDonald, Corrinne Mills, Toshio Namba, Leif J Robinson, Kate Scholberg, Michael Schwendener, Roger W Sinnott, Blake Stacey, Yoichiro Suzuki, Réda Tafirout, Carlo Vigorito, Brett Viren, Clarence Virtue, and Antonino Zichichi. Snews: the supernova early warning system. *New Journal of Physics*, 6(1):114, 2004.

[166] N. Yu. Agafonova, M. Aglietta, P. Antonioli, V. V. Ashikhmin, G. Bari, R. Bertoni, E. Bressan, G. Bruno, V. L. Dadykin, W. Fulgione, P. Galeotti, M. Garbini, P. L. Ghia, P. Giusti, E. Kemp, A. S. Mal'gin, B. Miguez, A. Molinario, R. Persiani, I. A. Pless, V. G. Ryasny, O. G. Ryazhskaya, O. Saavedra, G. Sartorelli, I. R. Shakyrianova, M. Selvi, G. C. Trinchero, C. Vigorito, V. F. Yakushev, A. Zichichi, and A. Razeto. Measurement of the velocity of neutrinos from the cngs beam with the large volume detector. *Phys. Rev. Lett.*, 109:070801, Aug 2012.

[167] G. Alimonti, C. Arpesella, H. Back, M. Balata, D. Bartolomei, A. de Bellefon, G. Bellini, J. Benziger, A. Bevilacqua, D. Bondi, S. Bonetti, A. Brigatti, B. Caccianiga, L. Cadonati, F. Calaprice, C. Carraro, G. Cecchet, R. Cereseto, A. Chavarria, M. Chen, A. Chepurnov, A. Cubaiu, W. Czech, D. D'Angelo, F. Dalnoki-Veress, A. De Bari, E. De Haas, A. Derbin, M. Deutsch, A. Di Credico, A. Di Ludovico, G. Di Pietro, R. Eisenstein, F. Elisei, A. Etenko, F. von Feilitzsch, R. Fernholz, K. Fomenko, R. Ford, D. Franco, B. Freudiger, N. Gaertner, C. Galbiati, F. Gatti, S. Gazzana, V. Gehman, M. Giammarchi, D. Giugni, M. Goeger-Neff, T. Goldbrunner, A. Golubchikov, A. Goretti, C. Grieb, C. Hagner, T. Hagner, W. Hampel, E. Harding, S. Hardy, F.X. Hartmann, R. von Hentig, T. Hertrich, G. Heusser, M. Hult, A. Ianni, An. Ianni, L. Ioannucci, K. Jaenner, M. Joyce, H. de Kerret, S. Kidner, J. Kiko, T. Kirsten, V. Kobychev, G. Korga, G. Korschinek, Yu. Kozlov, D. Kryn, P. La Marche, V. Lagomarsino, M. Laubenstein, C. Lendvai, M. Leung, T. Lewke, E. Litvinovich, B. Loer, F. Loeser, P. Lombardi, L. Ludhova, I. Machulin, S. Malvezzi, A. Manco, J. Maneira, W. Maneschg, I. Manno, D. Manuzio, G. Manuzio, M. Marchelli, A. Martemianov, F. Masetti, U. Mazzucato, K. McCarty, D. McKinsey, Q. Meindl, E. Meroni, L. Miramonti, M. Misiaszek, D. Montanari, M.E. Monzani, V. Muratova, P. Musico, H. Neder, A. Nelson, L. Niedermeier, S. Nisi, L. Oberauer, M. Obolensky, M. Orsini, F. Ortica, M. Pallavicini, L. Papp, R. Parcells, S. Parmeggiano, M. Parodi, N. Pelliccia, L. Perasso, A. Pocar, R. Raghavan, G. Ranucci, W. Rau, A. Razeto, E. Resconi, P. Risso, A. Romani, D. Rountree, A. Sabelnikov, P. Saggese, R. Saldhana, C. Salvo, R. Scardaoni, D. Schimizzi, S. Schönert, K.H. Schubeck, T. Shutt,

F. Siccardi, H. Simgen, M. Skorokhvatov, O. Smirnov, A. Sonnenschein, F. Soricelli, A. Sotnikov, S. Sukhotin, C. Sule, Y. Suvorov, V. Tarasenkov, R. Tartaglia, G. Testera, D. Vignaud, S. Vitale, R.B. Vogelaar, V. Vyrodov, B. Williams, M. Wojcik, R. Wordel, M. Wurm, O. Zaimidoroga, S. Zavatarelli, and G. Zuzel. The borexino detector at the laboratori nazionali del gran sasso. *Nuclear Instruments and Methods in Physics Research Section A: Accelerators, Spectrometers, Detectors and Associated Equipment*, 600(3):568–593, mar 2009.

[168] R. Abbasi, Y. Abdou, T. Abu-Zayyad, M. Ackermann, J. Adams, J. A. Aguilar, M. Ahlers, M. M. Allen, D. Altmann, K. Andeen, J. Auffenberg, X. Bai, M. Baker, S. W. Barwick, V. Baum, R. Bay, J. L. Bazo Alba, K. Beattie, J. J. Beatty, S. Bechet, J. K. Becker, K.-H. Becker, M. L. Benabderrahmane, S. BenZvi, J. Berdermann, P. Berghaus, D. Berley, E. Bernardini, D. Bertrand, D. Z. Besson, D. Bindig, M. Bissok, E. Blaufuss, J. Blumenthal, D. J. Boersma, C. Bohm, D. Bose, S. Böser, O. Botner, A. M. Brown, S. Buitink, K. S. Caballero-Mora, M. Carson, D. Chirkin, B. Christy, F. Clevermann, S. Cohen, C. Colnard, D. F. Cowen, A. H. Cruz Silva, M. V. D'Agostino, M. Danninger, J. Daughhetee, J. C. Davis, C. De Clercq, T. Degner, L. Demirörs, F. Descamps, P. Desiati, G. de Vries-Uiterweerd, T. DeYoung, J. C. Díaz-Vélez, M. Dierckxsens, J. Dreyer, J. P. Dumm, M. Dunkman, J. Eisch, R. W. Ellsworth, O. EngdegAstron. Astrophys. rd, S. Euler, P. A. Evenson, O. Fadiran, A. R. Fazely, A. Fedynitch, J. Feintzeig, T. Feusels, K. Filimonov, C. Finley, T. Fischer-Wasels, B. D. Fox, A. Franckowiak, R. Franke, T. K. Gaisser, J. Gallagher, L. Gerhardt, L. Gladstone, T. Glüsenkamp, A. Goldschmidt, J. A. Goodman, D. Góra, D. Grant, T. Griesel, A. Groß, S. Grullon, M. Gurtner, C. Ha, A. HajIsmail, A. Hallgren, F. Halzen, K. Han, K. Hanson, D. Heinen, K. Helbing, R. Hellauer, S. Hickford, G. C. Hill, K. D. Hoffman, B. Hoffmann, A. Homeier, K. Hoshina, W. Huelsnitz, J.-P. Hülß, P. O. Hulth, K. Hultqvist, S. Hussain, A. Ishihara, E. Jakobi, J. Jacobsen, G. S. Japaridze, H. Johansson, K.-H. Kampert, A. Kappes, T. Karg, A. Karle, P. Kenny, J. Kiryluk, F. Kislat, S. R. Klein, H. Köhne, G. Kohnen, H. Kolanoski, L. Köpke, S. Kopper, D. J. Koskinen, M. Kowalski, T. Kowarik, M. Krasberg, G. Kroll, N. Kurahashi, T. Kuwabara, M. Labare, K. Laihem, H. Landsman, M. J. Larson, R. Lauer, J. Lünemann, J. Madsen, A. Marotta, R. Maruyama, K. Mase, H. S. Matis, K. Meagher, M. Merck, P. Mészáros, T. Meures, S. Miarecki, E. Middell, N. Milke, J. Miller, T. Montaruli, R. Morse, S. M. Movit, R. Nahnhauer, J. W. Nam, U. Naumann, D. R. Nygren, S. Odrowski, A. Olivas, M. Olivo, A. O'Murchadha, S. Panknin, L. Paul, C. Pérez de los Heros, J. Petrovic, A. Piegsa, D. Pieloth, R. Porrata, J. Posselt, P. B. Price, G. T. Przybylski, K. Rawlins, P. Redl, E. Resconi, W. Rhode, M. Ribordy, A. S. Richard, M. Richman, J. P. Rodrigues, F. Rothmaier, C. Rott, T. Ruhe, D. Rutledge, B. Ruzybayev, D. Ryckbosch, H.-G. Sander, M. Santander, S. Sarkar, K. Schatto, T. Schmidt, A. Schönwald, A. Schukraft, L. Schulte, A. Schultes, O. Schulz, M. Schunck, D. Seckel, B. Semburg, S. H. Seo, Y. Sestayo, S. Seunarine, A. Silvestri, K. Singh, A. Slipak, G. M. Spiczak, C. Spiering, M. Stamatikos, T. Stanev, T. Stezelberger, R. G. Stokstad, A. Stößl, E. A. Strahler, R. Ström, M. Stüer, G. W. Sullivan, Q. Swillens, H. Taavola, I. Taboada, A. Tamburro, A. Tepe, S. Ter-Antonyan, S. Tilav, P. A. Toale, S. Toscano, D. Tosi, N. van Eijndhoven, J. Vandenbroucke, A. Van Overloop, J. van Santen, M. Vehring, M. Voge, C. Walck, T. Waldenmaier, M. Wallraff, M. Walter, Ch. Weaver, C. Wendt, S. Westerhoff, N. Whitehorn, K. Wiebe, C. H. Wiebusch, D. R. Williams, R. Wischnewski, H. Wissing, M. Wolf, T. R. Wood, K. Woschnagg, C. Xu, D. L. Xu, X. W. Xu, J. P. Yanez, G. Yodh, S. Yoshida, P. Zarzhitsky, and M. Zoll. IceCube sensitivity for low-energy neutrinos from nearby supernovae. *Astronomy*

& Astrophysics, 535:A109, nov 2011.

[169] E. Cappellaro, M. Turatto, S. Benetti, D. Y. Tsvetkov, O. S. Bartunov, and I. N. Makarova. The rate of supernovae. I - The data base, the recipe and the uncertainties. *Astron. Astrophys.* , 268:472–482, February 1993.

[170] E. Cappellaro, M. Turatto, D. Y. Tsvetkov, O. S. Bartunov, C. Pollas, R. Evans, and M. Hamuy. The rate of supernovae from the combined sample of five searches. *Astron. Astrophys.* , 322:431–441, June 1997.

[171] E. Cappellaro and M. Turatto. The rate of supernovae: biases and uncertainties. In P. Ruiz-Lapuente, R. Canal, and J. Isern, editors, *NATO Advanced Science Institutes (ASI) Series C*, volume 486 of *NATO Advanced Science Institutes (ASI) Series C*, page 77, 1997.

[172] E. Cappellaro, R. Evans, and M. Turatto. A new determination of supernova rates and a comparison with indicators for galactic star formation. *Astron. Astrophys.* , 351:459, November 1999.

[173] M. T. Botticella, M. Riello, E. Cappellaro, S. Benetti, G. Altavilla, A. Pastorello, M. Turatto, L. Greggio, F. Patat, S. Valenti, L. Zampieri, A. Harutyunyan, G. Pignata, and S. Taubenberger. Supernova rates from the Southern inTermediate Redshift ESO Supernova Search (STRESS). *Astron. Astrophys.* , 479:49–66, February 2008.

[174] W. Li, J. Leaman, R. Chornock, A. V. Filippenko, D. Poznanski, M. Ganeshalingam, X. Wang, M. Modjaz, S. Jha, R. J. Foley, and N. Smith. Nearby supernova rates from the Lick Observatory Supernova Search - II. The observed luminosity functions and fractions of supernovae in a complete sample. *Mon. Not. Roy. Astron. Soc.* , 412:1441–1472, April 2011.

[175] J. Leaman, W. Li, R. Chornock, and A. V. Filippenko. Nearby supernova rates from the Lick Observatory Supernova Search - I. The methods and data base. *Mon. Not. Roy. Astron. Soc.* , 412:1419–1440, April 2011.

[176] W. Li, R. Chornock, J. Leaman, A. V. Filippenko, D. Poznanski, X. Wang, M. Ganeshalingam, and F. Mannucci. Nearby supernova rates from the Lick Observatory Supernova Search - III. The rate-size relation, and the rates as a function of galaxy Hubble type and colour. *Mon. Not. Roy. Astron. Soc.* , 412:1473–1507, April 2011.

[177] Robert E. Rutledge. The astronomer's telegram: A web-based short-notice publication system for the professional astronomical community. *Publications of the Astronomical Society of the Pacific*, 110(748):754–756, jun 1998.

[178] B. J. Shappee, J. L. Prieto, D. Grupe, C. S. Kochanek, K. Z. Stanek, G. De Rosa, S. Mathur, Y. Zu, B. M. Peterson, R. W. Pogge, S. Komossa, M. Im, J. Jencson, T.W-S. Holoien, U. Basu, J. F. Beacom, D. M. Szczygieł, J. Brimacombe, S. Adams, A. Campillay, C. Choi, C. Contreras, M. Dietrich, M. Dubberley, M. Elphick, S. Foale, M. Giustini, C. Gonzalez, E. Hawkins, D. A. Howell, E. Y. Hsiao, M. Koss, K. M. Leighly, N. Morrell, D. Mudd, D. Mullins, J. M. Nugent, J. Parrent, M. M. Phillips, G. Pojmanski, W. Rosing, R. Ross, D. Sand, D. M. Terndrup, S. Valenti, Z. Walker, and Y. Yoon. THE MAN BEHIND THE CURTAIN: X-RAYS DRIVE THE UV THROUGH NIR VARIABILITY IN THE 2013 ACTIVE GALACTIC NUCLEUS OUTBURST IN NGC 2617. *The Astrophysical Journal*, 788(1):48, may 2014.

[179] Asras. `www.rochesterastronomy.org/snimages/`. Accessed: 2018-07-29.

[180] Transient name server. `https://wis-tns.weizmann.ac.il/`. Accessed: 2018-07-29.

[181] The open supernova catalog. `https://sne.space/`. Accessed: 2018-07-29.

[182] Central bureau for astronomical telegrams. `http://www.cbat.eps.harvard.edu/cbat.html`. Accessed: 2018-07-29.

[183] F. Huang, X. F. Wang, G. Hosseinzadeh, P. J. Brown, J. Mo, J. J. Zhang, K. C. Zhang, T. M. Zhang, D. A. Howell, I. Arcavi, C. McCully, S. Valenti, L. M. Rui, H. Song, D. F. Xiang, W. X. Li, H. Lin, and L. F. Wang. Sn 2016x: A type ii-p supernova with a signature of shock breakout from explosion of a massive red supergiant. 2018.

[184] L. Tartaglia, D. J. Sand, S. Valenti, S. Wyatt, J. P. Anderson, I. Arcavi, C. Ashall, M. T. Botticella, R. Cartier, T.-W. Chen, A. Cikota, D. Coulter, M. Della Valle, R. J. Foley, A. Gal-Yam, L. Galbany, C. Gall, J. B. Haislip, J. Harmanen, G. Hosseinzadeh, D. A. Howell, E. Y. Hsiao, C. Inserra, S. W. Jha, E. Kankare, C. D. Kilpatrick, V. V. Kouprianov, H. Kuncarayakti, T. J. Maccarone, K. Maguire, S. Mattila, P. A. Mazzali, C. McCully, A. Melandri, N. Morrell, M. M. Phillips, G. Pignata, A. L. Piro, S. Prentice, D. E. Reichart, C. Rojas-Bravo, S. J. Smartt, K. W. Smith, J. Sollerman, M. D. Stritzinger, M. Sullivan, F. Taddia, and D. R. Young. The early detection and follow-up of the highly obscured type II supernova 2016ija/DLT16am. *The Astrophysical Journal*, 853(1):62, jan 2018.

[185] Charles D. Kilpatrick and Ryan J. Foley. The dusty progenitor star of the type ii supernova 2017eaw, 2018.

[186] D. Yu. Tsvetkov, S. Yu. Shugarov, I. M. Volkov, N. N. Pavlyuk, O. V. Vozyakova, N. I. Shatsky, A. A. Nikiforova, I. S. Troitsky, Yu. V. Troitskaya, and P. V. Baklanov. The light curves of type ii-p sn 2017eaw: first 200 days, 2017.

[187] L.-X. Li. Shock breakout in type ibc supernovae and application to GRB 060218/SN 2006aj. *Monthly Notices of the Royal Astronomical Society*, 375(1):240–256, feb 2007.

[188] K. Gill and M. Zanolin. Calculating the On-Source Window of CCSNe and Introducing the Usage of the Expanding Photosphere Method. *LIGO Document Control Center*, (LIGO-T1600296), March 2017.

[189] E. Waxman and B. Katz. Shock breakout theory. *ArXiv e-prints*, July 2016.

[190] J. Vinkó and K. Takáts. The Expanding Photosphere Method: Progress and Problems. In S. Immler, K. Weiler, and R. McCray, editors, *Supernova 1987A: 20 Years After: Supernovae and Gamma-Ray Bursters*, volume 937 of *American Institute of Physics Conference Series*, pages 394–398, October 2007.

[191] S. Bose and B. Kumar. Distance Determination to Eight Galaxies Using Expanding Photosphere Method. *Astrophys. J.*, 782:98, February 2014.

[192] J. Emilio Enriquez, D. C. Leonard, D. Poznanski, A. V. Filippenko, R. Chornock, R. J. Foley, M. Ganeshalingam, W. Li, and J. M. Silverman. The Expanding Photosphere Method (EPM): Distance Calculations to Type II-P Supernovae and a Comparison with the Standard Candle Method. In *American Astronomical*

Society Meeting Abstracts #217, volume 43 of *Bulletin of the American Astronomical Society*, page 337.21, January 2011.

[193] D. C. Leonard, L. Dessart, D. J. Hillier, and G. Pignata. A spectropolarimetric comparison of the type II-Plateau supernovae SN 2008bk and SN 2004dj. In J. L. Hoffman, J. Bjorkman, and B. Whitney, editors, *American Institute of Physics Conference Series*, volume 1429 of *American Institute of Physics Conference Series*, pages 204–207, May 2012.

[194] V. Morozova, A. L. Piro, M. Renzo, C. D. Ott, D. Clausen, S. M. Couch, J. Ellis, and L. F. Roberts. Light Curves of Core-collapse Supernovae with Substantial Mass Loss Using the New Open-source SuperNova Explosion Code (SNEC). *Astrophys. J.*, 814:63, November 2015.

[195] S. Klimenko, G. Vedovato, M. Drago, F. Salemi, V. Tiwari, G. A. Prodi, C. Lazzaro, K. Ackley, S. Tiwari, C. F. Da Silva, and G. Mitselmakher. Method for detection and reconstruction of gravitational wave transients with networks of advanced detectors. *Phys. Rev. D*, 93:042004, Feb 2016.

[196] H.-T. Janka. Explosion Mechanisms of Core-Collapse Supernovae. *Ann. Rev. Nuc. Par. Sci.*, 62:407, November 2012.

[197] Anthony Mezzacappa, Stephen W. Bruenn, Eric J. Lentz, W. Raphael Hix, J. Austin Harris, O. E. Bronson Messer, Eirik Endeve, Merek A. Chertkow, John M. Blondin, Pedro Marronetti, and Konstantin N. Yakunin. Recent progress on ascertaining the core collapse supernova explosion mechanism, 2015.

[198] Thierry Foglizzo, Rémi Kazeroni, Jérôme Guilet, Frédéric Masset, Matthias González, Brendan K. Krueger, Jérôme Novak, Micaela Oertel, Jérôme Margueron, Julien Faure, Noël Martin, Patrick Blottiau, Bruno Peres, and Gilles Durand. The explosion mechanism of core-collapse supernovae: Progress in supernova theory and experiments. *Publications of the Astronomical Society of Australia*, 32, 2015.

[199] Jeremiah W. Murphy, Christian D. Ott, and Adam Burrows. A model for gravitational wave emission from neutrino-driven core-collapse supernovae. *The Astrophysical Journal*, 707(2):1173, 2009.

[200] Bernhard Müller, Hans-Thomas Janka, and Andreas Marek. A NEW MULTI-DIMENSIONAL GENERAL RELATIVISTIC NEUTRINO HYDRODYNAMICS CODE OF CORE-COLLAPSE SUPERNOVAE. III. GRAVITATIONAL WAVE SIGNALS FROM SUPERNOVA EXPLOSION MODELS. *The Astrophysical Journal*, 766(1):43, mar 2013.

[201] John M. Blondin, Anthony Mezzacappa, and Christine DeMarino. Stability of standing accretion shocks, with an eye toward core-collapse supernovae. *The Astrophysical Journal*, 584(2):971–980, feb 2003.

[202] H. A. Bethe. Supernova mechanisms. *Rev. Mod. Phys.*, 62:801, 1990.

[203] A. Burrows. Colloquium: Perspectives on core-collapse supernova theory. *Rev. Mod. Phys.*, 85:245, January 2013.

[204] S. E. Woosley and A. Heger. The progenitor stars of gamma-ray bursts. *The Astrophysical Journal*, 637(2):914–921, feb 2006.

[205] Hans-Thomas Janka. Explosion mechanisms of core-collapse supernovae. *Annual Review of Nuclear and Particle Science*, 62(1):407–451, nov 2012.

[206] M. Abernathy and others (ET science team). Einstein gravitational wave Telescope conceptual designstudy. Technical Report ET-0106C-10, 2011.

[207] M. Paterno. 2004. Tech. Rep. FERMILAB-TM-2286-CD.

[208] B. P. Abbott et al. Search for high frequency gravitational-wave bursts in the first calendar year of LIGO's fifth science run. *Physical Review D*, 80(10), nov 2009.

[209] J. Abadie et al. Calibration of the LIGO gravitational wave detectors in the fifth science run. *Nuclear Instruments and Methods in Physics Research Section A: Accelerators, Spectrometers, Detectors and Associated Equipment*, 624(1):223–240, dec 2010.

[210] F. Marion, B. Mours, and L. Rolland. 2010. Tech. Rep. VIR-0078A-08.

[211] July 2018. Calibration update.

[212] Brennan Hughey. 2014. Error propagation during review.

[213] J. Aasi et al. Search for gravitational radiation from intermediate mass black hole binaries in data from the second ligo-virgo joint science run. *Phys. Rev. D*, 89:122003, Jun 2014.

[214] J. Abadie et al. All-sky search for gravitational-wave bursts in the second joint ligo-virgo run. *Phys. Rev. D*, 85:122007, Jun 2012.

[215] Super-Kamiokande.

[216] Borexino.

[217] G. Alimonti et al. [BOREXINO Collaboration]. The Borexino detector at the Laboratori Nazionali del Gran Sasso. *Nuc. Inst. Meth. Phys. Res. A*, 600:568, March 2009.

[218] Large Volume Detector.

[219] C. Vigorito [LVD Collaboration]. Galactic supernovae monitoring at LVD. *Nuc. Phys. B Proc. Suppl.*, 221:410, December 2011.

[220] Pietro Antonioli, Richard Tresch Fienberg, Fabrice Fleurot, Yoshiyuki Fukuda, Walter Fulgione, et al. SNEWS: The Supernova Early Warning System. *New J.Phys.*, 6:114, 2004.

[221] J. F. Beacom and P. Vogel. Can a supernova be located by its neutrinos? *Phys. Rev. D.*, 60(3):033007, August 1999.

[222] F Acernese et al. Search for gravitational waves associated with grb 050915a using the virgo detector. *Class. Quantum Grav.*, 25(22):225001, 2008.

[223] F. Acernese et al. Gravitational wave burst search in the Virgo C7 data. *Class. Quantum Grav.*, 26:085009, 2008.

[224] M. Szczepanczyk et al. Hardware injections of supernova waveform in single detector case., 2018.

[225] Tomoya Takiwaki and Kei Kotake. Anisotropic emission of neutrino and gravitational-wave signals from rapidly rotating core-collapse supernovae, 2017. arXiv:1711.01905.

[226] Neil J Cornish and Tyson B Littenberg. Bayeswave: Bayesian inference for gravitational wave bursts and instrument glitches. *Classical and Quantum Gravity*, 32(13):135012, jun 2015.

[227] S. Mukherjee, L. Salazar, J. Mittelstaedt, and O. Valdez. New method for enhanced efficiency in detection of gravitational waves from supernovae using coherent network of detectors. *Phys. Rev. D*, 96:104033, Nov 2017.

[228] Takami Kuroda, Kei Kotake, and Tomoya Takiwaki. A NEW GRAVITATIONAL-WAVE SIGNATURE FROM STANDING ACCRETION SHOCK INSTABILITY IN SUPERNOVAE. *The Astrophysical Journal*, 829(1):L14, sep 2016.

[229] Bernhard Müller, Hans-Thomas Janka, and Andreas Marek. A NEW MULTI-DIMENSIONAL GENERAL RELATIVISTIC NEUTRINO HYDRODYNAMICS CODE OF CORE-COLLAPSE SUPERNOVAE. III. GRAVITATIONAL WAVE SIGNALS FROM SUPERNOVA EXPLOSION MODELS. *The Astrophysical Journal*, 766(1):43, mar 2013.

[230] H. Andresen, B. Müller, E. Müller, and H.-Th. Janka. Gravitational wave signals from 3d neutrino hydrodynamics simulations of core-collapse supernovae. *Monthly Notices of the Royal Astronomical Society*, 468(2):2032–2051, mar 2017.

[231] W. G. Anderson, P. R. Brady, J. D. Creighton, and É. É. Flanagan. Excess power statistic for detection of burst sources of gravitational radiation. *Phys. Rev. D.*, 63(4):042003, February 2001.

[232] N. J. Cornish and T. B. Littenberg. Bayeswave: Bayesian inference for gravitational wave bursts and instrument glitches. *Classical and Quantum Gravity*, 32(13):135012, July 2015.

[233] S. Klimenko, I. Yakushin, A. Mercer, and G. Mitselmakher. A coherent method for detection of gravitational wave bursts. *Classical and Quantum Gravity*, 25(11):114029, June 2008.

[234] S. Klimenko, G. Vedovato, M. Drago, F. Salemi, V. Tiwari, G. A. Prodi, C. Lazzaro, K. Ackley, S. Tiwari, C. F. Da Silva, and G. Mitselmakher. Method for detection and reconstruction of gravitational wave transients with networks of advanced detectors. *Phys. Rev. D.*, 93(4):042004, February 2016.

[235] T. B. Littenberg, J. B. Kanner, N. J. Cornish, and M. Millhouse. Enabling high confidence detections of gravitational-wave bursts. *Phys. Rev. D.*, 94(4):044050, August 2016.

[236] J. B. Kanner, T. B. Littenberg, N. Cornish, M. Millhouse, E. Xhakaj, F. Salemi, M. Drago, G. Vedovato, and S. Klimenko. Leveraging waveform complexity for confident detection of gravitational waves. *Phys. Rev. D.*, 93(2):022002, January 2016.

[237] M. Zevin, S. Coughlin, S. Bahaadini, E. Besler, N. Rohani, S. Allen, M. Cabero, K. Crowston, A. Katsaggelos, S. Larson, T. K. Lee, C. Lintott, T. Littenberg, A. Lundgren, C. Oesterlund, J. Smith, L. Trouille, and V. Kalogera. Gravity Spy: Integrating Advanced LIGO Detector Characterization, Machine Learning, and Citizen Science. *ArXiv e-prints*, November 2016.

[238] S. Klimenko, G. Vedovato, M. Drago, G. Mazzolo, G. Mitselmakher, C. Pankow, G. Prodi, V. Re, F. Salemi, and I. Yakushin. Localization of gravitational wave sources with networks of advanced detectors. *Phys. Rev. D.*, 83(10):102001, May 2011.

[239] B. Bécsy, P. Raffai, N. J. Cornish, R. Essick, J. Kanner, E. Katsavounidis, T. B. Littenberg, M. Millhouse, and S. Vitale. Parameter estimation for gravitational-wave bursts with the BayesWave pipeline. *ArXiv e-prints*, December 2016.

[240] C. Plapous, C. Marro, and P. Scalart. Improved signal-to-noise ratio estimation for speech enhancement. *IEEE Transactions on Audio, Speech and Language Processing*, 14(6):2098–2108, nov 2006.

[241] P. Scalart and J.V. Filho. Speech enhancement based on a priori signal to noise estimation. In *1996 IEEE International Conference on Acoustics, Speech, and Signal Processing Conference Proceedings*. IEEE.

[242] Y. Ephraim and D. Malah. Speech enhancement using a minimum-mean square error short-time spectral amplitude estimator. *IEEE Transactions on Acoustics, Speech, and Signal Processing*, 32(6):1109–1121, dec 1984.

[243] O. Cappe. Elimination of the musical noise phenomenon with the ephraim and malah noise suppressor. *IEEE Transactions on Speech and Audio Processing*, 2(2):345–349, apr 1994.

[244] P. Renevey and A. Drygajlo. Detection of reliable features for speech recognition in noisy conditions using a statistical criterion. In *Proc. Workshop Consistent Reliable Acoust. Cues Sound Anal., Aalborg, Denmark*, pages 71–4. IEEE, 2001.

[245] R. Martin. Noise power spectral density estimation based on optimal smoothing and minimum statistics. *IEEE Transactions on Speech and Audio Processing*, 9(5):504–512, jul 2001.

[246] S. Mukherjee, L. Salazar, J. Mittelstaedt, and O. Valdez. New method for enhanced efficiency in detection of gravitational waves from supernovae using coherent network of detectors. *Physical Review D*, 96(10), nov 2017.

[247] B P Abbott et al. Ligo: the laser interferometer gravitational-wave observatory. *Reports on Progress in Physics*, 72(7):076901, 2009.

[248] Chris L. Fryer and Kimberly C. B. New. Gravitational waves from gravitational collapse. *Living Reviews in Relativity*, 14(1), jan 2011.

[249] Jeremiah W. Murphy, Christian D. Ott, and Adam Burrows. A MODEL FOR GRAVITATIONAL WAVE EMISSION FROM NEUTRINO-DRIVEN CORE-COLLAPSE SUPERNOVAE. *The Astrophysical Journal*, 707(2):1173–1190, dec 2009.

[250] B P Abbott et al. Exploring the sensitivity of next generation gravitational wave detectors. *Classical and Quantum Gravity*, 34(4):044001, jan 2017.

[251] B Sathyaprakash et al. Scientific objectives of einstein telescope. *Classical and Quantum Gravity*, 29(12):124013, jun 2012.

[252] Haixing Miao, Huan Yang, and Denis Martynov. Towards the design of gravitational-wave detectors for probing neutron-star physics, 2017.

[253] Huan Yang and Denis Martynov. Testing gravitational memory generation with compact binary mergers, 2018.

[254] Hang Yu, Denis Martynov, Salvatore Vitale, Matthew Evans, David Shoemaker, Bryan Barr, Giles Hammond, Stefan Hild, James Hough, Sabina Huttner, Sheila Rowan, Borja Sorazu, Ludovico Carbone, Andreas Freise, Conor Mow-Lowry, Katherine L. Dooley, Paul Fulda, Hartmut Grote, and Daniel Sigg. Prospects for detecting gravitational waves at 5 hz with ground-based detectors. *Physical Review Letters*, 120(14), apr 2018.

[255] L. Cadonati, D. Shoemaker, A. Lazzarini, B. Berger, S. Rowan, H. Lueck, M. Evans, and B. Sathyaprakash. What comes next for ligo? planning for the post-detection era in gravitational-wave detectors and astrophysics, 2018.

[256] R. Adhikari, N. Smith, A. Brooks, et al. Ligo voyager upgrade concept, 2017.

[257] A. Burrows, T. Janka, A. Mezzacappa, P. Moesta, E. Mueller, et al. Workshop on core collapse supernovae, their signatures in gravitational waves and their detection with ground-based laser interferometers, 2017.

[258] G. Pagliaroli, F. Vissani, E. Coccia, and W. Fulgione. Neutrinos from supernovae as a trigger for gravitational wave search. *Physical Review Letters*, 103(3), jul 2009.

[259] Takami Kuroda, Kei Kotake, Kazuhiro Hayama, and Tomoya Takiwaki. Correlated signatures of gravitational-wave and neutrino emission in three-dimensional general-relativistic core-collapse supernova simulations. *The Astrophysical Journal*, 851(1):62, dec 2017.

[260] C. D. Ott, C. Reisswig, E. Schnetter, E. O'Connor, U. Sperhake, F. Löffler, P. Diener, E. Abdikamalov, I. Hawke, and A. Burrows. Dynamics and gravitational wave signature of collapsar formation. *Physical Review Letters*, 106(16), apr 2011.